

UNIVERSITY OF OKLAHOMA  
GRADUATE COLLEGE

OBSERVATIONS OF SUPERCELL TORNADO EVOLUTION USING A MOBILE,  
RAPID-SCAN, X-BAND RADAR

A DISSERTATION  
SUBMITTED TO THE GRADUATE FACULTY  
in partial fulfillment of the requirements for the  
Degree of  
DOCTOR OF PHILOSOPHY

By

JANA B. HOUSER  
Norman, Oklahoma  
2013

OBSERVATIONS OF SUPERCELL TORNADO EVOLUTION USING A MOBILE,  
RAPID-SCAN, X-BAND RADAR

A DISSERTATION APPROVED FOR THE  
SCHOOL OF METEOROLOGY

BY

---

Dr. Howard B. Bluestein, Chair

---

Dr. Brian Fiedler

---

Dr. Alan Shapiro

---

Dr. Sebastian Torres

---

Dr. May Yuan

© Copyright by JANA B. HOUSER 2013  
All Rights Reserved.

This dissertation is dedicated to all those who have helped me get to where I am today. To my parents, to my early childhood educators, to my second grade teacher Mrs. Roeder who inspired my passion for meteorology, to my high school and college teachers and professors, to my husband, to my adviser and my committee: each one of you has built me up, brick by brick, to where I am today. Thank you.

To my daughter, Caya, the love of my life: may you be a beacon of hope, righteousness, and love to those around you throughout your life and through eternity. Live your dreams, follow your passions, and you can do anything you put your mind to.



## **Acknowledgements**

I would like to acknowledge the contributions of all those who have helped me accomplish this work. Foremost, to my husband Cecil, who has been with me since day one of my graduate career: you are my strength when I am weak, you are my light when I can't see. Thank you for patiently getting through the lonely late nights while I burn the midnight oil, for comforting me when I am overwhelmed, and for all your help around our home. To my adviser, Dr. Howard Bluestein, who encouraged me to pursue this degree and who has been so patient and understanding with me. You have taught me to think more critically, to examine a problem more thoroughly, and to follow my instincts. Thank you to my committee members, Drs. Brian Fiedler, Alan Shapiro, Sebastian Torres, and May Yuan for your thought provoking insight and helpful comments and suggestions. John Tuttle and Matthew Kramar provided code for the TREC algorithm. Thank you to my current office mates, Jeff Snyder and Vivek Mahale, for your help, for participating in distracting rants, for random moral support, and for answering my sometimes silly questions. Thank you also to my former office mates Drs. Robin Tanamachi and Mike French for the knowledge you have passed down to me.

## Table of Contents

Acknowledgements .....	iv
Table of Contents .....	v
List of Tables .....	vii
List of Figures.....	viii
Abstract.....	xv
Chapter 1. Introduction.....	1
Chapter 2. Previous Work .....	6
Tornado Structure .....	9
Tornado Evolution.....	16
i. The Dynamic Pipe Effect .....	17
ii. Bottom-Up Process.....	19
iii. Tornado Intensification, Maintenance and Decay .....	20
iv. Tornadogenesis Failure .....	23
v. Role of Storm-Scale Features.....	24
vi. Cyclic Mesocyclogenesis and Tornadogenesis .....	26
Chapter 3. Project Design.....	31
Tornado Dynamics .....	34
Polarimetric Radar Overview .....	41
vii. Low-Level Inflow and Updraft Signatures: .....	43
viii. $Z_{DR}$ Arc Signature:.....	44
ix. $Z_{DR}$ Columns: .....	46
x. Tornadic Debris Signature:.....	47
Chapter 4. Instrumentation .....	48
Chapter 5. Dataset and Case Study Overview .....	54
Synoptic Overview .....	54
Dataset Details.....	56
Case Study Summary .....	59
i. Phase I (2036-2047) .....	59
ii. Phase II (2046-2057) .....	60
iii. Phase III (2057-2116).....	61
Chapter 6. Analysis Techniques .....	62
Dual-Doppler Analysis .....	62
i. Errors due to an unlevelled radar.....	64
ii. Errors due to mismatched volume samples .....	68
iii. Objective analysis.....	69
iv. Dual-Doppler synthesis .....	70
Single-Doppler Analyses: TREC .....	71
i. Comparison with dual-Doppler analyses.....	81
ii. Comparison with radial velocity .....	84
Pseudo Vorticity Calculations .....	85
Three-Dimensional and Constant Range Cross Sections .....	86
Chapter 7. Results.....	90
Storm Scale Features .....	90
i. Phase i: Tornado 1 ~2036-2048.....	90

ii.	Phase ii: Genesis and intensification of tornado 2 (2046-2057).....	95
iii.	Weak Reflectivity Band .....	101
iv.	Phase iii: Steady-state (2057-2116).....	105
	Kinematics and structure of the tornadoes .....	106
i.	Delta V calculations .....	106
ii.	Three-dimensional vortex structure and evolution.....	110
iii.	Angular momentum plots .....	115
iv.	Observations of the Tornadic Debris Signature .....	118
Chapter 8.	Discussion.....	121
i.	Tornado1 decay: .....	121
ii.	Tornado 2 genesis.....	125
iii.	Tornado 2 intensification.....	130
iv.	Polarimetric Observations .....	136
Chapter 9.	Conclusions.....	137
	Development and evolution of rotation: (Qs 1 and 2).....	138
	Tornado Structure (Q4): .....	141
	Polarimetric data contributions (Q5):.....	141
References	.....	145
Tables	.....	162
Figures	.....	165

## List of Tables

Table 1: Instrument specifications for RaXPol. (Pazmany et al. 2013). .....	162
Table 2: Summary of RaXPol scanning strategies, times, and specifications.....	162
Table 3: Summary of tornadoes observed by RaXPol used for this case study on 24 May 2011. ....	163
Table 4: Error comparisons for dual-Doppler analyses at constant RaXPol elevation angle and varying MWR-05XP angles. Comparisons were made between the analysis of the elevation angle listed and the 4° MWR-RaXPol analysis, which would be the best matched if MWR were perfectly level. ....	163
Table 5: Summary of dual-Doppler parameters for the MWR-05XP and RaXPol for the 2054 analysis. ....	163
Table 6: Root mean square error for the u and v components comparing the TREC-derived and dual-Doppler synthesized winds for different time steps between TREC analyses. Valid for the 205604 dual-Doppler analysis and the TREC times centered on 205604 at z=500m. ....	164

## List of Figures

Figure 1: The tornado vortex simulator at Purdue University (Church et al. 1979, their Fig. 2). .....	165
Figure 2: Radar image of a) a hook echo in the reflectivity field and b) a tornadic vortex signature in the radial velocity field corresponding with the hook echo in a. Image is from the KABR radar, 2313 17 June 2011 .....	166
Figure 3: Conceptual model illustrating the storm-scale structure of a tornadic supercell by Lemon and Doswell (1979) (Their Fig. 7) .....	167
Figure 4: Mesonet observations of air temperature (°F, red line), dewpoint (°F, blue line), wind direction (yellow line, ordinate midline = 180°), max wind gust (mph, purple line), and atmospheric pressure (mb, orange line) as tornadoes passed within close proximity to the instruments. A) Tipton, OK site 7 Nov 2011. B) El Reno, OK site 24 May 2011.....	168
Figure 5: The five regions of tornado flow structure according to Lewellen (1976; 1993). (Photo © Jana Houser). .....	169
Figure 6: Stages of tornado development according to Davies-Jones (1986). (Photos courtesy of H. Bluestein.).....	170
Figure 7: Illustration of tornadogenesis with (a and b) and without (c) the dynamic pipe effect. From Trapp and Davies-Jones (1997), their Fig. 14. ....	171
Figure 8: Illustration of the relative pressure perturbations and areas of convergence and vertical motion associated with the dynamic pipe effect. Left: configuration prior to the establishment of cyclostrophic balance. Right: configuration after some time, when cyclostrophic balance has been achieved and vertical perturbation pressure gradients have been equilibrated. Solid black lines approximate the extent of tornadic rotation. Red circles indicate cyclonic circulation.....	172
Figure 9: Graphical depiction of Walko’s (1993) hypothesis illustrating tilting of vorticity near the surface by a downdraft. Solid bold lines are vortex lines. A (C) indicates anticyclonic (cyclonic) vertical vorticity. (From Straka et al. 2007, their Fig. 4.).....	173
Figure 10: Representation of the cyclic mesocyclogenesis process according to the Burgess et al. (1982) conceptual model. Mesocyclones are indicated by the L. The thick black line represents the track of a tornado. ....	174
Figure 11: Conceptual model from Dowell and Bluestein (2002a) of the cyclic production of mesocyclones and tornadoes. Adapted from Burgess et al. 1982 but differing with the genesis location of the new mesocyclone along a bulge in the RFGF. ....	175
Figure 12: Schematic of the approximate surface patterns for occluding and nonoccluding cyclic mesocyclogenesis (Adlerman and Drogemeier’s Fig. 3). Scalloped black line indicates the surface cold-pool boundary. Red indicates area of vorticity maxima. Light blue indicates updraft areas, and dark blue indicates downdraft areas. Single yellow contour indicates the boundary of the rain area. ....	176
Figure 13: Summary of relationship between shear magnitude and hodograph shape to the cycling behavior of supercells. Hodographs on the left indicate heights (km) and radii of curvature. Numbers on the graphic indicate the 6 km BRN shear, the 0-1 km SRH, and the 0-3 km SRH. ....	177

Figure 14: Illustration of flow around a vortex with increasing swirl ratio ( $S$ ). Adapted from Davies-Jones (1986). ..... 178

Figure 15: Laboratory simulation of vortex breakdown and the transition from a one-cell, laminar vortex, to a turbulent two-cell vortex. .... 179

Figure 16: Generalized velocity profiles for: a. a Rankine vortex, b. a Burgers-Rott vortex. .... 180

Figure 17: Conceptual model of microphysical and polarimetric signatures in supercells. (Kumjian 2011). .... 181

Figure 18: The rapid-scanning, X-band, polarimetric radar (RaXPoI) (Photo courtesy of J. Snyder.) ..... 182

Figure 19: Illustration of the frequency hopping technique used by RaXPoI to obtain independent samples faster than conventional radars. PP indicates pulse pair, P indicates return power for the first pulse in the pair. The subscript H (V) denotes horizontal (vertical) polarization. (Pazmany et al. 2013). .... 183

Figure 20: Surface observations (T and  $T_d$  in  $^{\circ}\text{F}$ , winds in mph) and analyzed surface features valid 1400 24 May 2011. Brown line indicates dryline position. .... 184

Figure 21: Upper air observations and geopotential height (dam, contoured) for 1200 24 May: 850 mb (top) 500 mb (bottom). Temperatures and dewpoints in  $^{\circ}\text{C}$ . .... 185

Figure 22: 1800 UTC OUN rawinsonde. Top: Skew-T, bottom: hodograph. .... 186

Figure 23: Hourly WSR-88D reflectivity imagery from 1900 24 May – 0000 25 May plotted with Oklahoma Mesonet data (2 m wind barbs, air temperature (black,  $^{\circ}\text{F}$ ), Dew point temperature (green,  $^{\circ}\text{F}$ ), and dew point isodrosotherms (gray). .... 187

Figure 24: Tornado tracks and locations of the RaXPoI and MWR-05XP (black stars). Courtesy J. Snyder. .... 188

Figure 25: a) RaXPoI equivalent reflectivity factor ( $\text{dBZ}_e$ ) and b) radial velocity ( $\text{m s}^{-1}$ ) data from the early non-rapid scan data collection mode for an elevation angle of  $4^{\circ}$  at 202135 24 May 2011. The area of interest is circled. Range rings are denoted in km. .... 189

Figure 26: Visual observations of the developing tornado taken from the RaXPoI deployment location (© J. Houser). .... 190

Figure 27: Time of maximum observed radial velocity ( $124.84 \text{ m s}^{-1}$ ) of the deployment. Reflectivity (upper left); unfolded radial velocity (upper right), color bar is from  $\pm 120 \text{ m s}^{-1}$ ; cross correlation coefficient (lower left); and folded radial velocity (lower right), color bar is from  $\pm 42 \text{ m s}^{-1}$ ,  $V_{\text{nyq}} = 38.5 \text{ m s}^{-1}$ . Black arrow points to the pixel of  $124.84 \text{ m s}^{-1}$ . .... 191

Figure 28: Dual-Doppler grid domain and locations of MWR-05XP and RaXPoI for the 205448 analysis. .... 192

Figure 29: The magnitude ( $\text{m s}^{-1}$ ) and direction (vectors) of the errors between the synthesized horizontal wind fields at  $4^{\circ}$  (the reference angle which, according to the uncorrected raw data, most closely matched the height of the RaXPoI data) and the syntheses using the MWR-05XP a)  $1^{\circ}$ , b)  $2.5^{\circ}$ , c)  $5.5^{\circ}$ , d)  $7^{\circ}$  elevation angles. All images were from the 205448 volume and valid at an analysis height of 1 km ARL. .... 193

Figure 30: RaXPoI reflectivity ( $\text{dBZ}$ ) and horizontal wind vectors from dual-Doppler analyses at  $z=1 \text{ km}$  for the RaXPoI - MWR-05XP tilt and roll sensitivity tests valid at 205448. RaXPoI data are from the  $12^{\circ}$  elevation angle, with a beam height of 1 km at the tornado, corresponding with the height of the MWR-05 beam at  $4^{\circ}$ . The effects of

pitch and roll angles of  $1.5^\circ$  and  $3^\circ$  are simulated by using the MWR-05XP a)  $1^\circ$  elevation angle, b)  $2.5^\circ$  elevation angle, c)  $4^\circ$  elevation angle ('truth' if the radar were assumed to be leveled), d)  $5.5^\circ$  elevation angle 3)  $7^\circ$  elevation angle. .... 194

Figure 31: Schematic illustrating the TREC technique correlating reflectivity features at two different times and calculating a motion vector. (From Tuttle and Foote (1990), their Fig. 1.) ..... 195

Figure 32: Comparisons of reflectivity in the left hand panel and radial velocity in the right hand panel when the time difference between scans is 17 seconds (a vs. b), and  $\sim 2$  minutes (a vs. c). ..... 196

Figure 33: Comparison of box sizes for the 100m grid resolution TREC analysis at 2054: a.  $b=8$  grid points, b.  $b=10$  grid points, c.  $b=12$  grid points, and d.  $b=14$  grid points. .... 197

Figure 34: Simulated reflectivity fields for  $f =$  a) 0.1 (1 wave), b) 0.2 (2 waves), and c) 0.3 (3 waves). .... 198

Figure 35: Sine waves used to simulate reflectivity at an initial time (a) and some arbitrary later time where the pattern is shifted by a phase of  $\pi/8$  (b). ..... 199

Figure 36: TREC correlation coefficient values for  $dt=17s$  for each of the three pseudo reflectivity patterns. Top row:  $\phi=\pi/10$ , bottom row:  $\phi=\pi/8$ . ..... 200

Figure 37: Pseudo-reflectivity and TREC-resolved horizontal wind fields for the different patterns.  $Dt=17s$ . Pattern phase shifted by: left  $\phi=\pi/10$ , right  $\phi=\pi/8$ . ..... 201

Figure 38: Same as Figure 37 except for errors between TREC-resolved horizontal winds and actual horizontal winds. .... 202

Figure 39: Comparison of grid resolutions ( $\Delta x=\Delta y$ ) for TREC analyses: a. 50 m grid resolution, b. 100 m grid resolution, c. 250 m grid resolution. .... 203

Figure 40: TREC analysis for the 2-second update time: a. TREC wind vector analysis, b. Correlation coefficient, c. reflectivity field (dBZ) at 205701, d. reflectivity field at 205703. The radar was nearly due north of the center of the grid domain. .... 204

Figure 41: Magnitude and direction of errors in wind vectors comparing dual-Doppler analysis winds for 205557 with TREC-derived winds centered in time around 205601 for various  $\Delta t$ 's: a)  $\Delta t = 2$  s, b)  $\Delta t = 5$  s, c)  $\Delta t = 10$  s, d)  $\Delta t = 15$  s, e)  $\Delta t = 20$  s, f)  $\Delta t = 30$  s, g)  $\Delta t = 40$  s, h)  $\Delta t = 60$  s. All analyses are valid for  $z=500m$ . Areas within the analysis domain (i.e. not outside the curved boundary separating grid points with data from those without) that are white represent locations where correlation coefficients were  $< 0.5$ . .... 205

Figure 42: Observed RaXPoI reflectivity 205604 ( $1^\circ$  elevation angle) and a) TREC-derived storm-relative horizontal wind vectors; b) dual-Doppler derived storm-relative wind vectors. Areas with missing vectors in b have a between-beam angle  $< 20^\circ$ . .... 207

Figure 43: Performance of TREC compared with observed radial velocity data: a) Correlation coefficient and storm-relative TREC vectors computed between 205423 and 205445; b) Objectively analyzed RaXPoI reflectivity and storm-relative TREC vectors; c) Objectively analyzed storm-relative radial velocity ( $m s^{-1}$ ) and storm-relative TREC vectors. RaXPoI is located at the white star; d) TREC-derived storm-relative radial velocity ( $m s^{-1}$ ); e) The difference between the TREC-calculated SRVs and the observed SRVs, with the calculated TREC vectors overlaid; f) Objectively analyzed reflectivity with TREC vectors corrected for the observed radial velocity component. .... 208

Figure 44: Storm-scale view of the supercell at 203701, just after rapid-scan data collection had begun. Panels are a) Reflectivity (dBZ), b) unfolded radial velocities, c) differential reflectivity (dB), and cross-correlation coefficient (unitless). The red circles identify the hook (a) and the TVS (b). ..... 209

Figure 45: Four-panel images (Reflectivity, radial velocity, differential reflectivity, and cross-correlation coefficient) as in Figure 43, of the hook at (a), 8° (red lines depict the collocation of the hook echo and the narrow band of outbound radial velocities); (b) 12° and (c) 14° elevation (red lines identify two scales of circulation.) Times are 203705, 203709 and 203711 respectively. Range rings (dashed lines) are 15 and 30 km. Radar is located at the black dot. .... 210

Figure 46: Same as Figure 44 except for a) 14° at 203843 and b) 4° at 203843. Red ellipses indicate the two scales of rotation. .... 211

Figure 47: Reflectivity (left hand panels) and radial velocity (right hand panels), of a storm merger between the supercell and convection from its south. (a) 204100; (b) 204134; (c) 204207; (d) 204241. Red arrows point to non-supercell convection. .... 212

Figure 48: Series of 4-panel images depicting the evolution of midlevel (16° elevation, z~5 km) rotation. Valid at (a) 204020; (b) 204011; (c) 204202; (d) 204250; (e) 204344; (f) 204335; (g) 204525; (h) 204614. Red ellipses indicate cyclonic mesocyclones, black indicate the tornado circulation. Black arrows point to Zdr protrusion, red arrows point to jet of strong inbounds, red arrows point to jet of strong inbounds. .... 214

Figure 49: Reflectivity (left panel) and radial velocity (right panel) for 12° elevation (z~3 km). The tornado circulation (circled in black) becomes removed from the storm-scale mesocyclone between (a) 204215 and (b) 204504. .... 215

Figure 50: 4-panel images from (a) 204150, (b) 204315, (c) 204423, (d) 204530, and (e) 204637 at 4° elevation angle. Red and black circles indicate locations of tornado vortex, red arrow indicates location of wind shift associated with the primary RFGF. .... 216

Figure 51: 4° elevation angle 4-panel of secondary RFGF surge at 204818. RFGFs are indicated by black arrows. .... 217

Figure 52: Reflectivity and radial velocity of midlevel (z~3 km) rotation between tornadoes, at 204755. Vortex signatures and larger circulation are circled. .... 218

Figure 53: Four-panel images (18° elevation angle) of the development of a Z<sub>DR</sub> column and BWER. (a) 204454; (b) 204543; (c) 204633; (d) 204725; (e) 204815; (f) 204904. Red arrows point to the BWER, black to the Z<sub>dr</sub> column. The freezing level is indicated by the black line in the Z<sub>dr</sub> and  $\rho_{hv}$  panels in (a). .... 219

Figure 54: a) 4 panel plot from the 4° elevation angle at 204745 with overlays of the BWER (red) and Z<sub>dr</sub> (white) column from aloft. Stippled white outline indicate likely location of Z<sub>dr</sub> column even though the beam is below the freezing height at this level. B) 4 panel plot from the 18° elevation angle at 204741 with overlays of the leading edge of the reflectivity hammer head from the 4° sweep (red) and an indication of the location of the freezing level. .... 220

Figure 55: Evolution of low-level rotation from radial velocity at 4° elevation angle prior to tornadogenesis. Images are valid every 17 s from 204637 – 204835. Red circle indicates the remnant circulation from tornado 1. Black lines in (a) denote RFGF locations. .... 222

Figure 56: Evolution of rotation at increasing elevation angles every 17 s between 205015 and 205135. Left panels: 4° elevation angle, middle panels: 10° elevation angle,



right panels: 18° elevation angle. Tornadogenesis occurred between 205122 and 205138. ....	224
Figure 57: Storm merger process at 4° elevation angle. Left panels are reflectivity, right panels are radial velocity. (a) 204852; (b) 204941; (c) 205032; (d) 205122; (e) 205155. ....	225
Figure 58: 4-panel image of storm-scale structure during tornado intensification. Valid at 205401, at an elevation angle of 4° .....	226
Figure 59: Storm structure from dual-Doppler analysis at a height of 250 m. (a) RaXPol reflectivity and storm-relative horizontal (u v) wind vectors. (b) Same as (a) except for vertical velocity. Analyses valid at 205448.....	227
Figure 60: Series of 4-panel images of the radial velocity boundary between the hook and impinging non-supercellular convection at 205541, 205641, 205741 and 205841 from an elevation angle of 1° (z~100 m).....	228
Figure 61: 4-panel plots of the development of the WRB from 1° elevation angle at (a) 205603; (b) 205621; (c) 205639; (d) 205659; (e) 205715; and (f) 205735. The black line in (a) indicates a zone of reduced $\rho_{hv}$ . The black arrow in (b) indicates the developing WRB and the red indicates a band of slightly higher reflectivities. The red lines in (c) indicate the location of the WRB with respect to the velocity shift associated with the RFGF. ....	229
Figure 62: Dual-Doppler analyses valid at 205532 for z= 250 m. (a) reflectivity; (b) $\rho_{hv}$ ; (c) Zdr; (d) RaXPol storm-relative radial velocity. Reference vector below the sub-letter is 20 m s <sup>-1</sup> . ....	230
Figure 63: Zoomed-in radial velocity panel from Figure 61f. Red circles indicate locations of misovortices along the leading edge of the WRB. ....	231
Figure 64: Reflectivity and radial velocity for 205526, just prior to the development of the WRB. (a) RaXPol; (b) MWR-05XP. (Both images for 1° elevation angle.) .....	232
Figure 65: 4-panels illustrating the evolution of outflow surrounding tornado from 3° elevation angle for (a) 210223; (b) 210256; (c) 210401; (d) 210507; (e) 210613; (f) 210718; (g) 210823. Note that the time between figures b-g is constant (1 minutes 6 s), but there are only 33 seconds between a and b. This is done to better illustrate the evolution of the outflow winds between a and b and because 210223 is the first time data are available at 3° after the volume scans are resumed. ....	233
Figure 66: Plot of $\Delta V_{max}$ with time (abscissa, increasing to the right), and height (ordinate, increasing up) (a) for the entire first portion of volumetric data collection (2036-2054). The magnitude of $\Delta V_{max}$ is indicated by the color (m s <sup>-1</sup> ). Vertical lines indicate portion of graphic zoomed in for (b) and (c), and arrows point to increased circulation aloft that did not become tornadic (b) As in (a) except zoomed in on tornado decay. The ellipse indicates the region of initial weakening at mid-levels. (c) As in (a) except zoomed in on tornadogenesis.....	234
Figure 67: Distance between the maximum and minimum radial velocities of $\Delta V_{max}$ (y axis, km) with time (x axis).....	235
Figure 68: $\Delta V_{max}$ with time for the 1° elevation angle PPIs. ....	236
Figure 69: Same as Figure 66 except for 2102 – 2116.....	237
Figure 70: Pseudovorticity isosurfaces of the 0.15 s <sup>-1</sup> contour and shadow projection on the x-y plane over the duration of tornado 1 for which data are available. ....	238

Figure 71: Structure of tornado 1 over the duration observations are available (2036-2047). (a) Inclination angle (tilt) ( $0^\circ$ is vertically erect) between the center of the TVS at lowest elevation angle to the center of the TVS at the highest elevation angle (purple line), tilt bearing (azimuthal direction of tilt) (purple line), height of the beam for the top elevation angle at the TVS ( $Z_{\max}$ blue line), and height of the beam for the lowest elevation angle at the TVS ( $Z_{\min}$ red line). (b) Average area ( $\text{km}^2$ ) of the region bound by the $0.15 \text{ s}^{-1}$ vorticity isopleth. ....	239
Figure 72: Same as Figure 70 except for the $0.2 \text{ s}^{-1}$ isosurface. ....	240
Figure 73: Same as Figure 71 except for tornado 2. ....	241
Figure 74: Same as Figure 70 except for 2102-2116. $\Delta t=70 \text{ s}$ . ....	242
Figure 75: Radial velocity from 210345. Illustration of different lengths of axial and radial diameters of the tornado. Gray areas indicate radial velocities greater than or less than the color bar values. Specified color bar was retained for clarity of radial velocity gradients. ....	243
Figure 76: Constant radius cross section plots of pseudo angular momentum (contours, $\text{m}^2 \text{ s}^{-1}$ ) calculated from the storm-relative radial velocity for tornado 1. Time of the analysis is given in the title, as is the distance from the radar. Radial distance is the distance from the center of the tornado. Red arrow points to undulation. ....	244
Figure 77: Same as Figure 76 except for the pretornadic tornado 2 circulation. ....	245
Figure 78: Same as Figure 76 except for genesis and initial intensification of tornado 2. ....	246
Figure 79: Same as Figure 76 except for the last portion of tornado 2 volume scans. ....	247
Figure 80: Constant radius vertical cross sections of (top) radial velocity, and (bottom), $\rho_{\text{hv}}$ depicting oscillations along the inner wall of the tornado vortex at the 211429 analysis time. ....	248
Figure 81: Series of constant radius, (i.e. azimuthal) vertical cross sections of $\rho_{\text{hv}}$ and storm-relative radial velocity contours ( $\text{m s}^{-1}$ ). Times given in the titles of the images. The azimuth notation on the abscissa is arc length (km) from the center of the tornado. ....	249
Figure 82: Same as Figure 81 except for reflectivity. ....	250
Figure 83: Three-dimensional isopleths of constant $\rho_{\text{hv}} = 0.8$ for the evolution of the TDS of tornado 1. ....	251
Figure 84: As in Figure 83 except for the genesis of tornado 2. ....	252
Figure 85: Same as Figure 81 except for the genesis of tornado 2. ....	253
Figure 86: Same as Figure 82 except for the formation of tornado 2. ....	254
Figure 87: 4-panel images at $1^\circ$ elevation angle of horizontal extend of TDS and debris ball near the beginning (a) and end (b) of the $1^\circ$ PPI strategy. The circle identifies the TDS and the thin black line locates the band of low $\rho_{\text{hv}}$ from the RFGF. Range rings are in km. ....	255
Figure 88: Debris shedding and saw-tooth structure in $\rho_{\text{hv}}$ every 2 seconds between 205628 and 205637. ....	256
Figure 89: 4-panel illustration of a debris tail for $1^\circ$ elevation angle at 205841. Beam height $\sim 70 \text{ m}$ . ....	256
Figure 90: Constant radius vertical cross sections of $\rho_{\text{hv}}$ (left) and reflectivity (right) for (a, b) 210229, (c, d) 211218), (e, f) 211607. ....	257

Figure 91: Conceptual model of the cycling process observed between the dissipation of tornado 1 and the genesis of tornado 2. The green outline represents the 25 dBZ reflectivity contour at low-levels. a) Features observed at 4°. Red dot indicates low-level TDS, pink dot indicates subtornadic circulation, arrows indicate inflow/outflow, blue dashed curves indicate RFGF locations. b) Features observed at 18°. Blue dot = midlevel TVS, red and pink dots are the low-level circulation, as in (a), the red dashed circles indicate the locations of cyclonic mesocyclones, and the arrow indicates the location and magnitude of the rear inflow jet. .... 258

Figure 92: Conceptual model of vertical velocities and the collocation of rotation aloft and at low-levels. Arrows indicate dynamically-induced vertical motion from the low pressure perturbation associated with rotation: pink (red) circles indicate localized regions of subtornadic (tornadic) cyclonic vorticity. a) Transient vortices aloft, b) collocation of vorticity aloft with near-ground vorticity (magnitude of vorticity aloft is presumed to be larger than that below.) c) development of tornado by vertical stretching associated with mid-level rotation. Relative sizes of circulations are indicated by the size of ellipses. .... 259

Figure 93: Conceptual model of storm-scale features driving the rear-inflow jet and subsequent intensification of updraft. Green outline indicates approximate 25 dBZ reflectivity contour at low-levels. Red (pink) dots indicate tornadic (subtornadic) vortices. Mesocyclone (low-level mesocyclone) circulations indicated by the black (dashed red) circles. Areas of low perturbation pressure indicated by LP' and hydrostatic low pressure by LP<sub>h</sub>. Solid (outlined) arrows indicate horizontal (vertical) wind motion, length indicates magnitude. .... 260

Figure 94: Diagram of convergence and divergence as well as inferred vertical motion associated with the WRB. .... 261

Figure 95: Visual images of the horizontal vortex and tornado during the time the WRB was observed in radar. Note the funnels pendant from the horizontal vortex. The red arrow points to the clear area on the western side of the vortex. (Photos © Jeff Snyder.) .... 262

Figure 96: Conceptual figures illustrating the possible mechanisms of forming the horizontal vortex and WRB. Top row: Horizontal vorticity and the orientation of the resulting vorticity vectors induced by: (left) frictional effects on horizontal winds, (middle) vertical wind shear, and (right) a downdraft with a negative temperature perturbation. Purple arrows indicate direction of the shear vector, red (light blue) arrow indicates winds at the surface (1 km), green arrows indicate direction of horizontal vorticity. . Bottom row: Generation of horizontal vorticity by (left) gradients in w and (right) frictional generation behind the RFGF and by balance of environmental wind shear and RFGF shear. Dark blue arrows indicate vertical motion; green vectors indicate the magnitude and direction of the horizontal vorticity vector. The blue outline denotes the 25 dBZ contour near the surface; the green dashed circles indicate the horizontal roll. The dotted blue curve represents the RFGF, and the red circle represents the tornado. .... 263

Figure 97: Weak echo hole (top) and tornadic debris signature (bottom) with storm-relative radial velocity contours for the 211218 analysis. .... 264

## Abstract

On 24 May 2011, a series of supercell thunderstorms and violent tornadoes tore through central Oklahoma. A mobile, rapid-scan, X-band, polarimetric, Doppler radar (RaXPol), collected data from one of those storms as it produced two tornadoes west and northwest of Oklahoma City. Volume scans of 360° PPIs at nine elevation angles were collected every ~17 seconds for nearly 30 minutes, and single elevation angle (1°) PPI's were collected every ~ 2 seconds for 6 minutes. The first tornado, rated an EF3, was documented from intensification to decay, and the second tornado, reaching EF5 strength, was documented from genesis through mature phase. Maximum Doppler velocities in the second tornado were observed to reach 124 m s<sup>-1</sup>. The life cycles of the tornadoes and their parent supercell are examined herein, with particular emphasis on how their structures and features evolved over the short time scales observable by RaXPol.

The roles of storm-scale features in the formation, maintenance, and decay of the tornadoes are examined and placed into context with previous studies. In an effort to determine the chronology of how and when tornadic rotation evolves on short time scales, several analysis methods are employed to examine the time-height relationship of the circulation associated with the tornadoes. These methods include quantifying the difference between the maximum and minimum inbound and outbound velocities ( $\Delta V_{\max}$ ) associated with the Doppler radar detected vortex, and three dimensionally calculating and analyzing an estimate of vorticity based on the radial velocity field. Other rapidly evolving aspects of the tornadoes' life-cycles are examined as well. Polarimetric observations are used to enhance the kinematic and storm-scale analyses.

An attempt was made to retrieve the two and three-dimensional wind fields from single-Doppler data using the Tracking Radar Echoes by Correlation technique, with the desired end result of calculating trajectories. Unfortunately, this method did not prove to be accurate enough to determine confidently the wind field, which would have allowed for a more detailed examination of quantitative storm-scale properties. Even its qualitative accuracy was questionable. Therefore, this method is not used for analyzing the storm.

The most important conclusions from the results of this study include: 1) Prior to the formation of tornado 2, rotation initially is present only at the lowest analysis level, but tornadic-strength rotation develops nearly simultaneously (within ~30 s) over a depth of several km. No evidence of the dynamic pipe effect is observed. 2) The parent supercell exhibits an atypical mesocyclone and tornado cycling process prior to the formation of tornado 2. 3) A rear flank gust front surge acts detrimentally to tornado 1 but beneficially to tornado 2. 4) A horizontal vortex just ahead of the rear flank gust front coincident with a weak reflectivity band and a narrow channel of inbound velocities in the radar data appears to contribute to the intensification of the tornado. All conclusions significantly benefited from the rapid temporal observations available for this dataset since they all involved processes that evolved over periods of less than four minutes; (1) and (4) occurred in less than two minutes.

## Chapter 1. Introduction

Considerable attention has been given to tornadoes in the scientific literature over the past half-century. Hundreds of papers exist that utilize laboratory, numerical and observational techniques to document the structure, formation, evolution and dynamics of these violent atmospheric phenomena. However, despite many recent advances in the science, there is still much to learn about tornadoes.

The processes and environments driving the formation, evolution and decay of tornadoes seem to resist generalization. Often, there are conflicting conclusions drawn from different studies; one study finds conclusive evidence of the importance of a certain process or environmental factor while another refutes or counters the original conclusion. For example, Markowski (2002a, 2002b) found clear evidence that a warm, potentially buoyant rear flank downdraft (RFD) is more conducive for producing tornadoes than a cold RFD. However, Marquis et al. (2011) determined that in at least one situation, a surge of warm RFD air was associated with tornado *decay*. Klemp and Rotunno (1983) attributed the development of a low-level mesocyclone to the baroclinic generation of low level horizontal vorticity along the forward flank downdraft (FFD) gust front that subsequently was advected toward the updraft, tilted, and stretched in the vertical. However, Frame et al. (2009) observed a supercell with a weak low-level mesocyclone in which vorticity streamlines along the forward flank gust front were directed away from the updraft and parcel trajectories from the low-level mesocyclone did not originate in the FFD region. Additionally, Shabbott and Markowski (2006) concluded from in situ observations of forward flank downdrafts that tornadic storms had *weaker* baroclinically generated vorticity than nontornadic storms.

Not only do analyses of storm-scale and environmental features produce conflicting results about the preferred atmospheric and storm-scale conditions for tornado production, but the mode of tornado formation varies as well. Some studies have found evidence observationally (Burgess 1975; Brown et al. 1978), and numerically (Leslie 1971; Smith and Leslie 1979; Wicker and Wilhelmson 1995) that strong, possibly tornadic rotation initially develops at mid-levels of a storm (or entity representing a storm), and builds slowly downward with time, culminating in a tornado vortex when the rotation makes contact with the ground. Other studies (Vasiloff 1993; Trapp and Fiedler 1995; Alexander 2010; French et al. 2013a, b) have observed rotation developing initially near the surface and either building upward with time or nearly simultaneously intensifying over a relatively deep layer of the lower troposphere during tornadogenesis. These are just several examples illustrating the complexity of the problem associated with generalizing tornado-scale processes and environments.

Part of the challenge of understanding tornado-scale processes is the presumption that tornadoes form and evolve at timescales on the order of 10 seconds (Bluestein et al. 2003). Thus, conventional observational methods will miss the details of such processes due to inadequate temporal resolution. Recently, mobile rapid-scanning radars have been utilized in the field to attain data with improved temporal resolution (Wurman and Randall 2001; Bluestein et al. 2010; Wurman et al. 2011; Pazmany et al. 2013). All instruments except the one described by Pazmany et al. (which is the instrument used for this study) are steered mechanically in the azimuthal direction, and electronically in the vertical direction, allowing data to be collected simultaneously at multiple elevation angles, thus significantly reducing the amount of

time required to collect a volume of data. Unfortunately, these instruments have some disadvantages over conventional mobile radars; namely increased half-power beam-width and/or side-lobe contamination which respectively can reduce the spatial resolution and cause spurious echo returns.

The doctoral research presented herein uses a rare dataset obtained during the 24 May 2011 central Oklahoma tornado outbreak by a mobile, rapid-scan, X-band, polarimetric radar (RaXPoI, Pazmany et al. 2013). This dataset captured the intensification, mature phase and decay of an EF3 tornado and the subsequent genesis, intensification, and mature phase of a second tornado that was rated an EF5 and damaged outlying portions of El Reno and Piedmont, OK. The combination of fine temporal *and* spatial resolution observations of one strong tornado and one violent tornado makes this study unique. The ultimate goals of this project are to address the following questions:

- 1) How does the tornado develop, intensify and decay over short time scales? Particularly, how do the maximum azimuthal shear magnitude (as determined by the difference between maximum inbound and outbound velocities,  $\Delta V_{\max}$ ), and the radar-retrieved vorticity change during the lifecycle of the tornadoes?
- 2) During tornadogenesis, is there evidence that rotation develops aloft and builds downward, develops near the surface and builds upwards, or neither?
- 3) How are storm-scale and tornado-scale features related to the formation, intensification, and decay of the tornadoes?
- 4) How does the three-dimensional structure of the tornado change with time?
- 5) What additional information do the polarimetric observations add to the analyses?



While the questions posed here are not new scientific motivation, they remain largely unanswered or incompletely explained. The general approach to examining them in the past has been to increase spatial resolution and coverage of mobile instrumentation and utilize increasingly finer-scale numerical models. There has been considerably less effort put into increasing temporal resolution, particularly of observations. The Second Verification of Rotation in Thunderstorms Experiment (VORTEX2) was designed to address some of these questions. However, the primary thrust of VORTEX2 from the perspective of mobile Doppler radar objectives was to acquire polarimetric observations of supercells and coordinated dual-Doppler datasets on the storm-scale and mesocyclone-scale, but not tornado-scale. The data collection strategies employed during the project did not focus on rapid temporal updates. The dual-Doppler mode designed for the project collected synchronized volume scans every 2 minutes (Wurman 2012). Thus, the radar datasets collected during VORTEX2 are inadequate for examining tornado-scale processes that are evolving on time scales considerably shorter than 2 minutes.

To date, the only study documenting rapid volumetric observations of tornadoes is French et al. (2013a, b, collectively referred to as French et al. 2013), who examined data from four tornadoes using a rapid-scanning, mobile phased-array radar with volumetric update times ranging from 6-14 seconds. The studies looked at the time-height evolution of tornadogenesis and dissipation, rapid changes in the tornado Doppler velocities, and examined the three-dimensional evolution of tornado Doppler velocity profiles and structure. Unfortunately, the engineering that enabled rapid temporal updates with this radar also compromised the spatial resolution of the

instrument; the half-power beam width in the azimuthal direction is  $1.8^\circ$  and is  $2.0^\circ$  in the vertical. Thus, while the datasets analyzed by French et al. (2013) present a unique opportunity to examine the volumetric evolution of the storm over short time intervals, it is not possible to say with certainty that the actual tornado is being resolved because the distance between the radar and the tornado is too great.

It is the goal of the current dissertation to extend the work of French et al. to two additional tornadoes to determine whether or not their results are repeatable in this case, and to examine definitively the structure of the actual tornado, rather than the parent tornadic circulation. This dissertation will focus on the kinematic aspects of the structure and evolution of the tornado and its parent supercell. This work is not attempting to rectify any of the contradictions presented earlier with a single case study, but rather to lend credence to the findings of earlier studies by being able to more definitively analyze the supercell and tornado processes with the rapid temporal observations available from this dataset.

The remainder of this dissertation is organized as follows: In Chapter 2, summaries past studies are presented and major conclusions from these studies are stated. Specifically, the literature contributions to current scientific understanding of tornado structure, evolution, and dynamics will be reviewed. In Chapter 3, the project motivation and design are explained. Chapter 4 describes the instrumentation used for this work, and the incentive for using such instrumentation. A summary of the dataset and an overview of the case study, including a discussion of the synoptic-scale conditions and an abbreviation of the storm-scale evolution during the analysis time are presented in Chapter 5. In Chapter 6, analysis techniques will be described and

justified. A presentation of results is given in Chapter 7, followed by a discussion of the results in Chapter 8. A summary of the study and conclusions are presented in Chapter 9.

## **Chapter 2. Previous Work**

Because the tornadoes being studied herein were spawned from a supercell thunderstorm with a rotating updraft (mesocyclone), the subsequent discussion will be primarily focused on tornadoes produced from mesocyclones (type I tornadoes, Davies-Jones et al. 2001). Tornadoes can form without a parent mesocyclone (type II, Davies-Jones et al. 2001); however such events lie outside the scope of this paper and will not be discussed. Historically, three primary methods have been used to study tornadoes: 1. observations, 2. laboratory simulations, and 3. numerical models (analytical and computer). Observations were perhaps the first method employed, owing to the relative simplicity of watching a tornado and documenting incurred damage (Stevens 1916; Humphreys 1926; Stuart 1926). Despite the rudimentary instrumentation and observation networks available, Flora (1919) presented a concise, accurate tornado climatology based on thirty years of data from Kansas. Some early studies mention the contribution of data from surface instruments such as thermometers and barographs (e.g. Colyer 1913; Shipman 1927; Tepper and Eggert 1956; Fujita 1959).

Early attempts to resolve horizontal and vertical motions in the periphery of tornadoes made use of film cameras and motion picture cameras via photogrammetry (Hoecker 1960; Forbes 1976; Golden and Purcell 1977). This method is still practiced

today, often replacing traditional film cameras with digital ones (Wakimoto 2004; Wakimoto et al. 2011; Nolan et al. 2012). With the advent of the weather surveillance radar 1957 network (WSR-57), large scale, remote observations became possible, allowing observational tornado studies to become more detailed and insightful (Stout and Huff 1952; Fujita 1958; Browning and Fujita 1965; Fujita et al. 1970; Brandes 1977; Brown et al. 1978). The need for higher resolution data and better low-level observations of both storm structure and environmental conditions prompted a transition from fixed site to mobile radar (Bluestein and Unruh 1989; Bluestein et al. 1995; Wurman et al. 1997) and mobile mesonets (Rasmussen et al. 1994; Straka et al. 1996; Markowski 2002), both of which are still widely used today (Bluestein et al. 2007; Wurman et al. 2007; Karstens et al. 2010; Wurman et al. 2012).

Prior to the availability of high quality observational instrumentation and data, laboratory simulations proved to be an effective tool for studying certain physical properties of tornado-like vortices and their formation. Such simulations were generated in a variety of ways including chambers that withdrew fluid or air from the center (Long 1958, 1961; Ying and Chang 1970; Dessens 1971; Ward 1972; Church et al. 1977), injected buoyant fluid along the axis (Morton, 1963), or simulated buoyancy with carbonated water (Turner and Lilly 1963) (Figure 1). The engineering of many early vortex chambers was quite simplistic, involving the introduction of pre-existing vertical vorticity and a mechanically-induced (as opposed to buoyancy-driven) updraft or sink. Results from such simulations were therefore simplistic as well. Some of the more complex simulations were able to recreate processes such as multiple vortices and vortex breakdown (Ward 1972; Church et al. 1977; Church et al. 1979). The use of

tornado simulators has declined significantly during the past two decades, mostly in response to monetary cost and improved computational ability (Church and Snow 1993, Doswell and Grazulis 1998).

When computer power became capable of solving governing physical equations, tornado-like vortices were simulated using simple numerical models. Most early numerical models were two-dimensional or axisymmetric representations of laboratory simulations (Lilly 1962; Ogura and Charney 1962; Leslie 1971; Schlesinger 1973; Wilkins et al. 1974; Rotunno 1977, 1979,). Some models simulated convective processes that were constrained to a short vertical depth above the surface (Eskridge and Das 1976; Smith and Leslie 1978). Many neglected precipitation effects and produced unrealistic results such as an adiabatically generated warm downdraft that became an updraft after hitting the surface (Eskridge and Das, 1976). Others, however, were quite robust, simulating entire convective clouds and producing realistic features such as rotating updrafts, gust fronts and RFD occlusions (Klemp and Wilhelmson 1978; Schlesinger 1978; Klemp and Rotunno 1983). As computer power increased, model resolution improved allowing finer-scale, increasingly complex processes and features to be resolved (Wicker 1995; Alderman et al. 2002; Dowell et al. 2004; Markowski and Harrington 2005; Byko et al. 2009). Better understanding of the microphysical and turbulent processes involved with the storms that produce tornadoes also enhanced model performance.

The following discussion is a culmination of 60 years of laboratory, observational and numerical studies, and how these studies have advanced scientific understanding of tornado structure, dynamics and evolution to its current extent.

## **Tornado Structure**

At first glance, it would seem that tornado structure should be the easiest category to study; all one should have to do is merely observe the tornado. Indeed, visual observation does provide some idea of the structure of a tornado. One can easily observe differences in vortex width and height, as well as vortex structure (e.g. single vortex vs. multiple vortices). Discerning between a funnel cloud and a tornado with circulation reaching the ground seems as though it should be somewhat obvious, as does noting the difference between a debris cloud and condensation funnel. However, there are many situations where these differences are not clear. To quantify structural characteristics requires more precision than the human eye is capable of offering. Thus, it is necessary to study tornadic structure via the previously described methods.

Early radar studies of tornadic supercells revealed a common storm-scale structure in the radar reflectivity factor field (hereafter referred to as reflectivity) that came to be known as a hook echo (Figure 2a) (Huff et al. 1954; Van Tassel 1955; Garrett and Rockney 1962; Fulks 1962; Fujita 1965). Numerous studies attributed this feature to the cyclonic circulation of precipitation around the back side of the mesocyclone, and the inflow of precipitation-free air ahead of the appendage (Fujita 1958; Browning 1964; Brandes 1977; Klemp et al. 1981), although later studies hypothesized that the hook might actually be a result of a curtain of precipitation descending within the RFD (Lemon and Doswell 1979; Forbes et al. 1981; Markowski 2002a).

Using a combination of radar, instrumented aircraft, visual, and surface observations, Lemon and Doswell (1979) determined that a mesocyclonic tornado is

located at the tip of the hook echo of a supercell, where the rear flank gust front wraps around the updraft and meets the forward flank gust front (Figure 3). The tornado often is pendent from the southwestern flank of a wall cloud, which forms on the right-rear flank of the storm, in close proximity to but not within the primary core of precipitation, Fujita (1976) observed. Lemon and Doswell (1979) also noted that the tornado forms on the updraft side of a strong vertical velocity gradient associated with the updraft/RFD interface in a divided mesocyclone. They additionally documented a ‘clear slot’ of relatively cloud-free but not precipitation-free air to the northwest through southwest side of the tornado. Fujita (1981) observed that during the RFD occlusion process, the hook echo wraps up, spiraling around the circulation center.

In the Doppler velocity field, the tornado is evident as a tornadic vortex signature (TVS) (Brown et al. 1978). The TVS is defined as a couplet of strong inbound Doppler velocities azimuthally adjacent to strong outbound Doppler velocities (Figure 2b). Such a feature is indicative of very strong azimuthal shear, which is the radar’s representation of the tornadic rotation. The details of the TVS are dependent upon the size of the tornado, its distance to the radar, and the spatial resolution of the radar.

As radar technology improved and mobile radars became viable, higher resolution images of reflectivity and Doppler velocity became available, providing further insight to tornado structure (Bluestein and Unruh 1993, Bluestein et al. 1995; Wurman et al. 1997; Bluestein and Pazmany 2000). Features such as spiraling inflow bands, small-scale vortices, weak echo holes (seen by Fujita 1981), concentric rings of high reflectivity (a ‘double eye type’ feature), and wavelike asymmetries were observed

(Bluestein and Pazmany 2000; Wurman 2002; Bluestein et al. 2004; Wurman and Alexander 2005; Bluestein 2007; Wakimoto et al. 2011; Tanamachi et al. 2012). These features are not only interesting, but may have dynamical implications on tornado-scale processes (Bluestein and Pazmany 2000) and provide evidence that even though tornadoes are typically represented as axisymmetric phenomena in models, they are ultimately three-dimensional.

Using combined radar and photogrammetry methods, Wakimoto et al. (2011) determined that the radar-derived weak echo hole was slightly wider than the visible funnel, and that winds exceeding  $35 \text{ m s}^{-1}$  (the speed at which surface damage is assumed to occur) extended well outside the visible funnel cloud. Similarly, Alexander (2010) noted that radial velocities exceeded  $35 \text{ m s}^{-1}$  over a core diameter of 150 m three minutes prior to spotter reports of a condensation funnel on the ground.

A climatology describing the general characteristics of central plains supercellular tornadoes from over ten years' worth of Doppler on Wheels (DOW) observed tornadoes was compiled by Alexander (2010). It was found that the median distance between maximum inbound and outbound velocities was 300 m, and the median velocity difference across the TVS in the lowest 500 m was  $80\text{-}90 \text{ m s}^{-1}$ , although in the most extreme cases it exceeded  $220 \text{ m s}^{-1}$ . Maximum ground-relative velocities averaged  $55\text{-}60 \text{ m s}^{-1}$ , corresponding with the F/EF2 damage scale rating, indicating that this appears to be a 'preferred' tornado intensity. The absolute maximum radial velocity recorded in their climatology was  $135 \text{ m s}^{-1}$  during the 1999 Bridgecreek-Moore, OK tornado (Wurman et al. 2007). Doppler velocity observations exceeding  $100 \text{ m s}^{-1}$  are not unique to the DOWs. Such observations have been made



by a continuous-wave 3-cm portable Doppler radar (Bluestein and Unruh 1989, Bluestein et al. 1993), and with the RaXPol radar (see Chapter 6). Thus, the likelihood of such strong tornadic wind speeds appears viable.

It is generally accepted that the maximum wind speeds of a tornado occur at a height between 30-150 m AGL (Bluestein and Unruh 1993, Bluestein et al. 1993, 1997; Burgess et al. 2002; Lee and Wurman 2005; Wurman et al. 2007; Alexander and Wurman 2008). Below this height, it is assumed that the flow decelerates due to friction as wind speeds are substantially reduced at the ground. However, there are very few observations of tornado winds below  $\sim 30$  m due to a combination of lack of surface observation instruments, damage to surface instruments that have sampled tornado winds, and the inability of radars to acquire data in the lowest 30 m of the atmosphere due to beam broadening with distance, the effect of ground clutter contamination, and Earth's curvature. Therefore, this theory remains incompletely tested.

Recently, two Oklahoma mesonet instruments serendipitously observed tornado passage: Tipton, OK observed a maximum wind gust of  $37.5 \text{ m s}^{-1}$  before the instrument went offline during a tornado on 7 November, 2011 (Figure 4a). The El Reno, OK station observed a maximum wind gust  $67.5 \text{ m s}^{-1}$  on 24 May 2011 and remained online while an EF-4 tornado passed almost directly over it (Figure 4b). However, there were no low-level radar observations available for comparison coincident with these two surface observations. Wurman et al. (2007) found that observed winds collected from an armored mobile mesonet at 3 m AGL were 75 – 80% of the value of radar detected wind speeds at 18 m AGL. But, Wurman et al. (2013) determined that there was not

much difference between the radar-observed winds at ~30 m and the 3.5 m winds of the armored mobile mesonet in a different tornado. Despite these few observations, there remains a wide knowledge gap surrounding what actually occurs at the surface during a tornado.

Above the height of maximum velocity, the vortex tends to broaden slightly, resulting in weaker velocity due to conservation of angular momentum. While the tangential velocities typically weaken with height, the radius of maximum winds (RMW) appears to increase with height, an indication of a broadening vortex with height (Kuo 1966; Wurman 2002; Lee and Wurman 2005), as is often inferred from visual observations of the condensation funnel.

There is conflicting evidence about the relationship between the size of the tornado and its intensity. Several studies have concluded that tornado size grew as intensity increased (Brooks 2003; Kosiba et al. 2008). However Alexander (2008) does not find a definitive correlation between the RMW and the intensity of radial velocities. This is not entirely surprising considering that the RMW has been observed to contract as a tornado is intensifying and to broaden as the tornado is dissipating (Bluestein et al. 2003b).

Numerical and laboratory simulations also allowed for the finer-scale structure of tornado-like vortices to be analyzed. Lewellen (1977, 1993) describes five dynamically significant regions of the tornado: the core flow, the outer flow, the corner flow, the surface boundary layer, and the upper flow regions (Figure 5). The core flow region is the central portion of the tornado extending from the axis of rotation to the RMW, also called the core radius. Typically, the core radius of a tornado is 10's to

100's of meters and extends vertically from just above the surface to the cloud above. The central portion of the core is generally dominated by strong vertical motions that can be either upward, downward or have an interface separating upward motion below from downward motion above. The outer portion of the core has extremely strong horizontal winds. Within the core flow, the vortex usually can be represented by solid body rotation, although wide vortices do not always conform to this rule. In the latter case, angular velocity that is increasing radially outward within the core has been documented (Davies-Jones 2001). The core flow is typically cyclostrophic; the inward directed pressure gradient force balances the outward directed centrifugal force. Little external entrainment occurs and horizontal motions are dominated by tangential flow; radial velocity is small. The core is stable to radial displacements, but may support oscillatory perturbations.

The rotation of the vortex makes it less susceptible to turbulence (Lewellen 1993). Early research in the area of turbulence found that high helicity, like what occurs in a tornado, tends to inhibit the normal cascade of turbulent energy to smaller scales (Andre and Lesieur 1977; Polifke and Shtilman 1989). This creates stability in the vortex and also inhibits it from dissipating as easily as other organized flows. This may be why tornado condensation funnels often visually appear laminar. The outer flow region is comprised of the rotating air extending outward from the core by about 1 km. The wind in the outer flow region is not in solid body rotation, but it conserves angular momentum.

The vortex interacts with the ground in the surface boundary layer, which typically extends from the ground to a height of  $\sim 100$  m. Here, frictional forces act

upon the low-level flow, causing it to be turbulent, reducing the tangential velocity and increasing radial inflow. As a consequence of this effect, horizontal velocities above the surface, in the core become capable of reaching speeds greater than what they could attain if the flow remained in cyclostrophic balance. Friction temporarily decelerates the inflow, reducing the centrifugal force. This allows the horizontal pressure gradient force to overwhelm the centrifugal force, enabling the inflow to converge to a smaller radius than if friction had not decelerated the flow. A parcel conserving angular momentum will therefore spin faster as it approaches the axis of rotation and its velocity will overcome the frictional deceleration, resulting in super cyclostrophic flow. Because of the increased radial flow and convergence, a vortex often visually tapers inward near the ground.

Low-level horizontal inflow transitions abruptly into the vertical in the corner flow region, close to the axis of rotation. This is the location of the most violent surface winds, where debris is lofted into the air as rapidly spinning winds converge toward the central axis and erupt into a vertical jet that feeds the core. The lowest surface pressures, strongest velocity gradients, and strongest pressure gradients also occur in this region. The exact structure and dynamics of the corner flow and vertical jet can be quite complex and depend on the nature of the tornado-scale circulation, the horizontal convergence, the surface roughness, the tornado translation speed, the low-level inflow structure and the upper core structure (Lewellen et al. 2000). It has been found that the structure and dynamics in this region are highly dependent upon the swirl ratio (Rotunno 1979; Church et al. 1979; Lewellen 1993), which will be mathematically defined in Chapter 2c, but is essentially a ratio between tangential velocity and vertical

velocity, or, from a slightly different perspective, rotation and convergence. If the necessary conditions are met, multiple vortices may form in the corner flow region.

Above the visual portion of the vortex is the upper flow region. This is where the vortex interacts with the storm-scale flow above it. There is relatively little observational or numerical data available in this region, because the upper boundary condition in numerical models is often imposed here, and the models do not well represent the physical processes occurring in nature. Also, there are few Doppler radar observations at this level to document what is actually occurring in this region. It is hypothesized that a buoyant updraft in the flow above the tornado acts as a cork, preventing the low pressure in the low-level vortex from filling in by convergence aloft (Lewellen 1993). It is sometimes thought that the vortex terminates in this region (Lewellen 1993). However, some radar-based observations indicate a TVS or weak echo hole, (thought to be a manifestation of centrifuged hydrometeors due to the continuation of the tornado vortex aloft) well above the low-level vortex (Brown et al. 1978; Lemon et al. 1982; Rasmussen et al. 1994; Wakimoto et al. 1996; Tanamachi et al. 2012).

### **Tornado Evolution**

According to Davies-Jones (1986), there are five stages of tornado evolution: 1) The dust whirl stage, which is defined as the beginning of the tornado, when the circulation reaches the surface and picks up dust and small debris, forming an obvious dust cloud; 2) The organizing stage when the condensation funnel descends and the tornado wind speed is intensifying; 3) The mature stage, which defines the most intense time in the tornado's evolution, when the winds are strongest; 4) The shrinking stage,

during which the funnel cloud becomes narrow and begins to tilt; and 5) The decay stage, when the tornado becomes very thin, tilted and contorted, sometimes disconnected from the parent updraft, and ultimately dissipates (Figure 6).

The phases above begin with a tornado on the ground and do not include the description of what must occur for a tornado to form in the first place; the process of tornadogenesis is addressed separately. Considerable time and energy have been given to investigating the tornadogenesis process. Most early lab studies concluded that stretching of vorticity due to convergence of high angular momentum air was responsible for the formation of the vortex (Turner and Lilly 1963; Ward 1972; Smith and Leslie 1978). However, as observational and numerical technology improved, it became clear that the details surrounding this simple mechanism are quite complicated and contradicting explanations often appear in the literature. Currently, there are several hypotheses explaining tornadogenesis and there is evidence that all may be partially correct and incorrect. This study will focus on the two most popular theories: the dynamic pipe effect and the bottom-up process. Each will be examined individually.

*i. The Dynamic Pipe Effect*

One of the earliest observationally and numerically based hypotheses to explain tornadogenesis is the dynamic pipe effect (DPE). Leslie (1971) and Smith and Leslie (1978, 1979) analyzed simulated laboratory vortices and found the process of tornadogenesis began at mid-levels. According to their studies, as a vortex forms, rotating fluid converges into a region of relatively large vertical velocities, increasing the vertical vorticity by stretching until cyclostrophic balance is reached. Once the fluid

is in cyclostrophic balance, radial motions are inhibited, but tangential and vertical motions are not. Thus, convergence into the rotating column must come from a source outside of the primary vortex. Non-hydrostatic low pressure develops as a result of the strong rotation, increasing upward motion below the vortex (and downward motion above it). The spinning fluid entering from below is accelerated as a result of the convergence and enhanced vertical motion, allowing cyclostrophic balance to be attained at progressively lower and lower levels. The central pressure deficit essentially behaves like a tube or pipe, drawing air in from below and causing it to rotate faster. This process causes rotation to continuously descend at a relatively slow rate until the vortex meets the surface (Figure 7a, b). The in-up circulation below the vortex draws air closer to the axis of rotation at low-levels, transports mass upward and results in a vertically symmetric vortex (Figure 8). Smith and Leslie (1978) summarize this process by saying “the tornado is initiated from above by convergence of existing circulation possibly associated with large vertical accelerations in the updraft.” Similarly, the rotating air exiting the midlevel vortex is advected upward and the vortex extends up as well.

Once the vortex reaches the surface, it is affected by friction. The rotation near the surface exceeds that aloft owing to frictional disruption of cyclostrophic balance, allowing the rotation to converge to a smaller radius. Smith and Leslie (1978) found that once the vortex reached the surface, there was a simultaneous decrease in central pressure over the depth of the vortex, resulting in a nearly simultaneous, uniform intensification of the vortex. Davies-Jones et al. (2001) specified that high-momentum air will arrive first at or near the central axis aloft, as occurs in the DPE scenario, when

neither radial inflow nor circulation decreases with height, and one of the parameters increases with height. Such a configuration will cause a vortex to develop at mid-levels then descend downward. This theoretical process was given observational support by early Doppler radar studies (Burgess 1976; Brown et al. 1978; Lemon et al. 1978, Davies-Jones 1986) that found evidence of a TVS that was first visible aloft, then slowly (O 30 minutes) built downward prior to tornadogenesis.

*ii. Bottom-Up Process*

Other studies have found that a tornado formed without strong midlevel rotation preceding it. Rather, the strongest rotation was initially located at or near the ground and either built upward or nearly simultaneously intensified over a substantial vertical depth. In such cases, it appears that convergence of angular momentum is either strongest at low levels, causing intense rotation to develop first near the ground, then to stretch vertically upward (Figure 7c), or there is simultaneous convergence of high angular momentum air (flow with high vorticity) to the central axis over a relatively large low-level depth. Uniform intensification of vorticity causes the vortex to form cylindrically, independent of height. Although this process may be slightly different from the bottom up process, Trapp and Davies-Jones (1997) grouped tornadoes forming either from the bottom up, or from uniformly intensifying rotation over the near-surface to cloud-base layer as “mode II” tornadoes. Trapp and Fiedler (1995) conclude that formation of mode II tornadoes is not ‘triggered’, but rather is a consequence of the continuous, rapid process of vertical vorticity tilting and subsequent amplification.



The first observations of a tornado vortex that started at or near the surface and built upward can be traced to explanation of non-supercellular tornadoes (type II, Davies-Jones et al. 2001) (Wakimoto and Wilson 1989; Brady and Szoke 1989; Wilczak et al. 1992; Grasso and Cotton 1995). Even without observational evidence, theoreticians argued that this process should occur because vorticity and angular momentum are concentrated most efficiently in the surface boundary layer owing to frictional convergence. Davies-Jones et al. (2001) explained that a vortex will develop at the ground if either convergence or radial inflow or both is maximized at the ground, and neither parameter increases with height.

There is also evidence from observational and numerical studies that tornadogenesis in supercells may be initiated at low levels as well (Brandes 1981; Johnson et al. 1987; Wicker and Wilhelmson 1993, French et al. 2013 a, b). Vasiloff (1993) described the tornadogenesis process observed during the Binger, OK tornado from 22 May 1981 as “rapid intensification of the TVS over 2-3 km”. Trapp and Fiedler (1995) simulated this process of uniform, rapid strengthening of rotation to vortex intensity, and Alexander and Wurman (2008) found the tornadoes from the DOW datasets seemed to intensify simultaneously over the low-levels, despite the relatively coarse temporal sampling of their data. French et al. 2013a studied three tornado cases and determined that tornadogenesis was associated with an upward building tornadic vortex signature rather than a descending one.

*iii. Tornado Intensification, Maintenance and Decay*

Although understanding and predicting tornadogenesis is not a trivial problem, understanding the intensification, maintenance, and decay of tornadoes is arguably more

important given the implications that the intensity and the duration of the tornado have on impacting lives and property. According to Trapp and Fiedler (1995), either baroclinic or barotropic vorticity can provide the mechanism for sustaining the tornado vortex, in addition to tilting of horizontal vorticity produced by frictional processes in the boundary layer. Marquis et al. (2012) assimilated 4 DOW observed supercells into a computer model using the ensemble Kahlman filter method and found that the longest lived tornado in their dataset was located beneath the midlevel updraft, along the rear flank gust front, which fed considerable low-level horizontal vorticity to the tornado. The shortest-lived tornado occurred similarly beneath midlevel updraft within a horizontal convergence zone, but the updraft became tilted and the region of strongest low-level convergence became displaced from the tornado. They argue that there needs to be a combination of updraft above and horizontal convergence at the ground. The convergence zone does not necessarily have to be the primary RFGF. Marquis et al. (2008) observed a tornado that persisted behind the primary RFGF, along a secondary convergence zone. Dowell and Bluestein (2002b) determine that the longevity of tornadoes in a cyclic supercell is related to the motion vector of the tornadoes as compared to the motion of the parent updrafts. Longer lived tornadoes were found to have a component of motion more parallel to that of the parent supercell's updraft.

Wurman et al. (2010) studied the intensification and mature stages of a tornado using single and dual-Doppler analyses and also found that the tornado was behind the primary RFGF. They determined the circulation at a radius of 500 m increased several minutes prior to tornado intensification, but otherwise the circulation remained relatively constant with time. This observation suggests that the inward advection of

high angular momentum air was offset by some other force, possibly turbulent dissipation. The peak tornado wind speeds were achieved as the secondary RFGF surged forward and wrapped around the tornado circulation. After this occurred, the tornado quickly weakened. The decrease in tornado winds was also coincident with weakening convergence and variations in vertical velocity in the near-tornado region. Thus, stretching was removed and generation of vorticity by the variations in  $w$  was minimized.

In a high spatial-resolution (50 m horizontal grid spacing) numerical model simulation, Wicker and Wilhelmson (1995) conclude that the tornado decay process begins when the vertical pressure gradient force weakens or reverses near cloud base. This process weakens the updraft above the tornado and allows the low-level flow to advect the RFGF completely around the tornado. The occlusion is presumably a result of weakening inflow that had previously been able to confine the RFGF and inhibit it from wrapping around the mesocyclone. As a result of the occlusion, the tornado is cut off from its source of positively buoyant air and cyclonic vertical vorticity, and the tornado dissipates. Brandes (1978), Davies-Jones (2001), Marquis et al. (2011) similarly attribute the onset of tornado decay to a surge of outflow that overtakes the circulation. As this happens, the tornado becomes susceptible to the environmental shear, and it becomes tilted and elongated. In certain instances, the funnel cloud appears to dissipate in a wave-like manner, sometimes with portions of the funnel cloud disappearing then reappearing, suggesting that the tornado may become unstable to sinusoidal oscillations (Davies-Jones 2001). Marquis (2011) also found that tornadoes tended to dissipate when they became displaced from the midlevel mesocyclone. Some

tornadoes have been observed to widen at the end of their life (Agee et al. 1976), implying radial divergence and subsequent velocity reduction, possibly as a result of a sudden decrease in parent updraft intensity. Despite the somewhat robust documentation of tornado maintenance and decay from observations (Lemon and Doswell 1979; Brandes 1981; Dowell and Bluestein 2002a; Markowski et al. 2002; Wurman et al. 2007a; Wurman et al. 2010; Marquis et al. 2012; French et al. 2013b), all of these studies except for French et al. have either suffered from inadequate spatial or temporal resolution, warranting additional higher resolution studies like the one presented here.

*iv. Tornadogenesis Failure*

Many hypotheses and explanations have been offered to explain why a tornado does not form despite strong low-level rotation. Often, these explanations are made on a case-to-case basis and do not apply generally to all situations. Brooks et al. (1993) surmised that tornado failure occurs when either the low-level or midlevel mesocyclone fails to develop or persist, which can occur when the FFD or RFD is in an unfavorable location with respect to the updraft. Similarly, Smith and Leslie (1978) and Trapp and Davies-Jones (1997) state that tornadogenesis fails when low-level vorticity is insufficient to allow a mid-level vortex to descend to the surface. Wakimoto and Cai (2000) observed a supercell that did not produce a tornado and determined that structurally it was nearly identical to another supercell that did produce a tornado, with a strong low-level mesocyclone, an occlusion downdraft, and a spiraling updraft/downdraft structure. The only notable difference between the two storms was the far-flow characteristics away from the storms and a more extensive precipitation

field behind the RFD of the nontornadic storm. The differences in precipitation distribution may have contributed to differences in evaporational cooling and the subsequent strength of the rear flank downdrafts or the degree of buoyancy versus dynamically-driven vertical motions in the RFD. Lewellen et al. (2000) found that tornadogenesis failure occurred in simulated tornado-like vortices when a shallow layer of low angular momentum air near the surface reduced the swirl ratio of air entering into the corner region, preventing a surface vortex from developing. He attributed a decrease in the near-surface angular momentum to a sudden increase in storm motion or surface roughness which reduced the angular momentum through turbulent dissipation.

v. *Role of Storm-Scale Features*

The tornado is not an independent entity, despite what may be numerically modeled or simulated in the laboratory. Rather, it is continuously interacting with its parent storm and the nearby environment. Two storm-scale features in particular have been historically associated with tornadoes and tornadogenesis: 1) the RFD and 2) the low-level mesocyclone. Many studies have noted that a strong area of low-level rotation separate from the midlevel mesocyclone precedes tornadogenesis (Grasso and Cotton 1995; Wicker and Wilhelmson 1995; Wakimoto and Atkins 1996; Ziegler et al. 2001; Dowell and Bluestein 2002; Wurman et al. 2007). Klemp and Rotunno (1983) determined that the mechanism for forming rotation at low-levels of the parent storm was fundamentally different from the tilting of environmental shear into the vertical by an updraft, which generates the midlevel mesocyclone. Their study and a subsequent one (Rotunno and Klemp 1985) determined that the low-level mesocyclone was formed by the tilting of baroclinically generated horizontal vorticity along the forward flank

gust front and advected toward the updraft by the storm-relative inflow. This mechanism, however, is not sufficient for producing a surface-based vortex since an updraft would tilt the vortex lines and advect them away from the surface. Thus, there has been subsequent debate about how the strong vorticity makes it to the near-surface levels.

It is generally accepted that the origin of near-ground rotation must be associated with a downdraft that can tilt horizontally oriented vorticity into the vertical and advect it downward, toward the surface (Figure 9). The exact details of where this vorticity comes from and how it is generated remain debated. Wicker and Wilhelmson (1995) and Grasso and Cotton (1995) found that it came from baroclinically generated vorticity along the forward flank gust front. In comparison, Shabbott and Markowski (2006) found that FFDs in nontornadic supercells tended to be more negatively buoyant and produce a greater magnitude of baroclinically generated horizontal vorticity, but have weaker low-level mesocyclones than tornadic supercells. Davies-Jones and Brooks (1993), Alderman (1999), and Markowski (2008) attributed the vorticity development to baroclinic processes along the edge of the rear flank gust front. Davies-Jones (2008) demonstrated that a strong surface vortex could be generated by barotropic mechanisms as a simulated annular RFD transported high angular momentum air to the surface that subsequently converged beneath the updraft, tilted and stretched at very low levels.

Klemp and Rotunno (1983) indicated that the baroclinic vorticity generated in their simulations was proportional to  $1/U$ , where  $U$  is the advective timescale of the flow. This result implies that a balance may be required for the generation of the

appropriate amount of baroclinic vorticity. If a parcel moves too quickly through the baroclinic zone, it does not acquire sufficient vorticity. However, if it moves too slowly, the storm-relative inflow is likely weak and the cold pool may overwhelm the updraft, cutting it off from the inflow. Trapp and Fiedler (1995) found that conditions for optimal vortex genesis include a sufficiently strong downdraft and baroclinic generation of vorticity in some capacity, optimal storm propagation speed and storm-relative flow (to inhibit the gust front from overtaking the updraft), and a thin viscous boundary layer. Markowski (2003) determined that cold RFDs are less likely to produce tornadoes than those with less of an equivalent potential temperature deficit, presuming that the warmer RFDs allowed the air entering the low-level mesocyclone to be more positively buoyant and better capable of stretching vorticity to tornadic strength. From these studies, it appears that there may be a variety of mechanisms and storm-scale processes that contribute to the generation of vertical vorticity at low levels and to the ensuing process of tornadogenesis.

*vi. Cyclic Mesocyclogenesis and Tornadogenesis*

Under certain atmospheric conditions, supercell mesocyclones and often their associated tornadoes undergo a periodic process of formation, decay and reformation at a new location. Such a process is called ‘cycling’. Some of the earliest observations of cycling were made by Fujita (1970), Darko and Roos (1970) and Darko (1971), who noted visually that tornadoes periodically undergo a process of formation, decay and reformation within the same parent supercell. Often these events were called ‘tornado families’. Other studies from visual observations include Rasmussen et al. (1982), Jensen et al. (1983) and Bluestein et al. (1988). With the advent of Doppler radar came

a more formal understanding of the cyclic process and a better recognition of conditions that favor cyclic mesocyclogenesis and cyclic tornadogenesis (Brandes 1977; Burgess et al. 1982; Johnson et al. 1987; Wakimoto and Cai 2000; Dowell and Bluestein 2002 a, b; Beck et al. 2005; Tanamachi et al. 2012).

Burgess et al. (1982) proposed a conceptual model of the cyclic mesocyclogenesis process, and how it relates to associated tornado lifecycles, representing the supercell in a manner similar to a midlatitude cyclone, with the forward (rear) flank gust front in the same relative position as the synoptic warm (cold) front (Figure 10). According to their study, a mesocyclone (represented by an “L” in their figure) forms within a parent supercell, with a forward flank gust front (FFGF) extending to the east and a rear flank gust front (RFGF) to the south. The RFGF cyclonically wraps around the southern flank of the mesocyclone, and tornadogenesis occurs. The RFGF continues wrapping around the mesocyclone and intersects the FFGF, forming an occlusion, cutting the original mesocyclone and its tornado off from the inflow. Shortly after this occlusion, a new mesocyclone begins to form in the inflow to the east or northeast of the original mesocyclone, where the RFGF intersects the FFGF. The original mesocyclone and its tornado move rearward (in a storm-relative sense), or to the left of the mean storm motion, curving to the northwest before completely decaying. Meanwhile, the new mesocyclone intensifies and forms a new tornado.

In later studies (Dowell and Bluestein 2002 a, b, and Beck et al. 2005), there was little or no evidence requiring a FFGF for cyclic mesocyclo-(tornado)genesis. Dowell and Bluestein found that the wind shift associated with a FFGF was very subtle,



if present at all, and Beck et al. determined that there was no evidence of a near surface wind shift associated with the FFGF (although a wind shift was present aloft). Unlike the Burgess et al. study, Dowell and Bluestein found that the RFGF never surged ahead of the updraft location in their case study, although the temporal resolution of their study was quite coarse (5-6 minutes between analysis times). Rather, they concluded that a rear portion of the original ‘U’-shaped updraft was shed and advected toward the left of the storm motion vector, becoming removed from the initial updraft with time until it was completely cut off from the warm inflow. The original updraft persisted but strengthened in a new location above the convergence zone associated with the RFGF. They determined that the position of subsequent mesocyclogenesis was strongly correlated with bulges in the RFGF caused by localized surges in outflow. New mesocyclones did not form at the occlusion point of the RFGF and FFGF. Another difference between Burgess et al. and the Dowell et al. studies was Dowell et al. determined that the tornadoes moved to the left of the updraft earlier than what the Burgess et al. (1982) model depicted.

In their conceptual model (Figure 11), Dowell et al. summarize the cyclic mesocyclogenesis/tornadogenesis process as follows: A RFGF wraps around the mesocyclone and a tornado forms. The updraft becomes “u”-shaped as upward motion develops above the zone of convergence along the RFGF. A bulge develops in the RFGF due to surging outflow ahead and to the right (in a storm-relative sense) of the tornado, concentrating upward motion at that location and generating a new mesocyclone. The main updraft, a continuous entity, shifts to the new mesocyclone location and sheds the portion of the original updraft still attached to the tornado, which

moves rearward, away from the RFGF and warm inflow. The new mesocyclone begins to control the motion of the RFGF and wraps it around, producing a new bulge and possibly a new tornado.

Adlerman and Drogemeier (2005) simulated the effects that varying the magnitude and distribution of vertical wind shear had on cyclic mesocyclogenesis. They defined two modes of cyclic mesocyclogenesis: 1) an occluding cyclic mesocyclogenesis mode (OCM) where the storm cycles due to an RFGF occlusion and 2) a non-occluding cyclic mode (NOCM) when a new mesocyclone forms without an occlusion (Figure 12). Alternatively, mesocyclones can also remain in a steady state, without cycling. They determined the cyclic behavior of the mesocyclone is mostly dependent upon the distribution of vertical wind shear.

The occluding cyclic mesocyclogenesis (OCM) mode they observed was very similar to that described by Burgess et al. The original mesocyclone becomes removed from the rear flank gust front and entirely surrounded by outflow, cutting the original updraft off from the warm moist inflow, causing it to weaken and eventually decay. The original mesocyclone moves rearward in a storm-relative sense, often looping cyclonically toward the northwest before entirely decaying. A new mesocyclone develops at the new intersection between the forward and rear flank gust fronts, north or northeast of the original updraft location. Although the Dowell et al. study again is slightly different in the formation location of the new mesocyclone, it still represents the OCM mode.

During the non-occluding cyclic mesocyclogenesis (NOCM) mode, the original mesocyclone *and* the parent updraft are displaced by strong northerly outflow, and

move down the rear flank gust front, in a storm relative sense (usually to the S or SW) together. The original mesocyclone and updraft remain collocated together and an occlusion does not occur owing to the lack of westerly momentum behind the RFGF. As the original updraft and mesocyclone move farther south, they weaken and there is a transition in maximum updraft location up the forward flank (usually to the N), with a new mesocyclone developing in this location. While they note the formation of a new mesocyclone, the original low-level and mid-level mesocyclone never decouple from the each other or the original updraft. Rather, the system weakens together until it entirely decays. Meanwhile, the strongest upward motion shifts gradually northward, forming a new low-level and mid-level mesocyclone. There is no discrete ‘jump’ in updraft location.

They attributed the NOCM mode to strong flow behind the RFGF that is oriented parallel to the RFGF. They found that NOCM occurred for all simulations with straight hodographs, and for those hodographs characterized by extremely high-shear, strongly curved shapes. Additionally, the strongest mesocyclones were associated with NOCMs, which, given the tendency for NOCM to occur in highly sheared environments, is intuitive. When comparing the results of all of their simulations, they found that the shape of the hodograph and the vertical distribution of shear magnitude and direction impact whether or not a supercell is cyclic, and the type of cyclic mode it exhibits. In their words, “the distribution and location of vertical environmental shear can radically alter storm morphology.” Their results, summarized in Figure 13, conclude that in general, increasing the shear and the curvature of the hodograph *simultaneously*, tended to produce steady, non-cycling storms, although

curved hodographs with very low shear magnitudes also produced non-cycling storms. For straight hodographs, all supercells had NOCM as did those strong shear and curvature confined to the lowest 1-3 km. OCM was found to occur at intermediate values of shear and hodograph curvature.

Despite the prevalence of the NOCM mode in Adlerman and Drogemeier model, only one observational study has conformed to this mode of cyclic mesocyclogenesis. Clark (2012) studied a cyclic convective storm which they classified as non-supercellular during the cool season in the U.K. He found that mesovortices<sup>1</sup> in that case moved south and eastward along a bowing gust front, and consecutive mesovortices developed repeatedly to the north, in a region of strong horizontal shear close to the storm's core. It is worth noting that this study was also done with coarse temporal sampling (5-6 minutes between analysis times), which may have eliminated some details about the cycling process.

### **Chapter 3. Project Design**

Ultimately, the factors motivating most tornado studies are to improve forecasts, warning time and warning accuracy. As was mentioned earlier, scientists still do not understand the exact details of tornadogenesis and tornado evolution. However, in order to improve forecasts and warnings, the details about why tornadoes form, what happens in the storm and nearby environment just prior to tornadogenesis, what causes tornadoes to intensify and why they dissipate (which impacts their longevity) must be understood. In an attempt to fill in some of the gaps missing in the science of tornado

---

<sup>1</sup> Clark refrains from using the term 'mesocyclone' because the vortices do not entirely conform to the definition of a mesocyclone. Namely, the vortices are not long-lived nor very deep.

formation and to enhance the results of recent studies examining tornado processes (Alexander 2010; French et al. 2013; Kosiba et al 2013), a rapid-scanning mobile Doppler radar (RaXPol) was designed to collect data on supercells and tornadoes (see Chapter 4 for more information about the instrument). This dissertation utilizes data collected by RaXPol in a tornadic supercell on 24 May 2011 in central Oklahoma.

According to radar sampling theory (Gal Chen and Wyngaard 1982; Bluestein et al. 2010), in order to resolve a feature fully, the coarsest radar resolution dimension must be at least one-tenth of the scale of the feature. This specification makes it quite difficult to resolve fully the motions for a relatively small tornado of 100 m (i.e. beam width and range resolution must be 10 m or less). However, Bluestein et al. (2010) also state that in order to detect, but not necessarily fully resolve a feature, the spatial resolution of the radar can be reduced to one-quarter of the scale of the feature. For a tornado with a width of 1 km, this means that the radar beam would have to be less than 250 m wide, which corresponds to a maximum range between the tornado and the radar of  $\sim 14.3$  km for a radar like RaXPol with a  $1^\circ$  beam width. For a more typical tornado of considerably smaller size (200 m) (Alexander 2010), the beam width would have to be 50 m, which demands the radar to be located  $\sim 3$  km away.

Although the deployment location ideally should be within 3 km from the tornado, this deployment positioning is often very difficult to achieve. Logistical challenges including road network, accurate anticipation of storm motion and extrapolation of tornado position into the future are necessary. Additionally, it is desired that datasets are temporally continuous for as long as possible; it is not desirable to have many short deployments, even if they are all within the ideal range. The time it

takes to reposition to the ideal range is sometimes substantial and valuable data are lost during the repositioning transit. Therefore, the deployment strategy for this project was to position the instrument initially far away from the area of interest and let the storm approach the radar. Serendipitously, the storm in this case study produced a tornado that moved within 3 km of the deployment location and grew to be considerably larger than 200 m.

This dataset is ideal for examining the questions presented in Chapter 1: 1) how does a tornado develop, intensify and decay over short time scales, 2) how does rotation evolve during tornado formation, 3) how do external features impact tornado processes, 4) how does the three-dimensional structure of the tornado evolve, and 5) what additional insight can be acquired from the polarimetric analyses? During the time data were collected, one tornado strengthened, reached peak intensity, then dissipated, and a second tornado formed and intensified to EF-5 strength. Thus, the dataset captures the entire lifecycle of a tornado, even though it is not the same tornado that forms and dissipates. Additionally, the second tornado was long-lived and violent, remaining on the ground for nearly an hour. Such tornadoes represent a very small percentage of total tornadoes, but are responsible for the majority of deaths and property damage. Because violent, long-lived tornadoes occur infrequently, relatively few datasets have been collected on them making this dataset one of only a small pool of others (Burgess et al. 2002; Alexander and Wurman 2005; Wurman and Alexander 2005; Tanamachi et al. 2012) to document such a tornado.

The rapid-scan capabilities of the instrument allowed for volumetric updates every 17 seconds during tornado decay, formation and intensification. The information

available from this dataset is therefore better capable of clarifying the volumetric evolution of genesis, intensification and decay, including the structure of the tornado and wind field than nearly all previous studies. Because the spatial resolution is better than that of the French et al. (2013) studies, this study is able to resolve definitively the tornado during the latter portion of data acquisition, and resolve genesis more definitively.

In order to address the central questions posed here, data are used from both the raw radar fields and objectively analyzed Cartesian grids. Single-Doppler and dual-Doppler analysis techniques are employed to derive the horizontal and three-dimensional wind field, respectively. Details of these processes and analyses are given in Chapter 6.

### **Tornado Dynamics**

The first comprehensive analytical study of vortex dynamics was performed by Kuo (1966), who derived a system of equations to represent an atmospheric vortex by specifying an unstable vertical stratification and background rotation within the analysis domain. Two solutions were found: a single-cell solution having a central updraft along the axis of rotation, and a two-cell solution with a central downdraft along the axis, surrounded by an annular updraft. The study successfully produced low pressure at the center of the vortex and determined that friction has a pronounced effect on the flow distribution.

Early laboratory studies also successfully simulated tornado vortex dynamics and determined that the laboratory vortices were highly dependent upon the geometry of the large-scale flow and the physical structure of the vortex chamber (Ward 1972; Davies-Jones 1973, 1976; Rotunno 1979). One representation of the large-scale flow properties is the swirl ratio,  $S$  (Davies-Jones 1973). By definition, the swirl ratio is represented by:

$$S = \frac{R\Gamma_r}{2Q} \quad \text{Equation 1}$$

where  $2\pi\Gamma_r$  is the circulation at radius  $R$  and  $2\pi Q$  is the volumetric flow rate through the chamber. Physically,  $S$  represents the ratio of tangential velocity at the edge of the updraft to the average vertical velocity within the updraft. Alternatively,  $S$  also represents the ratio of vorticity to convergence of the ambient inflow:

$$S = \frac{v_o}{w_{ave}} \quad \text{Equation 2}$$

Rotunno (1979) stated “laboratory and numerical models indicate that the swirl ratio  $S$  is the single most important parameter governing vortex dynamics.”

The change in tornado vortex structure with  $S$  was documented by Rotunno (1979), and indirectly by Ward (1972). Rotunno (1979) found that for  $S=0$  (i.e. converging radial inflow only, no tangential velocity), the convergence of air along the central axis causes relative high pressure to build near the surface, resulting in a reversal of the boundary layer flow close to the axis of rotation (boundary layer separation) (Figure 14a). This effectively prevents circulation from converging close enough to the axis to form a vortex. When  $S$  is small ( $<1$ ) but non-zero, a weak single-cell vortex forms, but it does not become very concentrated because boundary layer separation still occurs, deflecting air with high angular velocity flow from the center. As  $S$  increases, a



strong single-cell vortex is produced (Figure 14b). This vortex is dominated internally by a strong central updraft and strong tangential winds. As  $S$  further increases, a central downdraft becomes evident within the upper portion of the central axis (Figure 14c, Figure 15). This marks a transition from a one-cell to a two-cell vortex, as mathematically hypothesized by Kuo (1966).

Where the central updraft meets the central downdraft, and the vortex discretely jumps from one stable state to another, a phenomenon known as vortex breakdown occurs (Maxworthy 1972; Church et al. 1977; Rotunno 1979; Lewellen 1993). Upstream from the jump (the lower portion of the vortex), flow is supercritical: the vertical velocity exceeds the speed at which inertial waves can travel. The vortex visually appears laminar and has high vertical and tangential wind speeds arising from the rapid transition from inflow to updraft in the corner region. Downstream from the jump, the flow is subcritical meaning the vertical velocity is weaker than the inertial wave speed. In this region, the vortex visually appears broader and more turbulent, and has weaker vertical and tangential wind speeds as a result of a decreased pressure gradient force. When the vortex is subcritical, waves can travel vertically along the vortex.

As  $S$  continues to increase, the height at which vortex breakdown occurs becomes progressively lower until it reaches the surface when  $S$  exceeds unity. At this point, the one-celled vortex becomes a two-celled vortex with a central downdraft surrounded by a ring of updraft (Figure 14d). Further increase of  $S$  causes a transition from a single-vortex structure to a multiple vortex structure, with several secondary vortices surrounding the central downdraft in an annular fashion (Figure 14e). These

secondary vortices can be associated with extreme winds, stronger than what would be present in a single vortex (Leslie 1977; Davies-Jones et al. 2001). One-cell vortices have stronger central pressure deficits than two-cell vortices, but secondary vortices surrounding the central axis of a two-cell vortex may have even greater pressure deficits (Snow et al. 1980). Observations of the various vortex structures in the free atmosphere have been observed visually and with mobile Doppler radar, validating these laboratory conclusions (Agee et al. 1975; Barnes 1976; Agee et al. 1977; Wurman and Gill, 1995; Bluestein and Pazmany, 2000; Wurman 2002; Bluestein and Wakimoto 2003).

In nearly all laboratory and numerical modeling simulations of tornado-like vortices, a no-slip lower boundary condition forms a more intense surface vortex than a free-slip boundary condition, which may not even generate a vortex (Leslie 1971; Wicker and Wilhelmson 1993; Trapp and Fiedler 1995; Davies-Jones 2008). This implies that friction plays an important role in surface vortex genesis and cannot be neglected in simulations.

The flow field surrounding tornado-like vortices is often described as a Rankine-combined vortex (Rankine 1882). Mathematically, a Rankine vortex is represented as:

$$V_{\theta}(r) = \begin{cases} \Gamma r / (2\pi R^2) & r \leq R \\ \Gamma / (2\pi r) & r > R \end{cases} \quad \text{Equation 3}$$

where  $V_{\theta}$  is the tangential velocity,  $\Gamma$  is the circulation,  $r$  is the radius at which the velocity is being calculated, and  $R$  is the radius of maximum winds. The inner region of rotation ( $r \leq R$ ) is in approximate solid body rotation with the tangential velocity increasing linearly with radius. Outside this area ( $r > R$ ), the velocity decreases according to  $1/r$  (Figure 16a). Lewellen (1993) suggests that the Burgers-Rott model

better represents tornado vortex flow (Figure 16b). This model is essentially similar to the Rankine-combined vortex, but has a smoother transition between the inner and outer flow regions at the RMW.

Theoretical estimates have been made on the maximum intensity a tornado can attain based on the thermodynamic speed limit – a measure of the fastest winds a hydrostatic environment can support for a given amount of buoyancy. Mathematically, the thermodynamic speed limit can be represented by:

$$v_{\theta max} = \sqrt{\Delta P_{hyd} / c\rho} \quad \text{Equation 4}$$

according to the notation of Nolan and Farrell (1999). Here,  $v_{\theta max}$  is the maximum attainable tangential wind speed,  $\Delta P_{hyd}$  is the hydrostatic pressure deficit at the center of the tornado,  $c$  is a constant that depends on the type of vortex (e.g. Rankine, Burgers-Rott, etc.), and  $\rho$  is the density of the air. Observational and numerical studies examining the relationship between the maximum wind within a tornado and the theoretical thermodynamic speed limit have yielded mixed results, with some cases exceeding the theoretical speed, sometimes significantly (Lewellen 1976; Snow and Pauley 1984; Fiedler and Rotunno 1986; Bluestein et al. 1993; Fiedler 1994) and other cases having maximum velocities near the thermodynamic speed limit (Trapp and Fiedler 1995). One non-negligible assumption in the derivation of  $v_{\theta max} =$

$$\sqrt{\Delta P_{hyd} / c\rho} \quad \text{Equation 4}$$

is that of hydrostatic and cyclostrophic balance, which are likely violated in the tornado. This is likely one reason why the theoretical thermodynamic speed limit is sometimes exceeded.

Since tornadoes are rotating entities, sources of atmospheric rotation and its transport should be discussed. Assuming a Boussinesq atmosphere, the full vorticity equation derived from the Navier Stokes equations of motion is:

$$\frac{\partial \boldsymbol{\omega}}{\partial t} = -(\mathbf{v} \cdot \nabla)(\boldsymbol{\omega} + f\mathbf{k}) + [(\boldsymbol{\omega} + f\mathbf{k}) \cdot \nabla]\mathbf{v} + 1/\rho^2 \nabla \rho \times \nabla p + \nabla \times \mathbf{F} \quad \text{Equation 5}$$

where  $\boldsymbol{\omega}$  is the three-dimensional vorticity vector,  $f$  is the Coriolis parameter,  $\mathbf{v}$  is the three-dimensional wind vector,  $\rho$  is density,  $p$  is pressure,  $\mathbf{F}$  is friction,  $\mathbf{k}$  is the unit vector in the  $z$  direction, and  $t$  is time. The first term represents advection of pre-existing vorticity, the second represents tilting and stretching of vorticity by horizontal and vertical wind shear, the third term is the baroclinic generation term, and the fourth term is the contribution to vorticity generation or dissipation due to frictional forces. Neglecting planetary vorticity ( $f\mathbf{k}$  terms), the equation for the vertical component of vorticity ( $\zeta = \partial v/\partial x - \partial u/\partial y$ ) is:

$$\frac{\partial \zeta}{\partial t} = -\mathbf{v} \cdot \nabla \zeta + \boldsymbol{\omega} \cdot \nabla \mathbf{w} + 1/\rho^2 \left( \frac{\partial \rho}{\partial x} \frac{\partial p}{\partial y} - \frac{\partial \rho}{\partial y} \frac{\partial p}{\partial x} \right) + \mathbf{k} \cdot \mathbf{F} \quad \text{Equation 6}$$

According to this equation, in the absence of pre-existing vorticity, vorticity can only be generated by baroclinic or frictional processes. Otherwise, vertical vorticity can change when it is advected either horizontally or vertically, when it is tilted from the horizontal into the vertical by wind shear, or when it is stretched by horizontal convergence or divergence.

Another important equation governing the behavior of supercells and tornadoes is the pressure perturbation equation. This equation is derived from describing pressure as a combination of a base-state pressure,  $\bar{p}(z)$  and a perturbation pressure  $p'(x, y, z, t)$ , with  $p'$  being a sum of the hydrostatic contribution and the non-hydrostatic contribution

to the perturbation pressure. The derivation begins with the Boussinesq equations of motion in the following form:

$$\frac{\partial \mathbf{v}}{\partial t} + \mathbf{v} \cdot \nabla \mathbf{v} = -1/\rho_0 \nabla p' + B\mathbf{k} - \mathbf{f}\mathbf{k} \times \mathbf{v} \quad \text{Equation 7}$$

Where  $\rho_0$  is the base-state density and  $B = -(\rho'/\rho)g$  is buoyancy, with  $p'$  representing the deviation of density from base-state, and  $g$  being gravity. Taking the divergence ( $\nabla \cdot$  equation) of  $\frac{\partial \mathbf{v}}{\partial t} + \mathbf{v} \cdot \nabla \mathbf{v} = -1/\rho_0 \nabla p' + B\mathbf{k} - \mathbf{f}\mathbf{k} \times \mathbf{v}$  Equation 7,

assuming incompressibility and neglecting planetary vorticity yields:

$$\begin{aligned} \alpha_0 \nabla^2 p' = & - [(\partial u / \partial x)^2 + (\partial v / \partial y)^2 + (\partial w / \partial z)^2] \\ & + 2(\partial v / \partial x \partial u / \partial y + \partial w / \partial x \partial u / \partial z + \partial w / \partial y \partial v / \partial z) \\ & + \partial B / \partial z \end{aligned} \quad \text{Equation 8}$$

Changes in pressure are therefore associated with fluid extension (term 1), deformation and rotation (term 2), and vertical gradients in buoyancy (term 3). Assuming a 'well behaved' pressure field, changes in  $p'$  can be approximated as being proportional to  $-\nabla^2 p'$ . This approximation implies that deformation will always be associated with high perturbation pressure and rotation will always be associated with low perturbation pressure. The latter term is particularly important for supercell and tornado dynamics as it is responsible for the generation of vertical pressure gradient forces and therefore vertical motions when rotation is not uniform with height. Strengthening rotation at mid-levels is associated with low perturbation pressure and therefore dynamically-driven upward motion occurs beneath the rotation and downward motion occurs above it.

## Polarimetric Radar Overview

In recent years, studies of supercells and tornadoes have benefited from the use of dual-polarized (otherwise known as polarimetric) radar observations (Bluestein et al. 2007, Romine et al. 2008, Frame et al. 2009, Palmer et al. 2011, Tanamachi et al. 2012). Polarimetric radars enable the retrieval of additional variables conventional radars cannot acquire. For this study, in addition to conventional horizontal reflectivity factor, the polarimetric variables differential reflectivity ( $Z_{DR}$ ), and co-polar cross-correlation coefficient ( $\rho_{hv}$ ) are used. (Differential phase ( $\phi_{DP}$ ) is available but is not utilized.) Attenuation was not corrected for because the reflectivity field was not used quantitatively in any capacity and the area of interest (namely the tornado) was not significantly affected by attenuation.

Measurements of  $Z_{DR}$  provide estimates of the mean ratio of the horizontal return power to the vertical return power and as such offer information about the shape, size, and orientation of the hydrometeors within a sample volume. Targets having a significantly larger horizontal axis than vertical have  $Z_{DR} > 0$ , those that are approximately spherical have values of  $Z_{DR} \sim 0$ , and those that are vertically oriented have  $Z_{DR} < 0$ . For meteorological hydrometeors, generally the value of  $Z_{DR}$  is between 0 and 5 dB (Ryzhkov 2005).

Measurements of  $\rho_{hv}$  quantify the magnitude of the correlation between returns in the horizontally and vertically polarized channels and are dependent upon the size, orientation, shape and dielectric constant of the hydrometeors within the sample volume. Values range from 0 to 1 and for meteorological targets, they generally exceed 0.95. When a variety of precipitation types (e.g. rain, hail, snow, graupel, etc.) coexist

within the same volume or non-meteorological scatterers are introduced,  $\rho_{hv}$  is reduced. For purely meteorological scatterers,  $\rho_{hv}$  does not decrease below  $\sim 0.8$  (Ryzhkov et al. 2005), but when there is debris (non-meteorological scatterers) within the sample volume, the values can get much lower. (For further review of polarimetric radar variables and their meteorological application, the reader is referred to Balakrishnan and Zrinc (1990), Herzegh and Jameson (1992), Zrinc and Ryzhkov (1999), and Bringi and Chandrasekar (2001)).

One of the major advantages of polarimetric radars over conventional radars is that they provide better understanding of storm microphysics (melting, size sorting, mixed-phase processes, etc.). When polarimetric variables are used in combination with each other, hydrometeor types can be inferred and, using fuzzy logic algorithms, the type can be classified (Vivekanandan et al. 1999, Zrinc and Ryzhkov 1999; Liu and Chandrasekar 2000; Straka et al. 2000; Park et al. 2009; Snyder et al. 2010). The microphysical information in turn can be used to infer information about the dynamics of the storm such as updraft and inflow intensity, hail generation and fallout regions, and the presence or absence of tornadoes.

Through the combined effort of multiple studies (Ryzhkov et al. 2002, Ryzhkov et al. 2005, Bluestein et al. 2007, Van den Broeke et al 2008, and Kumjian and Ryzhkov 2008), several distinct polarimetric signatures have been identified in supercells. These features include low-level inflow and updraft signatures, the  $Z_{DR}$  arc, the  $Z_{DR}$  column, midlevel  $Z_{DR}$  and  $\rho_{hv}$  rings, and the tornadic debris signature (Figure 17). An overview of each of these features now follows.

vii. *Low-Level Inflow and Updraft Signatures:*

Inflow winds flowing into the updraft region can be quite strong and are often devoid of precipitation. As a result, small, light debris and other non-meteorological scatterers such as insects and dust can become airborne in the inflow and transported into the vicinity of the storm. These non-meteorological scatterers are considerably more irregular in shape, size, and orientation, and as such have unique polarimetric properties. Most prevalent is a reduction in  $\rho_{hv}$  with values as low as 0.7 occurring in the inflow (Kumjian and Ryzhkov 2008). As this inflow encounters the updraft, it is ingested into the storm and advected vertically, resulting in a shallow column of reduced  $\rho_{hv}$  aloft, in the lower portion of the updraft. However, the interpretation of low  $\rho_{hv}$  near the updraft due to debris must be made cautiously. Often there are few hydrometeors in the updraft region as well, which results in a bounded weak echo region (BWER). When hydrometeors are absent or have low number concentrations, the signal to noise ratio becomes low, biasing the  $\rho_{hv}$  values as well. Additionally, tumbling hail often is present in the updraft causing a reduction of  $\rho_{hv}$ . Thus, the low  $\rho_{hv}$  in the updraft region can only truly indicate lofted debris if there is not a BWER present and if reflectivity values are lower than expected for hail signatures.

However, for all cases described above, the relative location of the updraft may be inferred from reduced values of  $\rho_{hv}$  regardless of the reason for the reduction, assuming the signature is present in areas where an updraft is expected (i.e., downshear from and to the left of the hook echo, near the area of the low-level inflow notch). To this extent, the relative intensity of the updraft may also be inferred from polarimetric signatures. The vertical extent of the BWER and depressed  $\rho_{hv}$  values can be used as a



proxy for updraft intensity, with lower values of both reflectivity factor and  $\rho_{\text{hv}}$  existing at higher heights for stronger updrafts.

*viii.  $Z_{\text{DR}}$  Arc Signature:*

In many supercell case studies, a narrow, arc-like region of high  $Z_{\text{DR}}$  values (often exceeding 4 dB at S-band) has been repeatedly observed along the storm-relative right side (usually the southern edge) of the forward flank reflectivity gradient (Figure 17). The feature, known as the  $Z_{\text{DR}}$  arc, is characteristically shallow, only extending to a maximum height of 2 km. Using preliminary results from a numerical model, Kumjian and Ryzhkov (2008) hypothesize that this feature denotes a region of size-sorting where small hydrometeors with relatively slow terminal fall speeds encounter strong vertical wind shear and are advected into the forward flank region, away from the source region. Large drops falling from the same location aloft, but with faster terminal fall speeds and more momentum, are not advected away from the source region as effectively. As a result, the hydrometeors falling on the inflow-side of the forward flank downdraft are large, oblate spheroids, since the trajectories of the smaller drops remove them from this area. Large raindrops have high  $Z_{\text{DR}}$  values but their number concentration is somewhat low and therefore the horizontal reflectivity factor is not very high.

$Z_{\text{DR}}$  arcs have also been used to infer dynamical and kinematic information about the supercell and nearby storm environment. Van den Broeke et al. (2008) suggested that the structure of the  $Z_{\text{DR}}$  arc might be associated with tornadogenesis. They noted that prior to tornadogenesis, the  $Z_{\text{DR}}$  arc extends back (in a storm-relative sense), toward the updraft as a result of the mesocyclone occlusion process. Kumjian and Ryzhkov (2009) extended the work of Van den Broeke et al. to nontornadic supercells and found

that the  $Z_{DR}$  arc displayed this tendency any time a mesocyclone occlusion was about to occur, regardless of whether or not the occlusion was associated with tornadogenesis. Kumjian and Ryzhkov hypothesized that prior to any mesocyclone occlusion, the low-level inflow increases due to strengthening convergence associated with a dynamically-induced pressure perturbation gradient generated by the strengthening low-level mesocyclone. The stronger inflow advects larger raindrops closer to the mesocyclone, therefore causing this signature to persist closer to the updraft.

Kumjian and Ryzhkov (2009) also noted that the  $Z_{DR}$  arc is affected by the storm relative wind speed and the directional wind shear, and consequently the storm relative helicity (SRH). When the SRH increases, size sorting due to wind shear increases as well, resulting in a more pronounced  $Z_{DR}$  signature as a greater number of smaller raindrops are advected away from the southern flank into the forward flank downdraft region. They concluded that the direction of the mean storm-relative wind in the shallow layer (~1-2 km) above the  $Z_{DR}$  arc could be inferred from the orientation of the  $Z_{DR}$  arc, with the mean wind perpendicular to the orientation of the arc's major axis. They also noted that for nontornadic storms, the  $Z_{DR}$  arc appeared to become 'disrupted' more frequently, meaning the signature was not as clearly persistent, and hypothesized that this may indicate that outflow from the FFD was undercutting the inflow.

An alternative hypothesis explaining the formation of the  $Z_{DR}$  arc is offered by Romine et al. (2008). They attribute the development of this signature to the development of a narrow drop spectrum associated with melting of frozen hydrometeors. Frozen hydrometeors above the  $Z_{DR}$  arc would have low values of  $Z_{DR}$  until they became mostly liquid, at which point they have a large effective

backscattering area and high  $Z_{DR}$  values. Additionally, coalescence of water drops increases as drops fall due to increased liquid water content from melting hydrometeors within the column, shifting the  $Z_{DR}$  values upward as a result of the increased mean drop diameter. However, this hypothesis explaining  $Z_{DR}$  arc formation remains mostly speculative and has not been substantiated by numerical modeling studies.

*ix.  $Z_{DR}$  Columns:*

Because updrafts transport heat and moisture vertically upward into the storm, they affect the microphysics of hydrometeors within them and around them. As such, they can be associated with polarimetric signatures, some of which have already been discussed here. The  $Z_{DR}$  column is a vertical extension of high  $Z_{DR}$  values above the freezing level, representing an area of upward motion. The feature is typically found on the inflow side of the storm, on the periphery of the updraft (as inferred from the location of the BWER.)  $Z_{DR}$  columns typically have values  $> 3$  dB (at S-band), are relatively narrow, spanning only 4-8 km, and can extend several km above the freezing level. Presumably, they indicate a region of lofted oblate raindrops or water-coated hailstones, as supported by Brandes et al. (1995) and Loney et al. (2002), who retrieved drop size distribution information via aircraft observations and confirmed that there are a small number of large (diameter  $> 2$  cm) raindrops and a few hailstones in this location.

It is hypothesized that the  $Z_{DR}$  column is caused by warm-rain collision and coalescence processes or from melting ice-type hydrometeors located initially in the reflectivity echo overhang or back-sheared anvil. It is most typically located on the inflow side of the updraft, and marks the periphery of the updraft and BWER, where

vertical motions are weak enough to allow some hydrometeors to fall. This observation is supported by Conway and Zrnic (1993) and Loney et al. (2002), who found that the maximum values of  $Z_{DR}$  were coincident with updraft locations having weak velocities. With stronger shear and stronger winds, the  $Z_{DR}$  column is expected to be less horizontally aligned with the actual updraft axis due to strong horizontal advection of the hydrometeors away from the updraft. Hubbert et al. (1998) noted that as the updraft intensity increased, so did the values of dB and the height of the  $Z_{DR}$  column.

*x. Tornadic Debris Signature:*

The tornadic debris signature (TDS) is a region of low  $\rho_{hv}$  and often low  $Z_{DR}$  that corresponds to the location where non-meteorological scatterers are lofted into the air by a tornado. Ryzhkov (2005) defined a tornadic debris signature as having  $Z_{DR}$  values  $< 0.5$  dB,  $\rho_{hv}$  values  $< 0.8$ , and reflectivity values  $> 45$  dBZ for S-band observations. He also noted, however, that if hydrometeors are in close proximity to the tornado, they may impinge upon the TDS causing the  $Z_{DR}$  values to increase above the 0.5 dB threshold. Thus, he argued that the  $\rho_{hv}$  signature is a more robust and reliable one. The TDS occurs as a result of the irregular sizes, large shapes, random orientation, and high dielectric constant of debris. The TDS cannot be used as a predictor of tornado events since it does not occur prior to tornado formation. Rather, it can be used to verify the presence of a tornado and validate tornado warnings.

In order for a tornado to have a TDS, wind speeds must be sufficiently strong to loft debris into the air, and the vertical motions in the tornado must be strong enough to transport the debris to a height high enough to be observed by the radar. In one case presented by Bluestein et al. (2007), a tornado was observationally confirmed but there

was no TDS evident in the data. The authors hypothesized that the beam was too high, despite it only being located several hundred meters above the ground. Studies by Ryzhkov (2005), Palmer et al. (2011), and Tanamachi et al. (2012) observed TDSs extending vertically through heights of at least 2.5-3 km, implying that vertical motions within the tornado can be quite substantial.

## Chapter 4. Instrumentation

Doppler radar data acquisition is a particularly desirable method for studying tornadoes because the instruments are able to sample remotely the three-dimensional structure of a tornado over a relatively large spatial extent. Early radar studies with limited spatial resolution provided the observational foundation to verify numerical and laboratory model studies of storm structure and basic dynamic information (Ray 1976, 1980; Brandes 1977, 1978, 1981; Brown et al 1978; Lemon and Doswell 1979; Klemp et al. 1981; Dowell and Bluestein 1997). There have been many more recent studies utilizing high-resolution single-Doppler radar data to reveal tornado structure and evolution (Wurman and Gill 2000; Bluestein and Pazmany 2000; Dowell and Bluestein 2002 a, b; Bluestein et al. 2003; Alexander and Wurman 2005; Dowell et al. 2005; Lee and Wurman 2005; Tanamachi et al. 2007; French et al. 2008; Palmer et al. 2011; Wakimoto et al. 2011).

Unfortunately, despite over 35 years of Doppler radar data availability, there have been few successful radar-based tornado studies with adequate temporal *and* spatial resolution to resolve *tornado-scale* processes (Wurman et al. 2007; Bluestein et

al 2010; Wakimoto et al. 2011). This limitation is due to a combination of instrument weakness (e.g. beam spreading with distance), logistical challenges in deploying mobile radars in close proximity to tornadoes, slow antenna rotation rates, and sometimes bad luck. Traditional (non-rapid-scan) mobile radars take 15 seconds or longer to complete a single  $360^\circ$  azimuthal planned-position indicator (PPI) scan. Even the fastest ones require at least 6 seconds to complete a  $360^\circ$  scan (Wurman 2001), implying a one minute acquisition time for a volume consisting of 10 elevation angles. Often, PPIs are acquired at a significantly slower rate, commonly with volume updates of 2-3 minutes. This time can be somewhat reduced by scanning small sectors of the atmosphere rather than a  $360^\circ$  PPI, however sector scanning requires slightly slower antenna rotation rates in order not to induce high stress on the pedestal. Because it is presumed that tornadoes evolve over timescales on the order of 10 s (Bluestein et al. 2003, 2010), it is obvious that volumetric temporal scanning strategies of this temporal magnitude are required to gain insight about tornado-scale processes.

In an attempt to achieve temporal resolution sufficient for resolving tornado-scale processes, a rapid-scanning phased array radar was acquired and transformed from a military instrument to a weather radar (Bluestein et al 2010). This instrument, the Mobile Weather Radar 2005 X-band phased-array (MWR-05XP) has been used successfully in field experiments from 2007-2011, and was used in the French et al. (2013) study. The radar is mechanically steered in the azimuth and electronically steered in elevation and can operate with a variety of scanning strategies specified by the user. The scanning strategy for which temporal resolution is maximized results in the acquisition of  $90^\circ$  sector volumes with 31 elevation angles in 10 s (Bluestein et al.

2010). Unfortunately, this instrument has a relatively large half-power beam width of  $1.8^\circ$  in azimuth and  $2^\circ$  in elevation. In order to obtain four independent azimuthal samples<sup>2</sup> across a 200 m wide tornado, the azimuthal resolution requires the vehicle to be  $\sim 1.6$  km away from the tornado. Such a limitation is a problem not only from a safety perspective, but also logistically, since maintaining such a distance would require almost constant adjustment of the vehicle position due to storm motion. It would be impossible to collect data at a given location for any substantial period of time. At a more appropriate distance of 15 km, the azimuthal resolution degrades to  $\sim 470$  m. Thus, while the temporal resolution of this instrument is superb, the wide beam angle inhibits it from adequately resolving most tornadoes.

The need for rapid temporal resolution while maintaining high spatial resolution motivated the design for the instrument used in the current study. The Rapid-Scan, X-band, polarimetric mobile radar (RaXPol) was designed by ProSensing Inc. in Amherst, MA, in collaboration with the University of Oklahoma, with the primary purpose of studying rapidly-evolving convective phenomena (Figure 18). It was first tested in the field during the 2011 spring storm season at the University of Oklahoma (Pazmany et al. 2013).

The radar is equipped with a 2.4 m diameter parabolic dish, capable of transmitting and receiving both horizontally and vertically polarized waves. Specifications for the instrument are summarized in Table 1. The truck on which RaXPol is mounted is equipped with a three-point hydraulic leveling system with external leveling balls, allowing the operator to level the system manually, ensuring that

---

<sup>2</sup>In order for an atmospheric feature to be well resolved by radar, at least four independent samples must be acquired across the feature in the radar-scanning plane (Gal Chen and Wyngaard 1982).

the beam is pointing at the exact azimuth and elevation angle that the processing software is recording. The exact position (latitude, longitude, altitude), including the pitch and roll of the truck is determined by a differential GPS with precision to  $10^{-6}$  degrees and 0.1 m respectively. These data are automatically fed into the computer system along with the truck heading, pitch and roll, and are stored in the file metadata. Recorded radar variables include standard radar reflectivity factor, Doppler velocity, spectrum width, differential reflectivity ( $Z_{DR}$ ), magnitude of the cross-correlation coefficient from the horizontal and vertical channel ( $\rho_{hv}$ ), and differential phase ( $\phi_{DP}$ ). The antenna mechanically rotates both azimuthally and in elevation, at a maximum azimuthal rate of just over  $180^\circ \text{ s}^{-1}$ , completing a nine-elevation volume scan in  $\sim 17$  seconds. Such a rapid scanning rate is enabled by a high-speed pedestal.

In order to obtain accurate estimates of reflectivity and radial velocity, a *typical* radar system must allow sufficient time to pass between consecutive pulses for the scatterers within the sample volume to decorrelate. The correlation between consecutive temporal samples is a function of radar parameters such as the pulse repetition time, the wavelength, the half-power beam width, and the antenna rotation rate. The time taken by the radar to acquire a sample volume (the dwell time  $T$ ), is a function of the azimuthal scan rate ( $v_{az}$ , rotations  $\text{s}^{-1}$ ), and the effective beam width ( $\theta_e$  degrees):

$$T = \theta_e / (360^\circ v_{az}) \quad \text{Equation 9}$$

In order to achieve the best azimuthal sampling possible and not smear the data, the desired effective beam width is equal to the 3 dB beam width of  $1^\circ$ . For  $\theta_e = 1^\circ$  and a maximum scan rate of  $180^\circ \text{ s}^{-1}$ , ( $v_{az} = 0.5 \text{ rotations s}^{-1}$ ),  $T = 5.5 \text{ ms}$ . Given the desired



antenna rotation rate and dwell time, the total number of samples ( $M$ ) collected is a function of the maximum unambiguous range ( $r_a$ ) desired:

$$M = \frac{\theta_{3dB}}{v_{az} * 2r_a / c} = \frac{T}{PRT} \quad \text{Equation 10}$$

where  $2r/c$  is the pulse repetition time (PRT, or  $T_s$ ), which is a function of the speed of light ( $c$ ). For RaXPol's specifications and a desired unambiguous range of 40 km, the maximum number of samples that can be collected during the 5.5 ms dwell time is 20, or 10 pulse pairs. .

According to Doviak and Zrnich (1992, pp 165), the decorrelation time required to obtain independent samples is:

$$\tau_d = \frac{\lambda}{2\sigma_v} \quad \text{Equation 11}$$

For a 3 cm wavelength ( $\lambda$ ) radar assuming a worst-case scenario spectrum width<sup>3</sup> ( $\sigma_v$ ) of  $5 \text{ m s}^{-1}$   $\tau_s$  is 3 ms. As previously mentioned, the dwell time of each  $1^\circ$  radial for RaXPol's  $180^\circ \text{ s}^{-1}$  antenna rotation rate is 5.5 ms.. Thus, in order to meet the demand of scanning at a rate of  $180^\circ \text{ s}^{-1}$  only one equivalent *independent* sample can be acquired. . As such, there is a problem of obtaining enough independent samples to calculate accurate estimates for the retrieved variables using a conventional scanning strategy. This problem is circumvented by using a frequency diversity technique called frequency hopping (Doviak and Zrnich 1992, pp 180). When this technique is applied, independent samples are acquired not by temporal decorrelation, but rather by sending out pairs of uniformly spaced pulses at frequencies that differ by increments of the pulse bandwidth (Figure 19).

---

<sup>3</sup>  $5 \text{ m s}^{-1}$  is assumed to be a high-end spectrum width value for most radar-observed events. However, spectrum width values within a tornado can be considerably higher than this.

The frequency hopping technique for this instrument allows for a maximum of 12 independent samples (24 pulses, 12 pulse pairs) to be acquired when the radar is in rapid-scan mode; however, the actual number of independent samples using the  $180^\circ \text{ s}^{-1}$  rotation rate is still a function of  $r_{\text{max}}$ . To get an idea of the quality of the velocity estimate ( $v_r$ ) obtained using the example of  $r_{\text{max}} = 40 \text{ km}$  (10 samples), the variance of the estimate can be calculated according to Doviak and Zrnic (p. 134):

$$\text{var}(v_r) \approx \lambda^2 / (32\pi^2 M \rho^2(T_s) T_s^2) - (1 - \rho^2(T_s)) \quad \text{Equation 12}$$

where  $\rho(T_s)$  is the correlation between two temporally consecutive pulses:

$$\rho(T_s) = e^{-8\left(\frac{\pi\sigma_v T_s}{\lambda}\right)^2} \quad \text{Equation 13}$$

For the same specifications of the variables already given ( $\sigma_v = 5 \text{ m s}^{-2}$ ,  $\lambda = .03 \text{ m}$ ,  $M = 10$ , and  $T_s = 267 \text{ } \mu\text{s}$  for  $R_{\text{max}}=40 \text{ km}$ ), the variance for the estimator of Doppler velocity is  $1.47 \text{ m s}^{-1}$ . For a more typical spectrum width of  $2 \text{ m s}^{-1}$ ,  $\text{var}(v_r) = 0.2 \text{ m s}^{-1}$ . One shortcoming of this technique is that ground clutter filter algorithms cannot be applied because these algorithms identify returns that are highly correlated. When using frequency hopping, ground clutter returns become uncorrelated and therefore mitigation algorithms do not work. However, the frequency hopping allows for mitigation of second-trip echoes by calculating non-velocity based products using only data collected from the first pulse transmitted and ignoring the power return from the second.

The software controlling data acquisition allows the user to specify multiple parameters in order to fine tune the desired sampling resolution. This capability provides adaptability to the system, enabling instrument use to be optimized for a variety of meteorological situations. The user can specify the antenna rotation rate, making the system capable of operating like a traditional, non-rapid-scan radar.

Additionally, the range resolution, range gate spacing, pulse repetition frequency, and other parameters can be user defined by specifying the pulse length, the number of pulse pairs and the antenna rotation rate.

Although the MWR-05XP can scan slightly faster than RaXPoI, especially since the antenna can rapidly scan sectors (RaXPoI cannot operate in rapid scan mode unless making 360° PPIs), the spatial resolution of RaXPoI is superior to that of the MWR-05XP. The capability of RaXPoI to provide finer spatial resolution allows for the conclusions from French et al. (2013 a, b) to be compared to a case where the tornado circulation, and at times the tornado itself can be definitively resolved.

## **Chapter 5. Dataset and Case Study Overview**

### **Synoptic Overview**

It is obvious from the synoptic environment on 24 May 2011 that the potential for a severe weather outbreak this day was high. In the morning (1400 UTC), a surface low pressure area was developing in the central Oklahoma panhandle (Figure 20). A warm front extended northeastward from the surface low through southeastern Nebraska. Temperatures in the warm sector were in the low to mid 70's (F) and dewpoints were predominately in the upper 60's to lower 70's. A dryline was oriented from the north to the south through the eastern Texas panhandle and a cold front extended west south-westward behind the low. From the 1200 upper-air analyses (Figure 21), a negatively tilted 500 mb trough is seen extending southeastward from the Washington coast through the Four-Corner region, into central Mexico, while a ridge is

located across much of the central and high Plains. A closed low at 850 mb is located in the western Oklahoma panhandle. The combination of the developing surface cyclone and its incipient surface boundaries, and the upper-level trough approaching from the west provided the necessary thermodynamics, kinematics and forcing mechanisms for the development of supercells.

From the 1800 UTC Norman profiler, it is seen that there was a deep (~1500 m), nearly saturated layer below a strong capping inversion (Figure 22a). The convective temperature was about 36° C. Above the inversion, lapse rates were nearly dry adiabatic through the 650 mb level, resulting in convective available potential energy (CAPE) for a surface parcel of almost 2900 J/kg. Winds veered and strengthened with height from southeasterly at 5 m s<sup>-1</sup> at the surface to 15 m s<sup>-1</sup> from the south-southwest 850 mb, to 37.5 m s<sup>-1</sup> from just south of westerly at 300 mb. It is seen from the hodograph (Figure 22b) that the 0-6 km wind shear is > 20 m s<sup>-1</sup>, which is sufficient for supercell development (Weisman and Klemp 1984).

Storms began to initiate on the dryline just prior to 1900 UTC (Figure 23a). By 2000, the storms had intensified into a series of several supercells and had moved off the dryline, heading east toward north central and central Oklahoma (Figure 23b). The southern-most storm became the target storm for field operations, and the case study storm for this dissertation. Over the next hour, storms developed all along the dryline, in a north-south orientation across the entire state of Oklahoma (Figure 23c). The target supercell became very large and was producing a violent tornado just west of El Reno, OK. By 2200, a string of supercells spanned the entire latitude of Central Oklahoma, most of which were tornadic (Figure 23d). The storms began to grow upscale and

develop into a line as outflow boundaries interacted with each other and new convection initiated between the supercells (Figure 23e). The convection moved eastward and sporadically continued to produce weak tornadoes, but the most violent tornadoes occurred earlier, across central Oklahoma (Figure 23f).

### **Dataset Details**

RaXPol began collecting data at 2021 UTC on 24 May, 2011 (hereafter all times are UTC), at which time the target storm's area of interest was located approximately 20 km WSW of Binger, OK over 30 km SW of the deployment site. RaXPol was deployed just south of exit 108 on Oklahoma I-40 (Figure 24). During the first 15 minutes of data collection, the radar was not operating in rapid-scan mode. A combination of factors including the range of the target, attenuation effects, noise at the periphery of the data, and poor azimuthal resolution made it difficult initially to discern the hook echo and mesocyclone (Figure 25).

Around 203100, a tornado was forming WSW of Lookeba, OK (NWS online). Data acquisition switched to rapid-scan mode at 203634. For this scanning configuration, volumes of 9 elevation angles increasing by  $2^\circ$  increments from  $2^\circ$  to  $18^\circ$ , were collected every  $\sim 17$  s. There were 11 independent samples, the range resolution was 150 m, oversampled with range gate spacing of 75 m and the Nyquist velocity was  $30.8 \text{ m s}^{-1}$ . At 205233, the pulse length was shortened to decrease the range resolution to 75 m and the range gate spacing to 30 m and increase the number of samples to 12. The volume acquisition time was reduced to 14 s and the Nyquist velocity increased to  $38.5 \text{ m s}^{-1}$ . By this time, the first tornado had dissipated and a second tornado was on the ground  $\sim 6.5$  km SSW of the radar. The scanning strategy

was yet again changed as the tornado was intensifying. At 205456, volume collection ceased and rapid-scan 360° PPIs were collected at a single elevation angle of 1° with an update time less than 2 s until 210141. During this period, the tornado rapidly strengthened and grew in width, attaining its maximum observed ground-relative Doppler velocity of 124.8 m s<sup>-1</sup> at 210034. Unfortunately, beam-blockage east of the radar impacted the data quality in the vicinity of the tornado as it moved northeastward through the blockage from ~ 210040 through the end of the rapid-scan time. (The magnitude of the maximum velocity at 210034 was not affected by the beam blockage because it was outside of the affected sector.) As the tornado was moving away from RaXPol and appeared to be in its mature phase, the scanning strategy was changed back to volumetric rapid-scan mode, and was maintained through the end of the dataset at ~211630. Unfortunately, data quality was compromised toward the end of the deployment due to differential attenuation through the back of the hook echo.

Table 2 summarizes the scanning strategies for RaXPol during the deployment. Although data acquisition began at 2021, the data were not of sufficient spatial or temporal quality for analysis until the transition to rapid-scan mode at ~2036. Thus, only data collected during rapid-scan mode will be used for this study. Between 2036 and 2116, the intensification and decay of the first tornado, the genesis of the second tornado and the intensification of the second tornado to EF-5 strength were captured by RaXPol (

Table 3). The dataset is thus decomposed into three phases according to the tornado-scale processes that were occurring. The first phase starts at the beginning of rapid-scan data collection when tornado 1 is on the ground, and continues until after

tornado 1 dissipated (203634 – 204800). The second phase starts at 204600, and includes the tornadogenesis and initial intensification of tornado 2. Phase II ends at 205700, when the tornado intensification plateaued. The time encompassed by phase 2 overlaps with the first phase because important features associated with the second tornado are independent from those associated with the first tornado, and warrant discussion prior to the end of the first phase. Phase III spans from 2057 through the end of data collection at 2116 and represents the quasi-steady state mature tornado 2.

The biggest limitation of this dataset is that the elevation angle transition from  $18^\circ$  to  $2^\circ$  occurred within the  $360^\circ$  PPI of the  $2^\circ$  elevation angle, effectively causing the data recorded as the  $2^\circ$  scan to be a downward spiral from  $18^\circ$  due to the rapid rotation rate of the antenna. Stated another way, at the azimuthal location where the  $2^\circ$  PPI began, the elevation angle was still approximately near  $18^\circ$  and the beam was high. As the elevation angle decreased, the antenna rotated azimuthally, spanning the vertical distance from  $18^\circ$  to  $2^\circ$  while rotating. The antenna then overshot its original target of  $2^\circ$ , and had to return upward to a small degree. This problem caused the actual  $2^\circ$  elevation scan to be reduced to a narrow sector of  $\sim 30^\circ$ . Thus, low-level ( $< 700$  m AGL) data are unavailable until after 2049, making it impossible to resolve the wind field near the surface. Although data at the lowest elevation angle were not retrieved at low heights, the  $2^\circ$  scan was still usable for analysis because the height information was stored, and therefore the scan was supplemental to data aloft. The transition of the elevation angle between subsequent elevations also had the same problem, but it was not nearly as pronounced going up by an increment of  $2^\circ$  as it was going down by  $16^\circ$ .

The MWR-05XP also collected data on this storm from 204930 – 205604 from a location 11.8 km to the ENE of RaXPol (Figure 24), during which period the RaXPol was also operating as previously mentioned. The MWR-05XP collected data through an elevation angle of 40° with 1.5° increments, so storm structure at mid to upper levels can be examined using data from this instrument. This is particularly valuable because during the operation time of the MWR, the tornado was within 6 km range of RaXPol, limiting the vertical extent of the RaXPol data acquisition. Additionally, it allowed for a series of dual-Doppler analyses to be generated.

### **Case Study Summary**

#### *i. Phase I (2036-2047)*

RaXPol data collection began at 2021 UTC (hereafter all times are UTC), 24 May 2011, at which time an approaching supercell's area of interest (mesocyclone region) was located approximately 35 km to the SW. From 2021 to 2036, data were NOT collected in rapid scan mode because the storm did not appear imminently tornadic and the area of interest was quite far away. Unfortunately, the storm did spawn a tornado (tornado 1) about 28 km SW of RaXPol (not visible to the radar crew) around 203100 UTC (NWS damage report). At about 203630, the data acquisition mode was switched to rapid-scan with 150 m range resolution and 360° PPIs collected at 9 elevation angles (2° - 18° at 2° increments), resulting in volumetric updates every 17 s.

When data acquisition in rapid-scan mode began at 203634 UTC, the tornado was nearly due west from Lookeba, OK at a range of approximately 23 km from the RaXPol deployment site (Figure 24). At this distance, the azimuthal resolution was ~ 400 m and the minimum beam height was 1.7 km, which were too large and high,



respectively, to resolve the tornado. However, the low-level mesocyclone was well resolved, having a diameter of  $\sim 1.5$  km at the minimum beam height. Because the minimum beam height was so high, near-surface processes could not be resolved, but there was a well-defined hook echo and low-level TVS associated with the tornado. The intensity of the tornado circulation, (crudely measured by  $V_{\max} - V_{\min}$ , or  $\Delta V$ ) reached its maximum intensity at 204258 with an azimuthal shear value across the TVS of  $109 \text{ m s}^{-1}$  at a height of 1.3 km (the lowest elevation angle for which data were available).

Tornado decay began around 204400, when the low-level circulation began to weaken considerably between consecutive volume scans. The tornado dissipated by 204700, according to the NWS damage survey and the radar data ( $\Delta V$  across the circulation decreased below  $35 \text{ m s}^{-1}$ ). During decay, the range to the tornado was between  $\sim 16$  km – 13 km, corresponding to a beam width of 280 – 225 m and a minimum height of  $\sim 1$  km. The tornado was not greater than 1 km in width at this time, and thus could not be resolved ideally during decay, nor could the near-surface winds be detected. However, the low-level circulation was resolvable. The remnant low-level circulation persisted for several additional scans, and ultimately played a role in the genesis of the second tornado.

*ii. Phase II (2046-2057)*

A new region of broad mid-level circulation began to develop northwest of the original one around 2045. According to the NWS damage survey, tornadogenesis (tornado 2) began around 2050, when the area of interest was  $\sim 9$  km away from RaXPOL. The beam width at this distance was  $\sim 160$  m and its lowest height was  $\sim 630$

m AGL. The wall cloud was visible from the RaXPol deployment location at this time (Figure 26) and a persistent condensation funnel developed at 205240 ( $\pm 5$  sec). Multiple vortices were observed from the deployment location but were not resolved in the radar data either because the features were too small, or they were located beneath the beam, which at this time was centered on a height of  $\sim 500$  m, or for both reasons. A broad area of low-level rotation was visible from 2050 onward in the radar data, but smaller-scale suction vortex features were not evident. The tornado quickly developed into a large wedge by 2055 (Figure 26f). At this time, the scanning strategy changed to collecting single  $360^\circ$  PPIs at  $1^\circ$  elevation angle. With the distance to the tornado now only  $\sim 4.5$  km, the beam width was  $< 80$  m and the height was  $< 80$  m ARL. The width of the tornado was approximately 500 m and thus the tornado was now well resolved. As the tornado grew, the TVS was increasingly well resolved, often with more than five radials separating the maximum inbound velocities from the maximum outbounds. The most rapid intensification of the tornado occurred between  $\sim 2054$  and 2057, when the maximum difference in radial velocities increased from  $\sim 90 \text{ m s}^{-1}$  to  $\sim 170 \text{ m s}^{-1}$ .

*iii. Phase III (2057-2116)*

After the initial period of rapid intensification, the tornado remained in an essentially steady-state condition, although there were brief periods of intensification and weakening within this phase. The tornado approached the RaXPol deployment site from the SW, passing about 3.2 km to the southeast of the RaXPol deployment site at 205830, which was the closest distance to the tornado. At this time, single elevation scans at  $1^\circ$  were still being collected. The beam was 55 m wide and  $\sim 50$  m AGL, fully resolving the tornado and the near-surface winds. The tornado was most intense

between ~2057 and 2102; the maximum radial velocity observed during the deployment ( $V_r \sim 125 \text{ m s}^{-1}$ ) was at 210034 (Figure 27). After 2102, the maximum velocities decreased somewhat steadily until data collection ceased at ~2116 because the storm was getting too far away from the radar for adequate spatial resolution.

## **Chapter 6. Analysis Techniques**

Prior to any analysis, the dataset was edited using NCAR's SOLOii (Oye et al. 1995) to remove noisy data and ground clutter, and dealias the Doppler velocities. Because the wind speeds were quite strong in this tornado and in the storm environment, and the Nyquist velocity was relatively low ( $30.8$  or  $38.5 \text{ m s}^{-1}$  depending on the scanning strategy), unfolding the velocities was time consuming and often unclear, particularly in the tornado region. The author tried to maintain consistency in velocity patterns and magnitudes between consecutive volume scans and adjacent elevation angles. Regardless, unfolding velocities is still a subjective process and there are likely some errors in the unfolded data.

### **Dual-Doppler Analysis**

As mentioned in Chapter 5a, there were six and a half minutes during which both the MWR-05XP and RaXPoI were simultaneously collecting data. Unfortunately, the MWR-05XP data are of limited use in generating dual-Doppler analyses for several reasons: 1) the MWR-05XP was not leveled during deployment; 2) the relatively coarse spatial resolution of the MWR-05XP creates a mismatch in sampling volumes between the two instruments; 3) the geometry of the deployment configuration was not ideal for

dual-Doppler analyses: the between beam angle to the tornado circulation was  $<20^\circ$  until  $\sim 2052$  and  $< 30^\circ$  until  $\sim 2054$ ; 4) RaXPoI switched to rapid-scan single elevation mode at 2055, making volumetric analyses unavailable after this time.

Despite these limitations, a series of dual-Doppler analyses was synthesized when the between beam angle was  $> 30^\circ$  at the tornado. This was done to determine the overall quality of the dual-Doppler analysis, to provide comparison for single-Doppler wind retrieval techniques (see Chapter 6), to retrieve horizontal wind estimates near the surface, and to resolve storm-scale features to aid in the interpretation of results (see Chapter 7). While it is acknowledged that there are surely errors in the dual-Doppler analyses, the analyses are still useful for qualitative purposes; no quantitative methods are used.

A three-dimensional analysis was performed at 205448 but this was the last time when volume scans were available from both MWR-05XP and RaXPoI. After this time, RaXPoI was collecting rapid-scan low-level data at a single elevation. Four other analyses were performed (205532, 205543, 205554, and 205604) all for a single vertical level. After 205604, the MWR-05XP ceased collecting data. The analysis times were chosen based on when MWR-05XP volumes were available. Because the MWR-05XP transmits multiple beams simultaneously in the vertical, while scanning horizontally, data from all elevation angles used were acquired nearly at the same time. To minimize the duration over which advection was a consideration for the 205448 analysis, RaXPoI sweeps were chosen such that PPIs were centered temporally on 205448. Data from each elevation angle collected by RaXPoI (from  $2^\circ$  through  $18^\circ$  with  $2^\circ$  increments – 9 total elevations) were used for the synthesis. However, only data from the seven lowest

elevation angles of the MWR-05XP (ranging from 1-10° with 1.5° increments) were used. The MWR elevation angles higher than 10° were above the height of available RaXPol observations. At this time, the between beam angle at the tornado was ~ 41°, which is sufficient to allow u, v, and w to be retrieved (Figure 28).

The single elevation analysis times were also chosen based on the times when MWR05-XP data were available. Because RaXPol scans were completed every ~2 s, there was at most 1 second difference between the MWR-05XP and the RaXPol timestamps and advection was minimal. Obviously, the three dimensional wind field cannot be retrieved after RaXPol stopped scanning volumetrically, but the low-level horizontal winds can. For these later analyses, only data from the MWR-05XP's lowest elevation angle were used to compute the horizontal winds.

*i. Errors due to an unleveled radar*

One potentially significant drawback of the MWR instrument is the absence of a truck leveling system. Additionally, the pitch and roll of the instrument are not internally recorded. Thus, the data are recorded as if the truck were level when in actuality it may not be. Therefore, there is no way of knowing if the radar beam is truly located where the internal software documents it being sent. These drawbacks are responsible for the first limitation. An attempt to mitigate the effects of this limitation was made by revisiting the deployment location using the truck GPS system (accurate to ~ .00001° latitude and longitude)) to verify the correct location to manually calculate the pitch and roll of the truck. These measurements were acquired by using a three foot level across the nose-to-rear and the left-to-right axes of the truck, and documenting the height difference between the bed of the truck and the level. Using this method, it was

determined that the MWR was off-level by +1.88° pitch (front of the truck was higher than the rear), and by +2.44° roll (the left side was higher than the right).

The original data could not be corrected for the pitch and roll and neglecting this information in the processed data generates two types of errors: 1) the observed radial velocity is slightly biased by the vertical wind component and the misrepresentation of the beam elevation angle, (which is a greater problem at higher elevation angles), and 2) the actual location of the beam is unknown. In order to determine the effect that the first type of error had on the velocity components of the dual-Doppler analyses, a simple mathematical equation solving for radial velocity from the three dimensional wind components was used to determine the error in VR:

$$V_R = w * \sin(\phi) + \sqrt{u^2 + v^2} * \cos(\phi) \cos(\theta - \tan^{-1}(u/v))$$

where  $\phi$  is the elevation angle,  $\theta$  is the azimuthal angle and u, v, and w represent the actual east-west, north-south, and vertical wind components. If the true wind is assumed to be:

$$\mathbf{V} = 0 \mathbf{i}, 15 \mathbf{j}, 0 \mathbf{k}$$

the true radial velocity acquired at a true elevation angle of 1°, and an azimuth of 360° (resolving the full out-bound component) would be  $V_R = 14.9977 \text{ m s}^{-1}$ . If a worst-case scenario of pitch and roll of +3° is assumed, the elevation angle off the front of the truck (azimuth = 360°) would be 4°, resulting in a radar-measured radial velocity of  $V_R = 14.934 \text{ m s}^{-1}$ , or an error of 0.2%. The highest MWR-05XP elevation angle used for the dual-Doppler analyses was 10°. A similar approach with  $\phi = 10^\circ$  as recorded, but really sampling  $\phi = 13^\circ$  yields an error in  $V_R$  of 1.1%. The errors are the same if the wind were out of the west and the azimuth were 270°.

For a situation where the tornado is being sampled, consider the extreme example of a measurement made on the east side of a tornado located due north of the radar with a wind field such that:

$$\mathbf{V} = 0 \mathbf{i}, 100 \mathbf{j}, 50 \mathbf{k}$$

For a true elevation angle of  $1^\circ$ , the radar-observed radial velocity would be  $100.86 \text{ m s}^{-1}$ . If the beam were actually at  $4^\circ$ , the radar-observed radial velocity would be  $103.2 \text{ m s}^{-1}$ , resulting in an error of 2.3%. Similarly, for a true elevation angle of  $10^\circ$ ,  $V_R$  would be  $107.16 \text{ m s}^{-1}$ , and the  $V_R$  for the tilted radar beam of  $\theta=13^\circ$  would be  $108.7 \text{ m s}^{-1}$ , resulting in an error of 1.4%. In all situations, this error is relatively negligible.

Another issue in the accuracy of dual-Doppler analyses synthesized without the proper pitch and roll information is misrepresentation of the vertical location of the beam. For a perfectly level instrument that is scanning a target 15 km away (such is the worst-case for the tornado location in the analyses presented herein), at an elevation angle of  $1^\circ$ , the height of the beam would be  $\sim 260 \text{ m}$ . However, if the instrument is recording an elevation angle of  $1^\circ$  but due to the pitch/roll of the deployment location it is actually at an elevation angle of  $4^\circ$ , the true height of the beam would be  $\sim 1 \text{ km}$ , resulting in a misrepresentation of the beam location of  $\sim 740 \text{ m}$ . This is the equivalence of an error of  $\sim 7$  grid points in the vertical. This negative effect is slightly mitigated because the critical radius for the objective analysis for the MWR is 1 km and therefore the true location of the beam lies within the critical radius and is thus accounted for in the analysis. Regardless, it is apparent that misrepresentation of the beam height is potentially a source of significant error, considerably more so than the erroneous

contribution to  $V_r$  from the vertical wind component and the inaccurate representation of the elevation angle.

For this reason, sensitivity tests were performed to determine how significant these effects were. Single elevation angle analyses were performed for one RaXPol elevation angle, and a series of MWR-05XP angles that spanned  $\pm 3^\circ$  in elevation centered on the angle which best matched the height of the RaXPol scan at the tornado, to simulate the effects that a roll and pitch angle of  $3^\circ$  would have on the analyses.

Analyses were performed for a height of 1 km ARL at the tornado. This corresponds with a RaXPol elevation angle of  $12^\circ$  and an MWR-05XP elevation angle of  $4^\circ$  (the reference angle). Four additional analyses were performed, all with the same RaXPol data: one for the  $1^\circ$ ,  $2.5^\circ$ ,  $5.5^\circ$  and  $7^\circ$  MWR elevation angles. The wind fields computed for each analysis were compared with the  $4^\circ$  reference analysis (Figure 29). Root mean square differences were calculated between the horizontal velocity components and wind directions for the various analyses compared to the  $4^\circ$  analysis (Table 4). Quantitatively, there were sometimes significant differences between the analyses. It was determined that the root mean square errors (RMSE) in the magnitude and direction of the u and v components were greatest for differences between  $4^\circ$  and both  $1^\circ$  and  $7^\circ$ . This is expected since the winds should decorrelate with height due to vertical wind shear among other factors. Values of RMSE were between 8 and  $\sim 16 \text{ ms}^{-1}$  for the magnitude and  $20\text{-}30^\circ$  in direction. Additionally, because the pitch was such that the left side of the MWR-05XP was higher than the right side and the tornado was to the left side of the truck, the error in vertical location is exacerbated for lower elevation angles since the difference between actual beam height and the recorded beam



height are greater for elevation angles below  $4^\circ$ . The most accurate analysis should actually be the one using data from the MWR-05XP at the  $5.5^\circ$  elevation angle.

Despite the quantifiable errors between analyses at different MWR-05XP tilts, qualitatively the analyses look similar (Figure 30). The reader is reminded that the analyses were generated to gather qualitative, not quantitative information about the storm structure and features. Because there are no major differences in storm structure between analyses, it was determined that the dual-Doppler syntheses, although imperfect, were capable of identifying storm-scale features (See Chapter 7).

*ii. Errors due to mismatched volume samples*

The tornado moved from 20-13 km away from the MWR location during the data collection period, corresponding to an azimuthal resolution that ranged from  $\sim 625$  -  $\sim 400$  m while RaXPol had an azimuthal resolution ranging from  $\sim 80$  -  $160$  m. Thus, the RaXPol data had significantly better horizontal spatial resolution than the MWR-05XP. Additionally, because the radar scanning strategies were different and MWR-05XP was  $\sim 10$  km farther from the storm than RaXPol, the data retrieved by each instrument are not perfectly collocated within the analysis volume. It is recognized that the differences in resolution and beam location are a potential source for error, particularly with the vertical height of the data.

The effects of these are reduced since the MWR-05XP's vertical beam width of  $2^\circ$  matches the elevation increment of the RaXPol, and the MWR-05XP oversampled in elevation with increments of every  $1.5^\circ$ . Thus, there is a contribution to the MWR-05XP variables from the same height that the RaXPol is scanning for all RaXPol elevation angles. Additionally, the data were objectively analyzed, which allows data

from adjacent elevation angles within a specified distance to influence the calculated value of each radar variable at a given height.

*iii. Objective analysis*

The raw radar data were objectively analyzed using NCAR's Reorder software, transposing the data from polar radar coordinates to a 10x10x7 km grid with 100 m horizontal and 250 m vertical resolution, centered on the center of circulation at the lowest elevation angle. The height of the radars' beams ranged from ~80 to ~150 m above radar level at the location of the tornado. The grid was specified to begin at a height of 0 m and data were interpolated to the lowest grid point. This was done in order to impose a lower boundary condition for the dual-Doppler analysis. It should be noted that the grid spacing is finer than the MWR beam width, and is therefore under-sampled. However, because the RaXPol data were of considerably finer spatial resolution, it was desired that the grid be made to utilize the better RaXPol resolution. An advection correction was not applied to the MWR-05XP analysis because data were collected simultaneously, but it was applied to the RaXPol analysis. Storm motion was calculated to be  $\sim 17.5 \text{ m s}^{-1}$  from  $241^\circ$  on the basis of the translation of the tornado signature during a 2-minute period spanning before and including the dual-Doppler time. By including storm motion effects, the data were advected linearly either forward or backward with respect to the storm motion vector, to the central grid time. This process removes any spurious tilt or shape to features caused by storm translation.

A modified Barnes analysis scheme was used for the objective analysis with a weighting function of:

$$W = \exp^{(ar^2/R^2)} \quad \text{Equation 14}$$

Here,  $r$  is the distance between the grid point and the data point (radar gate),  $R^2$  is the sum of the squared  $x$  (0.1),  $y$  (0.1), and  $z$  (0.25) grid spacing in km, which resulted in  $R^2 = 0.0825$ , and  $\alpha$  is a smoothing parameter which is a function of the coarsest data resolution in the analysis. Trapp and Doswell (2000) recommend that  $\alpha$  be chosen based on the most conservative data spacing ( $\Delta$ ), where the data are farthest apart, based on the following formula:

$$\Delta = \theta * D \quad \text{Equation 15}$$

where  $\theta$  is the beam width (rad) of the radar, and  $D$  is the distance (km) between the radar and the farthest data point on the grid. Trapp and Doswell (2000) recommend a radius of influence ( $r_i$ ) according to:

$$\sqrt{5 * \Delta^2} \leq r_i \leq \sqrt{5 * 2\Delta^2} \quad \text{Equation 16}$$

For the specified beam widths and distances between the radars and the tornado,  $r_i$  was chosen to be 1 km for the MWR-05XP and 500 m for RaXPoL. The values for  $\alpha$  were calculated according to:

$$\alpha = -\frac{R^2}{\kappa} \quad \text{Equation 17}$$

where  $\kappa = r_i^2/5$ . The value of  $\kappa$  for the MWR-05XP analysis was 0.2 making  $\alpha = -0.41$ . For the RaXPoL analysis,  $\kappa$  was 0.05 and  $\alpha$  was -1.65. A summary of the dual-Doppler parameters for each radar's objective analysis is given in Table 5.

*iv. Dual-Doppler synthesis*

After the objective analysis was completed, the dual-Doppler analysis was synthesized using NCAR's CEDRIC software. The horizontal wind components (Armijo 1969) were estimated by iteratively solving for the projection of motion along

the radial wind, and the vertical velocity was calculated by iteratively solving the continuity equation until the solutions converged between iterations (Miller and Fredrick 2009). Fall speeds of the hydrometeors were not subtracted out because reflectivities were not calibrated, which is another source of error in the wind calculations. However, the projection of the vertical component of the fall velocities onto the Doppler velocities is negligible at low elevation angles. The integration was done from the bottom up because the upper limit of data collection was well below the storm top, and therefore it could not be assumed that the vertical motion at the top of the analysis grid was zero.

In order to minimize errors in the calculation of U and V, velocity data lying within  $\pm 20^\circ$  from the baseline between RaXPol and MWR-05XP were removed. It is recommended that data should be removed within  $\pm 30^\circ$  (Davies Jones 1979); however, the storm was so close to the baseline that the  $30^\circ$  threshold would have made the earlier analyses nearly unusable. It is therefore accepted that there are inherent errors in the analysis, but qualitative information can still be gained from them. Horizontal divergence and the three components of vorticity were also calculated using a center differencing technique, then smoothed by a two-dimensional Leise filter (Leise 1982). Finally, the objectively analyzed reflectivity and radial velocity fields were assimilated into the dual-Doppler analyses to provide the objectively analyzed reflectivity and radial velocity data for both RaXPol and MWR-05XP.

## **Single-Doppler Analyses: TREC**

The availability of data with rapid temporal sampling makes it desirable to resolve the three-dimensional wind field and examine the rapid evolution of kinematic properties such as inflow, horizontal convergence, and vorticity when volumetric data are available. Additionally, trajectories are desired to determine source regions of parcels entering the tornadic circulation. Because of the limited availability and usefulness of dual-Doppler data during this event, a technique was sought to calculate the wind field from single-Doppler data in order to provide a more inclusive method of examining tornado structure and evolution. Several methods have been used in the past to retrieve three-dimensional winds from single-Doppler data.

The first method is the Tracking Radar Echoes by Correlation (TREC) technique, and was developed by Rinehart and Garvey (1978) for application to hail-producing supercells in Colorado, modified for clear-air studies by Tuttle and Foote (1990), and modified again for application to tropical cyclones by Tuttle and Gall (1999) and Harasti et al. (2004). Most recently, it was used to study the evolution of a storm-scale reflectivity feature in supercells by Kramar et al. (2005). Inherent to the technique is the assumption that the reflectivity field is only changing as a result of horizontal translation and vertical velocity is negligible; precipitation fall speeds, sources and sinks such as condensation and evaporation, and storm-scale evolution are neglected.

A second method of single-Doppler wind retrieval derives the three-dimensional wind by solving a system of equations based on 1) conservation of reflectivity, 2) conservation of mass for an incompressible atmosphere, and 3) a temporal constraint on

the radial velocity (Zhang and Gal-Chen 1996; Shapiro et al. 1995). In this method, it is assumed that the material derivative of reflectivity ( $dZ/dt$ ) is equal to the sum of source and sink terms, such as evaporation, condensation, etc. In order to solve the system of equations between 1) and 2), a second scalar must be defined. This second scalar is derived from the radial velocity field, assuming either velocity stationarity ( $\partial\mathbf{V}/\partial t = 0$ ), or frozen turbulence ( $\partial\mathbf{V}/\partial t + u \partial\mathbf{V}/\partial x + v \partial\mathbf{V}/\partial y = 0$ ), where  $u$  and  $v$  describe the motion of patterns in the radial velocity and  $\mathbf{V}$  describes the air motion. The solution that minimizes the least-squares error of the system is found by variationally minimizing a cost function and implementing Neumann boundary conditions. This method was expanded upon and refined by Weygandt et al. (2002).

The third method, often applied to rotating phenomena, is the ground-based velocity tracking display (GBVTD) technique. This method was developed by Lee et al. (1999) and was initially applied to the wind fields of land-falling tropical cyclones (Lee and Marks 2000), then to tornadoes (Bluestein et al. 2003; Lee and Wurman 2005; Tanamachi et al. 2007; Kosiba and Wurman 2010; Wakimoto et al. 2012). The technique assumes the flow field is mostly axisymmetric and that any asymmetries present are in the radial direction and are small compared to the azimuthal wind. This assumption breaks down, however, very close to the ground and in situations where the swirl ratio is high. The technique works best when the size of the tornado is relatively small compared to the distance of the radar. A distance of 1-2 km for a tornado 100-200 m in width is sufficiently far (Bluestein et al. 2003). ;

Although it appears that the GBVTD technique should be the most appropriate choice for single-Doppler velocity retrievals for this case, this method was not

employed. A recent study by Nolan (2013) determined that there can be significant errors generated by the ground-based velocity track display (GBVTD) technique. Nolan determined that using radial velocities to estimate vertical motions greatly overestimates the vertical motions due to neglecting mass flux into the tornado's core, and centrifuging effects on the radial velocity estimates. Additionally, the tornado became quite large ( $> 1$  km) within close range (3 km) of the radar, and appeared to be asymmetrical at times, based on the observed multiple vortices. Therefore, it was determined that this technique might not be particularly applicable for this dataset.

Instead of using the GBVTD technique for this dataset, the TREC method was chosen to generate horizontal wind vectors from the single-Doppler data. This method correlates reflectivity features at two different scan times ( $time_1$  and  $time_2$ ) and determines a horizontal velocity based on the distance the features moved over the time between scans (Figure 31). It was hypothesized that the rapid update time of this dataset would improve the correlation coefficients between two consecutive reflectivity scans when compared with previous studies using conventional radar data separated by several minutes between scans. This improvement was expected because the steady-state assumption of the reflectivity field is more justifiable when scans are separated by seconds compared to minutes (Figure 32).

To begin the analysis, volumetric radar data were objectively analyzed onto a three-dimensional Cartesian grid before the TREC process started, using the Observation Processing And Wind Synthesis (OPAWS) software (<http://code.google.com/p/opaws/>). This is a modification from previous TREC versions which analyzed data onto a single elevation angle for each analysis, rather than

simultaneously recreating the whole volume. The objectively analyzed volumes were structured so that each grid was centered on a common latitude/longitude location according to the area of the storm being studied. The two consecutive volumes for the analysis shared a common grid center. The interpolation used a 2-pass Barnes scheme with a smoothing parameter specified according to:

$$K = (1.33D)^2 \quad \text{Equation 18}$$

where D is the coarsest separation between two adjacent data points:

$$D = \sin(\theta_b \text{ (deg)}) * \text{farthest range in analysis (km)} \quad \text{Equation 19}$$

And  $\theta_b$  is the half-power beam width of the instrument. Grids having three different resolutions (250x250x250 m, 100x100x100 m, and 50x50x50 m) were generated to identify the most ideal grid domain that maximized correlation coefficients and minimized noise. The input PPIs were interpolated to a central time, accounting for translation of the storm between the first and last elevation scans in the volume, similar to the dual-Doppler analysis advection correction.

Once the data were objectively analyzed at two different times, centered on the same location, the TREC analysis could begin. In order to compute the two-dimensional velocities, a series of correlation boxes, or arrays, first are created for the earlier volume time. The user specifies the box dimensions including the number of x and y grid points contained by the box, and the distance between neighboring boxes. These dimensions are edited according to the type of features one desires to resolve. If the boxes are too large, resolution is sacrificed and TREC merely resolves the mean storm motion, but if the boxes are too small, the analyses can become noisy.



Next, all possible correlation boxes within a certain range ( $R_{\max}$ , which is governed by the maximum expected radial velocity in the analysis) are identified in the grid at the second time. Any data points that lie outside of  $R_{\max}$  are ignored. From here, correlation coefficients are calculated between the correlation box at  $\text{time}_1$  and all possible correlation boxes at  $\text{time}_2$ . The box at  $\text{time}_2$  that returns the highest correlation coefficient is considered to be the new location of the original box at  $\text{time}_1$ . The equation for correlation coefficient is:

$$r = \frac{\sum_{i=1}^n (x_i - \bar{x})(y_i - \bar{y})}{\sqrt{\sum_{i=1}^n (x_i - \bar{x})^2 * \sum_{i=1}^n (y_i - \bar{y})^2}} \quad \text{Equation 20}$$

which can also be written as:

$$r = \frac{\sum(x_i y_i) - \sum x_i \sum y_i / n}{\sqrt{\sum(x_i^2) - (\sum x_i)^2 / n} \sqrt{\sum(y_i^2) - (\sum y_i)^2 / n}}. \quad \text{Equation 21}$$

Here,  $x_i$  represents individual gridded reflectivity values within the initial correlation box at  $\text{time}_1$  and  $y_i$  represents individual reflectivity values within one of the possible correlation boxes within  $R_{\max}$  at  $\text{time}_2$ . Once the correlations between the specified box at  $\text{time}_1$  and all possible boxes at  $\text{time}_2$  are computed, the box with the maximum correlation at  $\text{time}_2$  is identified and its location stored. The difference in grid locations between the box at  $\text{time}_2$  and  $\text{time}_1$  is calculated, and the U and V component of motion of that box is determined according to the distance and time between analyses. These correlation and velocity calculations are repeated for all heights within the analysis domain.

One limitation of the TREC method is that only discrete velocity values are capable of being calculated according to the grid resolution. To illustrate this weakness, consider a situation in which the correlation of an initial reflectivity box is maximized at

an adjacent grid point. The velocity is defined as  $dx/dt$ , so if the grid spacing is 100 m and the time between analyses is 17 s, the u and v velocity components are restricted to multiples of  $100/17$ , or  $5.9 \text{ m s}^{-1}$ . Thus, the velocity field does not represent a continuous range of velocities, but rather a series of discrete velocity possibilities. In order to improve this, finer grid resolution must be utilized, or the time intervals between scans must be *increased*.

In an effort to maximize the quality of the TREC analyses, the number of pixels, or individual data points to include in the correlation boxes ( $n_{\text{box}}$ ) and the grid resolution were systematically adjusted. Results were analyzed qualitatively by determining the number and extent of vectors that deviated from what appeared to be the base-state local flow, and how much detail was retained in the analysis. The statistical standard deviation was not used because there was considerable variation over the grid domain in the presumed base-state flow. The number of pixels per correlation box was incrementally varied from 8x8 to 16x16 pixels (Figure 33). It was objectively determined that correlation boxes with about 14x14 pixels, or 196 data elements qualitatively seemed optimally to reduce the amount of noise in the TREC vectors, while retaining smaller-scale details. This result is consistent with what was found by Tuttle and Foote (1990) who determined that the highest quality analyses occurred for boxes with 12 -16 data points in each dimension.

In order to assess the ability of the TREC algorithm to calculate horizontal wind vectors based solely on two reflectivity fields some time  $dt$  apart, three synthesized reflectivity fields were generated to represent a geometrically symmetric precipitation

configuration (Figure 34). These fields were generated from two sin curves, one specifying a wave pattern in the x direction and one in the y direction such that:

$$x\sin_i = |(30\sin(2\pi fx_i + \phi_x))| \quad \text{Equation 22}$$

$$y\sin_j = |(30\sin(2\pi fy_j + \phi_y))| \quad \text{Equation 23}$$

$$\text{Ref}_{ij} = x\sin_i + y\sin_j \quad \text{Equation 24}$$

Here,  $x\sin_i$  ( $y\sin_j$ ) represents the value of the sin curve along the x (y) axis, at grid point i (j) (Figure 35a). The simulated reflectivity value ( $\text{Ref}_{ij}$ ) at the  $i^{\text{th}}$  x grid point and the  $j^{\text{th}}$  y grid point is the sum of the x and y values of the specified sin curve. The number of patterns is governed by the choice of f. The amplitude of 30 ensures pseudo reflectivity values in the range expected for convective precipitation (from 0 – ~60 dBZ). Taking the absolute value of the function removes any negative values and ensures two maxima for every  $2\pi$  along the curve.

The grid was constructed such that  $\Delta x = \Delta y = 100\text{m}$ . Three patterns were synthesized by changing the value of f (frequency of the wave across the grid domain): for  $f=0.1$  (1 wave in the x and y directions, 4 maxima, Figure 34a),  $f=0.2$  (2 waves, 16 maxima, Figure 34b), and  $f=0.3$  (3 waves, 36 maxima, Figure 34c). The pattern was then phase shifted equally by  $\phi_x = \phi_y$  in the x and y directions by either  $\pi/8$  or  $\pi/10$  to simulate the motion of the field due to pure translation (Figure 35b) in a southwesterly flow. A time difference of either 17 or 30 seconds between the two reflectivity fields was specified and a corresponding horizontal velocity field was generated. Thus, there were four combinations of dt and  $\phi$ , resulting in possible translation velocities for the simulations: 1)  $u = v = 37 \text{ m s}^{-1}$  for  $dt = 17$ ,  $\phi = \pi/8$ ; 2)  $u = v = 29.7 \text{ m s}^{-1}$  for  $dt = 17$ ,  $\phi =$

$\pi/10$ ; 3)  $u = v = 21 \text{ m s}^{-1}$  for  $dt = 30$ ,  $\phi = \pi/8$ ; 4) or  $u = v = 16.8 \text{ m s}^{-1}$  for  $dt = 30$ ,  $\phi = \pi/10$ .

The correlations and TREC-retrieved velocities were dependent upon both the symmetry of the pattern and the phase shift of the pattern, but not on the time difference. Although there were some slight differences between the simulations, they were all similar and had correlation coefficients between 0.95 and 1 (Figure 36). The time difference did not influence the correlations because the shape of the pseudo-reflectivity pattern did not change for the arbitrarily defined  $\Delta t$ 's and the equation for correlation coefficient is not time dependent. The velocities were also generally the same, although the retrieved magnitudes were slightly different due to grid-spacing constraints (Figure 37). The exception to this statement is the 2 wave analysis shifted by  $\pi/10$ . This analysis had slightly varying directions of the TREC-calculated velocity vectors. It is unclear why this is the only analysis to exhibit this behavior.

All velocity calculations, including the 2 wave  $\pi/10$  phase shift had errors  $< 7 \text{ m s}^{-1}$  except around the boundaries where the reflectivity pattern translated out of the grid domain (Figure 38). Thus, it is concluded that the TREC algorithm performs accurately given the constraints to velocity calculations by the finite grid spacing.

As previously mentioned, inherent to the TREC calculations is the assumption that vertical advection of precipitation is negligible. This is obviously not always the case, particularly in convective storms where  $w$  can potentially exceed  $50 \text{ m s}^{-1}$  in the vicinity of the maximum updraft. Despite this shortcoming, we can say with reasonable confidence that the effects of vertical advection are not of great consequence to most of our analysis domain owing to the short time duration between scans (17 s). To justify

this statement, consider a case where vertical velocities are  $14 \text{ m s}^{-1}$ , and horizontal velocities are  $30 \text{ m s}^{-1}$ , similar to what one might find in a weak tornado. With a time difference between scans of 17 seconds, a parcel would move 238 m vertically and 510 m horizontally between scans. Since the coarsest grid resolution is 250 m, the vertical parcel displacement would be contained within the sample volume, while the horizontal parcel would have spanned 2 grid points. This assumption breaks down for finer grid resolutions. A comparison of reflectivity features between two consecutive scans further justifies that vertical advection did not cause dramatic evolution between two scans (Figure 32a, b). Differences between the 17 sec scans are barely perceivable when compared with PPI scans separated by  $\sim 2$  minutes (Figure 32a, c).

As previously mentioned, objectively analyzed grids with resolutions of  $250 \times 250 \times 250 \text{ m}$ ,  $100 \times 100 \times 100 \text{ m}$  and  $50 \times 50 \times 50 \text{ m}$  in the x, y, and z directions were synthesized for the TREC analyses. It was determined that grid spacing of 100 meters was ideal for the analyses at the specified time of 2054 (Figure 39). The 250 m grids were too coarse and smoothed out important features in the reflectivity and velocity fields. The small-scale variations apparent in the 50 m grids negatively impacted the TREC analyses, introducing noisy vectors and reducing the correlation coefficients. The 100 m analyses retained important small-scale features but reduced the noise in the TREC vector calculations. The optimal performance of the 100 m analyses is likely a result of the match between the RaXPol data resolution and the grid spacing. For most locations and most times, the RaXPol beam was never less than 50 m wide, and the range resolution was never better than 75 m. Thus, the  $50 \times 50 \times 50 \text{ m}$  grids were under resolved and spurious noise may have been introduced to the analyses.

It was difficult to resolve the TREC vectors directly in the vicinity of the tornado. The correlation coefficients were consistently low in this area, likely as a combined result of the influence of debris in the reflectivity field, and vertical motions that caused vertical translation of reflectivity features to exceed the grid spacing.

Since data were collected every 2 s for several minutes, it was hypothesized that TREC might have even better correlations since the assumption that reflectivity field is conserved holds better for shorter time increments. However, when TREC was run for these observations, it was apparent that this was not the case. The correlation coefficients were high, but the velocity field was very noisy (Figure 40a, b). No well-organized flow pattern could be inferred from the analysis. The velocity retrievals were likely noisy because there was too little motion between consecutive input files (Figure 40c, d). Velocities would have to be  $50 \text{ m s}^{-1}$  in order for reflectivity features to translate from one grid point to the next. Because radial velocities were well below  $50 \text{ ms}^{-1}$  everywhere except very near the tornado, the translation of the reflectivity features was not being captured by TREC. Rather, it is likely that turbulence and noise features were being correlated instead of the true wind field.

In order to determine how well the TREC algorithm performed on the observed radar data, several tests were performed. 1) The TREC calculated winds were compared with the two-dimensional winds retrieved from the horizontal dual-Doppler analysis at 205604. 2) The TREC-retrieved component of radial velocity was compared with the observed radial velocity.

*i. Comparison with dual-Doppler analyses*

The availability of the 2 s RaXPoI observations and the determination that such a short time difference did not improve the TREC vectors prompted an investigation to determine what the ideal  $\Delta t$  between TREC scans is. TREC analyses were performed for a series of  $\Delta t$  values: 2 s, 5 s, 10 s, 15 s, 20 s, 30 s, 40 s, and 60 s. The analyses had various start and end times based on the desired  $\Delta t$ , but all were temporally centered on 205604. The TREC analyses were compared to the 205604 dual-Doppler analysis to gain a sense of TREC's performance at the various  $\Delta t$ s (Figure 41, Table 6). Although the differences between the TREC-derived and dual-Doppler calculated horizontal winds were sometimes quite significant (likely because both analysis methods have significant error sources), *the 15 s  $\Delta t$  provided the best TREC analyses when compared with the dual-Doppler analysis.* This time step minimized the magnitude of errors in addition to providing the best coverage with high correlation coefficients. Recalling that increasing the time between scans allows for more velocity increments between consecutive grid points, it becomes apparent that *there is a paradox in the TREC method such that decreasing the time (to a certain point) between scans improved correlations but decreased velocity sensitivity.*

Looking at the best TREC analysis when  $\Delta t = 15$  s, (Figure 41d), it is seen that the dual-Doppler analyzed wind field is more uniform than the TREC winds, and has less noise (Figure 42). However, TREC *is* capable of resolving storm-scale motions. It successfully resolves cyclonic shear in the vicinity of the tornado, southeasterly storm-relative inflow, a convergence zone along the rear flank gust front and a surge of northerly winds immediately west of the tornado circulation, with strong northwesterly

flow, associated with a secondary RFD. There are, however, vectors that are obviously outliers compared with the mean flow. As previously mentioned, reflectivity boxes in the vicinity of the tornado are not well correlated, resulting in erroneous horizontal velocity vectors. The poor correlation is likely due to a combination of factors including high velocities within the tornado center, vertical advection of reflectivity, turbulent motions, and source/sink terms such as evaporation and drop breakup, all of which cause the steady-state assumption to break down.

Comparing the TREC analysis with the dual-Doppler analysis gives credibility to the qualitative representation of the wind field by the TREC analysis method since both techniques resolved the wind field similarly. The tornadic circulation was better resolved in the dual-Doppler analysis owing to the poor TREC correlations in this region. The western portion of the dual-Doppler domain was unresolved due to the poor between-beam angle, but TREC was not inhibited by this limitation. It should be reiterated that the objective analysis technique used for the TREC analyses was different from that used for the dual-Doppler analysis. Thus, there are also some inherent differences in the base quantities from which each procedure was derived. The benefit of the TREC technique is the nearly complete resolution of  $u$  and  $v$  over the entire grid domain, while the dual-Doppler analysis cannot retrieve velocities where the between beam angle is too small, which is a significant percentage of the analysis domain. However, the dual-Doppler analysis is better capable of resolving the details of the flow, particularly in the vicinity of the tornado. When examining the differences between the TREC-derived winds and the dual-Doppler neglecting regions where the dual-Doppler analysis was unable to calculate the wind, 24% of the TREC wind vectors



have errors in magnitude  $> 20 \text{ m s}^{-1}$  and the average error is  $17.4 \text{ m s}^{-1}$ . This implies rather significant errors in the TREC method, although the dual-Doppler winds have potentially significant source of error as well. Thus, it is not entirely clear how well TREC performs, but it appears to have potentially large errors in the calculated wind vectors.

*ii. Comparison with radial velocity*

To get a more truthful representation of the TREC errors, another comparison was performed between the TREC-derived horizontal wind components and the observed storm-relative radial velocity (SRV). The original correlation coefficient overlaid with the TREC horizontal wind vectors are given in Figure 43a. Most obvious in Figure 43a is the region of low correlation coefficients in the immediate vicinity of the tornado, as previously mentioned. The TREC vectors were linearly interpolated back to the original grid domain and overlaid upon the objectively analyzed observed reflectivity (Figure 43b) and radial velocities (Figure 43c). (The TREC domain in Figure 43a is slightly smaller than the domains in b and c due to the requirement of having equal sized boxes. TREC grids have  $b \cdot 10$  fewer grid points where  $b$  is the size of the correlation box in km, requiring interpolation for the TREC grid domain to match that of the observations).

At first glance, the analysis looks reasonable. There is a general tendency for cyclonic circulation near the location of the tornado, southeasterly inflow, and easterly flow in the forward flank area and there is evidence of a rear flank gust front. The storm-relative radial velocity from the TREC U and V wind components was then calculated (Figure 43d) and the difference between the TREC-derived SRV and the

observed SRV was calculated (Figure 43e). It was determined that the average root mean square error between the TREC-derived SRVr and the observed SRVr was just under 12.5 m/s, with an average difference of 8.46 m/s over the whole domain. Nearly 91% of the data had errors less than  $20 \text{ m s}^{-1}$  and 84% had errors less than  $15 \text{ m s}^{-1}$ . The TREC-derived SRV was then replaced with the observed SRV and new horizontal wind components were generated (Figure 43f). This wind field was not as smooth as the original TREC-derived winds. However, it was more representative of the true wind field as recorded by Doppler velocity. *Despite the seemingly reasonable performance of TREC, there was not significant confidence in the TREC-computed wind vectors. For this reason the analyses were not pursued further and no results are contingent upon them.*

### **Pseudo Vorticity Calculations**

A proxy quantity representing the vorticity of the tornado circulation was approximated by examining the difference in the maximum inbound velocity and the maximum outbound velocity within the vortex ( $\Delta V$ ). The maximum/minimum values of Doppler velocity were determined manually by finding the pixel in the raw radar data display (*not* objectively analyzed grids) that had the most positive outbound or most negative inbound radial velocity value and the latitude and longitude of these values were noted. It was decided to not constrain the identification of  $\Delta V_{\max}$  to times when it exceeded a specific value representative of a tornadic vortex signature (TVS). This decision was made because the apparent tornadic threshold was  $\Delta V_{\max} = 55 \text{ m s}^{-1}$ , which is higher than that in many other studies (French et al. 2013), likely due to the spatial resolution of the grid. Additionally, information about the tendencies of subtornadic

$\Delta V_{\max}$  was desired as well to provide information about the pre-tornadic and post-tornadic evolution of rotation. In some situations, the location of the maximum or minimum value of radial velocity associated with the tornado was not explicitly clear due to strong environmental winds adjacent to the tornado cyclone. In such circumstances, the approximate range of the maximum or minimum radial velocity in question was estimated using a symmetric distance from the tornado center to the radial velocity extrema of the opposite sign. Also, outliers that had a single velocity pixel greater than  $10 \text{ m s}^{-1}$  above or below the next highest (lowest) maximum (minimum) were not included as they were presumed to be erroneous.

Between the time the first tornado dissipated and the second tornado formed, the circulations associated with the  $\Delta V$  calculations were often transient and not spatially coherent. When a velocity couplet was strong enough to be evident, it was documented regardless of its spatial or temporal continuity. At times when there was not a coherent velocity couplet and a  $\Delta V$  calculation could not be made,  $\Delta V$  was assigned a value of 0 for that PPI. At other times there were multiple vortices at one elevation angle. For such situations, vertical continuity was employed to track the vortex closest to the adjacent elevation angles. If there did not appear to be a vertically coherent vortex, the strongest  $\Delta V$  was recorded.

### **Three-Dimensional and Constant Range Cross Sections**

The structure of the tornado and tornadic circulation were examined using a series of vertical cross sections and three-dimensional isosurfaces. Cross sections were taken at a constant range from the radar or at a constant azimuth, through the center of the circulation, or through two arbitrarily chosen points. These analyses began with the

same objective analysis performed for the TREC routine, except all analyses were centered on the axis of rotation.

An algorithm was written that determined the distance between the radar latitude and longitude and the tornado latitude and longitude (the center of the grid). Because the grid was in a Cartesian reference frame, a constant radius arc and a constant azimuth angle were not native to the analyses. To circumvent this complication, the distances between the radar and all other grid points in the domain were calculated. To calculate the constant radius, the consecutive grid points whose distance to the radar closest matched the distance between the radar and the tornado were used to create an arc of data points that represented a constant radius from the radar. Similarly, the angle between the radar and the area of interest was calculated and angles for all data points over the domain were also calculated. Those grid points with adjacent angles closest to the angle at the area of interest were used for the constant azimuth cross section. For all other cross sections, two end points were specified and a cross section was linearly interpolated from the slope of the specified points.

During earlier analyses when the tornado was a great distance from the radar, the coarse resolution caused streaks to appear and in the constant radius cross section. This was an effect of the wide beam width at this range, and under-smoothing in the objective analysis resulting from an  $\alpha$  value that was too low. The streakiness should not qualitatively change the interpretation of the current analyses.

A second method of examining the rotation of the tornado and its surroundings was utilized to calculate a pseudo vorticity quantity from the 3-D objectively analyzed grids. Similar to the method used to generate constant radius cross sections, the range

from the radar to each point on the analysis grid was calculated, and a series of constant radius arcs were created for each grid point. Pseudovorticity ( $\zeta_{ps}$ ) was calculated as:

$$\zeta_{ps} = 2\Delta Vr / \Delta r \quad \text{Equation 25}$$

where  $Vr$  is the observed radial velocity and  $r$  is the distance between the grid points for which the  $\Delta Vr$  is calculated. Here, a center-differencing technique was applied.  $Vr$  from the nearest neighboring grid point on either side of the grid point for which the calculation was being made was used and  $\Delta r$  was calculated accordingly.

In an effort to quantify the size and vertical orientation of the tornado, the inclination angle of the axis of rotation and the area of tornadic vorticity at all vertical levels were calculated. The inclination angle was calculated from the raw sweep files by noting the latitude, longitude, and height of the beam at the center of the tornadic TVS. The horizontal and vertical distances between the two points were calculated, and the angle between them was determined. The inclination angle (or vortex tilt) is defined by the angular difference between the axis of rotation and the vertical axis. For a vertically erect tornado without any tilt, the inclination angle would be  $0^\circ$ . An inclination angle of  $90^\circ$  would indicate a horizontal vortex parallel to the ground. The azimuthal angle at which this inclination occurred was also documented, so that the compass direction of the tilt could be documented.

The ‘area’ of tornadic vorticity was calculated from the objectively analyzed grids as the area bound by the  $0.15 \text{ s}^{-1}$  pseudovorticity isopleth. It was determined that  $0.15 \text{ s}^{-1}$  was the best contour to plot because it did not contaminate the graphics with non-tornadic noise, but it also matched well with the times when tornadoes were known to be on the ground. The value is lower than what is expected from typical tornadic

scale vorticity (order  $\sim 1 \text{ s}^{-1}$ ) because it is not a true measure of vorticity calculated from the  $u$  and  $v$  wind components, and because the objective analysis process smoothed gradients in radial velocity, negatively biasing the wind extremes. Because the vortex area calculations were made from the objectively analyzed grids, calculating a meaningful value for the area of the vortex was complicated. This problem arose because the grid domain remained the same for all times ( $10 \times 10 \times 7 \text{ km}$ ), but the domain over which the radar sampled decreased with time as the tornado was approaching, and increased with time as the tornado moved away. While it was desired to determine the size of the tornado at each available vertical layer in the objective analysis, this would not provide a meaningful comparison since some of the analyses sampled the tornado over a considerably deep layer ( $\sim 7 \text{ km}$ ), while others only sampled the tornado through  $2 \text{ km}$ . Additionally, some of the early analyses did not have data available below  $1.5 \text{ km}$ , while others had data available down to  $\sim 100 \text{ m}$ .

Therefore, a different method was utilized. Instead of calculating a volumetric total of grid points exceeding the  $0.15 \text{ s}^{-1}$  threshold, or looking only at a relatively narrow span of heights for which data were available for all times, an average area where the vorticity threshold was met was calculated. The number of grid points with  $\zeta_p > 0.15 \text{ s}^{-1}$  was summed over all vertical levels of the domain. Then, the height at which data became unavailable in the analysis (i.e. the vertical extent of the interpolated radar observations, both on the upper and lower limits of the data) was found. The total number of observed vorticity points was then divided by the number of analysis heights over which data were available at the tornado. The number of grid points was multiplied by the horizontal area of the grid spacing (i.e.  $100 \times 100 \text{ m}$ ) to estimate the

spatial area. This process results in an *average area* calculation, representing the average area (km<sup>2</sup>) the vorticity constraint is met over all vertical levels for which data are available. This representation is not a perfect measure of the area of the vortex, but it is the best that could be determined given the sampling differences with time. The average area qualitatively appears to represent the physical size of the tornadic circulations well enough to assess the variation of their area with time.

## Chapter 7. Results

The questions motivating this study were addressed using primarily single-Doppler analysis methods, although some dual-Doppler analyses were included. Because of the variety of analysis methods and the amount of data available, the results will be organized topically first, as follows: the first section will explain the evolution of the storm-scale features, including storm-scale polarimetric features. The next section will describe kinematic properties and structure of the tornadoes.

### Storm Scale Features

#### *i. Phase i: Tornado 1 ~2036-2048*

When RaXPoI began collecting rapid-scan data at 203640, the first tornado had been on the ground for about 6 minutes (NWS). At the lowest elevation angle (4°, z=1.7 km AGL), there is an obvious hook echo and a small tornadic vortex signature associated with the circulation (Figure 44). The inflow region is contaminated by precipitation from a nearby non-supercellular storm. Thus, there is intervening precipitation south of the forward flank, providing Doppler velocity information about

the inflow in a region typically devoid of hydrometeors and thus velocity returns. The component of the inflow parallel to the radar, SE of the tornado is quite strong, greater than  $40 \text{ m s}^{-1}$ . There is a region of converging radial velocities about 5 km northwest of the tornadic circulation, collocated with the rear edge of the hook's reflectivity gradient, marking what is likely the interface between winds circulating around the rear side of the mesocyclone and the southerly environmental flow impinging upon the hook.

In the hook echo,  $Z_{DR}$  is low<sup>4</sup>, and  $\rho_{hv}$  is near 1, suggesting that the hook is primarily comprised of small, nearly spherical rain drops. The horizontal continuity of the hook appendage is broken above 5.5 km AGL (Figure 45c), but becomes progressively wider with higher reflectivities at lower elevation angles (Figure 45 a, b). Because  $Z_{DR}$  is low at all elevation angles, the higher reflectivities at lower levels likely implies an increased concentration of precipitation at lower heights rather than a change in hydrometeor shape. In other words, the increased reflectivity is not likely due to larger, oblate raindrops with strong return in the horizontal polarization, but rather an increased concentration of small nearly spherical drops.

Immediately below the elevation angle where the hook becomes discontinuous, the hook is quite narrow (Figure 45b). The collocation of the hook with a band of outbound velocities suggests that the hook precipitation is associated with advection around the back side of the mesocyclone. Because reflectivity values are higher at lower levels than aloft, it is hypothesized that horizontal advection around the mesocyclone is occurring through a deep layer, and as precipitation falls from the hook at middle levels ( $z \sim 5 \text{ km}$ ) into the lower portion of the hook, hydrometeor concentration

---

<sup>4</sup> It should be noted that the reflectivity (and therefore  $Z_{DR}$ ) was not calibrated for this deployment. Thus,  $Z_{DR}$  is described in a qualitative sense; exact values should be viewed with caution.



increases, contributing to higher reflectivity, as previously mentioned. The hydrometeors from aloft also have a longer fall time, allowing them to be horizontally advected by the ambient flow, displacing them from the narrow band aloft and causing the low-level hook echo to become wider. Thus, *it appears that the hook echo at low levels is a product of both a deep layer of advection around the mesocyclone and hydrometeors falling through the hook region from aloft. The precipitation aloft also appears to have been advected around the mesocyclone, not independently generated by a convective updraft.*

Midlevel rotation ( $z \sim 5.5$  km) is relatively broad, but there is evidence of two scales of rotation, with two separate areas of inbound velocity maxima (Figure 45c). Areas devoid of hydrometeors on the outbound-velocity side inhibit the full extent of the circulations from being resolved. The inner maximum is due to the tornadic circulation, and the outer is the mesocyclone. Several minutes later (203836), as the precipitation on the outbound-velocity side fills in, the distance between maximum inbound and outbound winds (DMW) of the tornadic circulation is  $\sim 1.5$  km while that of the mesocyclone is  $\sim 10$  km (Figure 46a). A similar double maximum is apparent at low-levels ( $z \sim 1.7$  km). The tornado circulation<sup>5</sup> was confined to a width of about 1 km (defined by the edges of the inbound and outbound radial velocity gradients associated with the vortex) (Figure 46b) while the low-level mesocyclone had a DMW of about 8 km. The tornado circulation at low-levels is azimuthally centered on the low-level mesocyclone, but radially on the storm-relative rear edge of it. Aloft, the tornado

---

<sup>5</sup> Because the radar was too far away to resolve fully the tornado at this point, terminology such as ‘tornado circulation’ and ‘tornadic vortex’ will be used.

rotation is near the center of the mesocyclone, significantly displaced to the northeast of the surface vortex.

Over the next several minutes, inflow strength increases to nearly  $50 \text{ m s}^{-1}$  and the tornado circulation intensifies. Beginning around 2041, precipitation from the non-supercellular convection to the south merges with the supercell along the southeastern edge of the hook echo and in the forward flank region (Figure 47). Although the mesocyclone appears to ingest precipitation from the storm merger over the next two minutes, the vortex associated with the tornado still intensifies, reaching its maximum strength about two minutes later, during the 204258 scan.

Between 2040 and 2043, the midlevel circulation ( $z \sim 5 \text{ km}$ ) becomes very broad and the tornado circulation at this height moves east-southeastward (Figure 48). A jet of strong in-bound radial velocities develops on the western flank of the midlevel TVS between 204300 and 204500, ( $z \sim 3 \text{ km}$ ). This feature is coherent in space and time, extending from the lowest elevation angle to the highest one, and is similar to the rear inflow jet observed by Bluestein and Gaddy (2001). The resulting flow field aloft now has two areas of cyclonic rotation: one associated with the tornado and the other immediately west-northwest associated with the surge of inbounds. Below this, at a height of  $\sim 3 \text{ km}$ , a similar process occurs, resulting in the complete removal of the tornado circulation from the gradient of the storm-scale mesocyclone (Figure 49). It appears that the original mesocyclone broadened and as the rear inflow jet impinged upon the mesocyclone, it essentially split the original mesocyclone into two regions of cyclonic circulation with the original inbound velocities bounding the eastern

circulation and the inbounds associated with the rear inflow jet bounding the western circulation.

From the polarimetric data, it appears that the updraft may have weakened around 2042 because the partial  $Z_{DR}$  ring on the periphery of the updraft weakened and grew smaller (Figure 48c). This corresponds with the time when the tornado circulation began to surge southeastward. It is inferred from an increase in high  $Z_{DR}$  above the freezing level in the vicinity of the hook ( $Z_{DR}$  column) that the updraft subsequently reintensified around 204525. This time also corresponds with a tightening of the nontornadic mesocyclone to the NW of the tornadic one (Figure 48g, h).

Throughout the mature phase of the low-level ( $4^\circ$  elevation angle,  $\sim 1.2$  km ARL) tornadic circulation, a northeast-southwest oriented band of near-zero radial velocities is juxtaposed with a region of relatively strong inflow, around  $45 \text{ m s}^{-1}$  (Figure 50a,b). This suggests a balance is achieved between the rear flank gust front (RFGF) and the inflow. Between 2041 and 2046, the inflow weakens and the outbound velocities associated with the RFGF increase (Figure 50). Presumably, the weakening inflow allows the RFGF to accelerate. Additionally, low  $\rho_{hv}$  associated with the RFGF becomes apparent between 204316 and 204423, suggesting increased convergence along the RFGF, which further supports the idea of a surge in outflow air. Animations of  $4^\circ$  reflectivity at this time also suggest a push of precipitation through the hook echo (Figure 50, upper right panels), leading to a hammer-head hook appearance (Figure 50d, e), which would support the hypothesis of an RFGF surge. The leading edge of the hammerhead feature is collocated with the leading edge of relatively weak radial velocities and low  $\rho_{hv}$  values (between  $\sim 0.65$  and  $0.8$ ) (Figure 50, lower right panels).

This feature marks the location of the outflow boundary, with an accumulation of non-meteorological scatterers along its leading edge. From the  $\rho_{hv}$  field, the boundary appears to wrap into the tornadic vortex region around 2044 (Figure 50c), implying an occlusion of outflow around the vortex. The occlusion contributes to vortex weakening since the tornado circulation becomes cut off by outflow air. This marks the beginning of the decay period.

During the last several minutes of the tornado's life, the tornadic circulation becomes removed from the tip of the hook, and is pushed ahead toward the southeastern flank of the hook, left of the apex of the hammerhead feature associated with the RFGF surge (Figure 50). A thin band of outbound radial velocities associated with the outflow behind the RFGF, also wraps around the east side of the hook echo, but the outflow boundary never surges into the inflow.

Two notable differences are apparent in the storm-scale environments when the tornado was intensifying compared to when it began to weaken: 1) the magnitude of the low-level inflow decreased from  $50 \text{ m s}^{-1}$  to  $35 \text{ m s}^{-1}$  and 2) the proximity of the low-level tornadic vortex to the inferred updraft location decreased from about 5 to 7.5 km. It is quite likely that these two factors are related: the weakening southeasterly inflow may have reduced the northwestward advection of the tornado toward the updraft, allowing the tornado to propagate to the right of the updraft motion, increasingly separating the two features. This provides evidence supporting Dowell and Bluestein's (2002b) finding that there needs to be a balance between inflow, outflow, and updraft motion to support tornado maintenance, and that long-lived tornadoes will have a motion vector nearly parallel to that of the updraft.

ii. *Phase ii: Genesis and intensification of tornado 2 (2046-2057)*

A narrow appendage at low-levels ( $z \sim 1$  km) of outbound radial velocities northwest of tornado 2's circulation surges into the hook region around 204530 (Figure 50d,e). This feature extends from the forward flank region and concentrates cyclonic shear about 4 km to the northwest of the decaying tornado 1. The development of a new low-level mesocyclone in this location causes the hook to wrap up farther northwest, away from the location of tornado 1. This new low-level mesocyclone is associated with the genesis of tornado 2. The outbounds do not extend above a height of  $\sim 2$  km. By 204654, this feature appears to be associated with a surge of heavier precipitation moving from northwest to southeast, on the western flank of the hook echo, suggesting that it may be a secondary RFGF surge. Over the next minute, the low-level hook echo begins to coil up at this northern tip of the secondary RFGF surge (Figure 51). The secondary RFGF surge propagates southeastward, away from the main region of outbounds. At this point, there are two RFGFs apparent in the radial velocity imagery: the leading one is associated with the original tornado and is located along the leading edge of the high reflectivity gradient of the hook echo. The western one is the secondary RFGF surge and is located at the leading edge of high reflectivity wrapping around the back side of the hook.

Aloft, the split mesocyclone previously mentioned persists. The western mesocyclone is broad and organized but the circulation with the eastern one remains relatively weak and diffuse. Multiple small, transient vortices are evident (Figure 52). Over the next several minutes ( $\sim 2045$ - $2049$ ), however, the inbound velocities of the

western mesocyclone weaken and the mesocyclone begins to reorganize into a single broad area of circulation. A smaller scale, vertically coherent vortex forms between 2 and 4 km around 204830, but it remains confined to mid-levels and fails to intensify at the lowest elevation angles (see Kinematics and Structure, part i on subsequent pages). Shortly after this spin-up, the mesocyclone at this height becomes broad and disorganized again. Because the storm is nearing the radar deployment site, the vertical extent of the domain progressively decreases with time. At the highest elevation angle ( $18^\circ$ ,  $z \sim 2.5$  km) the mesocyclone's DMW exceeds 8 km by 2049.

Between 2044 and 2048, a  $Z_{DR}$  column and a narrow crescent shaped bounded weak echo region (BWER) develop (Figure 53). These features suggest that the updraft suddenly intensifies over this period. The BWER and  $Z_{DR}$  column first become evident around 204530, and thus the onset of this updraft pulse is temporally coincident with the secondary RFGF surge previously mentioned. By examining the vertical and horizontal spatial continuity between these two features, it appears that the leading edge of the original RFGF is well matched with the western edge of the  $Z_{DR}$  column. The BWER is located immediately north of the leading low-level RFGF and on the inside of the  $Z_{DR}$  column – both of which are horseshoe shaped (Figure 54). The spatial correlation between these features is consistent with the notion of air rising up along the initial RFGF, and curving cyclonically into the middle levels of the hook echo, with the strongest vertical motions within the BWER region. It is hypothesized that the forward momentum of the secondary RFGF surge may have accelerated flow behind the original RFGF and concentrated low-level convergence along its leading edge, which convergence was associated with the updraft pulse.

At low-levels, the subtornadic circulation associated with tornado 1 remains intact. Several minutes prior to tornadogenesis, the two RFGFs are evident in the radial velocity data as wind shifts (Figure 55a). The leading one is associated with the original tornado and is located along the leading edge of the high reflectivity gradient of the hook echo. The western one is the remnants of the surge in outbound velocities mentioned earlier and is located at the leading edge of high reflectivity wrapping around the back side of the hook. Between 2047 and 2059, the remnants of the earlier tornadic circulation move up the *original* RFGF and are wrapped back into the new developing low-level mesocyclone (Figure 55). The secondary RFGF continues surging southeastward, merging with the original RFGF and begins to occlude the low-level mesocyclone. As this happens, the low-level rotation contracts and increases, strengthening the new low-level.

The organization and intensification of the rotation that develops into tornado 2 appears to occur first at lowest levels (Figure 56a). There is a noticeable lag between what occurs at the lowest levels and what occurs aloft (Figure 56b-d). Aloft, rotation remains broad without organization or coherency of smaller-scale features. There is some evidence, however, that tornadogenesis was coincident with suddenly intensifying rotation in the upper-most elevation angles between 205045 and 205101 (Figure 56d, rightmost panel). The low-level mesocyclone gradually contracted, became stronger, and organized relatively suddenly at  $z \sim 2.5$  km between 205048 and 205105. However, the circulation at middle levels was only weakly strengthening (Figure 56, middle panels). Just after this, rotation contracted over the depth data were collected and the tornado formed by 205138, evident by a TVS at  $4^\circ$  and  $18^\circ$ . This observation could

possibly indicate that there needs to be a match-up in rotation at low-levels and aloft, but the circulation does not have to be vertically continuous for a tornado to form. Such a result could imply convergence associated with the upper vortex might induce a small-scale updraft, stretching preexisting vorticity and causing it to contract and intensify continuously and simultaneously throughout the depth of the incipient tornado.

Just prior to tornadogenesis, a second storm merger begins as non-supercellular convection again impinges upon the forward flank and hook echo of the supercell (Figure 57). This merger does not appear to affect tornadogenesis nor does it appear to disrupt the tornado when the heaviest precipitation impinged upon the forward flank and inflow regions. The orientation of the radar truck was favorable for the detection of any outflow that may have been associated with the non-supercellular convection. No wind shift was evident in the velocities and thus no contribution to low-level vorticity could be inferred from the radar data. *Additionally, it does not appear that this convection had an outflow boundary and therefore it did not likely have a strong cold pool, which may explain why the supercell was not disrupted by the storm merger.*

Tornadogenesis occurs around 2051, according to the NWS damage survey, which is consistent with the time the radar observes an increase in rotation at all elevation angles (205138). The time over which the transition from no tornado to a large wedge (Figure 26) occurs is roughly the same time that it takes the WSR-88D radars to collect a single volume scan. Thus, it is easily seen that improved temporal resolution is required to resolve tornado processes. Several minutes after tornadogenesis, a wide swath of weak outbound velocities develops behind the RFGF (Figure 58). The leading edge of this swath is collocated with the leading RFGF;



however, there is radial divergence along the northern edge of it, implying the possibility of an occlusion downdraft immediately southeast of the tornado. The RFGF again remains confined to a nearly constant storm-relative location during intensification and throughout the mature phase of the tornado. It does not surge into the inflow region at any point during the deployment.

A dual-Doppler analysis was performed at 205448 and is representative of the storm-scale properties during the intensification phase of the tornado (Figure 59). The wind field at the low levels of the analysis is qualitatively similar (not shown), and good spatial coverage is only available below 2 km since the tornado was quite close to RaXPol at this time. There is an obvious cyclonic circulation associated with the tornado. Upward motion is resolved at the center of the circulation at all analysis levels and an occlusion downdraft is evident, as suspected from the raw radial velocity data, to the immediate southeast of the tornado. The RFGF is apparent by the wind shift to the southwest of the tornado. There is a zone of deformation to the southeast of the tornado, in the same general area as the occlusion downdraft. The strongest push in RFD outflow air is immediately west and south of the tornado, which is associated with the secondary RFGF surge. There is no evidence of a wind shift associated with the forward flank gust front. Winds merely gradually back from east-southeasterly to nearly easterly.

At 2055, the scanning strategy was changed from collecting volumetric data to single elevation PPIs at  $1^\circ$ , with the purpose of obtaining rapid-update, high resolution data near the ground. At 205530 a zone of weak outbound velocities separates the leading edge of the hook echo from the impinging non-supercellular convection to its

south (Figure 60). There is no evidence in  $\rho_{hv}$  that there are non-meteorological scatterers along this boundary, but it is suspected that the outbound velocities are associated with the residual boundary from the original RFGF. Because there was so much precipitation adjacent to the hook, it is presumed that the combination of wet ground and falling rain reduced the number and concentration of non-meteorological scatterers that had earlier been present along the zone of convergence, explaining why  $\rho_{hv}$  is no longer reduced. However, the scanning strategy changed at 2055, resulting in a 30 s gap in data coverage. Additionally, data were collected at a lower elevation angle than the previous volumes, using the new scanning strategy. Therefore, it is difficult to conclude definitively whether or not the boundary observed in the 1° data is the same as that observed in the 4° data. The outbound velocities associated with this boundary progressively strengthen, and do not appear to be associated with a subsequent RFGF approaching the boundary from behind.

*iii. Weak Reflectivity Band*

As the tornado intensifies, a very narrow (1-3 beam widths, O 100 m) band of cyclonically curved low reflectivity develops immediately southeast of the circulation center in the single-elevation data around 205535. This feature, dubbed the ‘weak reflectivity band’ (WRB) is initially collocated with a localized region of strong inbound radial velocities, with its leading edge just east of the strongest velocities in the eastern half of the tornado (Figure 61). Before the WRB is even visible in the reflectivity field, a band of low cross correlation coefficient values (~0.75-0.85) is evident (Figure 61a). Because the reflectivities are not low in this area yet, the lower  $\rho_{hv}$  values cannot be attributed to an SNR bias. Such low values of  $\rho_{hv}$  can only be

associated with non-meteorological scatterers. There is no evidence of a zone of convergence in the radial velocity field, and thus the reason for accumulation of non-meteorological scatters in this location is unclear.

The WRB begins to become obvious around 205613, and is associated with slightly stronger inbound velocities than its surroundings. It is positioned just ahead of a spiral band of higher reflectivities, but has moved outward (or east) away from the vortex center. The WRB continues to expand and reflectivity values decrease further. The rear edge of the feature is *ahead* of the RFGF (Figure 61c). The WRB is coincident with perturbations in the radial velocity field, with discontinuous pockets of strong velocities.

The WRB is collocated with the region of low  $\rho_{hv}$  ( $< .9$ ) previously mentioned. The  $\rho_{hv}$  feature is considerably wider than the reflectivity crescent. Around 205600, it is collocated with a relatively wide spiral band of low  $Z_{DR}$  bound to the east by a band of slightly higher  $Z_{DR}$  (1-2 dB) (Figure 61a). The spatial relationship between the reflectivity trough and the lower values of  $\rho_{hv}$  and  $Z_{DR}$  persist as the crescent becomes more pronounced (Figure 61c). The  $Z_{DR}$  and  $\rho_{hv}$  bands remain broader than the reflectivity crescent. Although the reflectivity decreased with time as the feature persisted, no obvious changes in the magnitude of the polarimetric fields can be observed; the features merely became more obvious. When the reflectivity crescent is most obvious, it is still collocated with only marginally lower  $\rho_{hv}$  and  $Z_{DR}$  values (Figure 61f) than initially. The combination of low reflectivity, low  $Z_{DR}$  and low  $\rho_{hv}$  values indicates that there was an accumulation of small, weakly reflective non-meteorological debris, presumably dust and/or small biological scatterers. Because

reflectivity values decrease below 20 dBZ, a portion of the reduction in  $Z_{DR}$  and  $\rho_{hv}$  is likely due also to a decrease in signal-to-noise ratio, which negatively biases both these polarimetric parameters. However, this is not likely the only cause of the low  $Z_{DR}$  and  $\rho_{hv}$  because low values of these parameters were visible prior to the onset of the low reflectivities, as mentioned earlier, and also because low values of these parameters extend in a tail farther rearward than the low reflectivities.

A single elevation dual-Doppler analysis was synthesized at the time when the WRB was forming in an effort to examine the feature's correlation with the nearby wind field (Figure 62). The WRB forms in the deformation zone along the RFGF boundary, separating the inflow from the outflow. Although it was not possible to solve for the vertical wind component, the analysis is qualitatively very similar to the one a minute prior when  $w$  was calculated (Figure 59). According to the 205448 analysis, there is a localized downdraft in the vicinity of the WRB.

By 205659, the feature is very well defined both in reflectivity and in radial velocity (Figure 61d). The reflectivity deficit within the WRB ranges from 15-30 dBZ less than surrounding reflectivities. The trailing edge of the reflectivity crescent is collocated with cyclonic misovortex signatures, and with a boundary of outbound velocities associated with the RFGF (Figure 63). A broad region of outbound velocities develops ahead of the feature resulting in a channel of strong inbounds (flow with a southerly component of motion) about the width of the reflectivity trough. The reflectivity deficit continues to increase and the crescent continues to lengthen through about 205750. The lowest reflectivity value of 2 dBZ is achieved at 205715, implying a deficit of 35 dBZ from the average surrounding reflectivity values outside of the

crescent. After 205750, the reflectivity trough narrows and the deficit decreases. The channel of strong inbound radial velocities also narrows and breaks up (not shown).

By 205817, the only evidence of the reflectivity crescent is the narrow trailing line of slightly reduced reflectivities southeast of the tornado, and a small pocket of inbound radial velocities embedded in the RFD outflow. The decay of this feature is coincident with outbound radial velocities, presumably associated with an RFD surge, encroaching on the western flank of the feature. Eventually, the channel of inbounds velocities that originally separated the two regions of outbounds dissipates and the entire region south of the tornado is characterized by outbound radial velocities consistent with outflow from the RFD.

Information about the evolution of this feature and its vertical structure were desired. Because RaXPol was only collecting data at one elevation angle when this feature appeared, the MWR-05XP data were examined to determine if this feature could be detected in that dataset as well. Unfortunately, the feature was not obvious in the MWR data because of the poor azimuthal resolution of this instrument (the range to the AOI was 14.6 km, and with a  $2^\circ$  beam width, the angular resolution at this range was  $\sim 510$  m, which was wider than the feature). When the weak reflectivity feature is evident in the RaXPol data at 205543, there is no definitive evidence to support the feature's presence in the MWR data (Figure 64). It is also possible that this feature was confined to near-surface heights and the MWR beam, which had a height of  $\sim 250$  m at 225521 at the area of interest, overshot the feature.

Because RaXPol was no longer collecting volumetric data and the MWR-05XP did not resolve this feature, it is not possible to determine whether this feature

developed at low levels and remained confined there, or if it was advected down from aloft. It is suspected, however, from the combination of the radar and visual observations, and the numerical models that appear to resolve some type of similar feature (Lewellen 2000; Schenkman, p.c.), that the reflectivity crescent likely developed at low levels and was confined to this location..

*iv. Phase iii: Steady-state (2057-2116)*

After the tornado intensifies, it reaches a quasi-steady state configuration. It is completely wrapped in rain from the constant influx of precipitation on its rear and forward flank. The storm-scale features during the 1° scans do not change very much over the six-minute increment 2° PPIs were collected. Occasionally, spiral bands of alternating weak and strong reflectivity are evident. As the storm moves to the northeast, the rear flank outflow becomes stronger, approaching 40 m s<sup>-1</sup> by 2100. The leading edge of the RFGF is very well defined since its component of motion is now nearly parallel to the radar beam. The maximum radial velocity value of 124.8 m s<sup>-1</sup> is observed at 210034 (Figure 27). Precipitation continues to impinge on the supercell from the west and south sides. Once volume scans resume ~2102, attenuation inhibits the ability to identify any storm-scale features other than the RFGF and beam blockage at low elevation angles becomes problematic.

The RFD winds at 2102 within 60 m AGL are incredibly strong, exceeding 53 m s<sup>-1</sup> within a 1 km wide swath of winds > 40 m s<sup>-1</sup> (Figure 65a, b). The strong RFD winds get absorbed by the tornado circulation by 2103 and the tornado weakens after this. Between 2104 and 2108, a swath of outbound velocities presumably associated

with outflow, appears to overtake the tornado on its *north* side, approaching the tornado from the *west*, resulting in a configuration where the tornado is completely surrounded by outbound (or wind with a westerly component) flow (Figure 65). The reason for this transition is unknown and is not investigated in this study. The tornado persists until data collection ceases at 2116.

## **Kinematics and structure of the tornadoes**

### *i. Delta V calculations*

In order to address how the rotation associated with the tornado evolved with time and height, a sequence of time-height analyses was made documenting the  $\Delta V_{\max}$  (difference between the maximum inbound and outbound radial velocities within a 3 km distance<sup>6</sup>) for every elevation angle over time (Figure 66). The tornadic vortex associated with tornado 1 below ~4 km intensifies somewhat slowly initially, then rapidly over a period of ~90 s. During the first four minutes of rapid-scan observations, the low-level (4°) velocity couplet strengthens by 51 m s<sup>-1</sup>, from having a  $\Delta V_{\max}$  of 43 m s<sup>-1</sup> to 94 m s<sup>-1</sup>. During a 90 s period of rapid intensification alone (between 203930 and 2041),  $\Delta V_{\max}$  increases 34 m s<sup>-1</sup> (from 58 m s<sup>-1</sup> to 94 m s<sup>-1</sup>). From nearly the beginning of data collection, the rotation above 4 km is more intense than that below 4 km. The reason for this will be discussed subsequently, in Chapter 8. By 204050, the TVS associated with this tornado extends through the highest elevation angle of data ( $z = 5$  km AGL).

---

<sup>6</sup> Note: the  $\Delta V_{\max}$  was not specifically defined as a tornado vortex signature. Rather, it was defined as an area of strong azimuthal shear, with local maxima in the magnitude of outbound and inbound velocities within 3 km of each other. Gate-to-gate shear was not required nor was a velocity threshold.

Toward the end of this period of low-level  $\Delta V$  intensification (204200), a tornadic debris signature (TDS) becomes evident in the data, manifest by a hole of low  $\rho_{\text{hv}}$  coincident with a weak reflectivity hole (Figure 50). The  $Z_{\text{DR}}$  values in the TDS are noisy. A brief period (50 seconds) of weakening follows the rapid increase in  $\Delta V_{\text{max}}$  which is preceded by another period of rapid intensification where  $\Delta V_{\text{max}}$  increases by  $35 \text{ m s}^{-1}$  in 68 seconds. The distance between maximum winds (DMW) generally decreases during the entire intensification process from roughly 800 m to 350 m, with the most rapid decrease occurring during the two scans prior to the first rapid increase in  $\Delta V_{\text{max}}$  at 203917 (Figure 67). This observation provides evidence that  $\Delta V_{\text{max}}$  increased as a response to contraction and vortex stretching. Despite the contraction of the vortex at low-levels, the mesocyclonic circulation aloft remains broad and does not intensify or weaken.

The maximum  $\Delta V$  associated with the first tornado reached its peak intensity at all elevation angles between 2042 and 2044, although not all elevation angles achieved their maximum  $\Delta V$  during the same volume within that two minute increment. The  $\Delta V_{\text{max}}$  at the lowest elevation angle ( $z \sim 1.3 \text{ km}$ ) occurs at 204258, with  $\Delta V_{\text{max}} = 110 \text{ m s}^{-1}$ . There was a large spread ( $50 \text{ m s}^{-1}$ ) in  $\Delta V_{\text{max}}$  with height at this time, with a general tendency of  $\Delta V_{\text{max}}$  to decrease with height. Values of  $\Delta V_{\text{max}}$  above 3.5 km peaked earlier than those below 3.5 km. There was not a gradual trend towards achieving  $\Delta V_{\text{max}}$  at lower heights with time. Rather, the timing of the maxima appear nearly bimodal, with all the  $\Delta V_{\text{max}}$  values aloft occurring within  $\sim$  three volume scans of each other, separated by several volumes without any maxima, followed by  $\Delta V_{\text{max}}$  values below 3 km occurring within  $\sim$  two volume scans of each other.



Although the maximum  $\Delta V$  at  $4^\circ$  decreases from 204258 until the tornado dissipates, the onset of tornado decay does not occur until 204400 - when the overall trend in  $\Delta V$  decreases consistently over all elevation angles (Figure 66b). This time also coincides with a sudden, rapid decrease in  $\Delta V_{\max}$  nearly simultaneously over the lowest 3 km AGL. Initially, rotation decreased rapidly, then it weakened more slowly. During this weakening phase,  $\Delta V_{\max}$  did not simultaneously decrease at all elevations, nor was weakening monotonic with time. After the initial rapid weakening, the  $\Delta V$ s then weakened more slowly for about a minute and a half before rapidly weakening again. At most elevation angles above  $\sim 2$  km, there were periods of intensification suggesting the process or processes driving tornado decay were not constant. The velocities weaken the earliest and the fastest between about 2 and 3 km. However, velocities at all heights become subtornadic<sup>7</sup> nearly simultaneously (within  $\sim 30$  s of each other). According to the NWS damage survey, the tornado officially ceased around 204700, which matches well with the time that the radar observed  $\Delta V_{\max}$  across the circulation decreased below  $55 \text{ m s}^{-1}$ .

During the interim between tornado decay and genesis of the second tornado, a slow increase in  $\Delta V$  was evident at  $4^\circ$  (Figure 66). Upper elevations were slower to recover and a coherent  $\Delta V$  signature often was absent. As previously mentioned, the mid-level mesocyclone had a large, broad area of rotation, but there were often several small, transient spin-ups that were temporally coherent only for two or three volumes

---

<sup>7</sup> For this case, the threshold for a tornado was defined as  $\Delta V_{\max} > 55 \text{ m s}^{-1}$  based on the NWS damage survey documenting when tornado damage began on the ground. Previous studies have defined tornadogenesis by a variety of thresholds based on instrument resolution and comparison of radial velocity values with the time when tornado damage was observed on the ground. It should be noted that the minimum beam height at the time of tornado decay was  $> 800$  m, and for tornadogenesis was  $> 600$  m. Therefore the  $\Delta V_{\max}$  near the ground at tornadogenesis could likely be different from what was observed higher up.

before they dissipated. Around 204830, a midlevel vortex is noticeable at upper elevation angles (Figure 66). The  $\Delta V_{\max}$  associated with the low-level mesocyclone in the 4° elevation scan remained broad and nearly constant during the mid-level spin-up.

There was a steady increase in  $\Delta V$  at low-levels, (4° and 6°), about a minute prior to tornadogenesis. A similar steady intensification was *not* apparent at higher elevation angles. At the highest elevation angles, there was no coherent circulation until the time of tornadogenesis. Just beneath this, circulations were evident in the radial velocity data, but they were broad and relatively weak. Tornadogenesis occurred just after 205100, according to the NWS damage survey, which is consistent with the lowest ( $z \sim 600$  m AGL) radar observations that  $\Delta V_{\max}$  increased by  $25 \text{ m s}^{-1}$  and the distance between the maximum winds decreased from  $\sim 1.5$  km to  $\sim 850$  m between 205100 and 205138 (Figure 67). At the time of tornadogenesis, the circulation in the upper half of the elevation angles consolidated and the oscillatory behavior in  $\Delta V$  ceased. When tornadogenesis occurred, rotation rapidly increased nearly simultaneously throughout the depth over which data were collected, crossing the threshold from subtornadic to tornadic over a period of  $\sim 30$  s. During the minute centered on tornadogenesis,  $\Delta V_{\max}$  increased from  $\sim 45$  to  $> 70 \text{ m s}^{-1}$  at nearly all heights. *There was no evidence that the tornadic rotation built downward from aloft; there was no descending TVS. Rather, tornadogenesis occurred nearly simultaneously over the depth of the sample domain, above the location of pre-existing low-level rotation.*

Once tornadogenesis occurred, the initial intensification process was not uniform. There was a relative minimum in  $\Delta V_{\max}$  around  $z \sim 1.5$  km, slightly below the

layer in which decay was first noted earlier. Above this height, the rotation intensified rapidly. Values of  $\Delta V_{\max}$  increased from  $\sim 55 \text{ m s}^{-1}$  to  $\sim 80 \text{ m s}^{-1}$  between 205100 and 205200. Below this height, however,  $\Delta V_{\max}$  increased more slowly, from  $\sim 55 \text{ m s}^{-1}$  to  $65 \text{ m s}^{-1}$  during the same time interval. When data collection resumed after a brief break at 2052 to change the scanning strategy, all  $\Delta V_{\max}$  values had increased to  $> 80 \text{ m s}^{-1}$  at all heights. The strengthening trend continues through the end of the volumetric data coverage.

While RaXPoI was scanning at  $1^\circ$  elevation angle only, the  $\Delta V_{\max}$  associated with the tornado continued to increase until  $\sim 205645$  – with a  $\Delta V_{\max}$  at this time of  $171 \text{ m s}^{-1}$  (Figure 68). After this time, there was a brief decrease in  $\Delta V_{\max}$ , followed by another gradual increase until  $\Delta V_{\max}$  plateaued. The maximum  $\Delta V_{\max}$  value of the dataset is acquired at 210014, just shy of  $192 \text{ m s}^{-1}$ . The highest radial velocity measurement observed in this dataset was just under  $125 \text{ m s}^{-1}$ , and was collected at 210034.

When volume collection resumed at 210200,  $\Delta V_{\max}$  was very high at all heights (Figure 69). The general trend after this was for  $\Delta V_{\max}$  to weaken with time, but there were periodic fluctuations in this trend. These periods of brief intensification only last for 2-3 volume scans, or less than one minute. Thus, they would be unresolved using conventionally-scanning mobile radar. Although these periods of intensification are interesting, it is unknown whether or not they are important to the dynamics of the storm. By the end of the deployment, as the tornado is moving away from the radar, the  $\Delta V_{\max}$  at nearly all heights has weakened, but remains relatively strong in comparison to other tornadoes, with  $\Delta V_{\max}$  between  $80\text{-}90 \text{ m s}^{-1}$ .

ii. *Three-dimensional vortex structure and evolution*

Another way of examining the trends of the rotation and tornado structure is to examine pseudovorticity three-dimensionally, using objectively analyzed grids (Figure 70). This method allows a more comprehensive analysis of total vorticity associated with the tornado, not just the  $\Delta V_{\max}$ . In addition, structural characteristics such as the size and the tilt of the vortex can easily be viewed. A sequence of the vorticity evolution associated with tornado 1, thresholded on the  $0.15 \text{ s}^{-1}$  contour, is presented in Figure 70. This analysis method utilized the three-dimensional, objectively analyzed grids as discussed in Chapter 6.

From Figure 70, it is apparent that tornado 1 is observed from its intensification through its decay. Initially (203649), the tornado is relatively weak and it is strongest above 3 km. This is in agreement with what is found later in tornado 2, that the upper portion of the tornado intensified more rapidly than lower portions. As the tornado strengthens, it becomes apparent that the vortex is strongly tilted to the northeast with height. Looking at the vortex tilt with time, it is seen that the vortex approaches a  $60^\circ$  inclination angle<sup>8</sup> around 2040, and over most of its intensifying and mature phases it has an inclination of at least  $35^\circ$  (Figure 71a). The vortex tilt bearing (azimuthal direction of the tilt) is primarily to the north-northeast until about 2042. At this time, the tilt becomes more east-northeasterly and the inclination angle gradually decreases. The vortex remains tilted by at least  $30^\circ$  until  $\sim 2045$ , when it weakens. *As the tornado decays, it becomes more vertically erect* with the exception of the very last time a TVS is observable at both low and high elevation angles. Although the height of the beam is

---

<sup>8</sup> Inclination angle is defined by the deviation from the vertical axis, with a vertically erect vortex having an inclination angle of  $0^\circ$ .

changing with time, it is not believed that this has a significant effect on the inclination angle or tilt bearing based on the 3-D pseudovorticity images that support a relatively constant inclination angle and bearing with height.

The average area of the tornado behaves generally as expected: as the tornado intensifies, its area increases (Figure 71b). Initially, the tornadic vorticity area is small, with an average area of  $0.15 \text{ km}^2$ . It peaks around 204130 with an average area per vertical analysis level of  $0.358 \text{ km}^2$ . As the tornado weakens, its area does as well. *There is a general tendency for stronger  $\Delta V$  maxima to be coincident with higher average area values.* A proxy for circulation was also calculated by multiplying the area over which vorticity exceeds the  $0.15 \text{ s}^{-1}$  threshold by the vorticity ( $0.15 \text{ s}^{-1}$ ). It is seen that the circulation gradually increases until the maximum  $\Delta V_{\text{max}}$  occurs around 2043. After this, it gradually decreases until the tornado decays.

To observe the evolution of rotation of tornado 2 in three dimensions, the  $0.2 \text{ s}^{-1}$  pseudovorticity contour was used instead of the  $0.15 \text{ s}^{-1}$  contour because the  $0.15 \text{ s}^{-1}$  threshold was not consistent with the times when a tornado was known to have been on the ground (Figure 71). Because the storm was closer, the resolution was higher and there was less smoothing of the wind field, allowing higher vorticity values to be measured. Just prior to genesis of tornado 2, the low-level vorticity began to intensify (205021) (Figure 72). It briefly weakened below the  $0.2 \text{ s}^{-1}$  threshold and at this time vorticity aloft suddenly increased (205054). Within one 17 second volume scan, vorticity  $> 0.2 \text{ s}^{-1}$  developed throughout the entire depth of data collection (through  $\sim 3$  km). The exception to this was the thin layer mentioned in the  $\Delta V_{\text{max}}$  discussion

between ~1.5 and 2 km that did not intensify simultaneously. A weakness in this layer is evident through 205144.

Tornado 2 is quite erect over the depth radar data are available. The inclination angle is between 20 and 30° and the tilt is generally to the northeast (Figure 73a). Caution must be used, however, when comparing tornado 1 to tornado 2 at this point. The heights of the analyses for tornado 2 are confined to  $z < 3$  km due to the limited vertical sampling domain. Tornado 1 was also more erect in the lower portion of the vortex than aloft; it tilted most severely above  $z \sim 2.5$  km. Therefore, it cannot be concluded at this point that tornado 2's vortex was more vertically upright than the previous one because data are unavailable over the same spatial domain. Similarly to the tornado 1, both the average area of tornadic vorticity and the circulation increased with increasing wind speeds. The size of the vortex aloft grew more rapidly than that near the ground (Figure 73b), in good agreement with the earlier observation that the  $\Delta V_{\max}$  strengthened more rapidly aloft than at the lower levels during this increment.

The vortex tilt and average area of tornadic vorticity become unavailable when the scanning strategy changes from volume scans to 1° PPIs. Although the area of the circulation in the single PPI scans could be calculated, the height at which data were being collected using this scanning strategy was several hundred meters lower than the lowest PPI available in the volume scanning strategy, making a comparison between the two unreliable.

When volume scans resumed at 2102, the 3-D vorticity plots have a different shape (Figure 74). They are confined to low levels since the tornado is so close to the radar, they are elongated in the north-south direction, and there is a region of tornadic

vorticity not attached to the main tornado (210229). The average area of tornadic vorticity had grown considerably (Figure 74). However, this calculation is misleading because there was tornadic-scale vorticity associated with very strong RFD winds. By 2104, the strong RFD winds had merged into the tornado circulation and the average area calculation was again representative of only the tornado, with a value of  $\sim 0.7 \text{ km}^2$ . During the times when the vortex is the largest, it appears elongated in the north-south direction. The elongation is due to a combination of the method used to calculate pseudovorticity and the geometry of the vortex. The radial velocity returns were considerably wider azimuthally (i.e. at a constant range), than they were in the radial direction (Figure 75), contributing to the elongated appearance. Also, the calculation for pseudovorticity is only a function of radial velocity at a constant range from the radar, and it therefore does not truly resolve the full vorticity.

The inclination angle is quite low, between  $5^\circ$  and  $15^\circ$  during this phase of the tornado, indicating that the portion of the tornado for which data are available is nearly vertically erect (Figure 73a). The calculation for tilt bearing between  $\sim 2102$  and  $2105$  is not very reliable; because the vortex is so large, there is an increased margin of error associated with manually determining the middle of the vortex. The inclination angle is also susceptible to this source of error, with a margin of error of about  $5^\circ$ . This error does not change the conclusion that the vortex is nearly vertically erect at this point in time.

As the tornado moves away from the radar, its structure at higher heights becomes apparent (Figure 74, after 2112 UTC). The tornado is definitely more vertical erect at this time than tornado 1 was, with inclination angles not exceeding  $20^\circ$ . Also,

as the vortex moves away, the average area of tornadic vorticity (Figure 73b) decreases slowly but steadily, and the  $\Delta V_{\max}$  values decrease, as does the circulation. Over the ~14 minute period during which volume scans were collected when the tornado is mature, its  $\Delta V_{\max}$  decreases from  $187 \text{ m s}^{-1}$  to  $93 \text{ m s}^{-1}$ , the average area decreases from  $0.8 \text{ km}^2$  to  $\sim 0.4 \text{ km}^2$ , and the circulation decreases from  $\sim 28 \times 10^6 \text{ m}^2 \text{ s}^{-1}$  to  $\sim 14 \times 10^6 \text{ m}^2 \text{ s}^{-1}$ .

iii. *Angular momentum plots*

In an effort to examine the evolution of rotation further, an estimate for angular momentum was calculated according to the storm-relative radial velocity ( $V_r$  - component of  $V_r$  from the storm motion) such that:

$$\Omega_p = V_{sr} * R_t \quad \text{Equation 26}$$

where  $V_{sr}$  is the storm-relative radial velocity and  $R_t$  is the radius to the center of the tornado from the location of  $V_{sr}$ . Vertical cross sections of  $\Omega_p$  at a constant range from the radar were generated from the single-Doppler data using the objectively analyzed grids to examine how  $\Omega_p$  changed with time throughout the lives of the two tornadoes (Figure 76 - Figure 79). According to Rasmussen and Straka (2007), different phases of the tornado should be characterized by differing evolution of angular momentum which can provide insight to the intensification and decay trends.

The pseudo angular momentum plots are generally unremarkable. At all times, angular momentum increases outward, but it does not do so monotonically. Perhaps the most notable characteristic is that  $\Omega$  is *not symmetric around the axis of rotation, implying asymmetry to the tornado flow*. Initially, the  $\Omega$  contours are nearly vertically erect on the radar-relative inbound velocity side of the tornado (from +2 - 0, or the left



half of the image in Figure 76). On the outbound side, the angular momentum is considerably lower than on the inbound side. This implies that the storm-relative winds are weaker in this half of the vortex. It is likely that the storm-relative motion vector had some error since it was manually determined by following the center of the vortex. It is possible that the manual determination was slightly inaccurate, and it is also possible that the storm as a whole was not traveling at the same velocity as the hook echo itself. This may account for at least part of the asymmetry in  $\Omega$ . Another possibility is that the vortex truly was not perfectly axisymmetric. The angular momentum above 4 km was more symmetric than at lower-levels, which implies that the vortex was approximately axisymmetric here and the storm-relative radial velocity was appropriate for the motion of the vortex at this height. Thus, it appears that there is likely a component of asymmetry to the tornado flow at low-levels. Strong inbound velocities associated with the storm inflow are evident just to the east of the inbound side of the tornado (Figure 44 and Figure 45a), which may have enhanced the angular momentum on this side of the tornado.

Periodic bulges are observed on the inbound-side where higher angular momentum air approaches the axis of rotation at one height, but lower angular momentum air bulges away from the axis above and below the positive prominence of higher  $\Omega$  (Figure 76). There is a general tendency for the angular momentum to weaken near the axis of rotation after ~204300, culminating with very weak low-level (below ~1.5 km)  $\Omega$  at 204609, just prior to tornado decay.

During the period between when tornado 1 dissipates and tornado 2 forms, the angular momentum near the ground becomes quite low, and is very asymmetric

throughout the cross section (Figure 77). There is a relative minimum in angular momentum between 2.5 and 4 km at a radius of  $\sim 1$  km on the inbound side of the area of interest. Prior to tornadogenesis, the angular momentum on the inbound side again becomes nearly vertically erect. However, the angular momentum on the outbound side does not and it remains weak. At the time of tornadogenesis, nothing in the angular momentum plots suggests that tornadogenesis is occurring (Figure 78). However, as tornado 2 intensifies, the gradient of angular momentum increases near the axis of rotation, and angular momentum increases, particularly at distances between 1 and 2 km away from the axis of rotation. After the 6 minute increment when volumetric data are unavailable, the angular momentum plots look much different than earlier (Figure 79). At 210214, a very strong angular momentum gradient is concentrated within the inner 500m of the tornado, with maximum values exceeding  $35,000 \text{ m}^2 \text{ s}^{-1}$ . The maximum angular velocity is concentrated at  $\sim 500$  m from the axis of rotation and  $\Omega$  is now quite symmetric. Over the next few minutes, there are some slight temporal variations in the strength and distribution of  $\Omega$ , but no clear trends are found except for an overall slight weakening of  $\Omega$ . The total distance between  $\Omega$  maxima is consistently  $\sim 1$  km.

Around 210846, oscillations are noted along the axis of rotation, and periodically are noted at later times as well. The wavelength and the amplitude of the oscillations are not regular. The wavelength ranges from 500 m to 2 km. These waves are also evident in the radial velocity cross sections, as would be expected since  $\Omega$  is a function of  $V_r$ , and in  $\rho_{hv}$  cross sections (Figure 80). The direction and speed of propagation is not clear from the analyses, despite the 17 s update time. Although the waves initially appear dubious, it is not believed that they are spurious. The distance

between RaXPol and the tornado during the times of the waves was between 10 and 16 km. Because RaXPol sampled every  $2^\circ$  in elevation angle, there was between 350 and 560 m between consecutive elevation angles at bore sight. While some of the shorter wavelength waves could be within the noise regime for  $2\Delta X$  waves, the longer wavelength waves are not. Additionally, tornado 1 was sampled at a similar range with the same objective analysis scheme and there was no evidence of such waves. It is unclear what these waves are, but assuming they are not spurious, it is hypothesized that they are likely due to shear instability on the inner velocity gradient of the tornado. (Rotunno 1984)

*iv. Observations of the Tornadoic Debris Signature*

When a tornado begins to loft non-meteorological debris into the air, the cross-correlation coefficient parameter will decrease significantly as a result of signal decorrelation in the x and y polarization planes. Decorrelation occurs due to varying sizes, shapes, orientations and dielectric constants of the targets within a sample volume. As a result, the  $\rho_{hv}$  parameter can be used to validate or determine when a tornado is on the ground. The resultant tornadoic debris signature (TDS) mitigates the ambiguity of determining whether or not a velocity couplet is tornadoic.

There are some caveats to this seemingly simple diagnostic variable. There must be a sufficient amount of debris available to be lofted in order for a TDS to develop. If the ground is dry or there is plentiful vegetation or structures available as debris sources, the TDS can readily form. However, if the soil is wet or there is not a good source for airborne targets such as leaves, grass, structures, etc., then the TDS may not be apparent. Another factor is beam height above the ground. If the vertical

motions within the tornado are weak, or the debris available does not get lofted high into the air, it is possible for the radar beam to overshoot the TDS. Presumably, these issues will not be a problem with larger, more intense tornadoes. However, establishing a baseline for the velocity required to generate a TDS may not yield consistently accurate results as there are non-meteorological factors that can contribute to its formation.

The evolution of the TDS is now examined through a series of vertical cross sections through the center of the tornadoes and three-dimensional images of  $\rho_{hv}$ . For tornado 1, the first evidence of a TDS<sup>9</sup> in the radar data does not occur until 204105, 10 minutes after tornado 1 was confirmed on the ground (Figure 80). The lag between tornadogenesis and the TDS observation is most likely due to the high height of the beam, which was  $> 1$  km prior to this time. Had the radar been scanning lower or been closer to the tornado, it is likely that a TDS would have been seen earlier. The onset of the TDS occurs just after the  $40 \text{ m s}^{-1}$  radial velocity contour develops at the lowest grid levels, and is coincident with the development of a reflectivity weak echo column (WEC, Tanamachi et al. 2012) (Figure 81).

Over the next several minutes, both the TDS and the WEC<sup>10</sup> grow vertically and horizontally (Figure 81 - Figure 83). The highest the TDS extends is  $\sim 3$  km AGL at 204213. After this, it becomes broader and shorter. The vertical extent of the TDS is not correlated with the magnitude of the radial winds. As the tornado decays, the TDS

---

<sup>9</sup> For this case, TDS is defined by a spatially and temporally coherent column of cross correlation coefficient values lower than 0.8 within a tornadic circulation

<sup>10</sup> The WEC is defined by a spatially and temporally coherent column of reflectivity  $< 30$  dBZ within a tornadic circulation.

shrinks until both decay. The TDS disappears by 204530 (Figure 50), about a minute and a half prior to the actual dissipation of the tornado.

The development of the TDS for tornado 2 is less discernible (Figure 84, Figure 85). There is a band of low  $\rho_{hv}$  associated with the RFGF that wraps into the center of the incipient tornado as the RFGF occludes. Thus, there is already a source of non-meteorological debris in the vicinity and a 'TDS' is present before the tornado officially forms. As tornado 2 intensifies, the TDS grows also, both vertically and horizontally. A weak echo column develops at 205128, but is confined to heights  $< 1$  km until 205245 (Figure 86). There is a gap in data collection between 205201 and 205245, so the exact onset of when the WEC exceeds a height of 1 km and the relationship with the radial winds cannot be determined.

During the single elevation rapid scan mode, the horizontal extent of the TDS continued to grow (Figure 87). A weak echo hole is *not* apparent in the reflectivity field. Instead, a debris ball of high reflectivity is. Since the beam is so low to the ground at this point, centrifuging and vertical motions do not siphon the scatterers away from the center of rotation. Instead, reflective debris fills the sample volumes and thus the reflectivity factor is high. As the tornado continues to intensify, debris is ejected from the TDS in a saw-tooth type configuration (Figure 88) and a long debris tail curving west-southwestward from the southeastern edge of the TDS becomes apparent by 2058 (Figure 89). This feature begins developing around 205700 and lasts until ~2100. Subsequent tails develop after this.

When volume scans again are collected at 2102, it is clear that the TDS and the WEC have grown in horizontal and vertical extent since the last volume scan (Figure

90a – note the change in the scale of the azimuth axis). As the tornado moves away from the radar and the vertical domain increases, *the TDS is visible through the entire column above the tornado for which there are data, through 5 km* (Figure 90c). The wave-like perturbations noted in the radial velocity field and the angular momentum plots are also visible in  $\rho_{hv}$ . As the tornado begins to weaken, the vertical extent of the TDS becomes reduced and the low-level TDS becomes wider (Figure 90e). This occurs as lofted debris falls out of the tornado and is centrifuged outward. Presumably the vertical motion within the tornado decreased as the radial velocities did, which caused debris that was suspended in the TDS to be overcome by gravity and fall to the ground.

## **Chapter 8. Discussion**

From the results described above, it is clear that there are many related factors that simultaneously contribute to tornado evolution. The complexity of the tornadogenesis and decay processes particularly is at once appreciable, with so many small details appearing to play important roles. This is likely why there are so many contradictory conclusions about these processes discussed in the literature. The availability of rapidly updating temporal observations from RaXPoI enabled processes associated with rapid changes in tornado intensity, including formation and dissipation, to be documented more thoroughly than standard mobile, and especially WSR-88D instruments permit. The events and processes associated with the tornadoes' evolutions and their structures are intertwined and cannot be isolated from each other. A

discussion bringing all aspects of tornado evolution together is now presented chronologically.

*i. Tornado1 decay:*

The traditional paradigm of tornado decay involves a surge in outflow air, typically associated with the rear flank downdraft, resulting in an occlusion of outflow around the tornado (Brandes 1978; Lemon and Doswell 1979; Brooks et al. 1994; Davies-Jones 2001; Marquis et al. 2012). This process cuts the tornado off from its source of warm, buoyant inflow, causing the supporting updraft to weaken, which reduces convergence of high angular-momentum air into the vortex, causing it to decay. Often, it has been observed that dissipating tornadoes move rearward relative to the updraft motion, sometimes nearly making a full loop (Bluestein et al. 2010; Tanamachi et al. 2012). Dowell and Bluestein (2002a) found that this occurs when tornados become decoupled from the parent updraft and are advected rearward with the outflow air circulating around the mesocyclone. Similarly, Wicker and Wilhelmson (1995) conclude from a high-resolution numerical simulation of a tornado that the tornado decay process begins when the vertical pressure gradient force weakens or reverses near cloud base. This weakens the updraft above the tornado and allows the rear flank downdraft to wrap completely around the tornado, presumably due to weakening inflow that had previously been able to confine the RFD and inhibit it from wrapping around the mesocyclone.

In this case, it does not appear that an occlusion caused tornado 1 to decay. From the sequence of events describing the weakening and dissipation of tornado 1, it appears that the inflow weakens, allowing the RFGF to accelerate and advect the low-

level tornadic circulation *downstream from the low-level mesocyclone* and parent updraft. This result supports the hypothesis suggested by Dowell and Bluestein (2002) that in order for a tornado to be maintained, a balance must exist between the inflow and outflow. If one or the other becomes too strong, the tornado is adversely affected. The behavior of the low-level vortex at this time is similar to the non-occluding cyclic mesocyclone mode discussed by Adlerman and Drogemeier (2005) where the decaying tornado vortex moves down the RFGF, away from the mesocyclone. Nearly coincident with the time when the low-level circulation is advected toward the leading edge of the RFGF, a pulse in updraft intensity is inferred by the formation of a BWER and  $Z_{DR}$  column. This again is similar to the NOCM mode of Adlerman and Drogemeier except that a new updraft and mesocyclone do not form northeast of the old updraft and mesocyclone. Rather, the original updraft and the western portion of the original split mesocyclone located to the northwest of the tornado appear to intensify and reorganize.

Figure 91 summarizes the evolution of the tornadic circulation and mid-level rotation as tornado 1 decayed and tornado 2 formed. Similarly to the traditional decay paradigm, it appears that upward motion above the tornado weakened which allowed the RFGF to advect the tornado away from the updraft. However, the tornado was not advected around the mesocyclone but rather toward the leading edge of the RFGF surge and away from the original midlevel mesocyclone, similar to the NOCM mode. The midlevel mesocyclone briefly split into two cyclonic circulations as a rear-inflow jet impinged upon the rear side of the original mesocyclone. An updraft pulse and reorganization of the mesocyclone followed this event but occurred to the northwest of the decaying tornado. The RFGF remained contained and did not surge into the inflow,



allowing the ‘new’, or rather reorganizing mesocyclone to continue having access to warm, moist inflow air. Thus, *it appears that the process occurring here is a type of hybrid cyclic mesocyclone/decay process that to the author’s knowledge has not been documented before.*

The onset of tornado decay was nearly simultaneous across all elevation angles between several hundred m AGL and 5 km. The highest three elevations with beam heights between 3 and 5 km AGL lagged the lower elevations by 1 or 2 volume scans, but unambiguously the onset of tornado decay occurred concurrently over the depth of the data domain within 30 s. The decay process was not monotonic; there were brief periods of reintensification before the tornado finally dissipated. The non-linear behavior of  $\Delta V$  during dissipation suggests that the process or processes driving tornado decay were not constant.

Although the onset of tornado decay was nearly simultaneous, it progressed most rapidly within a layer between  $\sim 1.5$  and 2.5 km AGL. The TVS at all heights reached subtornadic criteria ( $\Delta V_{\max} < 55 \text{ m s}^{-1}$ ) between the same two volume scans. However, the complete dissipation of the *velocity couplet* did not behave in this way. Rather, the velocity couplet first disappeared at 2.5 km, then above this height. The subtornadic low-level couplet persisted for several volume scans after the official NWS tornado dissipation time, finally completely dissipating about a minute later. The observation of *velocity couplet* behavior with height is consistent with what French et al. 2013b found in their rapid-scan study of 4 tornadic TVSSs.

From the observations presented above, there is a discrepancy between the behavior of tornado ‘dissipation’, based upon the threshold of shear across the velocity

couplet used to define the TVS. In this situation, the velocity couplet was considered tornadic when  $\Delta V_{\max} > 55 \text{ m s}^{-1}$  based on the value of  $\Delta V_{\max}$  at the times when the NWS damage survey specified there was a tornado on the ground. It is seen here that the velocity couplet at all heights except the very mid-levels persists longer than the reported tornado. If the tornado were defined by a different value of  $\Delta V_{\max}$ , then the decay of the TVS would not have matched the behavior of the actual tornado demise. So, using a criterion of  $\Delta V_{\max} > 55 \text{ m s}^{-1}$ , the tornado decayed nearly simultaneously, within  $\sim 30 \text{ s}$  at all elevations. However, using a threshold of say  $35 \text{ m s}^{-1}$ , the tornado would have appeared to decay first at mid-levels, then aloft, and lastly at the surface. This implies that the dissipation tendency of a ‘TVS’ is contingent upon the threshold one uses to define a TVS. If one applies a TVS threshold too liberally, a ‘TVS’ may exist without a tornado, however if a TVS threshold is applied too conservatively, the true behavior of the rotation may be overlooked.

The structure of the decaying tornado is atypical from what is usually observed. The observation that the tornado becomes *more* vertically erect prior to decay is in contrast to what is typically found: when tornadoes decay their tilt often increases (Bluestein et al. 2003; French et al. 2013). This contradictory behavior occurred because the vortex translation near the ground was different from that aloft. Several minutes prior to decay, the low-level circulation was advected eastward (in a storm relative sense) by a surging secondary RFGF (Figure 49). At the same time, the upper-level vortex decoupled from the strongest radial velocities in the mesocyclone. As a result, the upper-level portion of the tornadic vortex remained nearly stationary over

this period. This configuration allowed the low-level vortex to ‘catch up’ with the upper level vortex, resulting in a more vertically erect vortex (Figure 91).

*ii. Tornado 2 genesis*

There are two primary hypotheses generally accepted to explain tornadogenesis. The dynamic pipe effect describes tornadogenesis as occurring first at mid-levels of the storm when strong convergence contracts rotation aloft. The tornado builds upward and downward simultaneously over a relatively long period of time (order minutes). Radar observations of a descending TVS (Burgess 1976; Brown et al. 1978; Lemon et al. 1978, Davies-Jones 1986) were used to bolster the evidence for this hypothesis. The second hypothesis describes tornadogenesis as being the result of either preexisting vertical vorticity at low levels that becomes stretched by an updraft and amplified to tornadic magnitude, or of a deep layer of convergence acting upon a region of rotation, nearly simultaneously stretching the vorticity to tornadic magnitudes.

In this case, there was no evidence of a descending TVS, implying that tornadogenesis was not associated with the dynamic pipe effect. This conclusion reinforces recent sentiment that supercell tornadoes may not form via the dynamic pipe effect. Rather, the appearance of a descending TVS may be an artifact of poor temporal sampling (French et al. 2013b). It appears that tornadogenesis occurred as a result of rapid convergence of air toward the axis of rotation both aloft and at low levels. Tornadic rotation developed simultaneously within one volume scan (17 s) over the depth of the observations.

Subtornadic rotation began to intensify first at low levels as a low-level mesocyclone formed. Aloft, the mesocyclone was broad and relatively weak, with

transient, small-scale vortices often spinning up. There was evidence from the pseudovorticity plots and the raw radar observation images that tornadogenesis occurred when there was strengthening vorticity both at the lowest elevation angle and the highest, although rotation in between these levels remained weak. This finding might imply that a region of upper-level rotation was necessary to initiate tornadogenesis since low-level vorticity remained relatively constant over several volume scans, and a tornado only formed when the rotation aloft intensified also. It is hypothesized that the sudden increase in rotation aloft contributed to the tornadogenesis process by dynamically inducing low pressure which drove an updraft beneath it, vertically stretching the preexisting low-level vorticity to tornadic intensity (Figure 92). If this were the case, this process is similar to the dynamic pipe effect except it occurs much more rapidly, and there is already preexisting vorticity near the surface. Once the tornado formed, the tornado intensified rapidly above ~ 1.5 km, but more slowly below this.

It is intriguing that both the tornado decay and tornadogenesis processes appear to have a disparity between what happens above and what happens below ~ 1.5 – 2 km AGL. According to the 1800 UTC Norman sounding (Figure 22), there is a capping inversion between ~1.5 km and 3 km. This layer of stable air may explain why the rotation decayed here initially, and why rotation below this height intensified more slowly than that above it. Presumably, the rotating upward motion below the inversion hit the stable layer and was unable to continue rising very quickly, relying on dynamically induced vertical motions, as air became less buoyant compared to its surroundings. This would reduce the amount of vorticity stretching occurring, causing

the tornado to only slowly intensify. Above the stable layer, however, the air could freely rise and vorticity stretching could rapidly act to intensify the rotation. A similar argument can be made about the decay process. This is similar to the explanation offered by French et al. (2013a) who hypothesized that the height of the vertical discontinuity in TVS evolution they observed is near the height of the level of free convection and that vortex evolution behaves differently above and below this level.

Storm-scale features also appeared to play an integral role in tornado formation. Several minutes prior to tornadogenesis, the original mesocyclone broadened and split, but rotation increased with the western member of the split. The split occurred when a rear inflow jet aloft developed, and was coincident with a surge in outflow air near the surface. It is hypothesized that a sudden increase in downward motion associated with a rear flank downdraft generated the surge in outflow air at low levels (Figure 93). The evacuation of mass at mid-levels would have generated a low pressure perturbation hydrostatically, which would draw air in from the rear of the storm in the form of the rear inflow jet. This rear inflow jet temporarily split the original mesocyclone and generated increased rotation on its northwestern flank which nonlinearly generated a dynamically-induced region of low pressure aloft. The combination of low-level convergence associated with the RFGF surge and the dynamically-induced low pressure aloft generated an updraft pulse. The increased upward motion was associated with low-level convergence, which, acting on a broad field of preexisting low-level rotation, strengthened the rotation via stretching, forming an organized low-level mesocyclone. The circulation of the low-level mesocyclone advected the remnant vorticity from

tornado 1 up the leading edge of the RFGF, back into the updraft region, providing a source of low-level vorticity associated with the genesis of tornado 2.

It is important to note that vertical motions cannot be directly inferred from the single-Doppler observations. Speculation for locations of updrafts and downdrafts is based on the presence and locations of storm-scale features known to be associated with vertical motion (e.g. surges in rear flank outflow, BWERS,  $Z_{DR}$  columns, etc.). Thus, the sequence of events described above is based upon the best information available and may not be entirely representative of the processes that occurred in reality. For this reason, a data assimilation modeling study would be very useful to diagnose the full three-dimensional wind field and the dynamics of the storm.

It is also important to recall that the minimum beam height during tornado decay was  $\sim 1$  km AGL, and it was  $\sim 650$  m AGL during tornadogenesis. Therefore, the processes occurring below these heights remain unresolved. Despite this shortcoming, there is no reason to believe trends would be different if the lowest level data were available. The tornadogenesis process still would not display a descending tornadic vortex signature and tornado decay would still likely be similar, just with additional information about how the vortex at the lowest level was evolving. Unfortunately, the question about what occurs at these lowest levels remains unanswered from these data.

Because the entirety of the southern flank of the supercell (south of both the RFD and the FFD) was covered to some extent with precipitation, it begs the question of how much baroclinic generation of horizontal vorticity contributed to the tornadogenesis process. Although gradients in precipitation existed, presumably there was not much of a thermal gradient owing to the constant precipitation in the vicinity of

the forward flank and rear flank gust fronts. Presumably, the outflow from the non-supercellular storm was relatively warm considering it did not hinder tornado formation, nor was there evidence of outflow boundaries. Given the proximity of this storm to the supercell, there is little likelihood that the outflow from the FFD or RFD would be much different thermally. According to both the 1800 UTC KOUN rawinsonde sounding (Figure 22) and visual observations of cloud base (Figure 26), the low-level relative humidity was quite high (relative humidity > 90% from 610 – 1550 m). Thus, evaporational cooling likely did not contribute to strong cold pools which would aid in the generation of baroclinic vorticity. Unfortunately, without thermodynamic data available, this conjecture cannot be substantiated.

*iii. Tornado 2 intensification*

During the intensification of tornado 2, a weak reflectivity band (WRB) developed to the east of the tornado, wrapping around to its south. The deficit in reflectivity within the WRB is collocated with a channel of inbound velocities. It is unclear whether this channel of inbound velocities is due to dynamically-driven accelerations, or if the inflow accelerated faster because of a reduction in hydrometeor size and/or number concentration, as implied by the reduced reflectivity. There is radial divergence along the leading edge of the feature, and convergence just behind it (Figure 94). Such a configuration of horizontal winds implies a downdraft along the leading edge of the feature, which would be associated with divergence near the surface beneath the downdraft. The zone of convergence behind is associated with the boundary demarking the outflow air surging southeastward around the rear flank of the storm and

the northward flow behind the downdraft at the eastern edge of the reflectivity crescent. (Figure 94)

The radar crew visually observed a strong horizontal vortex to the east of the tornado at the time the WRB becomes well-defined in the radar observations, from their location several km north of the tornado (Figure 95). Consistent with the analysis of the wind field presented above, rapid *sinking motion was observed on the eastern side* of the horizontal vortex, and *upward motion was evident on the western side*. Thus, the vorticity vector was directed toward the north or northeast. The visual location of the feature matches well with the location of the WRB noted in the radar data, and the two features are believed to be related. Visually, there was a brighter area beneath the horizontal vortex and the clouds on the western side of the horizontal vortex (Figure 95). No precipitation was seen falling from either of these areas, which likely corresponds to the reflectivity trough.

One possible explanation of the reflectivity deficit is that the upward motion on the western flank of the horizontal vortex lofted falling hydrometeors upward, and prevented rain from falling through the updraft, creating the narrow crescent of lower reflectivity. Unfortunately, data are unavailable from higher elevation angles to determine the vertical continuity of the feature and add plausibility to this hypothesis. Additionally, this hypothesis does not explain why the reflectivity trough extends several hundred meters east of the updraft position inferred from the radial convergence pattern. It is possible that the rapid rotation of the horizontal vortex centrifuged falling hydrometeors and ejected them into the updraft. It is also possible, however, that the downdraft may be associated with hydrometeor-free air, particularly if it is a



dynamically-driven downdraft rather than a buoyancy-driven one. Thus, it is also feasible that the reflectivity trough could have been created by a downdraft. The lack of ability of the observations to resolve vertical motions prevents either of these hypotheses from being substantiated. The beam height at the reflectivity crescent is only ~55 m AGL, so it is reasonable to believe that the hydrometeors are being impacted by the strong vertical and rotational motions above the beam, associated with the horizontal vortex, creating a region devoid of precipitation beneath.

Over the two-minute increment the reflectivity crescent existed, the maximum difference between inbound and outbound radial velocities ( $\Delta V_{\max}$ ) increased from ~120  $\text{ms}^{-1}$  to 180  $\text{m s}^{-1}$ , then settled into a consistent ~150  $\text{m s}^{-1}$ . The time frame during which the  $\Delta V_{\max}$  increased the most is coincident with the time when the WRB was developing and intensifying (~205540 - ~205700). According to both the radar data and visual observations, the WRB and the horizontal vortex both appeared to wrap into the tornado. After ~205700, the intense horizontal vortex dissipated. The time when the horizontal vortex decays, is coincident with the cessation in intensification of  $\Delta V_{\max}$ . Based on this evidence, *it is hypothesized that the horizontal vorticity associated with this feature was ingested into the tornado, was tilted by the vertical motions in the tornado, and contributed to the intensification of the vortex* at this time and when this source of vorticity was removed, the tornado weakened slightly.

The causes of the WRB are somewhat unclear based upon the observations alone. To the author's knowledge, this is the first time that such a feature has been documented observationally in radar data. Similar features of horizontal vorticity have, however, been documented in simulations. Lewellen (2000) noted bands of vorticity

within the surface layer spiraling into the simulated vortex from the southeastern flank in his study. The feature was attributed to the ingestion of low angular momentum air (possibly due to frictional damping of angular momentum) by the inflow in this region. The feature was only evident in the simulation that included vortex translation; not in that where the vortex was stationary, suggesting frictional processes are likely associated with the formation of the band generated in the simulations.

Schenkman (2012) also noticed an elongated roll of high horizontal vorticity to the south and southeast of the tornado-like vortex in his simulation. Similarly to the Lewellen study, this feature was only apparent in the simulations when friction was turned on and is hypothesized to be the result of surface drag in the inflow accelerating towards the tornado. In his simulation, the vorticity is initially generated frictionally and is oriented in a crosswise manner, but becomes streamwise as the flow curves into the tornado, and is subsequently stretched by the horizontal wind. However, the radar simulator of Schenkman's simulation did not generate a low-reflectivity feature. The clearly low-level location of the horizontal vortex visually observed by the radar crew would support either of these hypotheses, which may actually be the same process simulated slightly differently. According to the dual-Doppler analysis at 205532 (Figure 62), the inflow winds are southeasterly, and if it is assumed that in the lowest levels the southeasterly wind increases with height as surface friction decreases with height, the horizontal vorticity vector would be directed in the southwesterly direction. It is seen in the dual-Doppler analyses that the flow just ahead of the RFGF curves around to southwesterly, which would result in anti-streamwise vorticity. However, the

orientation of vorticity described is opposite that which was observed, making this explanation appear implausible.

Baroclinically generated horizontal vorticity also can form along the interface between the RFD and the environmental air. This method would result in downward motion near the downdraft and upward motion ahead of it, presuming the downdraft is colder than the ambient air. The resulting horizontal vorticity vector along the eastern flank of the RFD interface would again be directed to the south: with sinking motion on the western flank and rising motion on the eastern flank. Because both the radial velocity configuration and visual observations indicate upward motion on the western flank and downward motion on the eastern flank, it appears that this is not the mechanism by which the horizontal vortex was created. However, there was an occlusion downdraft analyzed to the *east* of the tornado just prior to the development of this feature. A similar argument, but with the *western* interface of a downdraft, as is the configuration with the occlusion downdraft, would result in a vorticity vector directed toward the north, in the direction observed. This is a possible explanation for the initial development of the WRB. Stretching of the vorticity, which would have a large streamwise component, could enhance the horizontal vorticity. However, the reflectivity feature spanned considerably farther south than the analyzed occlusion downdraft, suggesting this process was likely not the only source explaining the formation of the WRB.

Similar to the explanation of horizontal vorticity generation in the inflow air, an alternative explanation for this feature is that the horizontal vorticity was frictionally generated in the *outflow air* behind the RFGF. According to the dual-Doppler analysis,

flow behind the RFGF was northwesterly. If it is assumed that flow very near the surface is slower than flow several hundred meters aloft, the frictional generation of vorticity due to the vertical wind shear would be directed to the NE (Figure 96). This is roughly the same orientation the vortex was observed to have. The crux of this hypothesis is explaining why the WRB was immediately *ahead* of the RFGF boundary evident in radial velocity data, particularly as it was forming around 205600-205630.

Lastly, it is possible that the horizontal vortex formed as a result of a balance between environmental shear-vorticity ahead of the RFGF and shear-induced vorticity associated with the buoyancy gradients along the RFGF, similar to that proposed by Rotunno et al. (1988). The environmental vorticity vector from the low-level vertical wind shear ahead of the RFGF point toward the north, while that associated with the baroclinically-generated horizontal vorticity along the RFGF points toward the south. These two vorticity dipoles may have reached a balanced state, supporting a persistent updraft along the leading edge of the RFGF and a downdraft ahead. This hypothesis, however, does not explain why the WRB and horizontal vortex formed when they did, or why they would have been so relatively short-lasting.

Figure 96 presents a summary of mechanisms generating horizontal vorticity and possible configurations of storm-scale and environmental features that are consistent with the visual and radar observations of the horizontal vortex. It is proposed that the development of the WRB and horizontal vortex most likely formed by one of two ways: 1) Initially, dynamically-driven subsidence occurred associated with the downdraft to the east of the tornado. This downdraft should have been devoid of hydrometeors. However, precipitation impinging upon the hook echo from the south

filled most of the occlusion downdraft with rain, contributing to the overall wet appearance of this region of the storm. Strong horizontal vorticity developed between the tornado updraft and occlusion downdraft, generating a horizontal vortex with a vorticity vector aligned with the narrow band of southwesterly winds visible in the dual-Doppler analysis, immediately ahead of the RFGF. The vorticity got stretched by the inflow, generating stronger upward and downward motions associated with the horizontal vortex, and the WRB became more pronounced. Once the horizontal vortex was established and the RFGF caught up with it, the frictionally-induced horizontal vorticity in the outflow may have contributes to an even stronger vortex.

The other possibility is that the southward-directed horizontal vorticity associated with the horizontal gradient of vertical velocity across the north-south oriented RFD matched the northward-directed horizontal vorticity generated by low-level environmental shear. A balance was achieved just ahead of the RFGF, with upward motion along its leading edge, and downward motion both ahead and behind it. The horizontal vorticity ahead of the RFGF was accelerated into the tornadic circulation and was consequently stretched, enhancing the vorticity and organizing it into a single band.

#### *iv. Polarimetric Observations*

The availability of polarimetric data enables further analysis of the storm-scale and tornado-scale features of this study. Storm-scale features such as the  $Z_{DR}$  column, and low  $\rho_{hv}$  in the vicinity of gust fronts were used as proxies to examine vertical motions and horizontal boundaries respectively that would not have been as easy to identify with only the standard reflectivity and Doppler velocity fields. The WRB was

associated with bands of very low values of  $\rho_{\text{hv}}$  and  $Z_{\text{DR}}$ . Although these estimates are likely biased by low SNR the bands are wider than the reflectivity crescent associated with the original feature and therefore cannot be explained by a low signal-to-noise ratio alone. Thus, there must have been a significant amount of non-meteorological debris within the horizontal vortex. However, the reflectivity factor data were not high like what is typically found in a tornado debris signature indicating the debris is likely not large or highly reflective.

By examining the relationship between the radial velocity contours, the TDS and the WEC, it is clear that the WEC is narrower than the TDS. In fact, some times the TDS is considerably wider (Figure 90). The WEC is confined to the region with the strongest horizontal gradient of the radial winds, regardless of what the actual maximum values are, as long as the velocities initially exceed  $\sim 30 \text{ m s}^{-1}$ . On the other hand, the periphery of the TDS in many cases seemed to closely match the  $35 \text{ m s}^{-1}$  isopleth (Figure 97). It appears that  $35 \text{ m s}^{-1}$  is the velocity at which debris becomes lofted sufficiently to become visible to a radar. This observation is consistent with what Wakimoto et al. (2012) found in their combined dual-Doppler - photogrammetric analysis.

## **Chapter 9. Conclusions**

This study describes the evolution of two tornadoes and attendant storm-scale properties by examining the structure and single-Doppler kinematics of the storm using a rapidly scanning mobile radar. The questions that motivated this study are: 1) How

does the tornado develop, intensify and decay over short time scales? 2) During tornado formation is there evidence that rotation develops aloft and builds downward, develops near the surface and builds upwards, or neither? 3) How are storm-scale and tornado-scale features related to the formation, intensification, and decay of the tornadoes? 4) How does the three-dimensional structure of the tornado change with time? 5) What additional information do the polarimetric observations add to the analyses?

### **Development and evolution of rotation: (Qs 1 and 2)**

#### Tornadogenesis (Tornado 2):

- Subtornadic rotation develops first at near the ground ( $z < 1$  km).
- Tornadogenesis occurs immediately (16 s) after a sudden intensification of vorticity at upper levels ( $z > 3$  km).
- Within 30 s the  $\Delta V_{\max}$  increases from subtornadic to tornadic intensity ( $> 55$  m s<sup>-1</sup>) over all heights except 1.5 km.
- There is no evidence of a descending TVS prior to tornadogenesis. If the dynamic pipe effect occurs, it is over extremely rapid time scales.
- The mesocyclone above the location of tornadogenesis was weak and broad, occasionally having transient, small-scale spin-ups.

#### Tornado Intensification (Tornado 2):

- After the initial spin-up, tornado 2 undergoes a ~2 minute period of rapid intensification where  $\Delta V_{\max}$  increases by  $\sim 50$  m s<sup>-1</sup>.
- This intensification was associated with a small-scale O(100 m) horizontal vortex and weak reflectivity band. It is hypothesized that the horizontal vortex

contributed to intensification of the tornado by providing a source of horizontal vorticity at low levels that was tilted into the vertical by the tornado updraft, strengthening the tornado.

- It is hypothesized that the onset of this horizontal vortex is associated with an occlusion downdraft to the immediate east of the tornado, and possibly frictional generation of horizontal vorticity due to vertical shear of the near-surface winds behind the RFGF.
- The reason for the low reflectivities in the WRB is not known, but it is proposed that it was associated with vertical motions that acted to reduce the number of falling hydrometeors, either by upward lofting of the precipitation, or the development / vertical advection of strong subsidence and downward motion preventing the formation of hydrometeors and resulting in a reduction of scatterers.

#### Tornado Decay (Tornado 1):

- The tornado decay process begins nearly simultaneously (within 30 s) at all levels. The vortex weakens most rapidly at mid-levels, initially, but the  $\Delta V_{\max}$  becomes non-tornadic nearly simultaneously at all levels.
- The weakening process occurs over a duration of  $\sim 3$  minutes and is not monotonic with time; there are brief periods of reintensification.
- The subtornadic velocity couplet ( $\Delta V_{\max}$ ) entirely dissipates first between 1.5 and 2.5 km. It next dissipates aloft, and lastly at lowest elevation angles, implying a slight difference in behavior between the actual tornado (as determined both by the velocity couplet strength and the NWS damage survey) and the subtornadic velocity couplet.



### **Storm Scale Features (Q 3):**

- Rapidly evolving storm-scale features were found to play an important role in tornado-scale processes.
- A non-occlusion hybrid cycling process was observed where the tornado was advected forward, toward the RFGF, and a new mesocyclone intensified aloft to the *northwest* of the original location of strongest rotation.
- Rear flank gust front surges played counteracting roles in tornado evolution: the first tornado dissipated as a result of an RFGF surge, but the second tornado formed in part due to an RFGF surge.

### Tornadogenesis:

- An updraft pulse preceded tornadogenesis by ~ 4 minutes.
- A rear flank gust front surge was associated with the development of the low-level mesocyclone from which the tornado formed.
- The remnant circulation associated with tornado 1 was advected along the RFGF toward the developing low-level mesocyclone and likely enhanced the low-level vorticity in that region.

### Tornado Decay:

- Tornado decay was associated with a weakening of the mesocyclone and a decoupling of tornado circulation at mid-levels from the strongest shear associated with the midlevel mesocyclone.
- At low-levels, the tornado was displaced to the southeast of the primary updraft, removing it from the best source of low-level convergence.

- Additionally, the flow behind the rear-flank gust front strengthened and occluded the tornado vortex, cutting it off from the inflow region, but the RFGF did not surge into the inflow or cut off the parent mesocyclone.

#### **Tornado Structure (Q4):**

- Tornado 1 was consistently tilted at an inclination angle  $> 35^\circ$  throughout the majority of its life cycle including its most intense phase, sometimes approaching  $60^\circ$ , yet the tornado persisted for  $\sim 16$  minutes.
- Decay of tornado 1 was associated with a tendency for the vortex to become *more* vertically erect, likely as a result of differential storm-relative motion between the lower and middle levels.
- During the mature phase of tornado 2, the vortex inclination angle was considerable lower (angles between  $15$  and  $25^\circ$ ) than that of tornado 1, suggesting that long-lived tornadoes may require processes allowing them to remain more erect than shorter-lived ones.
- The average area of the tornadoes was directly proportional to the strength of  $\Delta V_{\max}$ .
- Angular momentum plots were not always very symmetric, suggesting the tornado's flow is somewhat asymmetric.

#### **Polarimetric data contributions (Q5):**

- Polarimetric observations contributed to a better understanding of storm-scale structure and provided the ability to better infer tendencies in updraft strength by examining trends in the  $Z_{DR}$  column and in horizontal motions associated with the rear flank gust front.

- The strength of vertical motions within the tornado could be inferred by the vertical extent and tendencies of the TDS. During the most intense phases of the tornado, debris was lofted to altitudes exceeding 5 km. Debris fallout was observed when the tornado and presumably its central updraft weakened.
- The WEC was confined to the radius of the largest radial wind gradient, but the TDS extended radially outward to the location bounding the 30-40 m s<sup>-1</sup> radial velocities.

**Other Conclusions:**

- There appears to be a difference in the evolution of rotation above and below ~1.5 km. This height was near the base of a strong capping inversion in the 1800 KOUN sounding. Thus, the stable layer likely inhibited vertical motions below it. Above the inversion, parcels reached their level of free convection and could freely rise, accelerating rapidly according to the buoyancy of the air parcels. Similarly, it is hypothesized that rotation dissipated fastest and took the longest to form between 1.5 and 2 km because this was within the stable layer and vertical motions and therefore vorticity stretching were weak. When parcels were unable to make it through the stable layer, rotation above weakened while the strong vertical motions in the updraft advected rotation away, causing dissipation to occur somewhat rapidly above the stable layer. Below the inversion, changes in rotation take longer to respond because their source is likely located below this level and vertical motions can continue longer.

- Several storm mergers occur but do not appear to impact the evolution of the supercell or the tornado. It is suspected that the storms merging with the supercell did not have strong cold pools because there are no outflow boundaries evident, and therefore do not negatively affect the supercell.

The high temporal frequency at which observations were collected was imperative to come deducing the conclusions above. Tornadogenesis and tornado dissipation occurred over a period less than 30 s, and the processes occurring just prior to this happened on the order of two minutes for tornadogenesis and four minutes for dissipation. A period of rapid intensification transpired over two minutes, and storm-scale processes affecting tornadogenesis and decay (RFGF surges and cycling) happened on the order of two-four minutes. Hence, nearly all processes examined in this study would not be resolvable with a WSR-88D radar, even if it were located very close to the tornado (for superior spatial resolution), owing to the slow temporal update speed of the NEXRAD system. Likewise, non-rapid scanning mobile radars would not have been able to adequately temporally resolve these processes either. The superb temporal update speed and high spatial resolution of RaXPoI provided great detail about the evolution of storm-scale and tornado-scale features. Without a rapid scanning radar, the conclusions drawn in this study would not have been possible.

Although this study made extensive use of the radar data that were available, it left a lot to be desired. It contributed to a more comprehensive understanding of rapidly evolving tornado and storm-scale processes, but unfortunately data were not available to quantify these important processes. The sources and transport of vorticity are of

particular interest in this case, but could not be determined with the data available. If three-dimensional wind data were able to be calculated, the rapid temporal updates make this dataset a good candidate for trajectory analyses. However the single-Doppler technique attempted herein was not sufficient to quantify the wind field, and the dual-Doppler coverage was not only geometrically suboptimal, but the accuracy of dual-Doppler wind estimates was questionable. This case would make an ideal data assimilation study to analyze the properties of the storm that radar data fail to do (Marquis et al. 2012; Tanamachi et al. 2013). It would be interesting to examine pressure tendencies and vertical motion during the storm-scale processes that were deemed important to tornado processes. Additionally, it would be interesting to see if the model can resolve a feature like the WRB or horizontal vortex.

Finally, this is only one case study in a growing pool of studies that appear to argue against the dynamic pipe effect hypothesis of tornado formation in supercells. It would be ideal to examine many cases of varying tornado intensity with high temporal resolution to determine if, in fact, observations of a descending TVS may indeed be an artifact of insufficient temporal sampling, as was suggested by French et al. (2013b).

## References

- Adlerman, E. J., K. K. Droegemeier, Robert Davies-Jones, 1999: A numerical simulation of cyclic mesocyclogenesis. *J. Atmos. Sci.*, **56**, 2045–2069.
- \_\_\_\_\_, and \_\_\_\_\_. (2002) The sensitivity of numerically simulated cyclic mesocyclogenesis to variations in model physical and computational parameters. *Monthly Weather Review* **130**:11, 2671-2691
- Agee, E., C. Church, C. Morris, and J. Snow, 1975: Some synoptic aspects and dynamic features of vortices associated with the tornado outbreak of 3 April 1974. *Mon. Wea. Rev.*, **103**, 318–333.
- \_\_\_\_\_, J. T. Snow, F. S. Nickerson, P. R. Clare, C. R. Church, and L. A. Schaal, 1977: An observational study of the West Lafayette, Indiana, tornado of 20 March 1976. *Mon. Wea. Rev.*, **105**, 893–907.
- Alexander, C. R., and J. Wurman, 2005: The 30 May 1998 Spencer, South Dakota, storm. Part I: The structural evolution and environment of the tornadoes. *Mon. Wea. Rev.*, **133**, 72–97.
- \_\_\_\_\_, 2010: A mobile radar based climatology of supercell tornado structure and dynamics. Ph.D. Dissertation, University of Oklahoma, Norman, OK 229 pp.
- Andre, J. C., and M. Lesieur, 1977: Influence of helicity on high Reynolds number isotropic turbulence. *J. Fluid. Mech.*, **81**, 187-207.
- Armijo, L., 1969: A theory for the determination of wind and precipitation velocities with Doppler radars. *J. Atmos. Sci.*, **26**, 570–573.
- Atkins, N. T., A. McGee, R. Ducharm, R. M. Wakimoto, and J. Wurman, 2012: The LaGrange tornado during VORTEX 2. Part II: Photogrammetric analysis of the tornado combined with dual-Doppler radar data. *Mon. Wea. Rev.*, **140**, 2939–2958.
- Barnes, S. L., 1978: Oklahoma thunderstorms on 29–30 April 1970. Part II: radar-observed merger of twin hook echoes. *Mon. Wea. Rev.*, **106**, 685–696.
- Beck, J. R., J. L. Schroeder, and J. M. Wurman, 2006: High-resolution dual-Doppler analyses of the 29 May 2001 Kress, Texas cyclic supercell. *Mon. Wea. Rev.*, **134**, 3125-3148.
- Balakrishnan, N. and D. S. Zrnic, 1990: Use of polarization to characterize precipitation and discriminate large hail. *J. Atmos. Sci.*, **47**, 1525–1540.

Bluestein, H. B., and W. P. Unruh, 1989: Observations of the wind field in tornadoes, funnel clouds, and wall clouds with a portable Doppler radar. *Bull. Amer. Meteor. Soc.*, **70**, 1514–1525.

\_\_\_\_\_, and W. P. Unruh, 1993: On the use of a portable FM-CW Doppler radar for tornado research. *The Tornado: Its Structure, Dynamics, Prediction, and Hazards, Geophys. Monogr.* **79**, Amer. Geophys. Union, 367-376.

\_\_\_\_\_, J. G. Ladue, H. Stein, D. Speheger, and W. F. Unruh, 1993: Doppler radar wind spectra of supercell tornadoes. *Mon. Wea. Rev.*, **121**, 2200–2222.

\_\_\_\_\_, A. L. Pazmany, J. C. Galloway, and R. E. Mcintosh, 1995: Studies of the substructure of severe convective storms using a mobile 3-mm-wavelength Doppler radar. *Bull. Amer. Meteor. Soc.*, **76**, 2155–2169.

\_\_\_\_\_, W. P. Unruh, D. C. Dowell, T. A. Hutchinson, T. M. Crawford, A. C. Wood, and H. Stein, 1997: Doppler radar analysis of the Northfield, Texas, Tornado of 25 May 1994. *Mon. Wea. Rev.*, **125**, 212–230.

\_\_\_\_\_, and A. L. Pazmany, 2000: Observations of tornadoes and other convective phenomena with a mobile, 3-mm wavelength, Doppler radar: The Spring 1999 field experiment. *Bull. Amer. Meteor. Soc.*, **81**, 2939–2951.

\_\_\_\_\_, and R. M. Wakimoto, 2003: Mobile radar observations of severe convective storms. *Meteorological Monographs*, **30**, 105–105.

\_\_\_\_\_, W. C. Lee, M. Bell, C. C. Weiss, and A. L. Pazmany, 2003: Mobile Doppler radar observations of a tornado in a supercell near Bassett, Nebraska, on 5 June 1999. Part II: Tornado-vortex structure. *Mon. Wea. Rev.*, **131**, 2968–2984.

\_\_\_\_\_, C. C. Weiss, and A. L. Pazmany, 2004: The vertical structure of a tornado near Happy, Texas, on 5 May 2002: High-resolution, mobile, W-band, Doppler radar observations. *Mon. Wea. Rev.*, **132**, 2325–2337.

\_\_\_\_\_, M. M. French, R. L. Tanamachi, S. Frasier, K. Hardwick, F. Junyent, and A. L. Pazmany, 2007: Close-range observations of tornadoes in supercells made with a dual-Polarization, X-band, mobile Doppler radar. *Mon. Wea. Rev.*, **135**, 1522–1543.

\_\_\_\_\_, M. M. French, I. PopStefanija, R. T. Bluth, and J. B. Knorr, 2010: A mobile, phased-array Doppler radar for the study of severe convective storms. *Bull. Amer. Meteor. Soc.*, **91**, 579–600.

Brady, R. H. and E. J. Szoke, 1989: A case study of non-mesocyclone tornado development in Northeast Colorado: Similarities to waterspout formation. *Mon. Wea. Rev.*, **117**, 843–856.

Brandes, E. A., 1977: Flow in a severe thunderstorm observed by dual-Doppler radar. *Mon. Wea. Rev.*, **105**, 113–120.

\_\_\_\_\_, 1978: Mesocyclone evolution and tornadogenesis: Some observations. *Mon. Wea. Rev.*, **106**, 995–1011.

\_\_\_\_\_, 1981: Finestructure of the Del City-Edmond tornadic mesocirculation. *Mon. Wea. Rev.*, **109**, 635–647.

\_\_\_\_\_, J. Vivekanandan, J. D. Tuttle, C. J. Kessinger, 1995: A study of thunderstorm microphysics with multiparameter radar and aircraft observations. *Mon. Wea. Rev.*, **123**, 3129–3143.

Bringi, V.N. and Chandrasekar, V. (2001), “Polarimetric Doppler Weather Radar: Principles and Applications”. Cambridge University Press.

Brooks, H. E., C. A. Doswell, and R. Davies-Jones, 1993: Environmental helicity and the maintenance and evolution of low-level mesocyclones. *The Tornado: Its Structure, Dynamics, Prediction, and Hazards, Geophys. Monogr.* **79**, Amer. Geophys. Union,

Brown, R. A., L. R. Lemon, and D. W. Burgess, 1978: Tornado detection by pulsed Doppler radar. *Mon. Wea. Rev.*, **106**, 29–38.

Browning, K. A., and Fujita, T., 1965: A family outbreak of severe local storms: A comprehensive study of the storms in Oklahoma on May 26, 1963, Part 1, *Special Reports*, No. 32, Contract No. AFCRL-65-695(1), U.S. Air Force Cambridge Research Laboratories, Bedford, Mass., 346 pp.

\_\_\_\_\_, 1964: Airflow and precipitation trajectories within severe local storms which travel to the right of the winds. *J. Atmos. Sci.*, **21**, 634–639.

Burgess, D. W., L. R. Lemon, and R. A. Brown, 1975: Tornado characteristics revealed by Doppler radar. *Geophys. Res. Lett.*, **2**, 183-184.

\_\_\_\_\_ 1976: “Single Doppler radar vortex recognition: part I - mesocyclone signatures”. *Proc. 17th AMS Conf. on Radar Met.*, Seattle, 97–103.

\_\_\_\_\_, V. T. Wood, and R. A. Brown, 1982: Mesocyclone evolution statistics. Preprints, *10th Conf. on Severe Local Storms*, Omaha, NE, Amer. Meteor. Soc., 422–424.

\_\_\_\_\_, M. A. Magsig, J. Wurman, D. C. Dowell, and Y. Richardson, 2002: Radar observations of the 3 May 1999 Oklahoma City tornado. *Wea. Forecasting*, **17**, 456–471.



- Byko, Z., P. Markowski, Y. Richardson, J. Wurman, and E. Adelman, 2009: Descending reflectivity cores in supercell thunderstorms observed by mobile radars and in a high-resolution numerical simulation. *Wea. Forecasting*, **24**, 155–186.
- Church, C. R., J. T. Snow, and E. M. Agee, 1977: Tornado vortex simulation at Purdue University. *Bull. Amer. Meteor. Soc.*, **58**, 900–908.
- \_\_\_\_\_, J. T. Snow, G. L. Baker, and E. M. Agee, 1979: Characteristics of tornado-like vortices as a function of swirl ratio: A laboratory investigation. *J. Atmos. Sci.*, **36**, 1755–1776.
- \_\_\_\_\_, and J.T. Snow, 1993: Laboratory models of tornadoes. *The Tornado: Its Structure, Dynamics, Prediction, and Hazards*, Geophys. Monogr. 79, Amer. Geophys. Union, 277-295.
- Cifelli, R., S. A. Rutledge, D. J. Boccippio, and T. Matejka, 1996: Horizontal divergence and vertical velocity retrievals from Doppler radar and wind profiler observations. *J. Atmos. Oceanic Technol.*, **13**, 948–966.
- Clark, M. R., 2012: Doppler radar observations of non-occluding, cyclic vortex genesis within a long-lived tornadic storm over southern England. *Q. J. R. Meteorol. Soc.*, **138**, 439-454.
- Colyer, F. H., 1913: Tornado in southern Illinois. *Mon. Wea. Rev.*, **41**, 383–383.
- Conway, J. W. and D. S. Zrnić, 1993: A study of embryo production and hail growth using dual-Doppler and multiparameter radars. *Mon. Wea. Rev.*, **121**, 2511–2528.
- Davies-Jones, R. P., 1973: The dependence of core radius on swirl ratio in a Tornado Simulator. *J. Atmos. Sci.*, **30**, 1427–1430.
- \_\_\_\_\_, 1976: Laboratory simulations of tornadoes. *Proc. Symp. On Tornadoes*. Lubbock, Dept. of Civil Engr., Texas Tech University, 151-173.
- \_\_\_\_\_, 1979: Dual-Doppler radar coverage area as a function of measurement accuracy and spatial resolution. *J. Appl. Meteor.*, **18**, 1229-1233.
- \_\_\_\_\_, 1986: Tornado dynamics. *Thunderstorm Morphology and Dynamics*, 2nd ed., E. Kessler, Ed., University of Oklahoma Press, 197–236.
- Davies-Jones, R. P., and H. E. Brooks, 1993: Mesocyclogenesis from a theoretical perspective. *The Tornado: Its Structure, Dynamics, Prediction, and Hazards*, Geophys. Monogr., No. 79, Amer. Geophys. Union, 105–114.

\_\_\_\_\_, R. J. Trapp and H. B. Bluestein, 2001: Tornadoes and Tornadic Storms. *Meteorological Monographs*, **28**, 167–222.

\_\_\_\_\_, 2008: Can a descending rain curtain in a supercell instigate tornadogenesis barotropically? *J. Atmos. Sci.*, **65**, 2469–2497.

Darkow, G. L., and J. C. Roos, 1970: Multiple tornado producing thunderstorms and their apparent cyclic variations in intensity. Preprints, *14th Conf. on Radar Meteorology*, Tucson, AZ, Amer. Meteor. Soc., 305–308.

Darkow, J. M., 1971: Periodic tornado production by long-lived parent thunderstorms. Preprints, *Seventh Conf. on Severe Local Storms*, Kansas City, MO, Amer. Meteor. Soc., 214–217.

Dessens, J., 1972: Influence of ground roughness on tornadoes: A laboratory simulation. *J. Appl. Meteor.*, **11**, 72–75.

Doswell, C. A., and T. P. Grazulis, 1998: A demonstration of vortex configurations in an inexpensive tornado simulator. **P1.5**, *19th Conf. Severe Local Storms*, Minneapolis, MN, 85-88.

Dowell, D.C., and H.B. Bluestein, 1997: The Arcadia, Oklahoma, storm of 17 May 1981: Analysis of a supercell during tornadogenesis. *Mon. Wea. Rev.*, **125**, 2562–2582.

\_\_\_\_\_, and H.B. Bluestein, 2002a: The 8 June 1995 McLean, Texas, storm. Part I: Observations of cyclic tornadogenesis. *Mon. Wea. Rev.*, **130**, 2626–2648.

\_\_\_\_\_, and H.B. Bluestein, 2002b: The 8 June 1995 McLean, Texas, storm. Part II: Cyclic tornado formation, maintenance, and dissipation. *Mon. Wea. Rev.*, **130**, 2649–2670.

\_\_\_\_\_, F. Zhang, L. J. Wicker, C. Snyder, and N. A. Crook, 2004: Wind and temperature retrievals in the 17 May 1981 Arcadia, Oklahoma, supercell: Ensemble Kalman filter experiments. *Mon. Wea. Rev.*, **132**, 1982–2005.

\_\_\_\_\_, C. R. Alexander, J. M. Wurman, and L. J. Wicker, 2005: Centrifuging of hydrometeors and debris in tornadoes: Radar-reflectivity patterns and wind-measurement errors. *Mon. Wea. Rev.*, **133**, 1501–1524.

Eskridge, R. E., and P. Das, 1976: Effect of a precipitation-driven downdraft on a rotating wind field: A possible trigger mechanism for tornadoes?. *J. Atmos. Sci.*, **33**, 70–84.

Fiedler, B. H., and R. Rotunno, 1986: A theory for the maximum windspeeds in tornado-like vortices. *J. Atmos. Sci.*, **43**, 2328–2340.

\_\_\_\_\_, 1994: The thermodynamic speed limit and its violation in axisymmetric numerical simulations of tornado-like vortices. *Atmos. Ocean*, **32**, 335-359.

Flora, S. D., 1919: Kansas tornadoes. *Mon. Wea. Rev.*, **47**, 447-448

Forbes, F. S., 1976: "Photogrammetric characteristics of the Parker tornado of April 3, 1974." Proceedings, Symposium on Tornadoes: Assessment of Knowledge and Implications for Man, Lubbock, TX. Texas Tech University, Lubbock, pp 58-77.

Frame, J., P. Markowski, Y. Richardson, J. Straka, and J. Wurman, 2009: Polarimetric and dual-Doppler radar observations of the Lipscomb County, Texas, supercell thunderstorm on 23 May 2002. *Mon. Wea. Rev.*, **137**, 544-561.

French, M.M., H.B. Bluestein, D.C. Dowell, L.J. Wicker, M.R. Kramar, and A.L. Pazmany, 2008: High-resolution, mobile Doppler radar observations of cyclic mesocyclogenesis in a supercell. *Mon. Wea. Rev.*, **136**, 4997-5016.

\_\_\_\_\_, H. B. Bluestein, I. PopStefanija, C. A. Baldi, and R. T. Bluth 2013a: Mobile, phased-array, Doppler observations of tornadoes at X band. *Mon. Wea. Rev.*, **Submitted**.

\_\_\_\_\_, H. B. Bluestein, I. PopStefanija, C. A. Baldi, and R. T. Bluth 2013b: Reexamining the vertical development of tornadic vortex signatures in supercells. *Mon. Wea. Rev.*, **Accepted subject to major revisions**.

Fujita, T. T., 1958: Mesoanalysis of the Illinois tornadoes of 9 April 1953. *J. Meteor.*, **15**, 288-296.

\_\_\_\_\_, 1959: A detailed analysis of the Fargo tornados of June 20, 1957. *Tech. Rep.* No. 5. Severe Local Storms Project, University of Chicago, 129 pp.

\_\_\_\_\_, 1965: Formation and steering mechanisms of tornado cyclones and associated hook echoes. *Mon. Wea. Rev.*, **93**, 67-78.

\_\_\_\_\_, D. L. Bradbury, C. F. Van Thullenar, 1970: Palm Sunday tornadoes of April 11, 1965. *Mon. Wea. Rev.*, **98**, 29-69.

\_\_\_\_\_, G. S. Forbes, and T. A. Umenhofer, 1976. Close-up view of 20 March 1976 tornadoes: sinking cloud tops to suction vortices. *Weatherwise* 29: 116-131, 145.

\_\_\_\_\_, 1981: Tornadoes and downbursts in the context of generalized planetary scales. *J. Atmos. Sci.*, **38**, 1511-1534.

J. R. Fulks, On the mechanics of the tornado, *National Severe Storms Project Report*, No. 4, U.S. Weather Bureau, **1962**.

- Garrett, R. A., and V. D. Rockney, 1962: Tornadoes in northeastern Kansas, May 19, 1960. *Mon. Wea. Rev.*, **90**, 231–240.
- Golden, J. H., and D. Purcell, 1978: Airflow characteristics around the Union City Tornado. *Mon. Wea. Rev.*, **106**, 22–28.
- Grasso, L. D., and W. R. Cotton, 1995: Numerical simulation of a tornado vortex. *J. Atmos. Sci.*, **52**, 1192–1203.
- Harasti, P. R., C. J. McAdie, P. P. Dodge, W. C. Lee, J. Tuttle, S. T. Murillo, and F. D. Marks, 2004: Real-time implementation of single-Doppler radar analysis methods for tropical cyclones: Algorithm improvements and use with WSR-88D display data. *Wea. Forecasting*, **19**, 219–239.
- Herzogh, P. H., and A. R. Jameson, 1992: Observing precipitation through dual-polarization radar measurements. *Bull. Amer. Meteor. Soc.*, **73**, 1365–1374.
- Hoecker, W. H., 1960: Wind speed and air flow patterns in the Dallas tornado of April 2, 1957. *Mon. Wea. Rev.*, **88**, 167–180.
- Hubbert, J., V. N. Bringi, L. D. Carey, and S. Bolen, 1998: CSU-CHILL polarimetric radar measurements from a severe hail storm in Eastern Colorado. *J. Appl. Meteor.*, **37**, 749–775.
- F. A. Huff, H. W. Hisrr and S. 6. Bigler, Study of an Illinois tornado using radar, synoptic weather and field survey data, Illinois State Water Survey Division, *Report of Investigation* No. 22, 1954, 73 pp.
- Humphreys, W. J., 1926: The tornado. *Mon. Wea. Rev.*, **54**, 501–503.
- Karstens, C. D., T. M. Samaras, B. D. Lee, W. A. Gallus, and C. A. Finley, 2010: Near-ground pressure and wind measurements in tornadoes. *Mon. Wea. Rev.*, **138**, 2570–2588.
- Klemp, J. B., and R. B. Wilhelmson, 1978: The simulation of three-dimensional convective storm dynamics. *J. Atmos. Sci.*, **35**, 1070–1096.
- \_\_\_\_\_, \_\_\_\_\_, and P. S. Ray, 1981: Observed and numerically simulated structure of a mature supercell thunderstorm. *J. Atmos. Sci.*, **38**, 1558–1580.
- \_\_\_\_\_, and R. Rotunno, 1983: A study of the tornadic region within a supercell thunderstorm. *J. Atmos. Sci.*, **40**, 359–377.

Kosiba, K. A., R. J. Trapp and J. Wurman, 2008: An analysis of the axisymmetric three-dimensional low level wind field in a tornado using mobile radar observations. *Geophys. Res. Letters*, **35**, 6 pp.

\_\_\_\_\_, and J. Wurman, 2010: The three-dimensional axisymmetric wind field structure of the Spencer, South Dakota, 1998 tornado. *J. Atmos. Sci.*, **67**, 3074–3083.

\_\_\_\_\_, J. Wurman, Y. Richardson, P. Markowski, and P. Robinson, 2013: The genesis of the Goshen County, Wyoming, tornado (5 June 2009). *Mon. Wea. Rev.*, **141**, 1157–1181.

Kramar, M. R., H. B. Bluestein, A. L. Pazmany, and J. D. Tuttle, 2005: The “owl horn” radar signature in developing Southern Plains supercells. *Mon. Wea. Rev.*, **133**, 2608–2634.

Kumjian, M. R., and A. V. Ryzhkov, 2008: Polarimetric signatures in supercell thunderstorms. *J. Appl. Meteor. Climatol.*, **47**, 1940–1961.

\_\_\_\_\_, \_\_\_\_\_, 2009: Storm-relative helicity revealed from polarimetric radar measurements. *J. Atmos. Sci.*, **66**, 667–685.

\_\_\_\_\_, 2011: Precipitation properties of supercell hook echoes. *Electronic J. Severe Storms Meteor.*, **6** (5), 1–21.

Kuo, H. L., 1966: On the dynamics of convective atmospheric vortices. *J. Atmos. Sci.*, **23**, 25–42.

Lee, W. C., B. J.-Dao Jou, P. L. Chang, and S. M. Deng, 1999: Tropical cyclone kinematic structure retrieved from single-Doppler radar observations. Part I: Interpretation of Doppler velocity patterns and the GBVTD technique. *Mon. Wea. Rev.*, **127**, 2419–2439.

\_\_\_\_\_, and F. D. Marks, 2000: Tropical cyclone kinematic structure retrieved from single-Doppler radar observations. Part II: The GBVTD-simplex center finding algorithm. *Mon. Wea. Rev.*, **128**, 1925–1936.

\_\_\_\_\_, and J. Wurman, 2005: Diagnosed three-Dimensional axisymmetric structure of the Mulhall tornado on 3 May 1999. *J. Atmos. Sci.*, **62**, 2373–2393.

Leise, J. A., 1982: A multidimensional scale-telescoped filter and data extension package. NOAA Tech. Memo. ERL WPL-82, 19 pp. [Available from NOAA ERL, 325 Broadway, Boulder, CO 80303.]

- Lemon, L. R., D. W. Burgess, and R. A. Brown, 1978: Tornadic storm airflow and morphology derived from single-Doppler radar measurements. *Mon. Wea. Rev.*, **106**, 48–61.
- \_\_\_\_\_, and C. A. Doswell, 1979: Severe thunderstorm evolution and mesocyclone structure as related to tornadogenesis. *Mon. Wea. Rev.*, **107**, 1184–1197.
- \_\_\_\_\_, D. W. Burgess, and L. D. Hennington, 1982: A tornado extending to extreme heights as revealed by Doppler radar. *Preprints, 12<sup>th</sup> Conf. on Severe Local Storms*, San Antonio, TX American Meteorological Society, Boston, pp. 430-432.
- Leslie, F. W., 1977: Surface roughness effects on suction vortex formation: A laboratory simulation. *J. Atmos. Sci.*, **34**, 1022–1027.
- Leslie, L. M., 1971: “The development of concentrated vortices: a numerical study. *J. Fluid. Mech.* **48**, 1-21.
- Lewellen, D. C., W. S. Lewellen, and J. Xia, 2000: The influence of a local swirl ratio on tornado intensification near the surface. *J. Atmos. Sci.*, **57**, 527–544.
- Lewellen, W. S. 1976. Theoretical models of the tornado vortex. *Proc. Symp. on Tornadoes: An assessment of knowledge and implications for Man*, Lubbock, TX. Texas Tech University, Lubbock, pp. 107-143.
- \_\_\_\_\_, 1977: Influence of body forces on turbulent transport near a surface. *Z. Angew. Math. Phys.*, **28**, 825–834.
- \_\_\_\_\_, 1993: Tornado vortex theory. *The Tornado: Its Structure, Dynamics, Prediction, and Hazards, Geophys. Monogr.*, No. 79, Amer. Geophys. Union, 19–40.
- Lilly, D. K., 1962: On the numerical simulation of buoyant convection. *Tellus*, **14**, 148-172.
- Liu, H., and V. Chandrasekar, 2000: Classification of hydrometeors based on polarimetric radar measurements: Development of fuzzy logic and neuro-fuzzy systems, and in situ verification. *J. Atmos. Oceanic Technol.*, **17**, 140–164.
- Loney, M. L., D. S. Zrníć, J. M. Straka, and A. V. Ryzhkov, 2002: Enhanced polarimetric radar signatures above the melting level in a supercell storm. *J. Appl. Meteor.*, **41**, 1179–1194.
- Long, R. R., 1958: Vortex motion in a viscous fluid. *J. Met.* **15**, 108-1 12.
- \_\_\_\_\_, 1961: A vortex in an infinite viscous fluid. *J. Fluid Mech.* **11**, 611-624.

- Markowski, P. M., 2002: Mobile mesonet observations on 3 May 1999. *Wea. Forecasting*, **17**, 430–444.
- \_\_\_\_\_, 2002: Hook echoes and rear-flank downdrafts: A review. *Mon. Wea. Rev.*, **130**, 852–876.
- \_\_\_\_\_, J. M. Straka, and E. N. Rasmussen, 2002: Direct surface thermodynamic observations within the rear-flank downdrafts of nontornadic and tornadic supercells. *Mon. Wea. Rev.*, **130**, 1692–1721.
- \_\_\_\_\_, J.M. Straka, and E.N. Rasmussen, 2003: Tornadogenesis resulting from the transport of circulation by a downdraft: Idealized numerical simulations. *J. Atmos. Sci.*, **60**, 795–823.
- \_\_\_\_\_, and J. Y. Harrington, 2005: A simulation of a supercell thunderstorm with emulated radiative cooling beneath the anvil. *J. Atmos. Sci.* **62**, 2607-2617.
- \_\_\_\_\_, Y. Richardson, E. Rasmussen, J. Straka, R. Davies-Jones, and R. J. Trapp, 2008: Vortex lines within low-level mesocyclones obtained from pseudo-dual-Doppler radar observations. *Mon. Wea. Rev.*, **136**, 3513–3535.
- \_\_\_\_\_, \_\_\_\_\_, J. Marquis, R. Davies-Jones, J. Wurman, K. Kosiba, P. Robinson, E. Rasmussen, and D. Dowell, 2012: The pretornadic phase of the Goshen county, Wyoming, supercell of 5 June 2009 intercepted by VORTEX2. Part II: Intensification of low-level rotation. *Mon. Wea. Rev.*, **140**, 2887–2915.
- Marquis, J., Y. Richardson, J. Wurman, and P. Markowski, 2008: Single- and dual-Doppler analysis of a tornadic vortex and surrounding storm-scale flow in the Crowell, Texas, supercell of 30 April 2000. *Mon. Wea. Rev.*, **136**, 5017–5043.
- \_\_\_\_\_, Y. Richardson, P. Markowski, D. Dowell, and J. Wurman, 2012: Tornado maintenance investigated with high-resolution dual-Doppler and EnKF analysis. *Mon. Wea. Rev.*, **140**, 3–27.
- Maxworthy, T. 1972: On the structure of concentrated columnar vortices. *Acta. Acto.*, **17**, 363-374.
- Miller, L. J., and S. M. Fredrick 2009: CEDRIC Custom Editing and Display of Reduced Information in Cartesian space. *Manual* National Center for Atmospheric Research, 130 pp.
- Morton, B. R., 1963: Model experiments for vortex columns in the atmosphere. *Nature*, **197**, 840-842.

Murillo, S. T., W. –C. Lee, M. M. Bell, G. M. Barnes, F. D. Marks, and P. P. Dodge, 2011: Intercomparison of ground-based velocity track display (GBVTD)-retrieved circulation centers and structures of hurricane Danny (1997) from two coastal WSR-88Ds. *Mon. Wea. Rev.*, **139**, 153–174.

National Weather Service (OK damage survey)  
<http://www.srh.noaa.gov/oun/?n=events-20110524-pns1>

Nissen, R., D. Hudak, S. Laroche, R. de Elía, I. Zawadzki, and Y. Asuma, 2001: 3D wind field retrieval applied to snow events using Doppler radar. *J. Atmos. Oceanic Technol.*, **18**, 348–362.

Nolan, D. S. 2013: On the use of Doppler radar-derived wind fields to diagnose the secondary circulations of tornadoes. *J. Atmos. Sci.*, **70**, 1160-1215.

Ogura, Y. and J. G. Charney, 1962: A numerical model of thermal convection in the atmosphere. *Proc. Intern. Symp. Num. Wea. Prediction*, Tokyo, 431-451.

Oye, R., C. Mueller, and S. Smith, 1995: Software for radar translation, visualization, editing, and interpolation. *Preprints, 29th Conf. on Radar Meteorology*, Vail, CO, Amer. Meteor. Soc., 359-361.

Palmer, Robert D., and Coauthors, 2011: Observations of the 10 May 2010 tornado outbreak using OU-PRIME: Potential for new science with high-resolution polarimetric radar. *Bull. Amer. Meteor. Soc.*, **92**, 871–891.

Park, H. S., A. V. Ryzhkov, D. S. Zrnić, and K. E. Kim, 2009: The Hydrometeor classification algorithm for the polarimetric WSR-88D: Description and application to an MCS. *Wea. Forecasting*, **24**, 730–748.

Pazmany, A. L., J. B. Mead, H. B. Bluestein, J. C. Snyder, and J. B. Houser, 2013: A mobile rapid-scanning X-band polarimetric (RaXPoL) Doppler radar system. *J. Atmos. Oceanic Technol.*, **30**, 1398–1413.

Polifke, W., and L. Shtilman, 1989: The dynamics of helical decaying turbulence, *Phys. Fluids A*, **1**, 2025-2033.

Rasmussen, E. N., J. M. Straka, R. Davies-Jones, C. A. Doswell, F. H. Carr, M. D. Eilts, D. and R. MacGorman, 1994: Verification of the origins of rotation in tornadoes experiment: VORTEX. *Bull. Amer. Meteor. Soc.*, **75**, 995–1006.

Ray, P.S., 1976: Vorticity and divergence fields within tornadic storms from dual-Doppler observations. *J. Appl. Meteor.*, **15**, 879–890.



\_\_\_\_\_, B.C. Johnson, K. W. Johnson, J. S. Bradberry, J.J. Stephens, K.K. Wagner, R.B. Wilhelmson, and J.B. Klemp, 1981: The morphology of several tornadic storms on 20 May 1977. *J. Atmos. Sci.*, **38**, 1643–1663.

Rinehart, R. E., and E. T. Garvey, 1978: Three-dimensional storm motion detection by conventional weather radar. *Nature*, **273**, 287–289.

Romine, G. S., D. W. Burgess, and R. B. Wilhelmson, 2008: A dual-polarization-radar-based assessment of the 8 May 2003 Oklahoma City area tornadic supercell. *Mon. Wea. Rev.*, **136**, 2849–2870.

Rotunno, R., 1977: Numerical simulation of a laboratory vortex. *J. Atmos. Sci.*, **34**, 1942–1956.

\_\_\_\_\_, 1979: A study in tornado-like vortex dynamics. *J. Atmos. Sci.*, **36**, 140–155.

\_\_\_\_\_, 1984: An investigation of a three-dimensional asymmetric vortex. *J. Atmos. Sci.*, **41**, 283–298.

\_\_\_\_\_, and J. B. Klemp, 1985: On the rotation and propagation of simulated supercell thunderstorms. *J. Atmos. Sci.*, **42**, 271–292.

\_\_\_\_\_, \_\_\_\_\_, and M. L. Weisman, 1988: A theory for strong, long-lived squall lines. *J. Atmos. Sci.*, **45**, 463–485.

Ryzhkov, A. V., D. S. Zrnic, J. C. Hubbert, V. N. Bringi, J. Vivekanandan, and E. A. Brandes, 2002: Polarimetric radar observations and interpretation of co-cross-polar correlation coefficients. *J. Atmos. Oceanic Technol.*, **19**, 340–354.

\_\_\_\_\_, T. J. Schuur, D. W. Burgess, and D. S. Zrnic, 2005: Polarimetric tornado detection. *J. Appl. Meteor.*, **44**, 557–570.

Schankman, A. D. 2012: Exploring tornadogenesis with high-resolution simulations initialized with real data. *Ph.D. Dissertation*, University of Oklahoma, Norman, OK 162 pp.

Schlesinger, R. E., 1973: A numerical model of deep moist convection: Part I. Comparative experiments for variable ambient moisture and wind shear. *J. Atmos. Sci.*, **30**, 835–856.

\_\_\_\_\_, 1978: A three-dimensional numerical model of an isolated thunderstorm: Part I. Comparative experiments for variable ambient wind shear. *J. Atmos. Sci.*, **35**, 690–713.

- Shabbott, C. J., and P. M. Markowski, 2006: Surface in-situ observations within the outflow of forward-flank downdrafts of supercell thunderstorms. *Mon. Wea. Rev.*, **134**, 1422–1441.
- Shapiro, A., S. Ellis, and J. Shaw, 1995: Single-Doppler velocity retrievals with Phoenix II data: Clear air and microburst wind retrievals in the planetary boundary layer. *J. Atmos. Sci.*, **52**, 1265–1287.
- Shipman, T. G., 1927: Observing a tornado's life. *Mon. Wea. Rev.*, **55**, 183–184.
- Smith, R. K. and L. M. Leslie, 1978. Tornadogenesis. *Quart. J. Roy. Meteor. Soc.*, **105**, 107-127.
- \_\_\_\_\_, and \_\_\_\_\_, 1979: A numerical study of tornadogenesis in a rotating thunderstorm. *Quart. J. Roy. Meteor. Soc.*, **104**, 189-199.
- Snow, J. T., C. R. Church, and B. J. Barnhart, 1980: An investigation of the surface pressure fields beneath simulated tornado cyclones. *J. Atmos. Sci.*, **37**, 1013–1026.
- \_\_\_\_\_, and R. L. Pauley, 1984: On the thermodynamic method for estimating maximum tornado windspeeds. *J. Climate Appl. Meteor.*, **23**, 1465–1468
- Stevens, A. W., 1916: A tornado in Utah. *Mon. Wea. Rev.*, **44**, 459–459.
- Stout, G. E. and F. A. Huff, 1953: Radar records Illinois tornadogenesis. *Bull. Amer. Meteor. Soc.*, **34**, . 281-284.
- Straka, J. M., E. N. Rasmussen, and S. E. Fredrickson, 1996: A mobile mesonet for finescale meteorological observations. *J. Atmos. Oceanic Technol.*, **13**, 921–936
- \_\_\_\_\_, D. S. Zrnić, and A. V. Ryzhkov, 2000: Bulk hydrometeor classification and quantification using polarimetric radar data: Synthesis of relations. *J. Appl. Meteor.*, **39**, 1341–1372.
- \_\_\_\_\_, E. N. Rasmussen, R. P. Davies-Jones, and P.M. Markowski, 2007: An observational and idealized numerical examination of low-level counter-rotating vortices toward the rear flank of supercells. *Electron. J. Severe Storms Meteor.*, **2** (8)
- Stuart, W. P., 1926: A Wisconsin tornado. *Mon. Wea. Rev.*, **54**, 298–298.
- Tanamachi, R. L., H. B. Bluestein, W. C. Lee, M. Bell, and A. Pazmany, 2007: Ground-based velocity track display (GBVTD) analysis of W-band Doppler radar data in a tornado near Stockton, Kansas, on 15 May 1999. *Mon. Wea. Rev.*, **135**, 783–800.

\_\_\_\_\_, \_\_\_\_\_, J. B. Houser, S. J. Frasier, and K. M. Hardwick, 2012: Mobile, X-band, polarimetric Doppler radar observations of the 4 May 2007 Greensburg, Kansas tornadic supercell. *Mon. Wea. Rev.*, **140**, 2103–2125.

\_\_\_\_\_, L. J. Wicker, D. C. Dowell, H. B. Bluestein, D. T. Dawson, and M. Xue, 2013: EnKF assimilation of high-resolution, mobile Doppler radar data of the 4 May 2007 Greensburg, Kansas, supercell into a numerical cloud model. *Mon. Wea. Rev.*, **141**, 625–648.

Tepper, M., and W. E. Eggert, 1956: Tornado proximity traces. *Bull. Amer. Meteor. Soc.*, **37**, 152–159.

Trapp, R. J. and B. H. Fiedler, 1995: Tornado-like vortexgenesis in a simplified numerical model. *J. Atmos. Sci.*, **52**, 3757–3778.

\_\_\_\_\_, and R. Davies-Jones, 1997: Tornadogenesis with and without a dynamic pipe effect. *J. Atmos. Sci.*, **54**, 113–133.

\_\_\_\_\_, E. D. Mitchell, G. A. Tipton, D. W. Effertz, A. I. Watson, D. L. Andra, and M. A. Magsig, 1999: Descending and nondescending tornadic vortex signatures detected by WSR-88Ds. *Wea. Forecasting*, **14**, 625–639.

\_\_\_\_\_, and C. A. Doswell, 2000: Radar data objective analysis. *J. Atmos. Oceanic Technol.*, **17**, 105–120.

Turner, J. S., and D. K. Lilly, 1963: The carbonated-water tornado vortex. *J. Atmos. Sci.*, **20**, 468–471.

Tuttle, J. D., and G. B. Foote, 1990: Determination of the boundary layer airflow from a single Doppler radar. *J. Atmos. Oceanic Technol.*, **7**, 218–232.

\_\_\_\_\_, and R. Gall, 1999: A single-radar technique for estimating the winds in tropical cyclones. *Bull. Amer. Meteor. Soc.*, **80**, 653–668.

van Tassel, E. L., 1955: The North Platte Valley tornado outbreak of June 27, 1955. *Mon. Wea. Rev.*, **83**, 255–264.

Van Den Broeke, M. S., J. M. Straka, and E. N. Rasmussen, 2008: Polarimetric radar observations at low levels during tornado life cycles in a small sample of classic southern Plains supercells. *J. Appl. Meteor. Climatol.*, **47**, 1232–1247.

Vasiloff, S. V., 1993: Single-Doppler radar study of a variety of tornado types. *The Tornado: Its Structure, Dynamics, Prediction, and Hazards, Geophys. Monogr.*, No. 79, Amer. Geophys. Union, 105–114.

- Vivekanandan, J., S. M. Ellis, R. Oye, D. S. Zrnica, A. V. Ryzhkov, and J. Straka, 1999: Cloud microphysics retrieval using S-band dual-Polarization radar measurements. *Bull. Amer. Meteor. Soc.*, **80**, 381–388.
- Wakimoto, R. M., and J. W. Wilson, 1989: Non-supercell Tornadoes. *Mon. Wea. Rev.*, **117**, 1113–1140.
- \_\_\_\_\_, and N. T. Atkins, 1996: Observations on the origins of rotation: The Newcastle tornado during VORTEX 94. *Mon. Wea. Rev.*, **124**, 384–407.
- \_\_\_\_\_, and W. C. Lee, H. B. Bluestein, C. H. Liu, P. H. Hildebrand, 1996: ELDORA Observations during VORTEX 95. *Bull. Amer. Meteor. Soc.*, **77**, 1465–1481.
- \_\_\_\_\_, and H. Cai, 2000: Analysis of a nontornadic storm during VORTEX 95. *Mon. Wea. Rev.*, **128**, 565–592.
- \_\_\_\_\_, H. V. Murphy, and H. Cai, 2004: The San Angelo, Texas, supercell of 31 May 1995: Visual observations and tornadogenesis. *Mon. Wea. Rev.*, **132**, 1269–1293.
- \_\_\_\_\_, N. T. Atkins, and J. Wurman, 2011: The LaGrange tornado during VORTEX2. Part I: Photogrammetric analysis of the tornado combined with single-Doppler radar data. *Mon. Wea. Rev.*, **139**, 2233–2258.
- \_\_\_\_\_, P. Stauffer, W. C. Lee, N. T. Atkins, and J. Wurman, 2012: Finescale structure of the LaGrange, Wyoming tornado during VORTEX2: GBVTD and photogrammetric analyses. *Mon. Wea. Rev.*, **140**, 3397–3418.
- Walko, R. L., 1993: Tornado spin-up beneath a convective cell: Required basic structure of the nearfield boundary layer winds. *The Tornado: Its Structure, Dynamics, Prediction, and Hazards*, Amer. Geophys. Union, 89-95.
- Ward, N. B., 1972: The exploration of certain features of tornado dynamics using a laboratory model. *J. Atmos. Sci.*, **29**, 1194–1204.
- Weisman, M. L., and J. B. Klemp, 1984: The structure and classification of numerically simulated convective storms in directionally varying wind shears. *Mon. Wea. Rev.*, **112**, 2479–2498.
- Weygandt, S. S., A. Shapiro, and K. K. Droegemeier, 2002: Retrieval of model initial fields from single-Doppler observations of a supercell thunderstorm. Part I: Single-Doppler velocity retrieval. *Mon. Wea. Rev.*, **130**, 433–453.
- Wicker, L. J., and R. B. Wilhelmson, 1993: Numerical simulation of tornadogenesis within a supercell thunderstorm. *The tornado: Its structure, dynamics, prediction, and hazards*. AGU Monograph Series, C. R. Church (Ed.). **79**, 75-88.

\_\_\_\_\_, \_\_\_\_\_, 1995: Simulation and analysis of tornado development and decay within a three-dimensional supercell thunderstorm. *J. Atmos. Sci.*, **52**, 2675–2703.

Wilkins, E. M., Y. Sasaki, R. L. Inman, and L. L. Terrell, 1974: Vortex formation in a friction layer: A numerical simulation. *Mon. Wea. Rev.*, **102**, 99–114.

Wilczak, J. M., D. E. Wolfe, R. J. Zamora, B. Stankov, and T. W. Christian, 1992: Observations of a Colorado tornado. Part I: Mesoscale environment and tornadogenesis. *Mon. Wea. Rev.*, **120**, 497–521.

Wurman, J., J. Straka, E. Rasmussen, M. Randall, and A. Zahrai, 1997: Design and deployment of a portable, pencil-beam, pulsed, 3-cm Doppler radar. *J. Atmos. Oceanic Technol.*, **14**, 1502–1512.

\_\_\_\_\_, and S. Gill, 2000: Finescale radar observations of the Dimmitt, Texas (2 June 1995) tornado. *Mon. Wea. Rev.*, **128**, 2135–2164.

\_\_\_\_\_ and M. Randall, 2001: An inexpensive, mobile, rapid-scan radar. *Preprints, 30th Conf. on Radar Meteorology*, Munich, Germany, Amer. Meteor. Soc., 98–100.

\_\_\_\_\_, 2002: The multiple-vortex structure of a tornado. *Wea. Forecasting*, **17**, 473–505.

\_\_\_\_\_, and C. R. Alexander, 2005: The 30 May 1998 Spencer, South Dakota, storm. Part II: Comparison of observed damage and radar-derived winds in the tornadoes. *Mon. Wea. Rev.*, **133**, 97–119.

\_\_\_\_\_, Y. P. Richardson, C. Alexander, S. Weygandt, and P. F. Zhang, 2007: Dual-Doppler analysis of winds and vorticity budget terms near a tornado. *Mon. Wea. Rev.*, **135**, 2392–2405.

Wurman, J., K. Kosiba, P. Markowski, Y. Richardson, D. Dowell, and P. Robinson, 2010: Finescale single- and dual-Doppler analysis of tornado intensification, maintenance, and dissipation in the Orleans, Nebraska, supercell. *Mon. Wea. Rev.*, **138**, 4439–4455.

\_\_\_\_\_, D. Dowell, Y. Richardson, P. Markowski, E. Rasmussen, D. Burgess, L. Wicker, and H. Bluestein 2012: The second verification of the origins of rotation in tornadoes experiment: VORTEX2. *Bull. Amer. Meteor. Soc.*, **93**, 1147–1170.

Xue, M., K. K. Droegemeier, and V. Wong, 2000: The Advanced Regional Prediction System (ARPS) – A multiscale nonhydrostatic atmospheric simulation and prediction tool. Part I: Model dynamics and verification. *Meteor. Atmos. Phys.*, **75**, 161–193.

\_\_\_\_\_, and Coauthors, 2001: The Advanced Regional Prediction System (ARPS) – A multiscale nonhydrostatic atmospheric simulation and prediction tool. Part II: Model physics and applications. *Meteor. Atmos. Phys.*, **76**, 143-165.

\_\_\_\_\_, D.-H. Wang, J.-D. Gao, K. Brewster, and K. K. Droegemeier, 2003: The Advanced Regional Prediction System (ARPS), storm-scale numerical weather prediction and data assimilation. *Meteor. Atmos. Phys.*, **82**, 139-170.

Ying, S. J., and C. C. Chang, 1970: Exploratory model study of tornado-like vortex dynamics. *J. Atmos. Sci.*, **27**, 3–14.

Ziegler, C. L., E. N. Rasmussen, T. R. Shepherd, A. I. Watson, and J. M. Straka, 2001: The evolution of low-level rotation in the 29 May 1994 Newcastle–Graham, Texas, storm complex during VORTEX. *Mon. Wea. Rev.*, **129**, 1339–1368.

Zrnic, D. S., and A. V. Ryzhkov, 1999: Polarimetry for weather surveillance radars. *Bull. Amer. Meteor. Soc.*, **80**, 389–406.

Zhang, J., and T. Gal-Chen, 1996: Single-Doppler wind retrieval in the moving frame of reference. *J. Atmos. Sci.*, **53**, 2609–2623.

## Tables

Parameter	Value
Center Frequency	9.73 GHz $\pm$ 20 MHz
Transmit Power	20 kW peak, 200 W ave.
Transmit Pulse Width	0.1 – 40 $\mu$ s
Transmit Waveform	RF Pulse, Linear or Custom Chirp
Transmit Polarization	Equal Power V&H
PRF	Uniform or Staggered
Antenna type	Dual-linear Polarized Parabolic Reflector
Antenna Diameter	2.4 m
Antenna Beamwidth	1.0 $^\circ$
Half-power Antenna Gain	44.5 dB
Pedestal Type	Elevation over Azimuth
Pedestal Scan Rate	180 $^\circ$ s $^{-1}$ Azimuthal; 36 $^\circ$ s $^{-1}$ Elevation
Receiver type	Dual-channel ( V & H-pol)
Receiver Noise Figure	3 dB
Receiver Bandwidth	0.5 to 40 MHz, or Custom
Range Gate Spacing	7.5 to 75 m
IF Frequency	90 MHz
Digital Receiver	Dual-channel, 16 bit ADC
Dynamic Range	90 dB @ 1 MHz Bandwidth
Processor	Industrial PC, Dual Quad-core 2.66 GHz Xeon
Clutter Filter	Coherent, User Defined Bandwidth

Table 1: Instrument specifications for RaXPOL. (Pazmany et al. 2013).

Start Time	End Time	Scanning Strategy	Range Resolution (m)	Gate spacing (m)	Elevation Angles	Volume Update Time
202116	202920	Standard	150	75	2, 4, 6, ... 18	113 s
203101	203515	Standard	150	75	2, 4, 6, ... 18	105 s
203634	205210	Rapid Scan	150	75	2, 4, 6, ... 18	17 s
205232	205456	Rapid Scan	75	30	2, 4, 6, ... 18	16 s
205524	210140	Rapid Scan	75	30	1	2 s
210207	211631	Rapid Scan	75	30	2, 3, 5, 7, ... 17	16s

Table 2: Summary of RaXPOL scanning strategies, times, and specifications.

Parameter	Value
Tornado #	1
EF Rating	EF3
Estimated peak winds (ground survey)	140 mph
Start Time	2031 UTC
Start Location	4 WSW Lookeba, OK
End Time	2047 UTC
End Location	4 NE Lookeba, OK
Damage Path Length	9 miles
Damage Width	Unknown
Tornado #	2
EF Rating	EF5
Estimated peak winds (ground survey)	>210 mph
Start Time	2050 UTC
Start Location	4 ESE Hinto, OK
End Time	2135 UTC
End Location	4 NE Guthrie, OK
Damage Path Length	65 miles
Damage Width	Unknown

Table 3: Summary of tornadoes observed by RaXPOL used for this case study on 24 May 2011.

Elevation angle	U wind RMSE	V wind RMSE	Direction RMSE
1°	16.34 ms <sup>-1</sup>	12.97 ms <sup>-1</sup>	33.83°
2.5°	9.92 ms <sup>-1</sup>	8.77 ms <sup>-1</sup>	22.55°
5.5°	8.21 ms <sup>-1</sup>	8.37 ms <sup>-1</sup>	22.07°
7°	10.65 ms <sup>-1</sup>	11.86 ms <sup>-1</sup>	30.03°

Table 4: Error comparisons for dual-Doppler analyses at constant RaXPOL elevation angle and varying MWR-05XP angles. Comparisons were made between the analysis of the elevation angle listed and the 4° MWR-RaXPOL analysis, which would be the best matched if MWR were perfectly level.

Parameter	MWR-05XP	RaXPOL
$\theta_b$	1.8° az, 2°el	1° az, 1°el
$D_{max}$	20 km	10 km
$R^2$	0.0825	0.0825
Range for $r_{i\ell}$	0.78-1.1 km	.39-.55 km
Choice for $r_i$	1 km	.5 km
K value	0.2	0.05
$\alpha$ value	-0.41	-1.65

Table 5: Summary of dual-Doppler parameters for the MWR-05XP and RaXPOL for the 2054 analysis.



<b>dt (s)</b>	<b>URMSE</b>	<b>VRMSE</b>
2	20.65	23
5	15.99	19.66
10	15.13	17.24
15	14.32	14.62
20	14.71	14.87
30	16.54	15.06
40	16.84	15.75
60	17.88	15.53

Table 6: Root mean square error for the u and v components comparing the TREC-derived and dual-Doppler synthesized winds for different time steps between TREC analyses. Valid for the 205604 dual-Doppler analysis and the TREC times centered on 205604 at z=500m.

## Figures

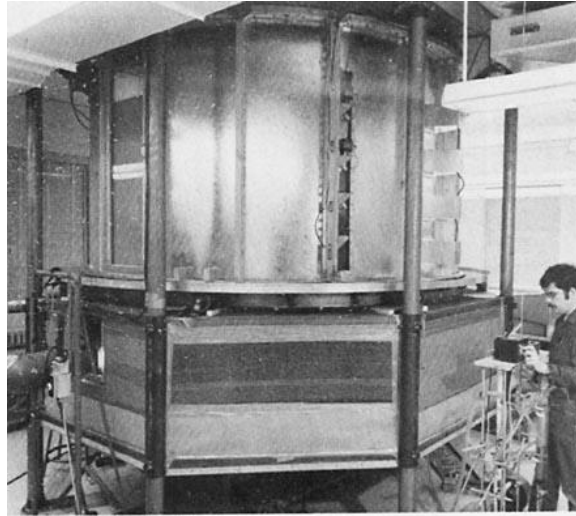


Figure 1: The tornado vortex simulator at Purdue University (Church et al. 1979, their Fig. 2).

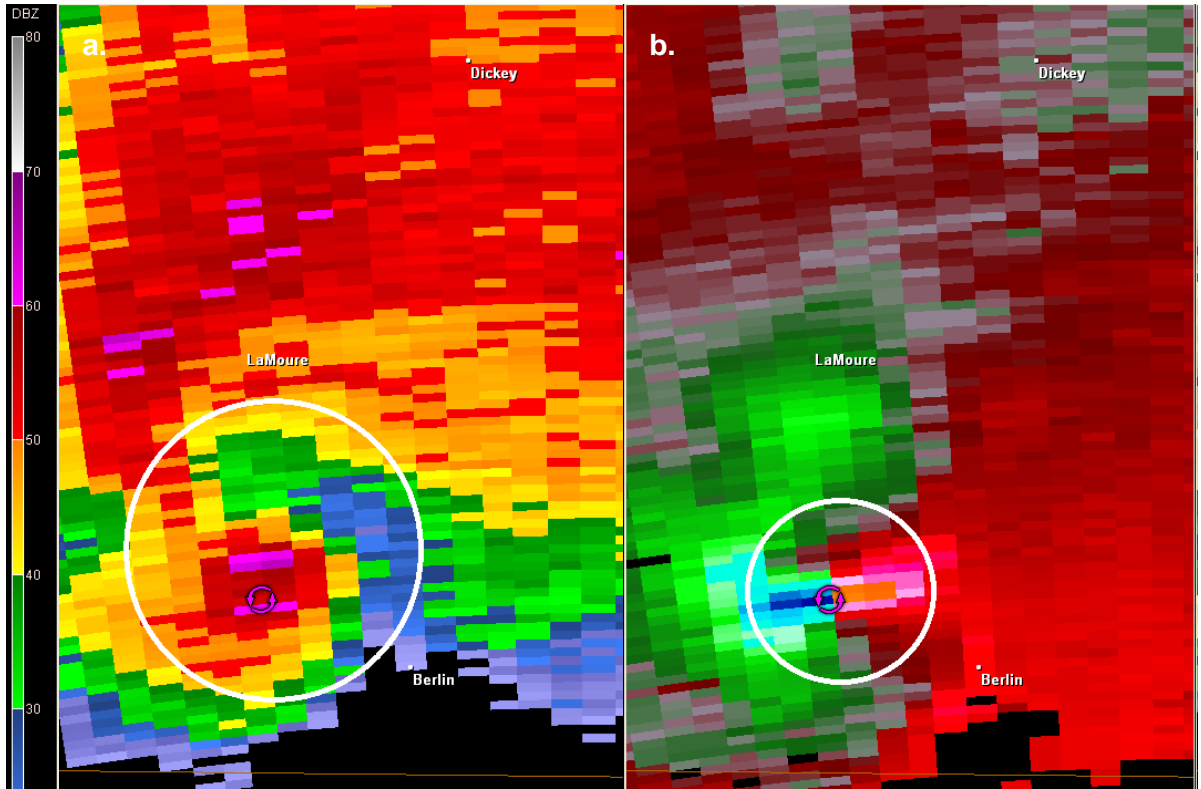


Figure 2: Radar image of a) a hook echo in the reflectivity field and b) a tornadic vortex signature in the radial velocity field corresponding with the hook echo in a. Image is from the KABR radar, 2313 17 June 2011.

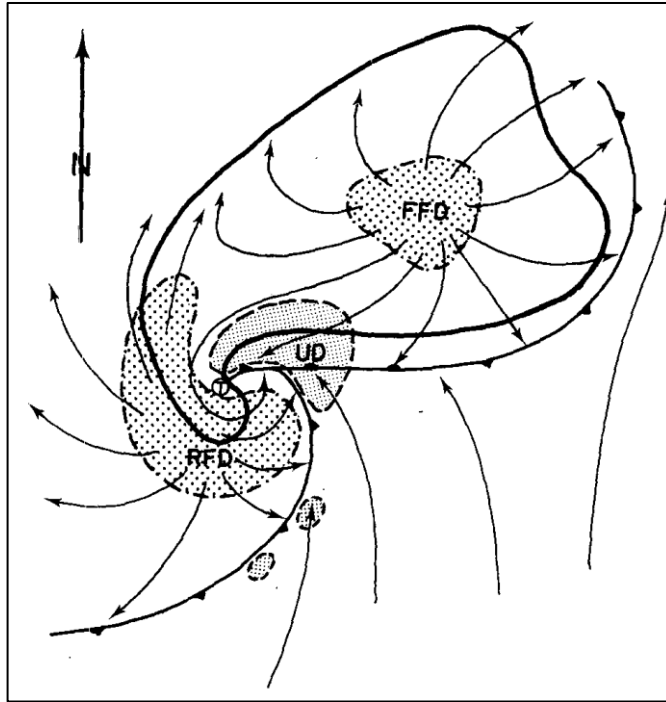


Figure 3: Conceptual model illustrating the storm-scale structure of a tornadic supercell by Lemon and Doswell (1979) (Their Fig. 7)

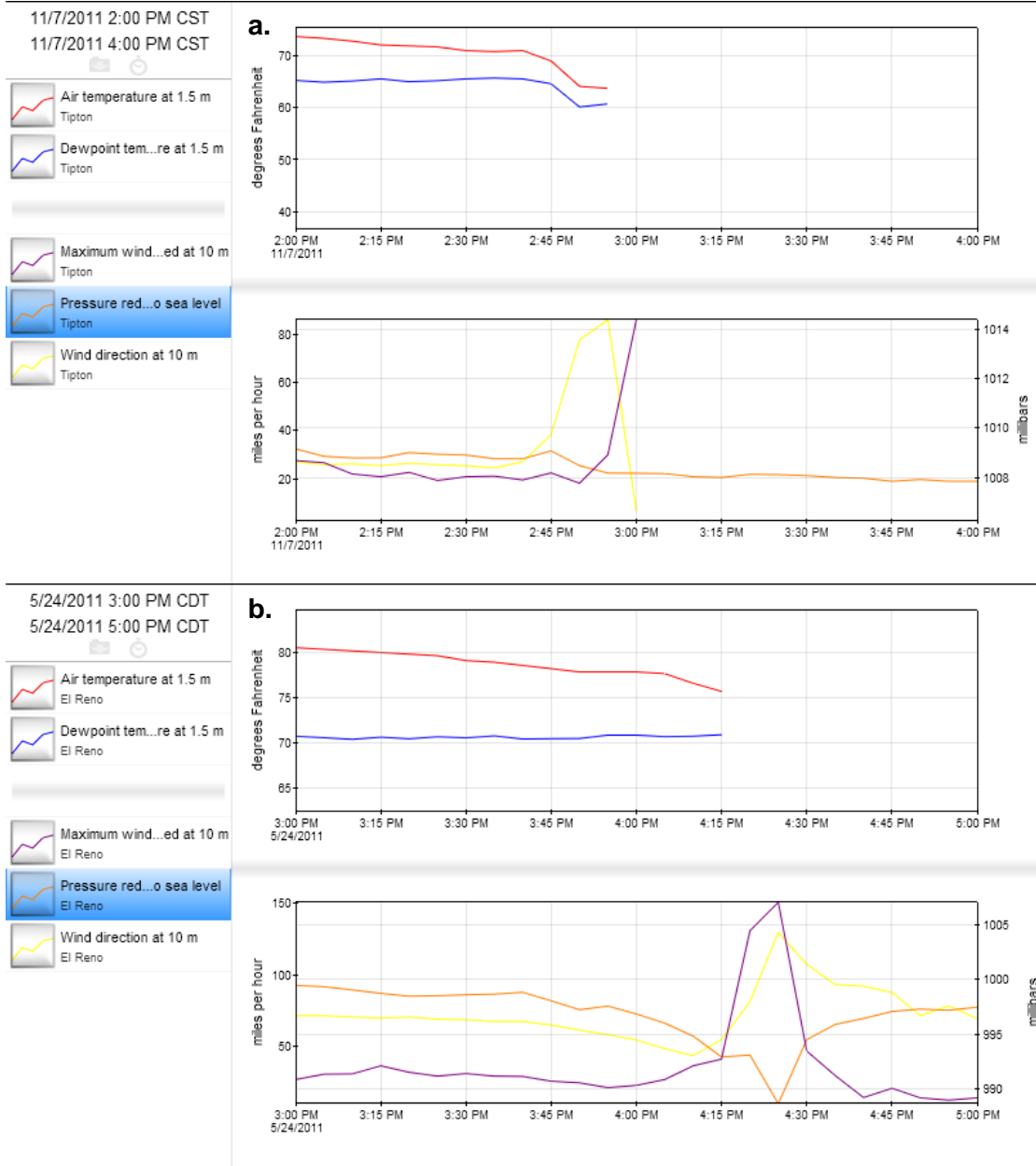


Figure 4: Mesonet observations of air temperature ( $^{\circ}\text{F}$ , red line), dewpoint ( $^{\circ}\text{F}$ , blue line), wind direction (yellow line, ordinate midline =  $180^{\circ}$ ), max wind gust (mph, purple line), and atmospheric pressure (mb, orange line) as tornadoes passed within close proximity to the instruments. A) Tipton, OK site 7 Nov 2011. B) El Reno, OK site 24 May 2011.

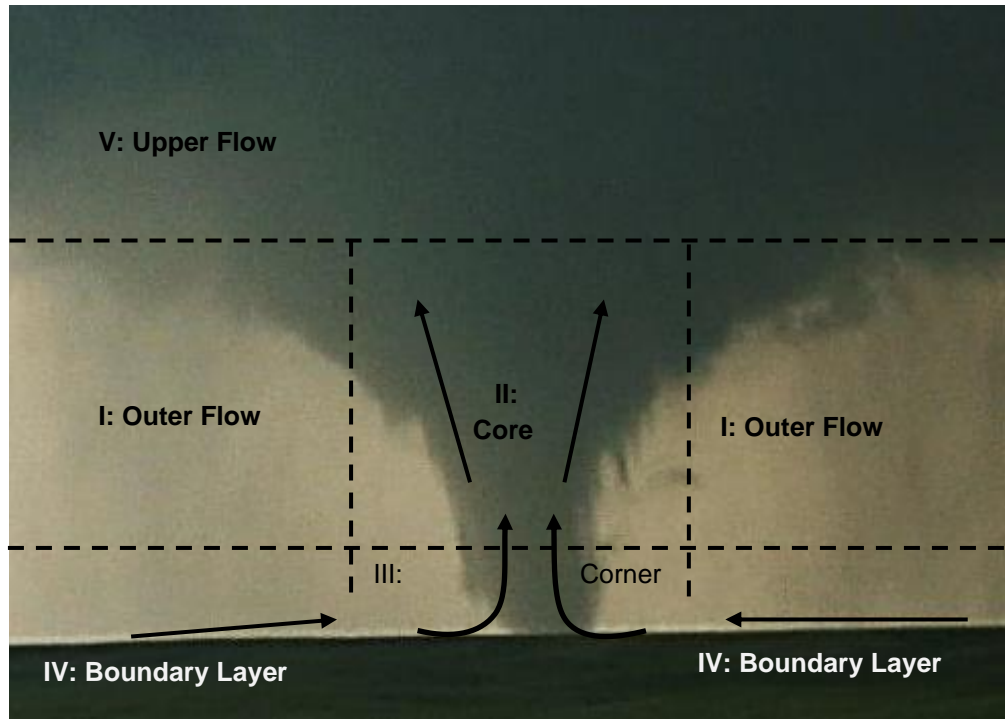


Figure 5: The five regions of tornado flow structure according to Lewellen (1976; 1993). (Photo © Jana Houser).



Figure 6: Stages of tornado development according to Davies-Jones (1986). (Photos courtesy of H. Bluestein.)

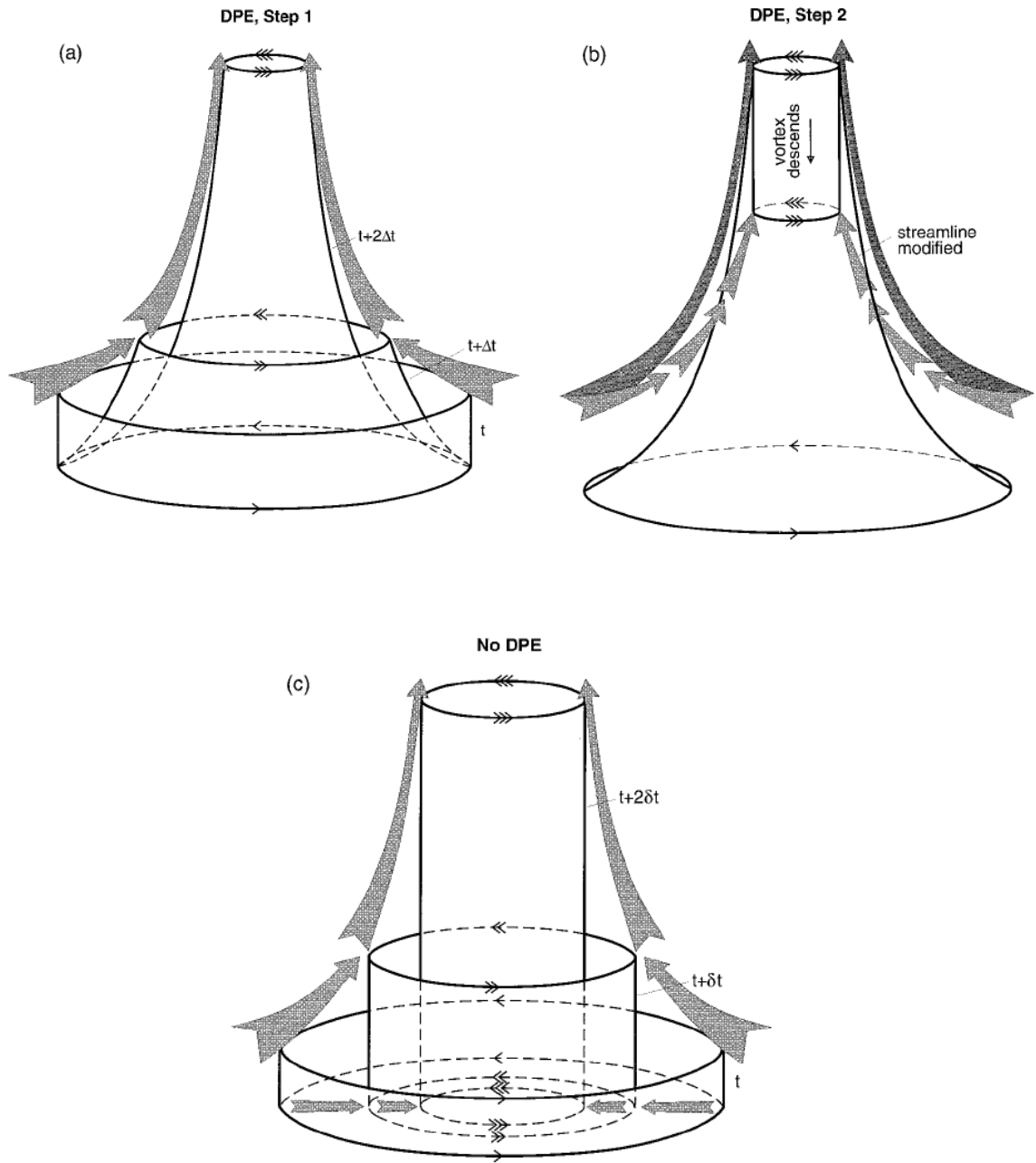


Figure 7: Illustration of tornadogenesis with (a and b) and without (c) the dynamic pipe effect. From Trapp and Davies-Jones (1997), their Fig. 14.



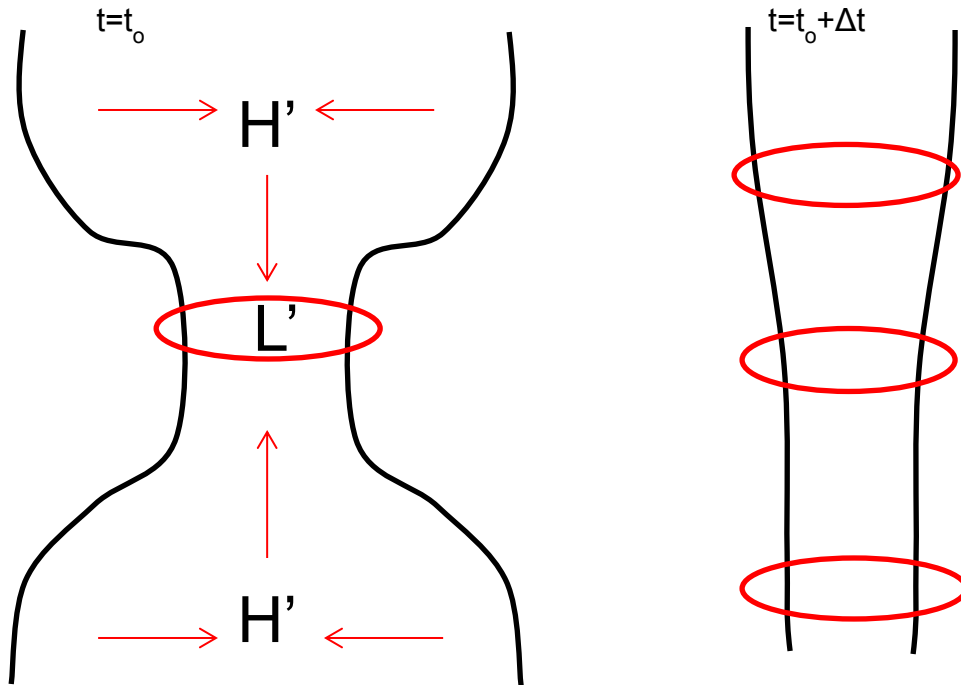


Figure 8: Illustration of the relative pressure perturbations and areas of convergence and vertical motion associated with the dynamic pipe effect. Left: configuration prior to the establishment of cyclostrophic balance. Right: configuration after some time, when cyclostrophic balance has been achieved and vertical perturbation pressure gradients have been equilibrated. Solid black lines approximate the extent of tornadic rotation. Red circles indicate cyclonic circulation.

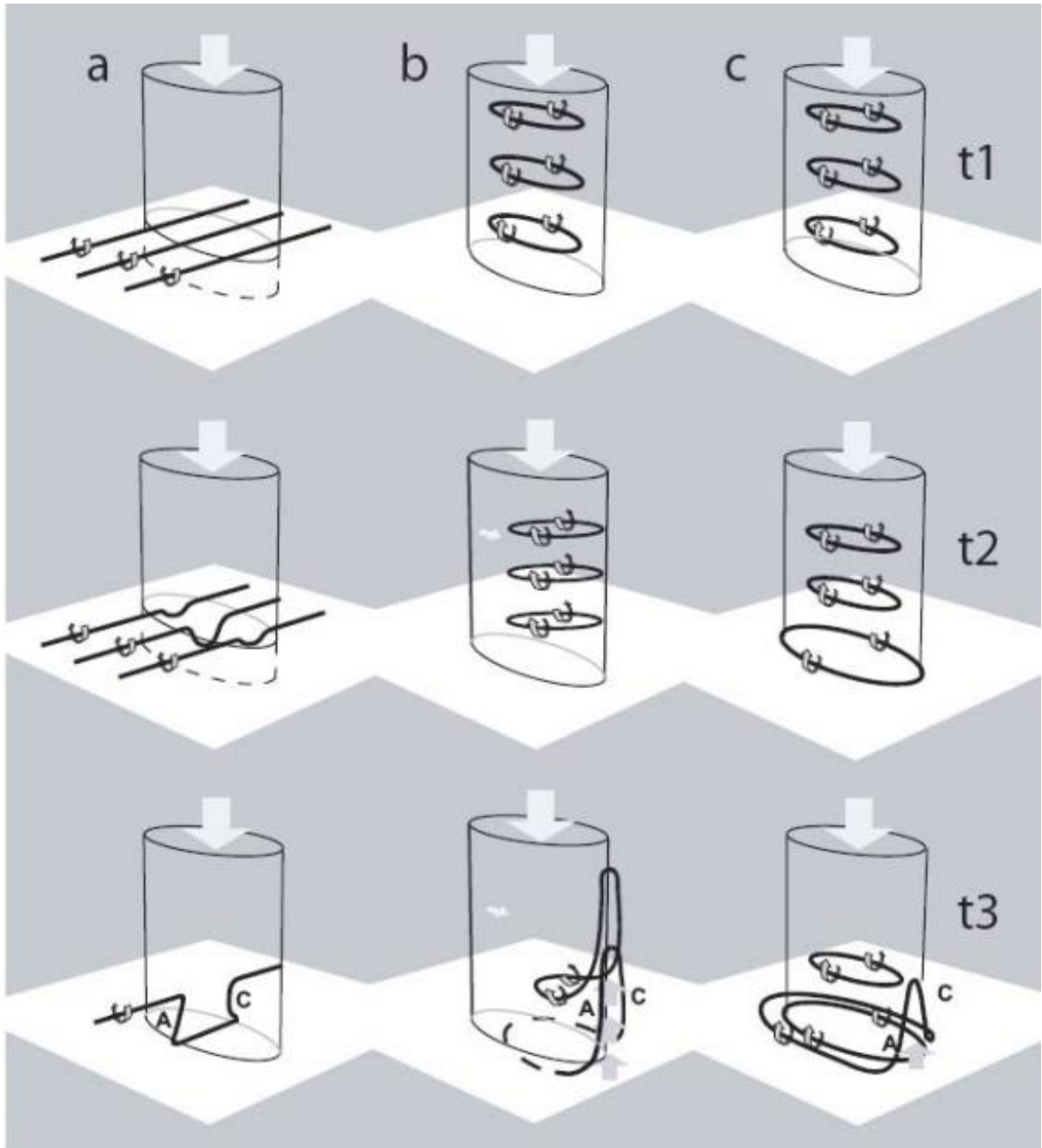


Figure 9: Graphical depiction of Walko's (1993) hypothesis illustrating tilting of vorticity near the surface by a downdraft. Solid bold lines are vortex lines. A (C) indicates anticyclonic (cyclonic) vertical vorticity. (From Straka et al. 2007, their Fig. 4.)

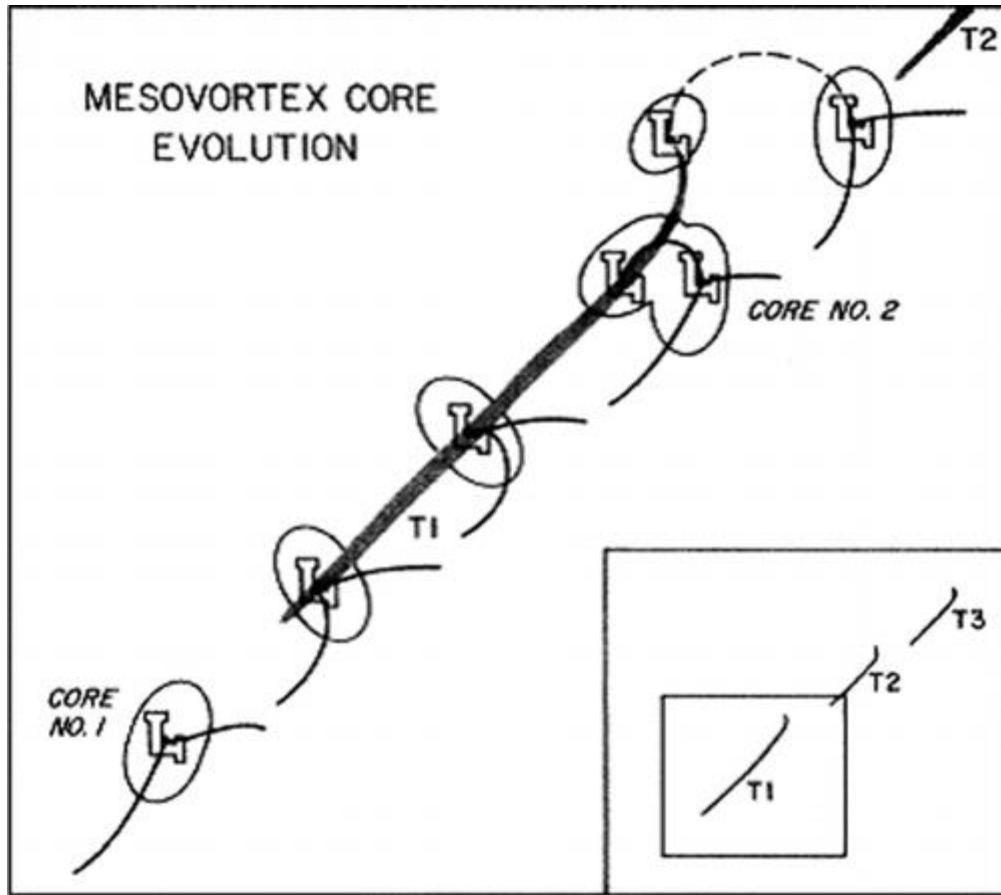


Figure 10: Representation of the cyclic mesocyclogenesis process according to the Burgess et al. (1982) conceptual model. Mesocyclones are indicated by the L. The thick black line represents the track of a tornado.

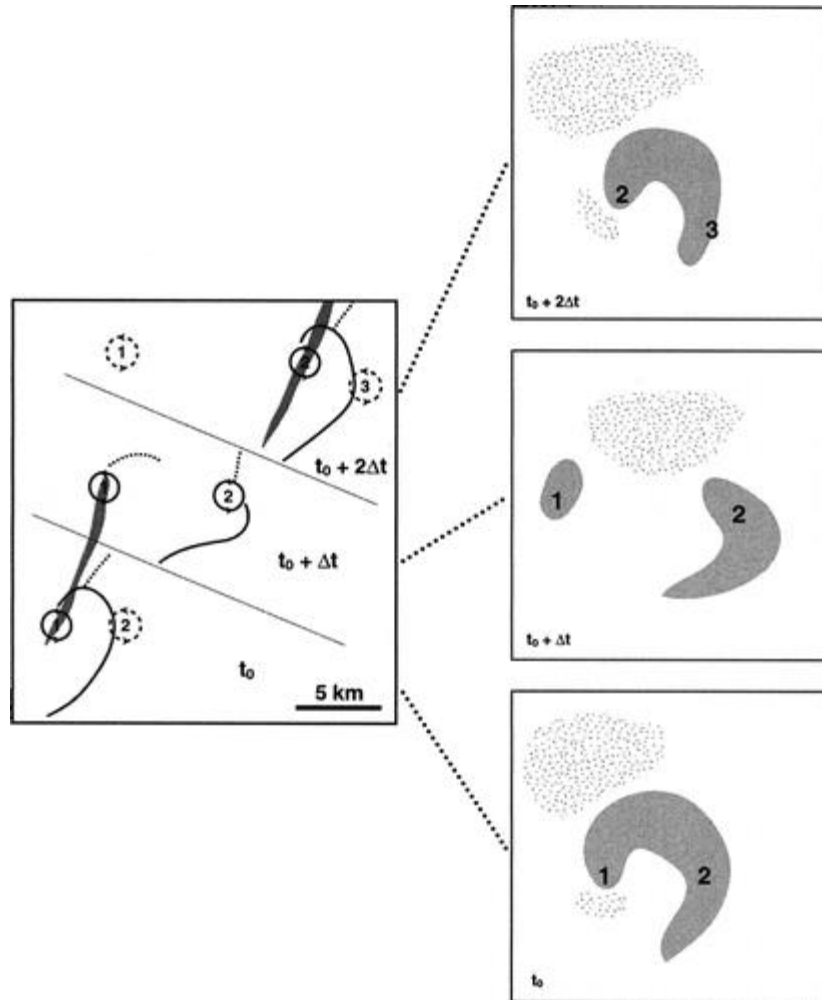


Figure 11: Conceptual model from Dowell and Bluestein (2002a) of the cyclic production of mesocyclones and tornadoes. Adapted from Burgess et al. 1982 but differing with the genesis location of the new mesocyclone along a bulge in the RFGF.

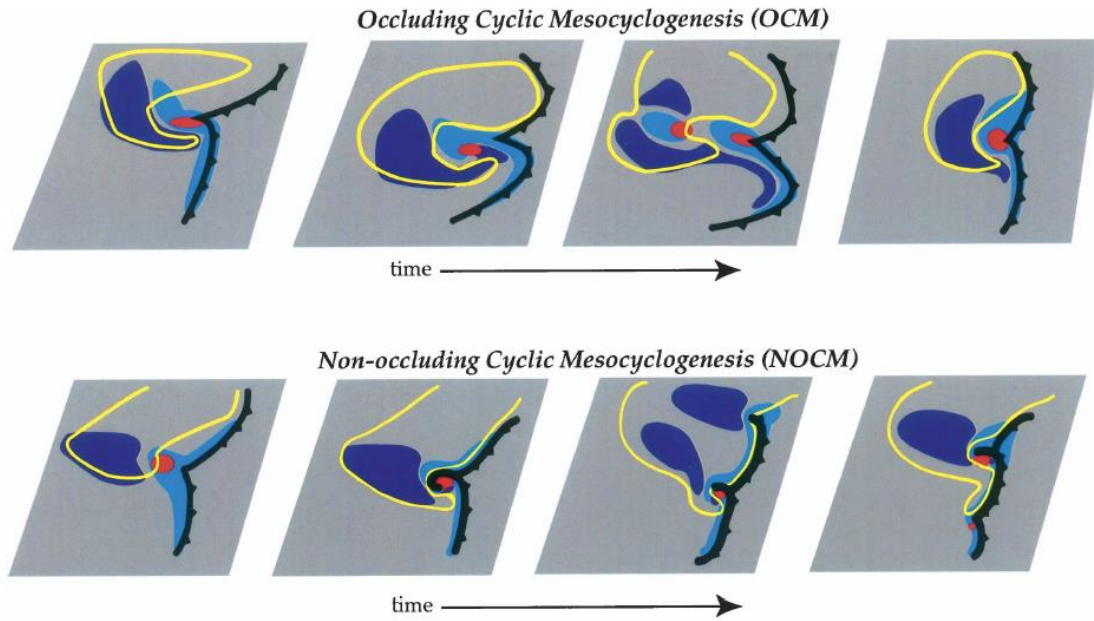


Figure 12: Schematic of the approximate surface patterns for occluding and nonoccluding cyclic mesocyclogenesis (Adlerman and Drogemeier's Fig. 3). Scalloped black line indicates the surface cold-pool boundary. Red indicates area of vorticity maxima. Light blue indicates updraft areas, and dark blue indicates downdraft areas. Single yellow contour indicates the boundary of the rain area.

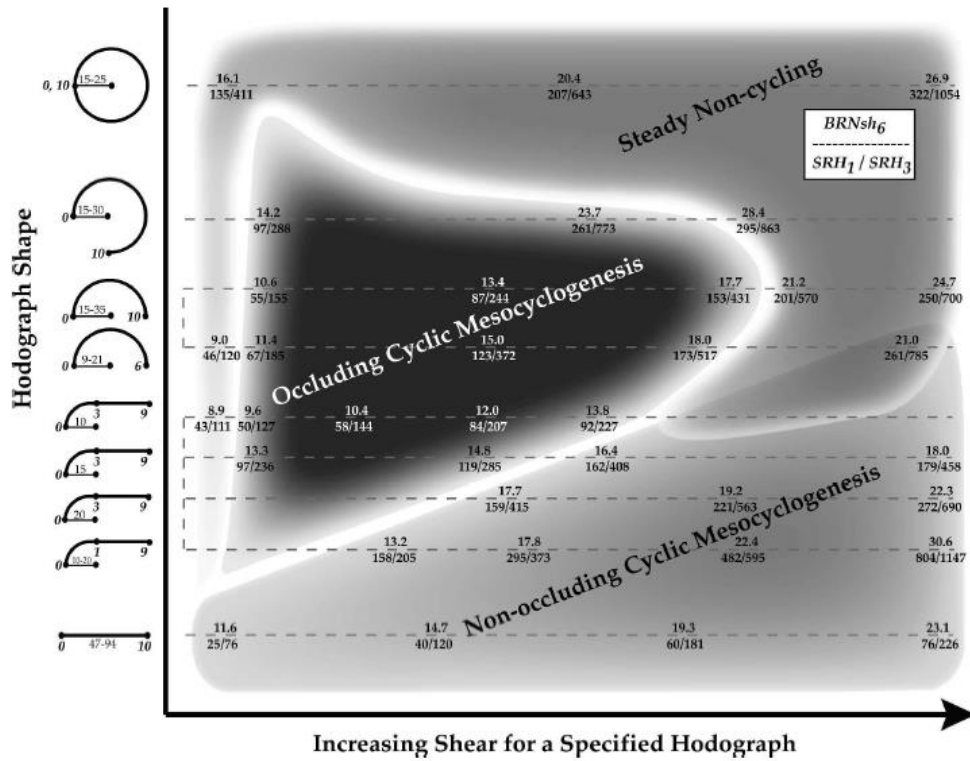


Figure 13: Summary of relationship between shear magnitude and hodograph shape to the cycling behavior of supercells. Hodographs on the left indicate heights (km) and radii of curvature. Numbers on the graphic indicate the 6 km BRN shear, the 0-1 km SRH, and the 0-3 km SRH.

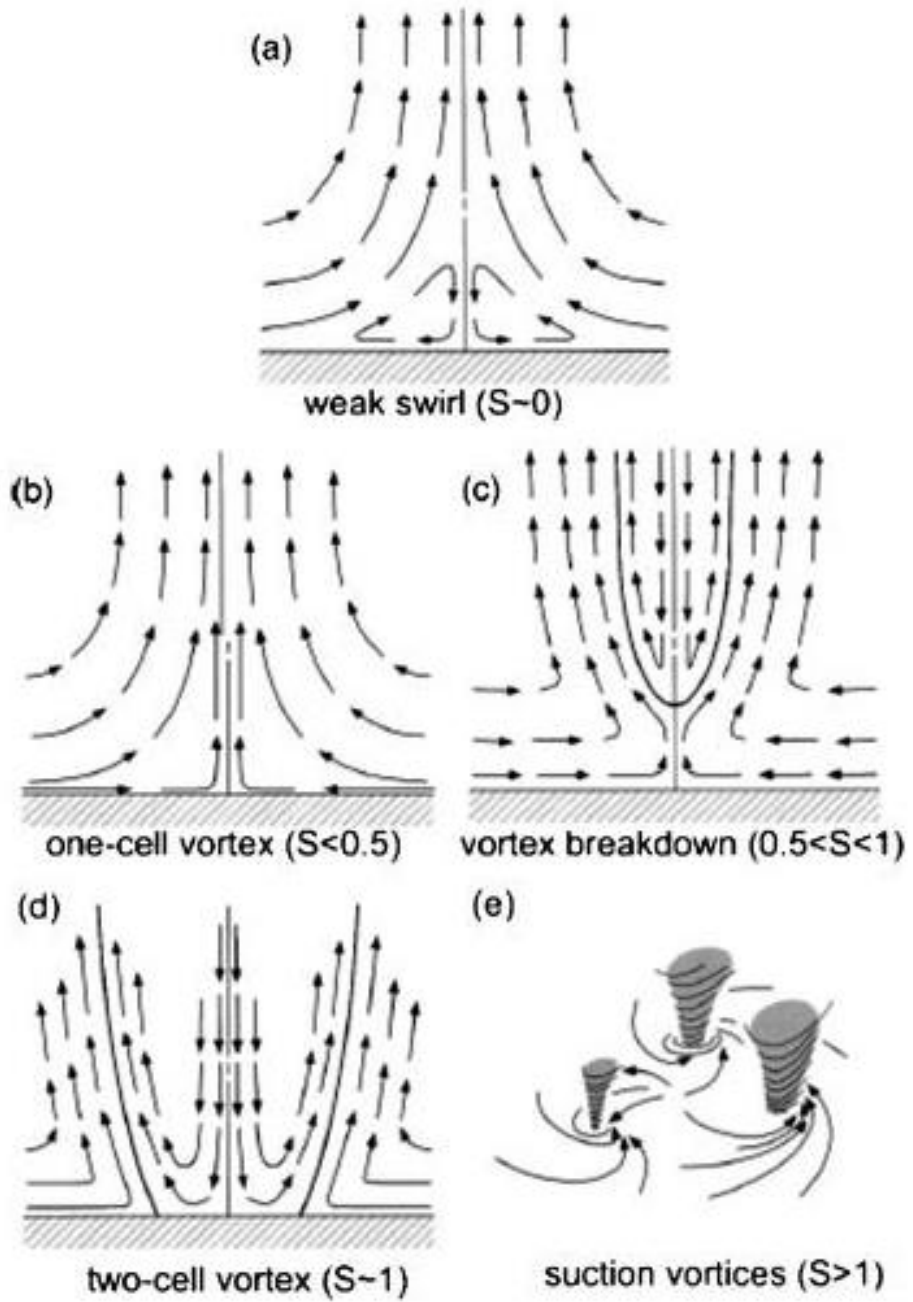


Figure 14: Illustration of flow around a vortex with increasing swirl ratio ( $S$ ). Adapted from Davies-Jones (1986).

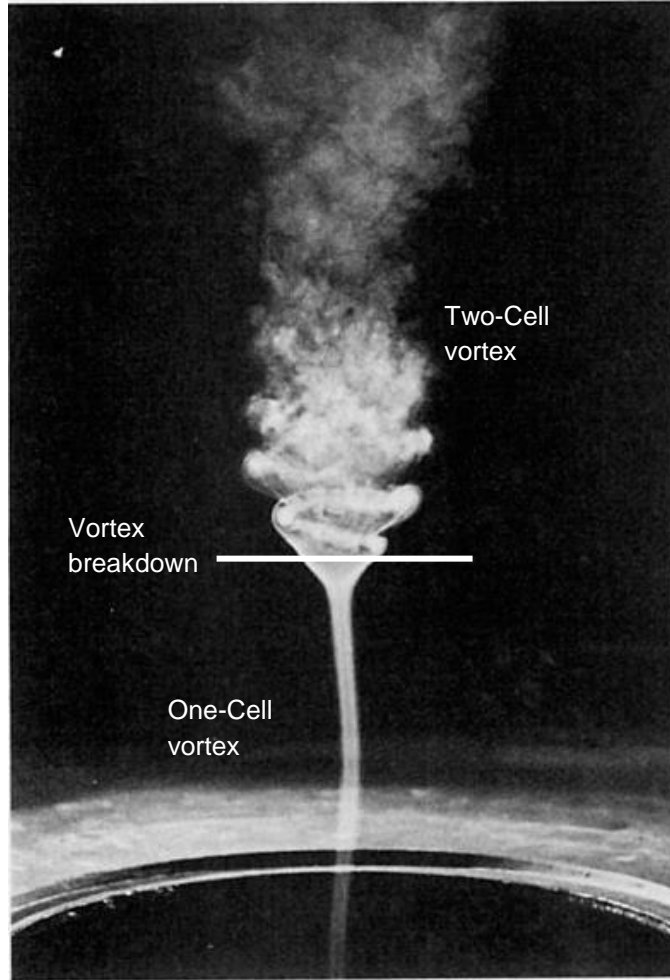


Figure 15: Laboratory simulation of vortex breakdown and the transition from a one-cell, laminar vortex, to a turbulent two-cell vortex.



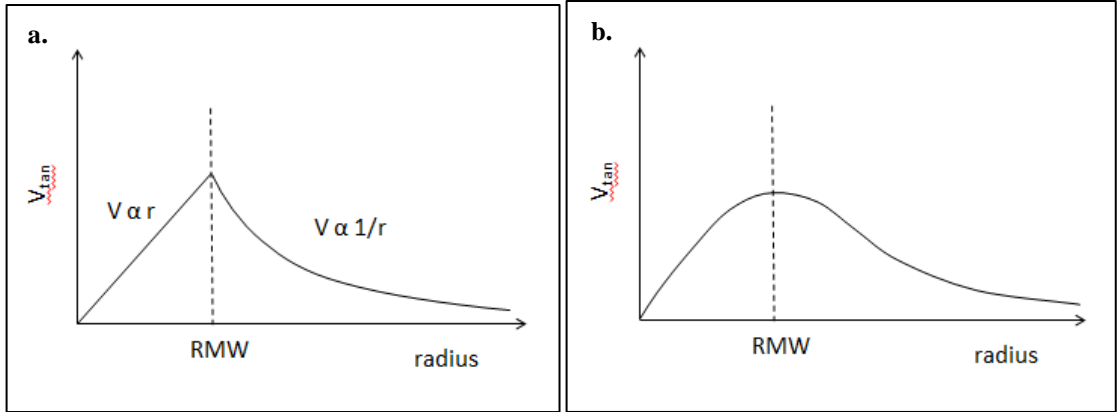


Figure 16: Generalized velocity profiles for: a. a Rankine vortex, b. a Burgers-Rott vortex.

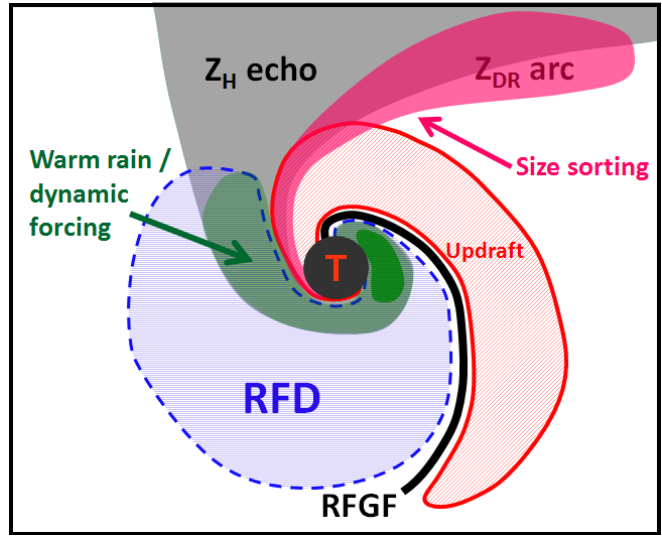


Figure 17: Conceptual model of microphysical and polarimetric signatures in supercells. (Kumjian 2011).



Figure 18: The rapid-scanning, X-band, polarimetric radar (RaXPOL) (Photo courtesy of J. Snyder.)

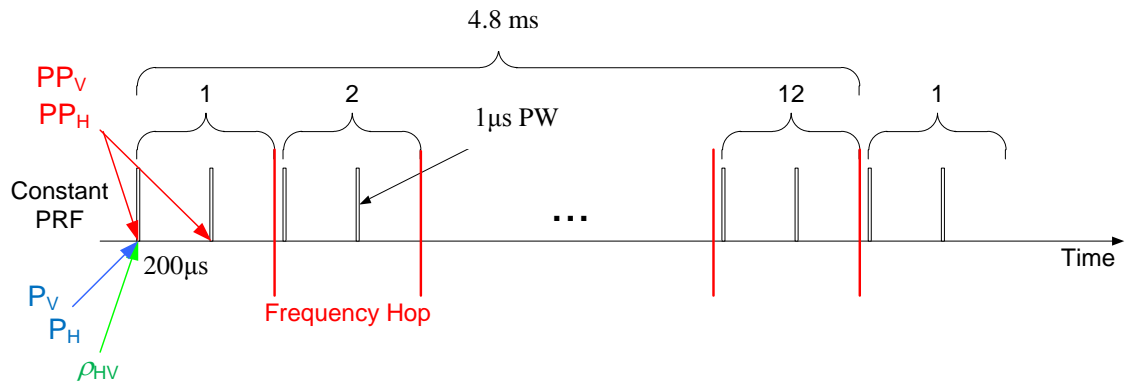


Figure 19: Illustration of the frequency hopping technique used by RaXPol to obtain independent samples faster than conventional radars. PP indicates pulse pair, P indicates return power for the first pulse in the pair. The subscript H (V) denotes horizontal (vertical) polarization. (Pazmany et al. 2013).

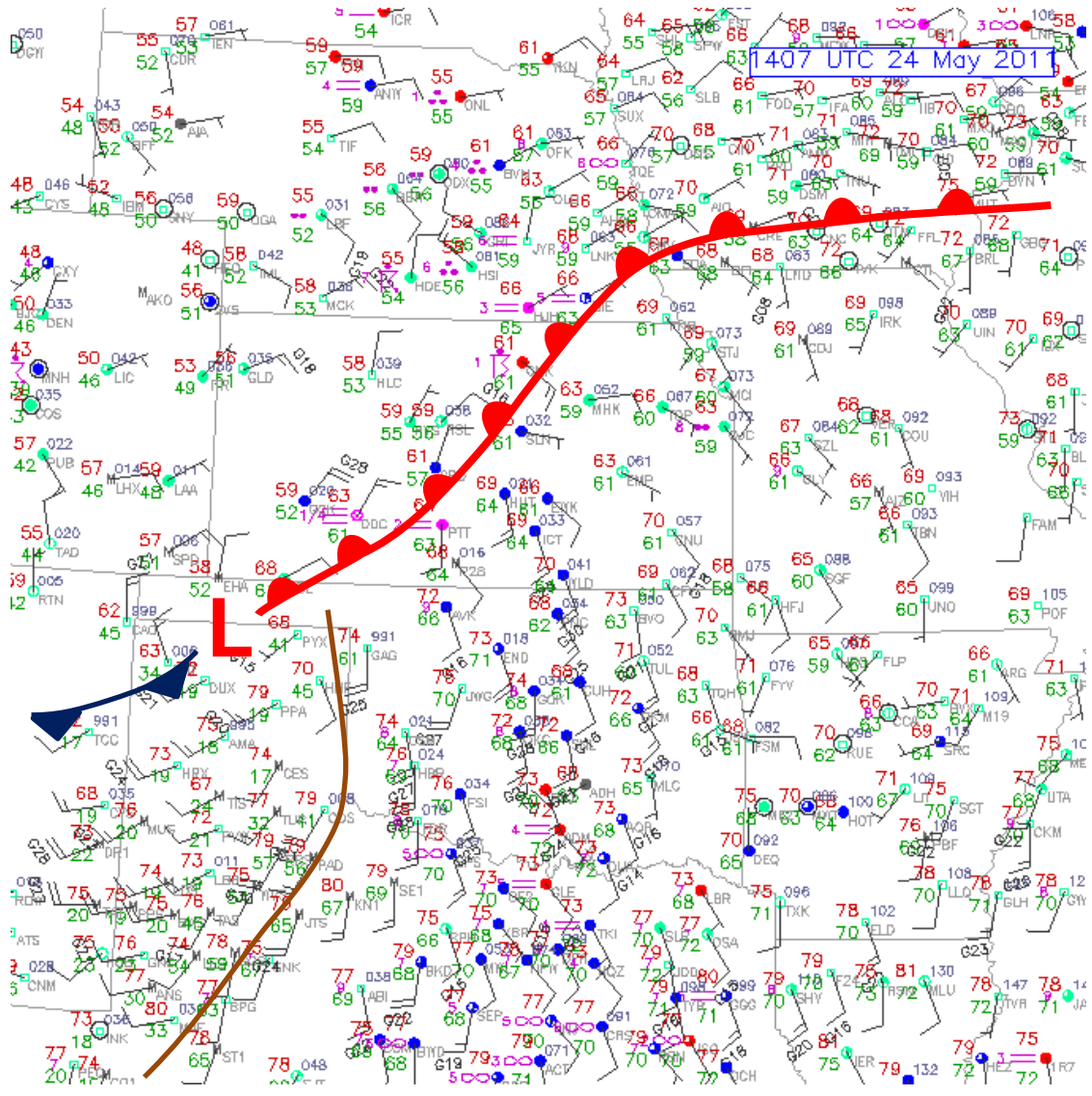
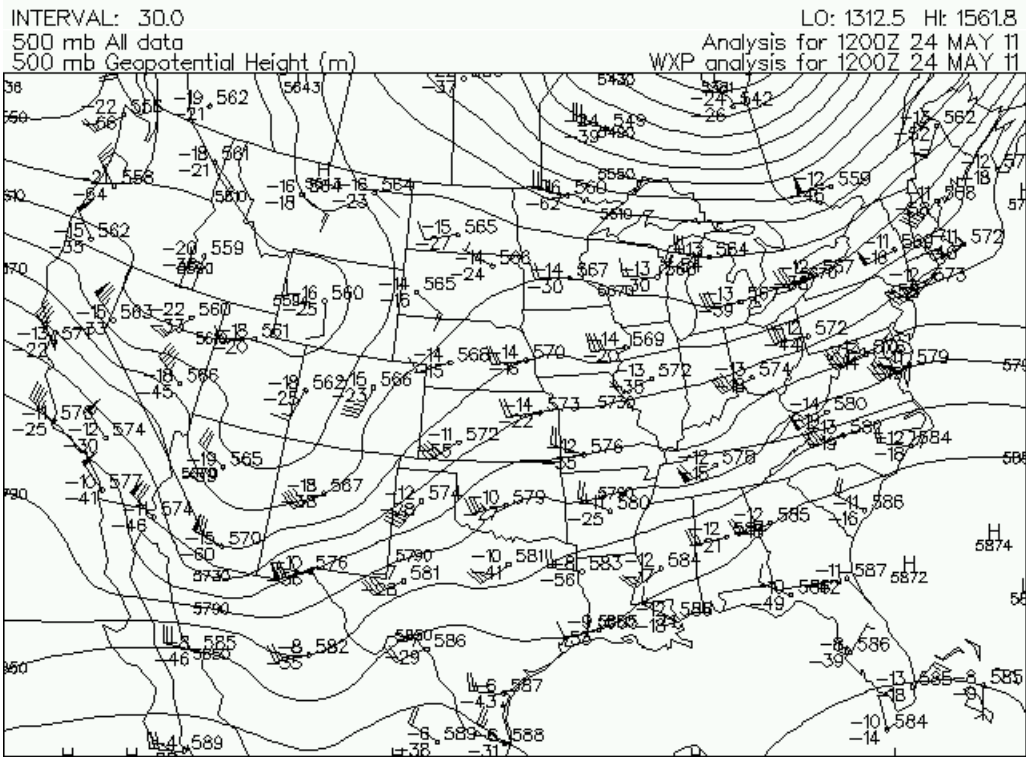
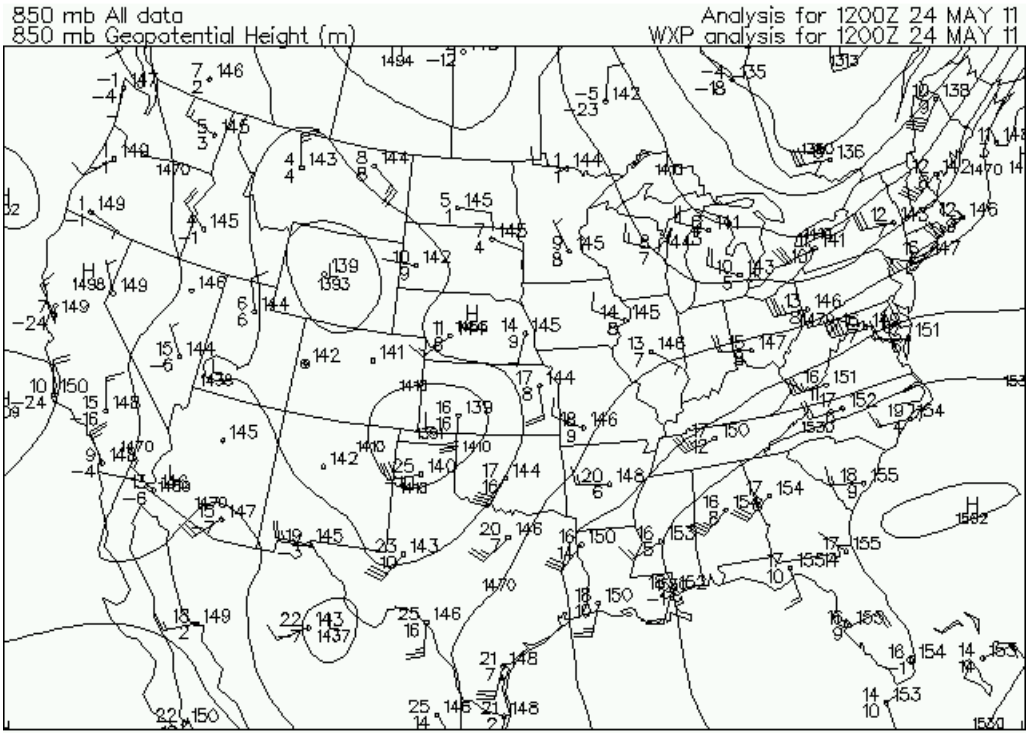


Figure 20: Surface observations (T and T<sub>d</sub> in °F, winds in mph) and analyzed surface features valid 1400 24 May 2011. Brown line indicates dryline position.



INTERVAL: 30.0

LO: 5380.5 Ht: 5894.4

Figure 21: Upper air observations and geopotential height (dam, contoured) for 1200 24 May: 850 mb (top) 500 mb (bottom). Temperatures and dewpoints in °C.

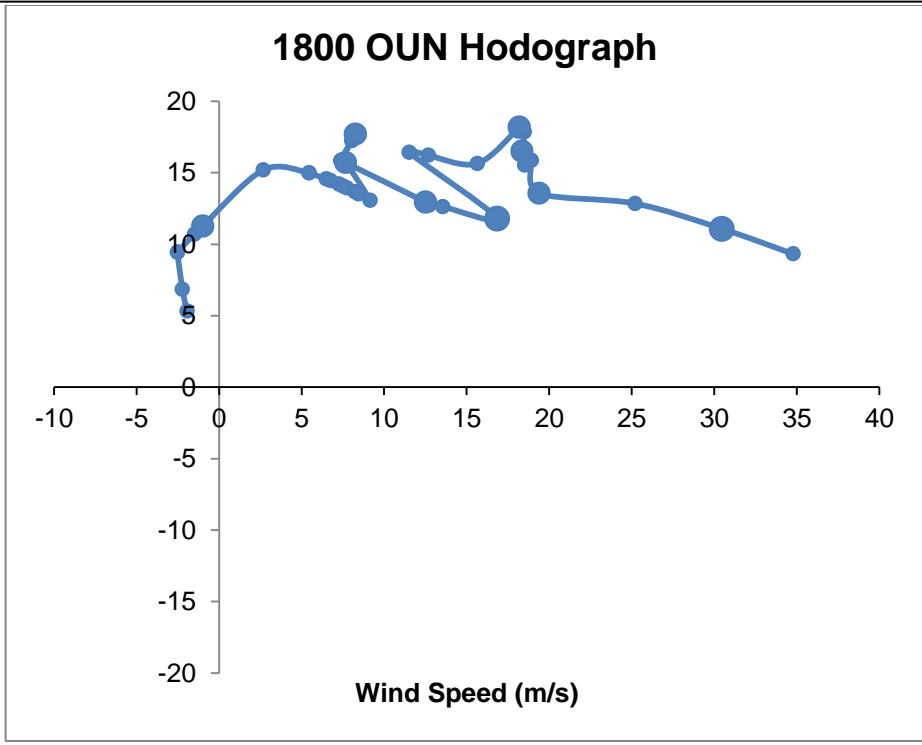
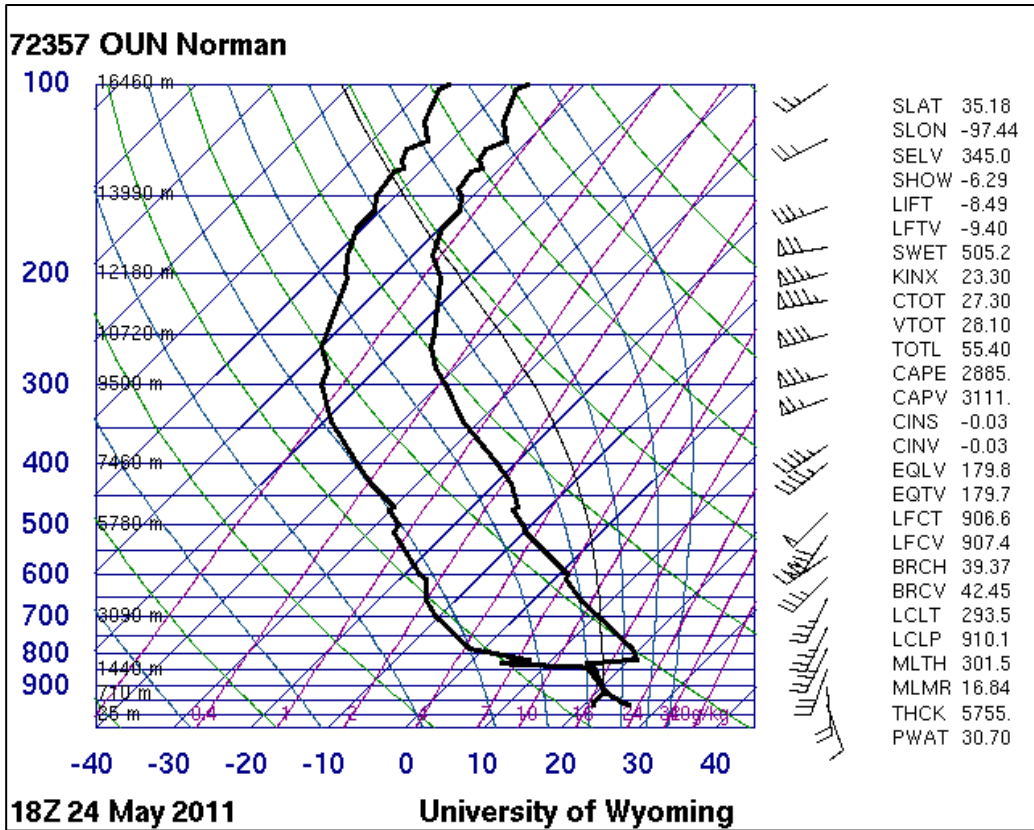


Figure 22: 1800 UTC OUN rawinsonde. Top: Skew-T, bottom: hodograph.



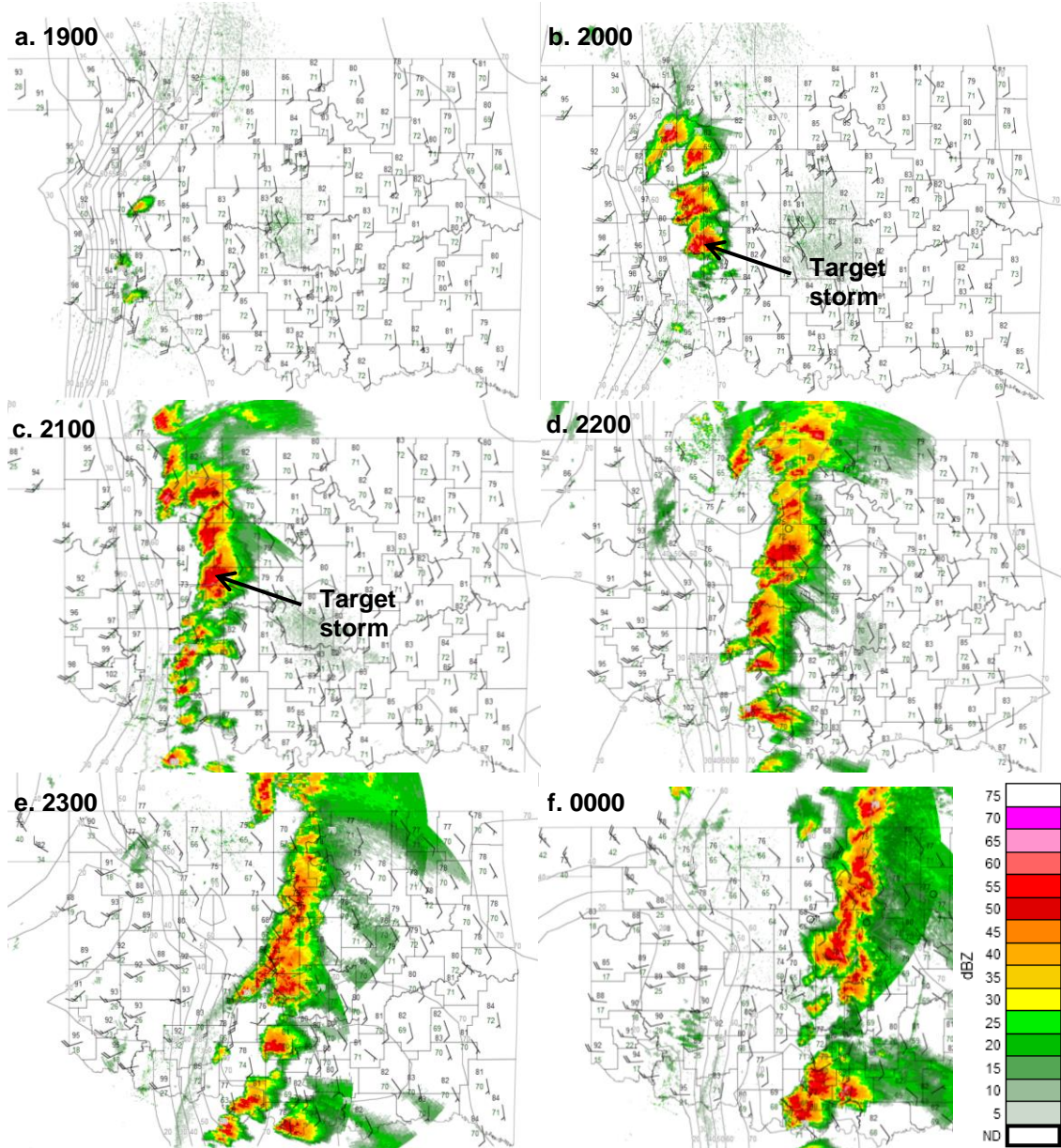


Figure 23: Hourly WSR-88D reflectivity imagery from 1900 24 May – 0000 25 May plotted with Oklahoma Mesonet data (2 m wind barbs, air temperature (black, °F), Dew point temperature (green, °F), and dew point isodrosotherms (gray).



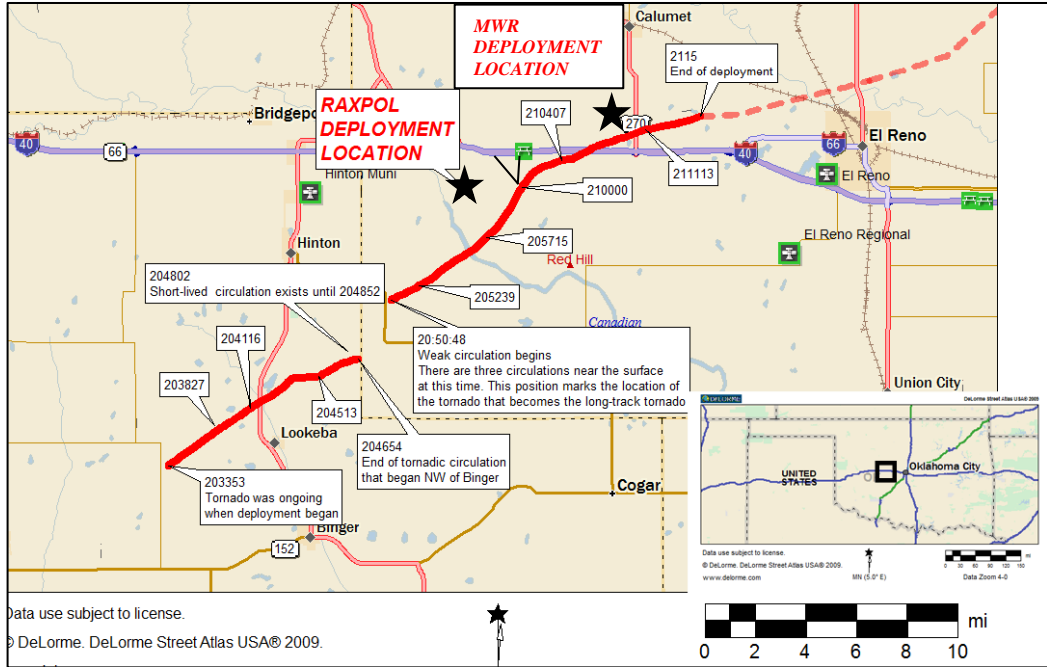


Figure 24: Tornado tracks and locations of the RaXPol and MWR-05XP (black stars). Courtesy J. Snyder.

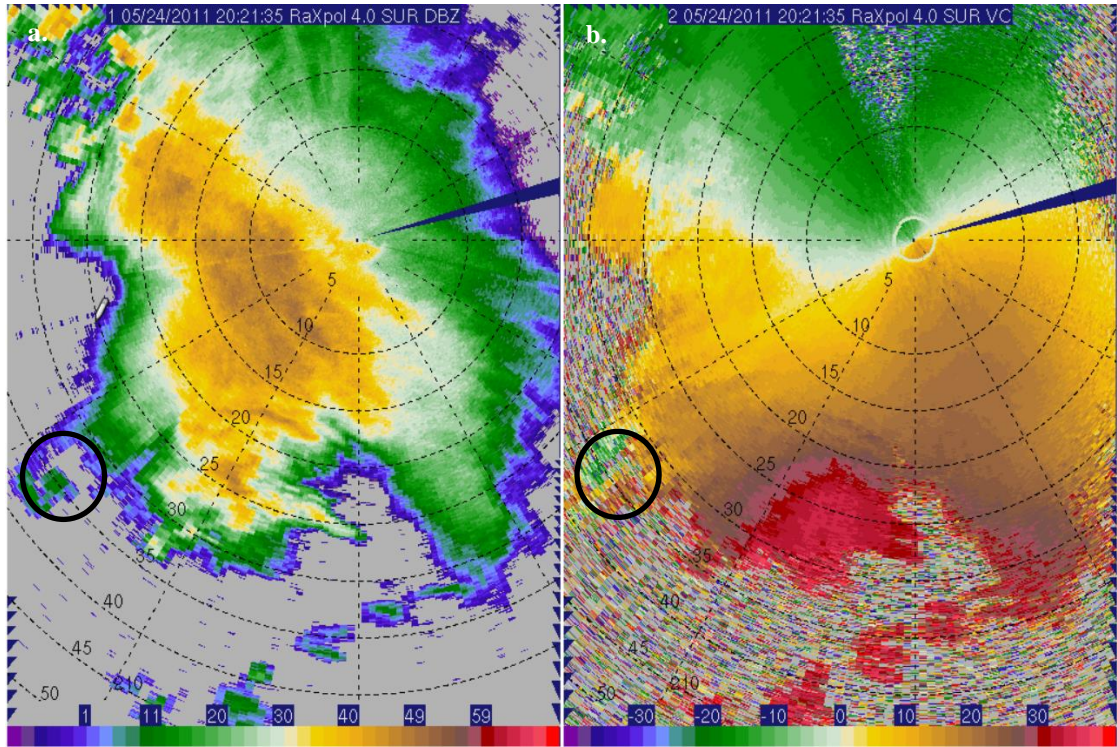


Figure 25: a) RaXPol equivalent reflectivity factor ( $\text{dBZ}_e$ ) and b) radial velocity ( $\text{m s}^{-1}$ )<sup>11</sup> data from the early non-rapid scan data collection mode for an elevation angle of  $4^\circ$  at 202135 24 May 2011. The area of interest is circled. Range rings are denoted in km.

<sup>11</sup> Hereafter, all equivalent reflectivity factor references will be referred to simply as ‘reflectivity’. Reflectivity always has units  $\text{dBZ}_e$  and radial velocity always has units of  $\text{m s}^{-1}$  unless otherwise noted.



Figure 26: Visual observations of the developing tornado taken from the RaXPoI deployment location (© J. Houser).

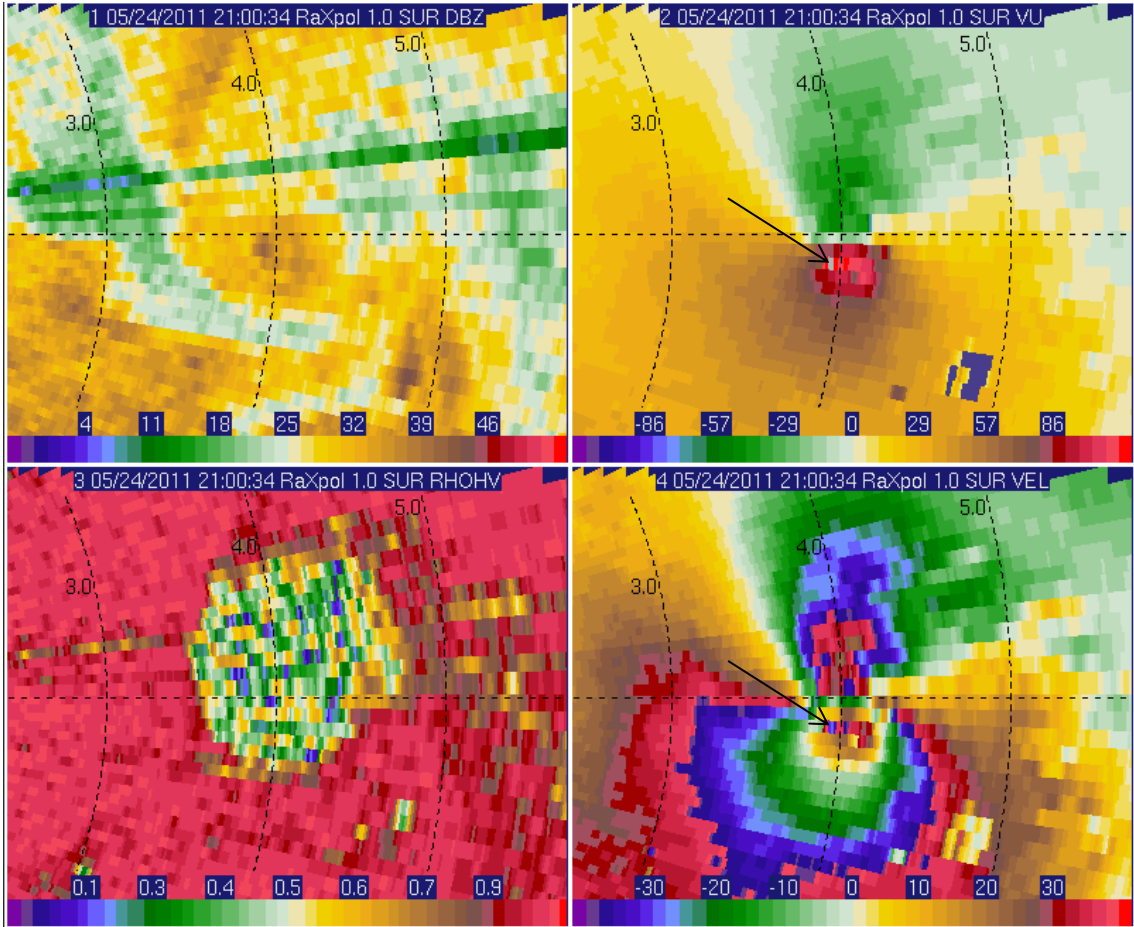


Figure 27: Time of maximum observed radial velocity ( $124.84 \text{ m s}^{-1}$ ) of the deployment. Reflectivity (upper left); unfolded radial velocity (upper right), color bar is from  $\pm 120 \text{ m s}^{-1}$ ; cross correlation coefficient (lower left); and folded radial velocity (lower right), color bar is from  $\pm 42 \text{ m s}^{-1}$ ,  $V_{\text{nyq}} = 38.5 \text{ m s}^{-1}$ . Black arrow points to the pixel of  $124.84 \text{ m s}^{-1}$ .

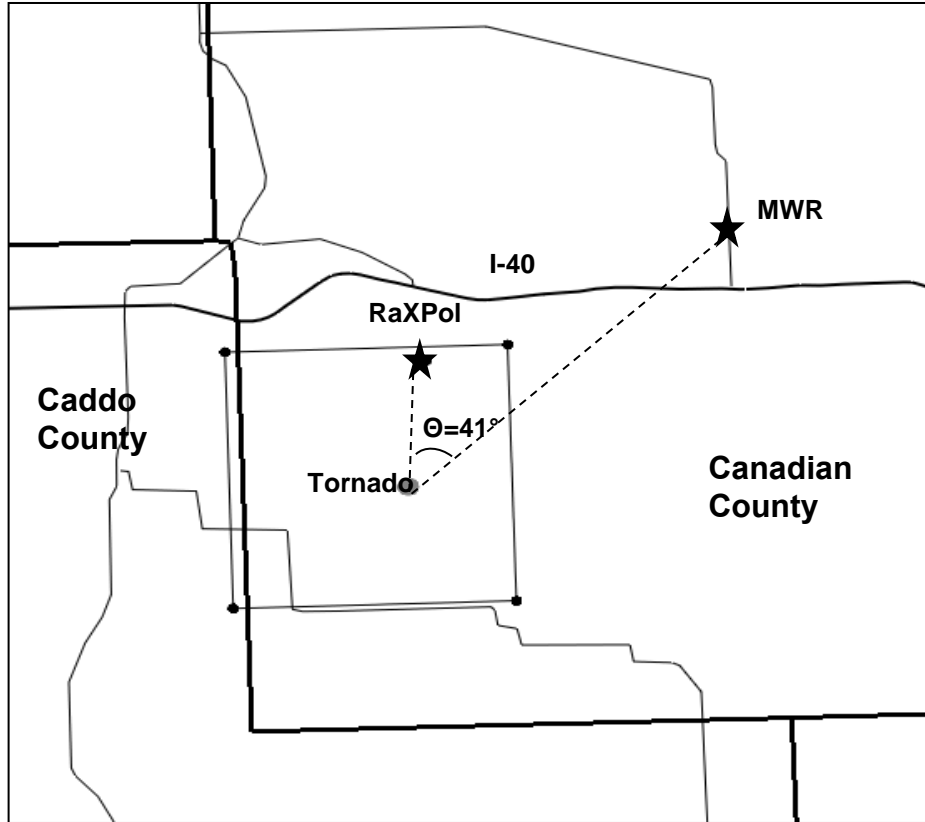


Figure 28: Dual-Doppler grid domain and locations of MWR-05XP and RaXPol for the 205448 analysis.

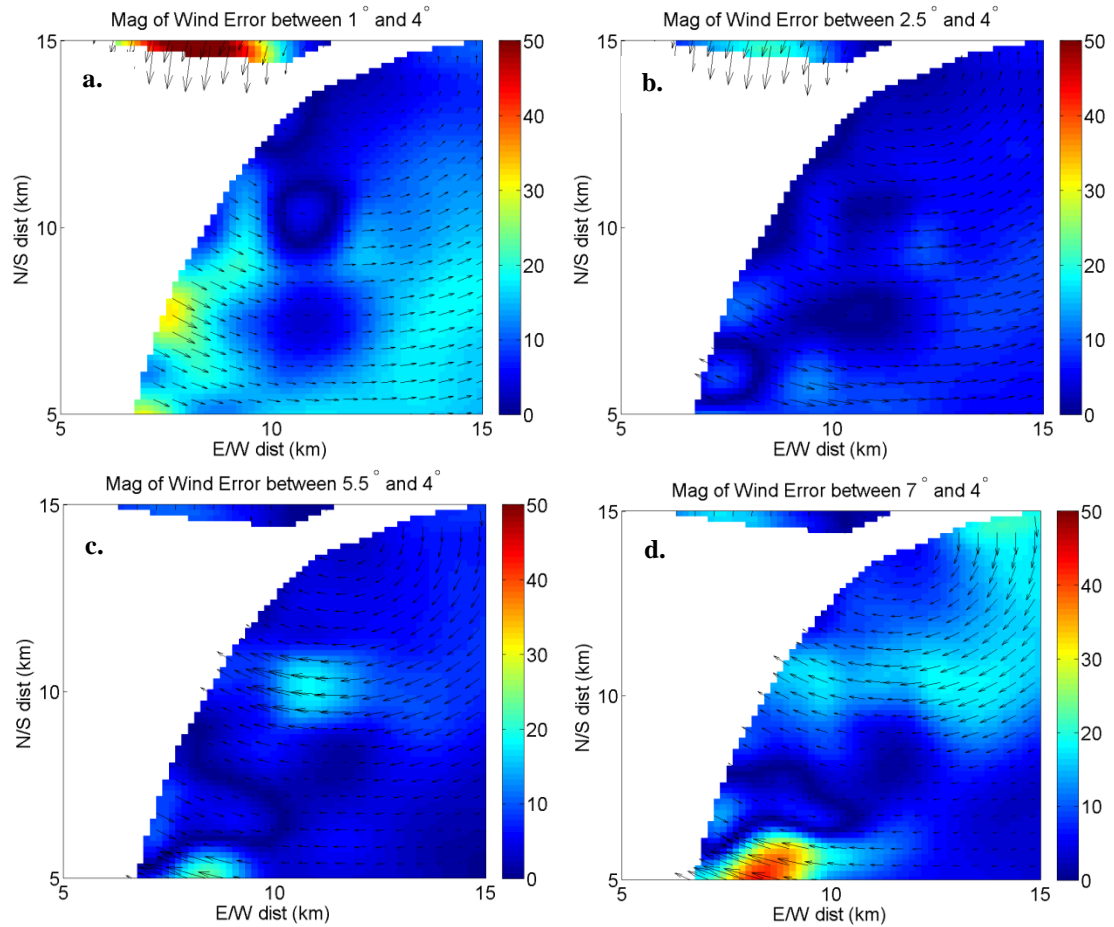


Figure 29: The magnitude ( $\text{m s}^{-1}$ ) and direction (vectors) of the errors between the synthesized horizontal wind fields at  $4^\circ$  (the reference angle which, according to the uncorrected raw data, most closely matched the height of the RaXPOL data) and the syntheses using the MWR-05XP a)  $1^\circ$ , b)  $2.5^\circ$ , c)  $5.5^\circ$ , d)  $7^\circ$  elevation angles. All images were from the 205448 volume and valid at an analysis height of 1 km ARL.



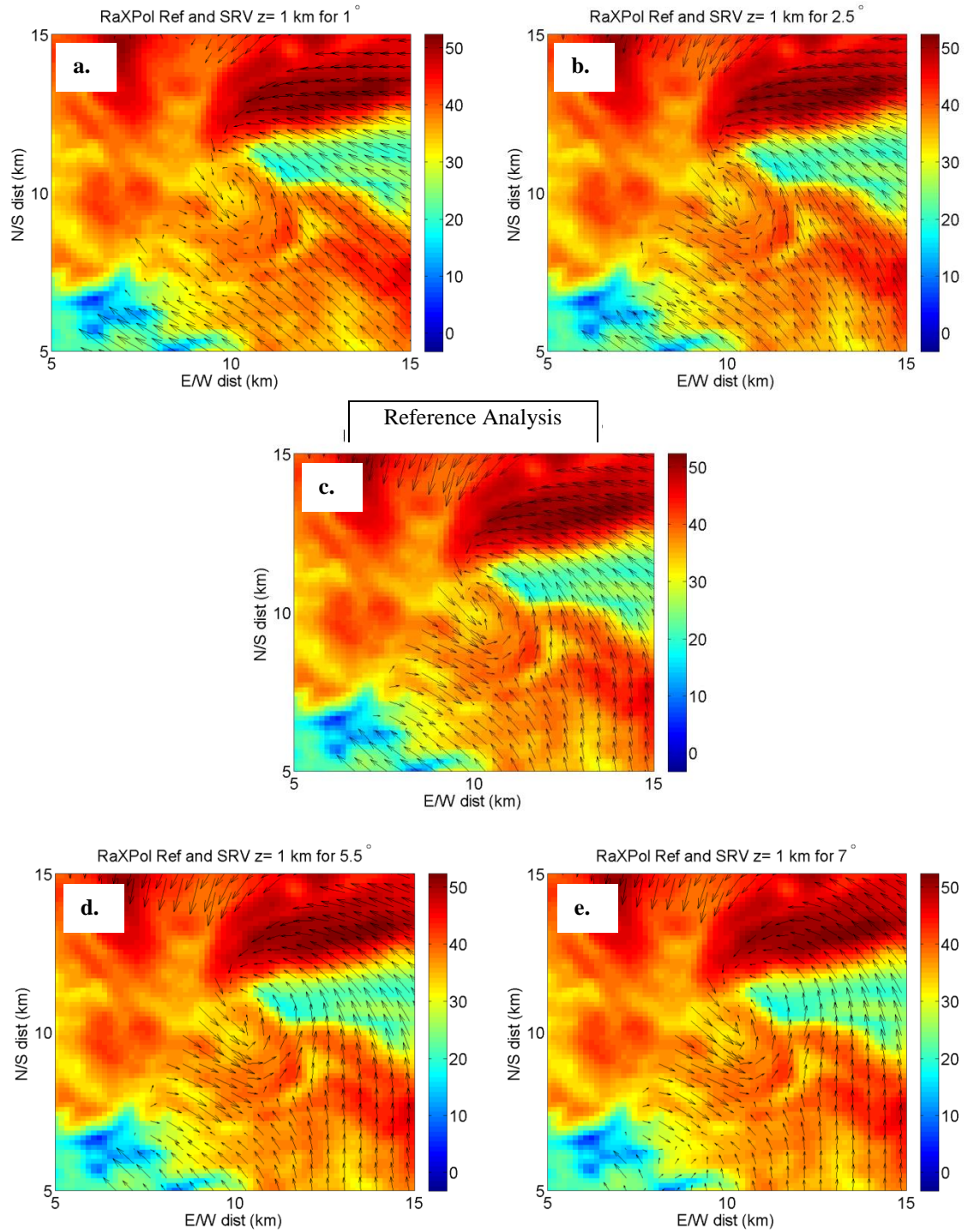


Figure 30: RaXPol reflectivity (dBZ) and horizontal wind vectors from dual-Doppler analyses at  $z=1$  km for the RaXPol - MWR-05XP tilt and roll sensitivity tests valid at 205448. RaXPol data are from the  $12^\circ$  elevation angle, with a beam height of 1 km at the tornado, corresponding with the height of the MWR-05 beam at  $4^\circ$ . The effects of pitch and roll angles of  $1.5^\circ$  and  $3^\circ$  are simulated by using the MWR-05XP a)  $1^\circ$  elevation angle, b)  $2.5^\circ$  elevation angle, c)  $4^\circ$  elevation angle ('truth' if the radar were assumed to be leveled), d)  $5.5^\circ$  elevation angle 3)  $7^\circ$  elevation angle.

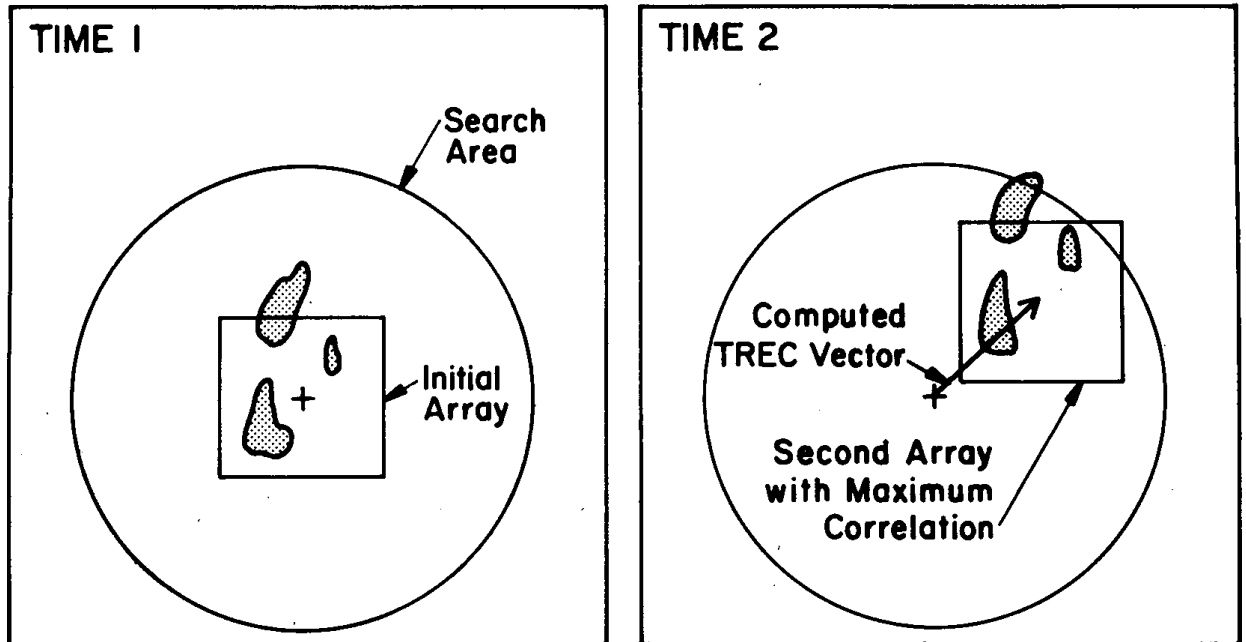


Figure 31: Schematic illustrating the TREC technique correlating reflectivity features at two different times and calculating a motion vector. (From Tuttle and Foote (1990), their Fig. 1.)



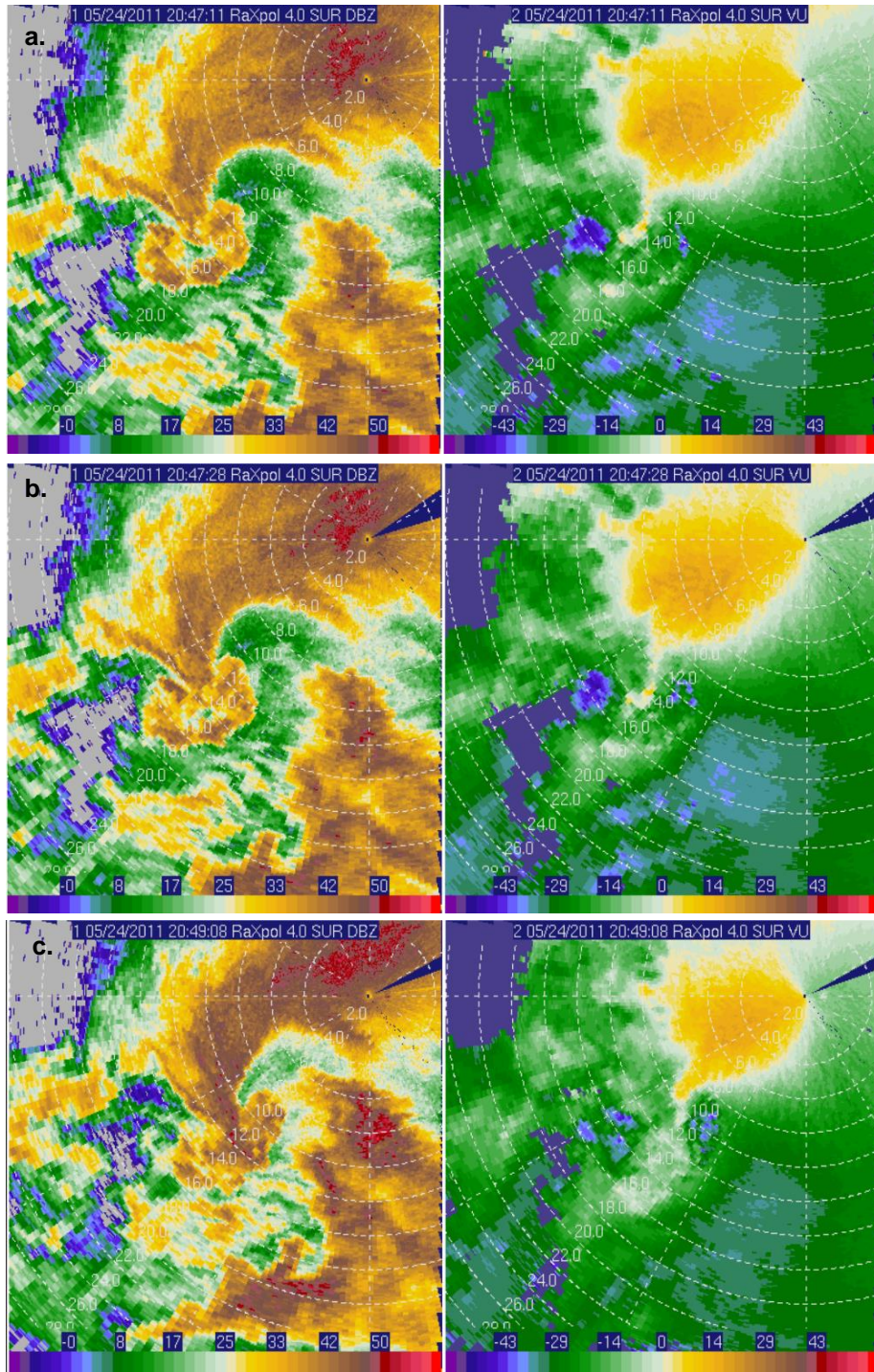


Figure 32: Comparisons of reflectivity in the left hand panel and radial velocity in the right hand panel when the time difference between scans is 17 seconds (a vs. b), and ~ 2 minutes (a vs. c).

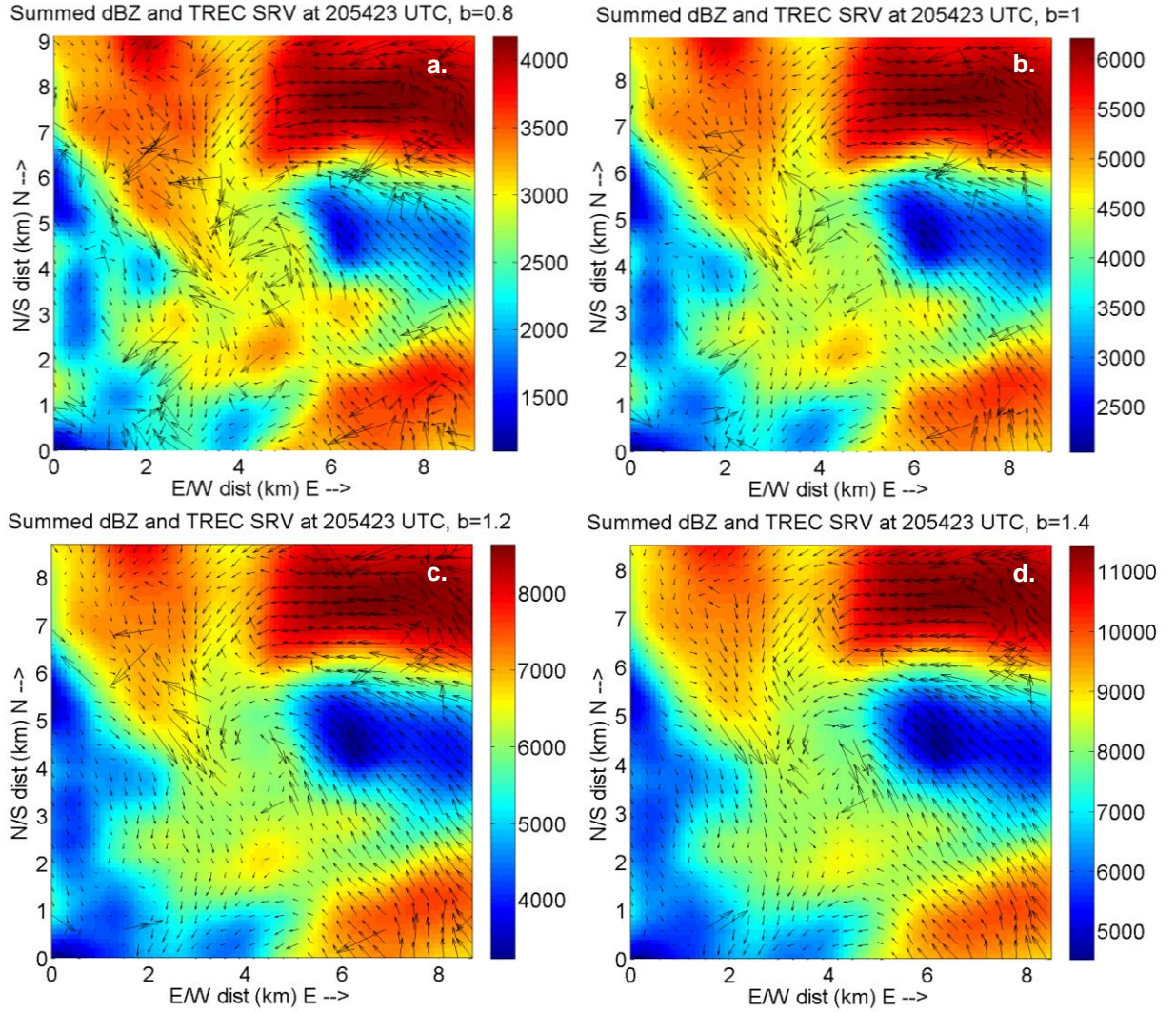


Figure 33: Comparison of box sizes for the 100m grid resolution TREC analysis at 2054: a. b=8 grid points, b. b=10 grid points, c. b=12 grid points, and d. b=14 grid points.



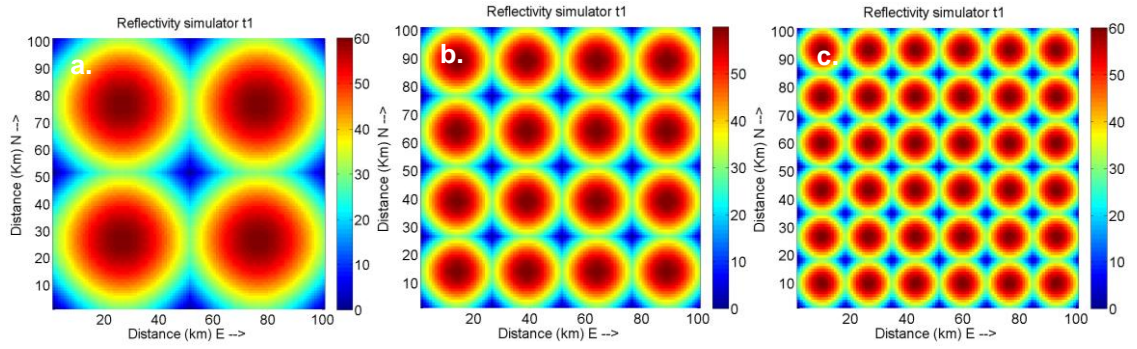


Figure 34: Simulated reflectivity fields for  $f =$  a) 0.1 (1 wave), b) 0.2 (2 waves), and c) 0.3 (3 waves).

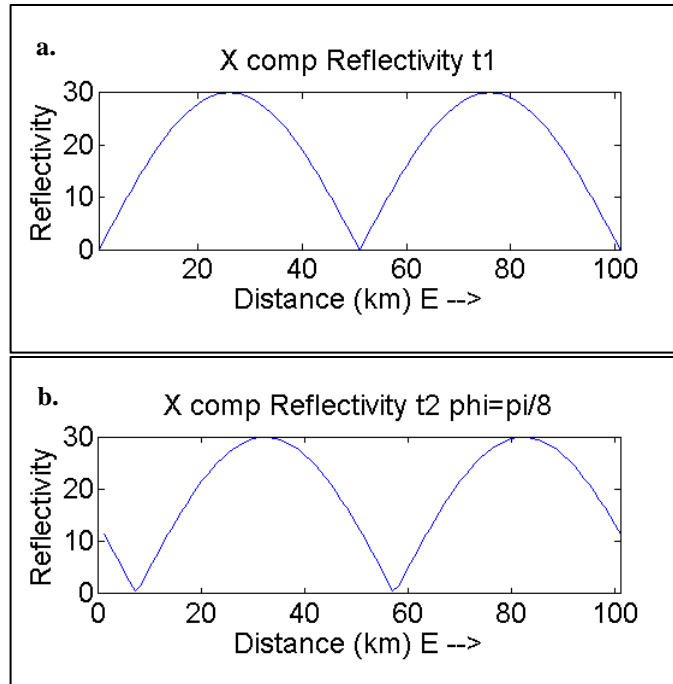


Figure 35: Sine waves used to simulate reflectivity at an initial time (a) and some arbitrary later time where the pattern is shifted by a phase of  $\pi/8$  (b).

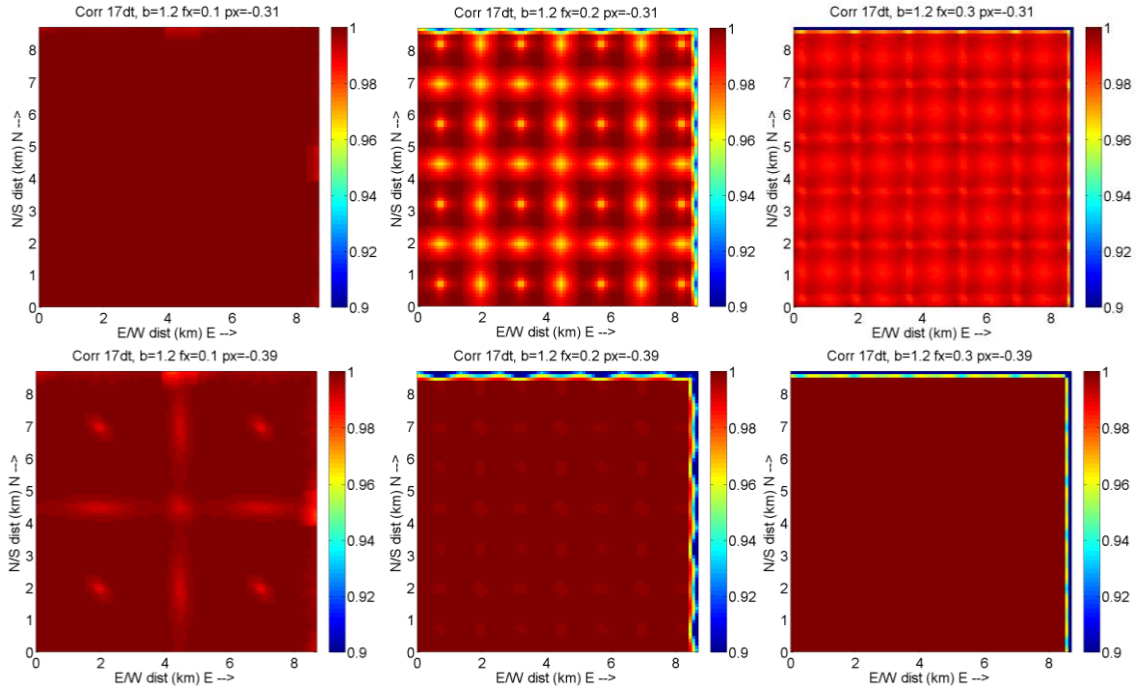


Figure 36: TREC correlation coefficient values for  $dt=17s$  for each of the three pseudo reflectivity patterns. Top row:  $\phi=\pi/10$ , bottom row:  $\phi=\pi/8$

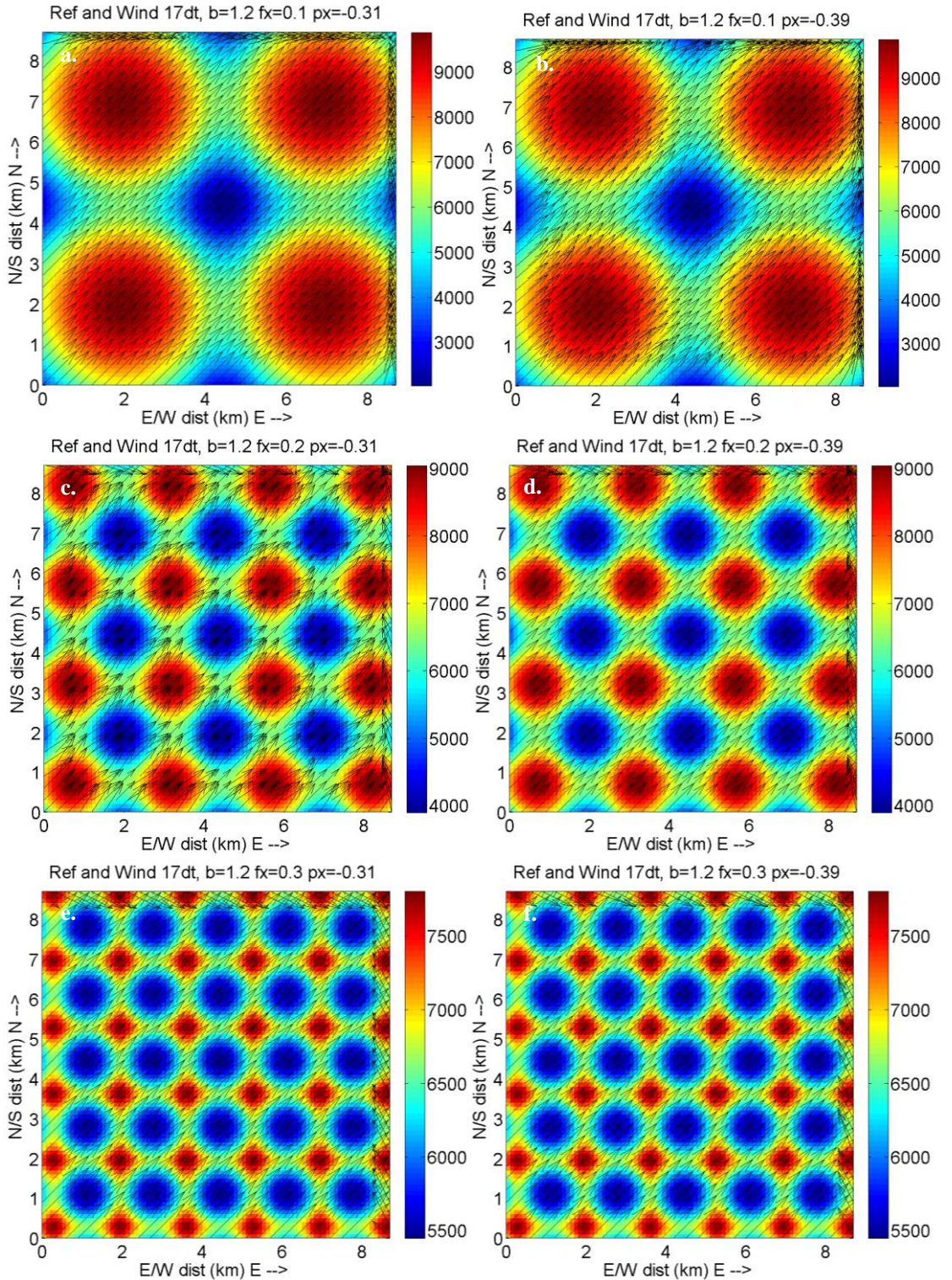


Figure 37: Pseudo-reflectivity and TREC-resolved horizontal wind fields for the different patterns.  $Dt=17s$ . Pattern phase shifted by: left  $\phi=-10$ , right  $\phi=\pi/8$ .



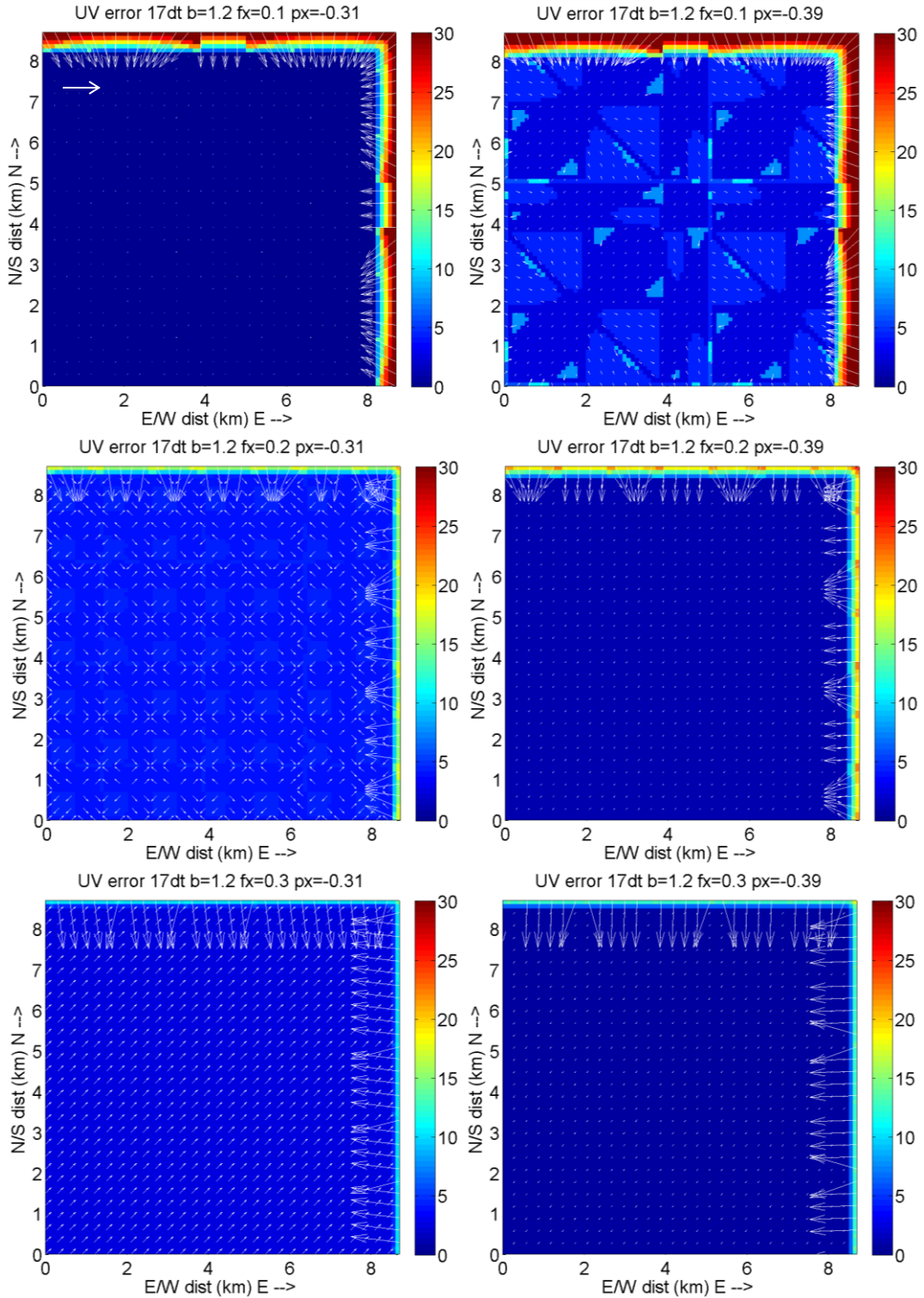


Figure 38: Same as Figure 37 except for errors between TREC-resolved horizontal winds and actual horizontal winds. White vector in upper-left corner of upper-left panel indicates a reference vector of  $20 \text{ m s}^{-1}$ .

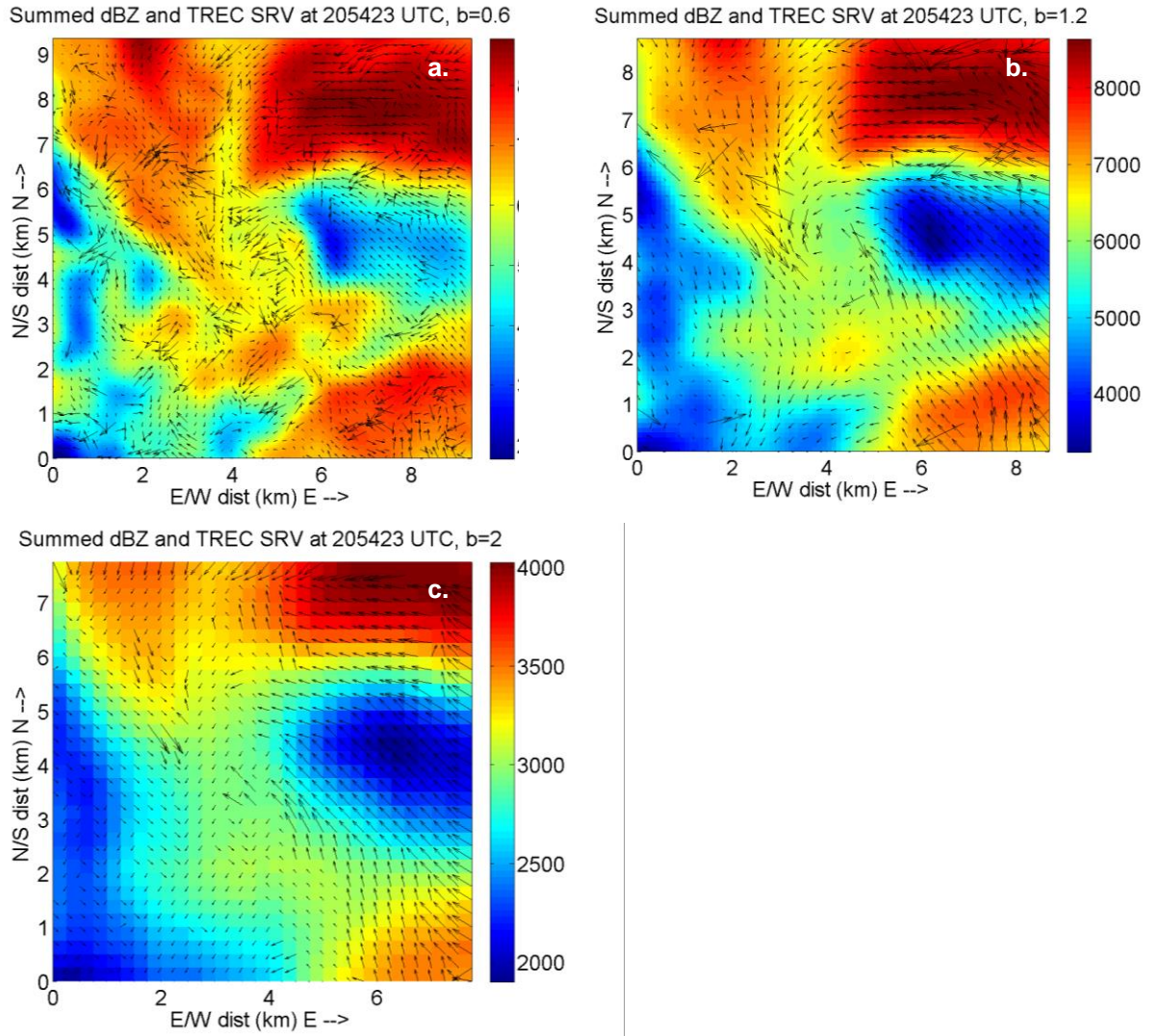


Figure 39: Comparison of grid resolutions ( $\Delta x = \Delta y$ ) for TREC analyses: a. 50 m grid resolution, b. 100 m grid resolution, c. 250 m grid resolution.



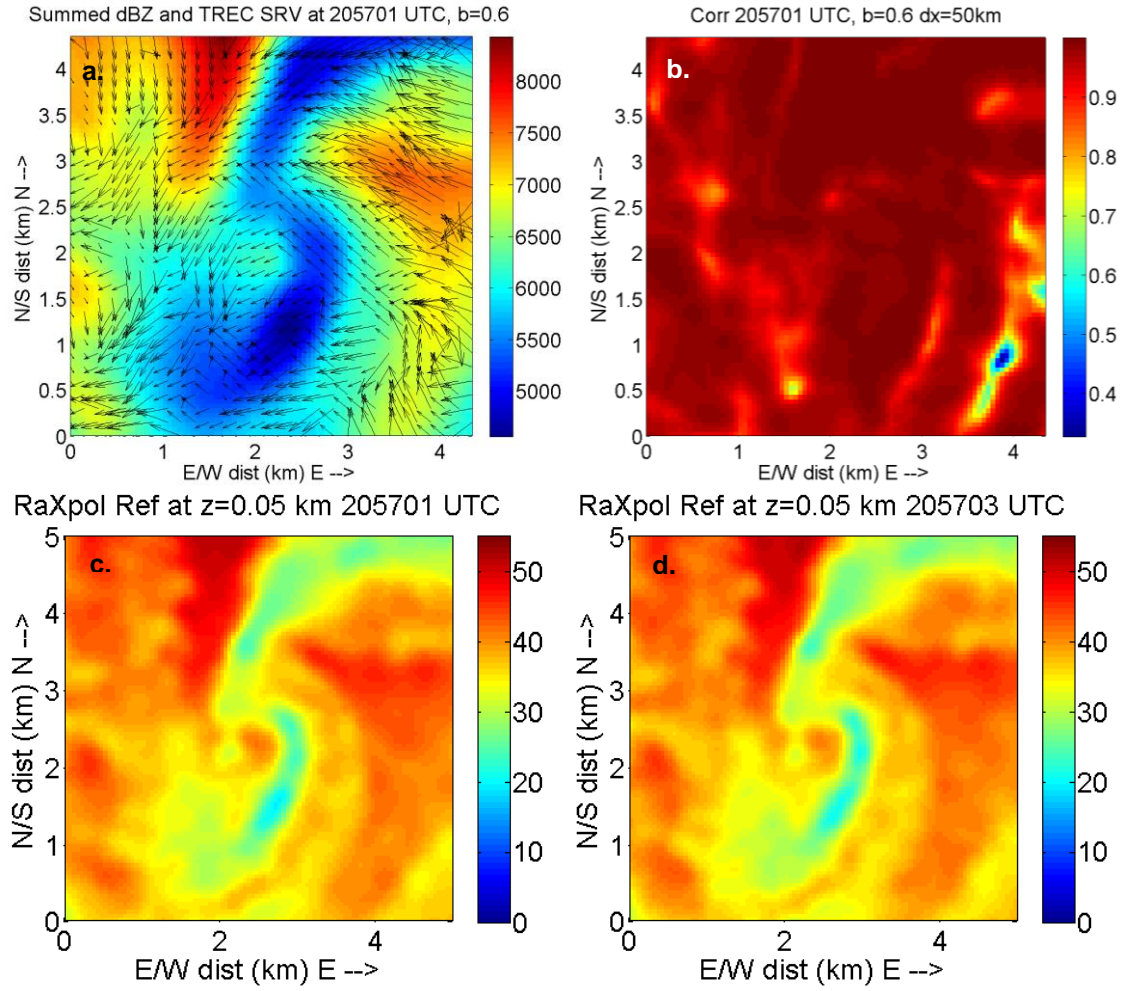


Figure 40: TREC analysis for the 2-second update time: a. TREC wind vector analysis, b. Correlation coefficient, c. reflectivity field (dBZ) at 205701, d. reflectivity field at 205703. The radar was nearly due north of the center of the grid domain

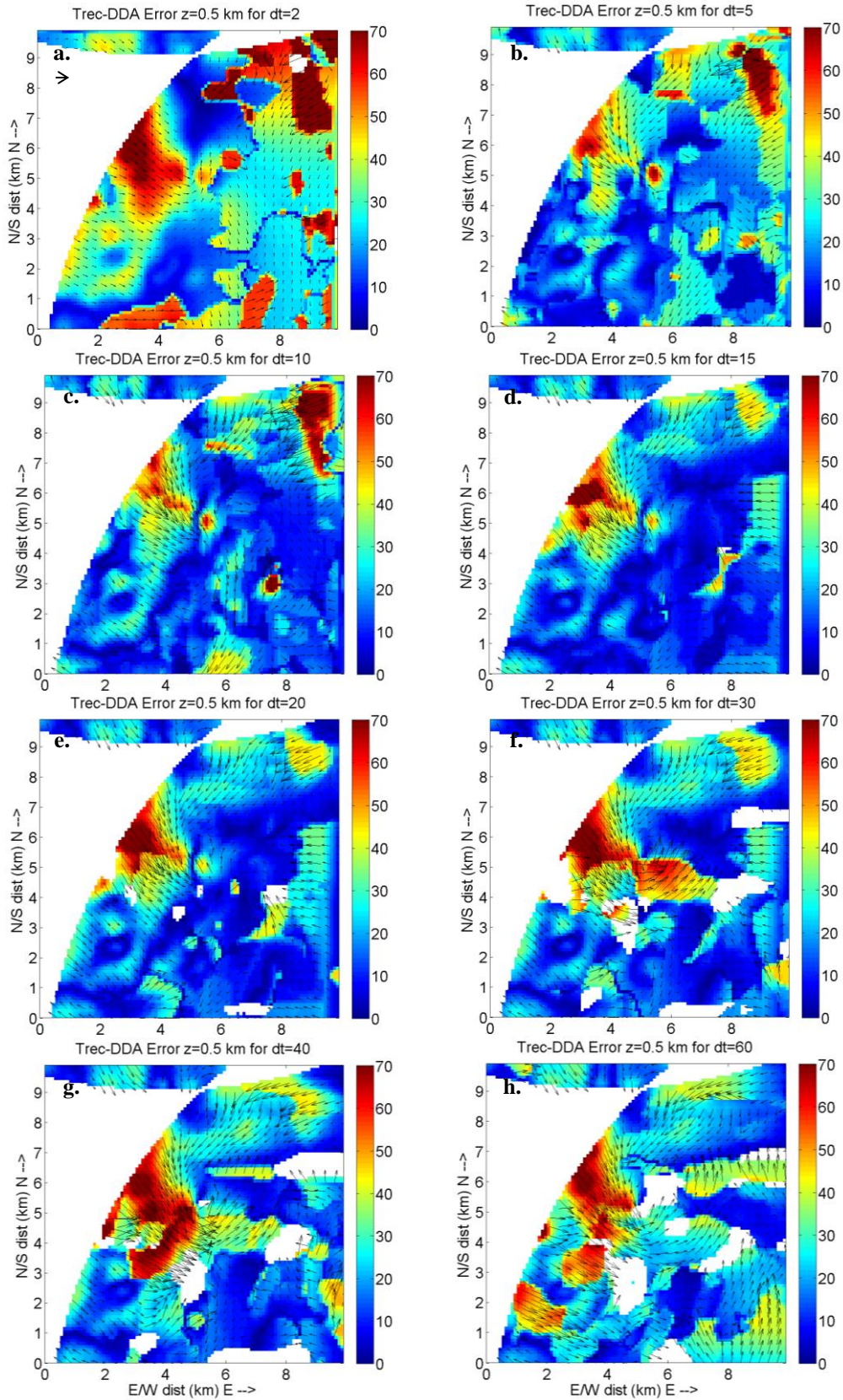


Figure 41: Magnitude and direction of errors in wind vectors comparing dual-Doppler analysis winds for 205557 with TREC-derived winds centered in time around 205601 for various  $\Delta t$ 's: a)  $\Delta t = 2$  s, b)  $\Delta t = 5$

s, c)  $\Delta t = 10$  s, d)  $\Delta t = 15$  s, e)  $\Delta t = 20$  s, f)  $\Delta t = 30$  s, g)  $\Delta t = 40$  s, h)  $\Delta t = 60$  s. All analyses are valid for  $z=500$ m. Areas within the analysis domain (i.e. not outside the curved boundary separating grid points with data from those without) that are white represent locations where correlation coefficients were  $< 0.5$ . Arrow in A below the letter 'a' indicates reference vector of  $20 \text{ m s}^{-1}$ .

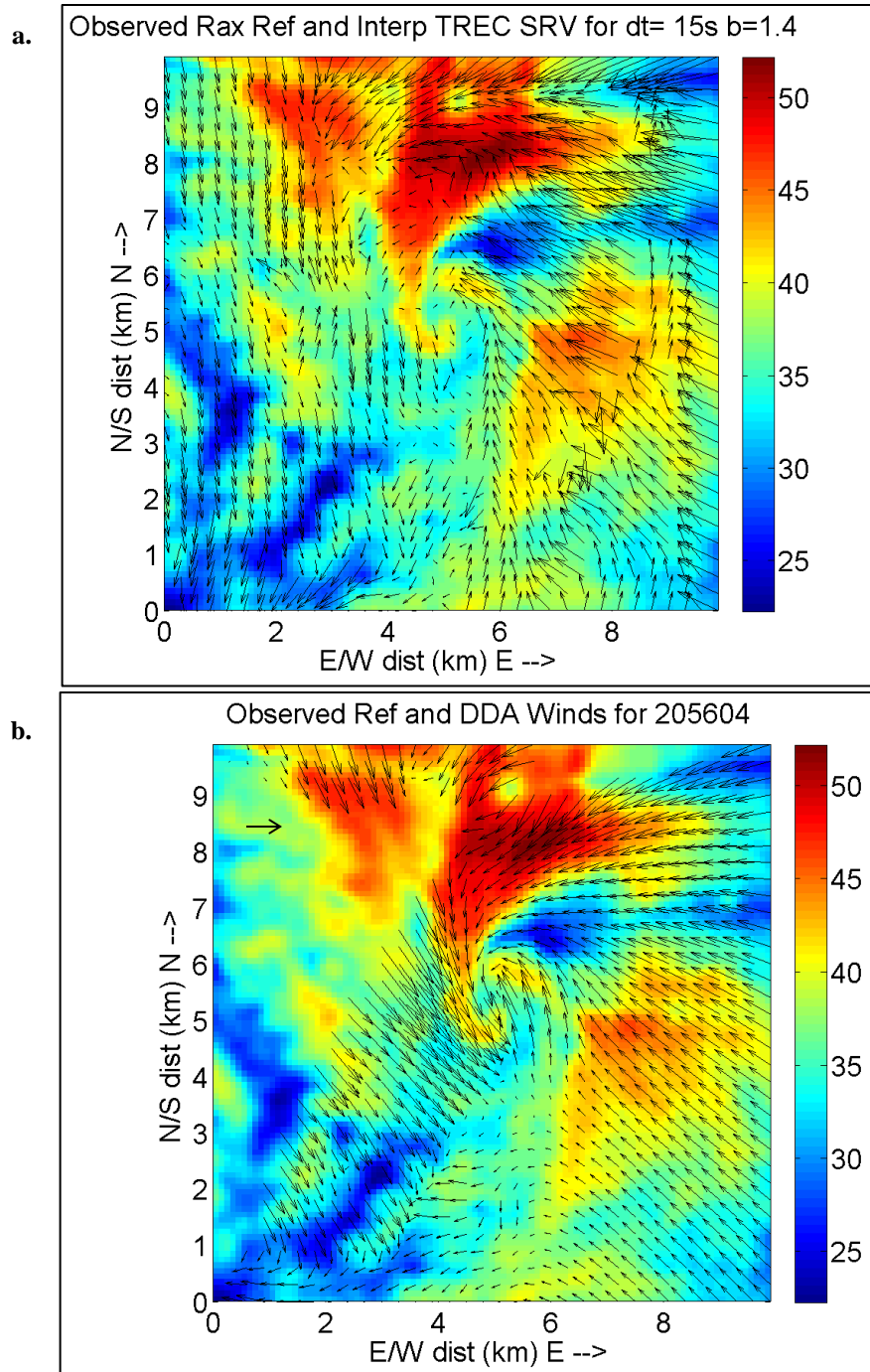


Figure 42: Observed RaXPoI reflectivity 205604 (1° elevation angle) and a) TREC-derived storm-relative horizontal wind vectors; b) dual-Doppler derived storm-relative wind vectors. Areas with missing vectors in b have a between-beam angle < 20°. Arrow indicates 20 m s<sup>-1</sup> reference vector.



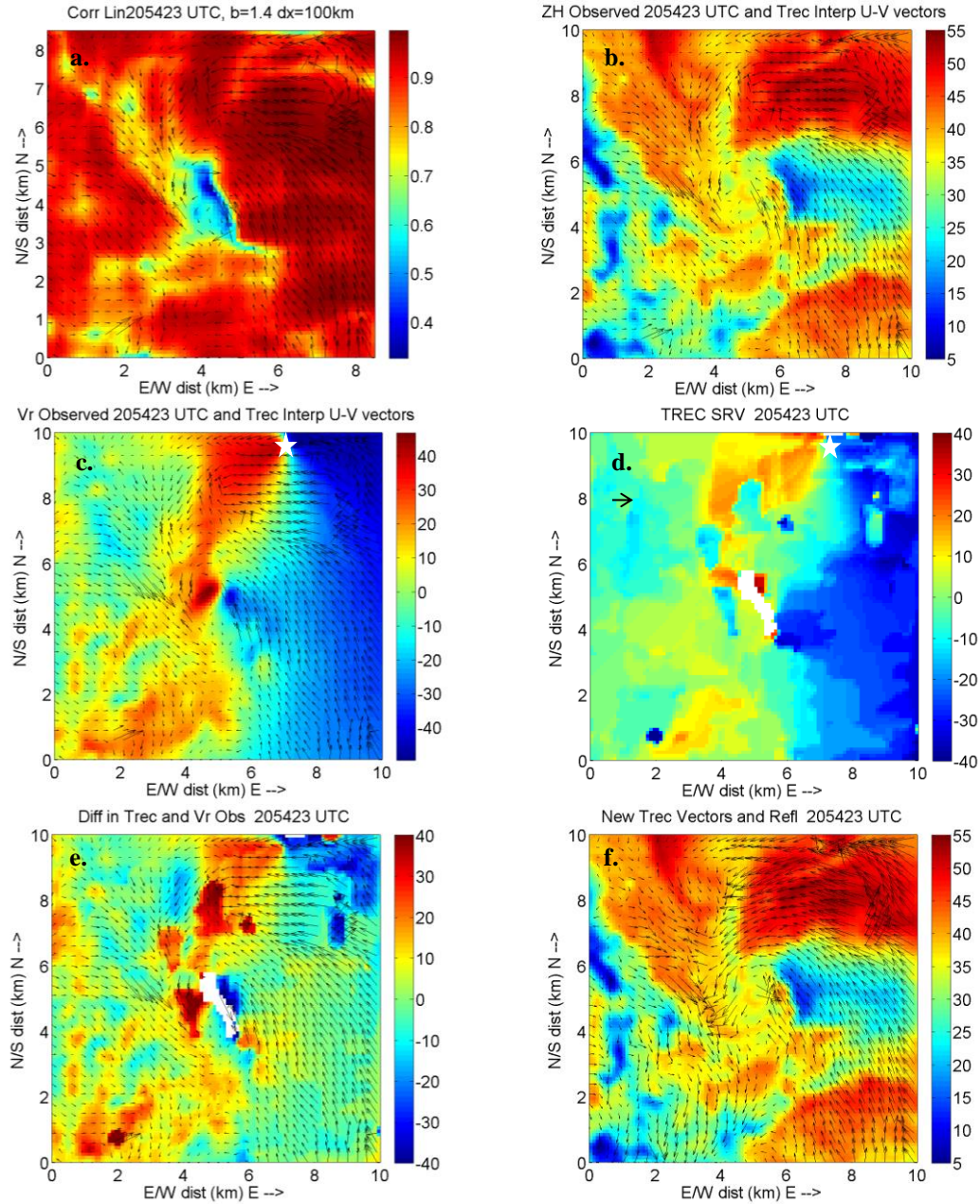


Figure 43: Performance of TREC compared with observed radial velocity data: a) Correlation coefficient and storm-relative TREC vectors computed between 205423 and 205445; b) Objectively analyzed RaXPoI reflectivity and storm-relative TREC vectors; c) Objectively analyzed storm-relative radial velocity ( $\text{m s}^{-1}$ ) and storm-relative TREC vectors. RaXPoI is located at the white star; d) TREC-derived storm-relative radial velocity ( $\text{m s}^{-1}$ ). Arrow indicates reference vector of  $20 \text{ m s}^{-1}$  for a-f; e) The difference between the TREC-calculated SRVs and the observed SRVs, with the calculated TREC vectors overlaid; f) Objectively analyzed reflectivity with TREC vectors corrected for the observed radial velocity component.

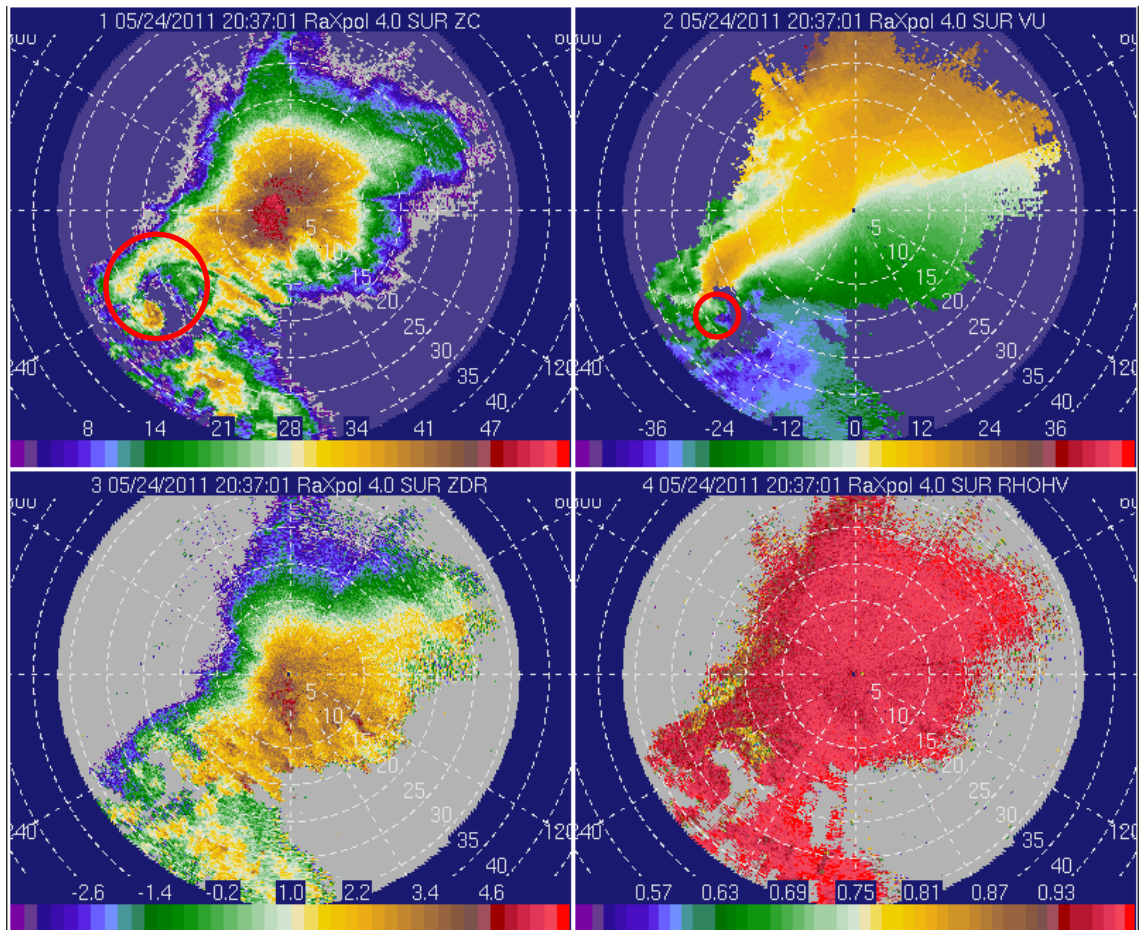


Figure 44: Storm-scale view of the supercell at 203701, just after rapid-scan data collection had begun. Panels are a) Reflectivity (dBZ), b) unfolded radial velocities, c) differential reflectivity (dB), and cross-correlation coefficient (unitless)<sup>12</sup>. The red circles identify the hook (a) and the TVS (b).

<sup>12</sup> Hereafter, all 4-panel images will be the same as that described here unless otherwise noted.



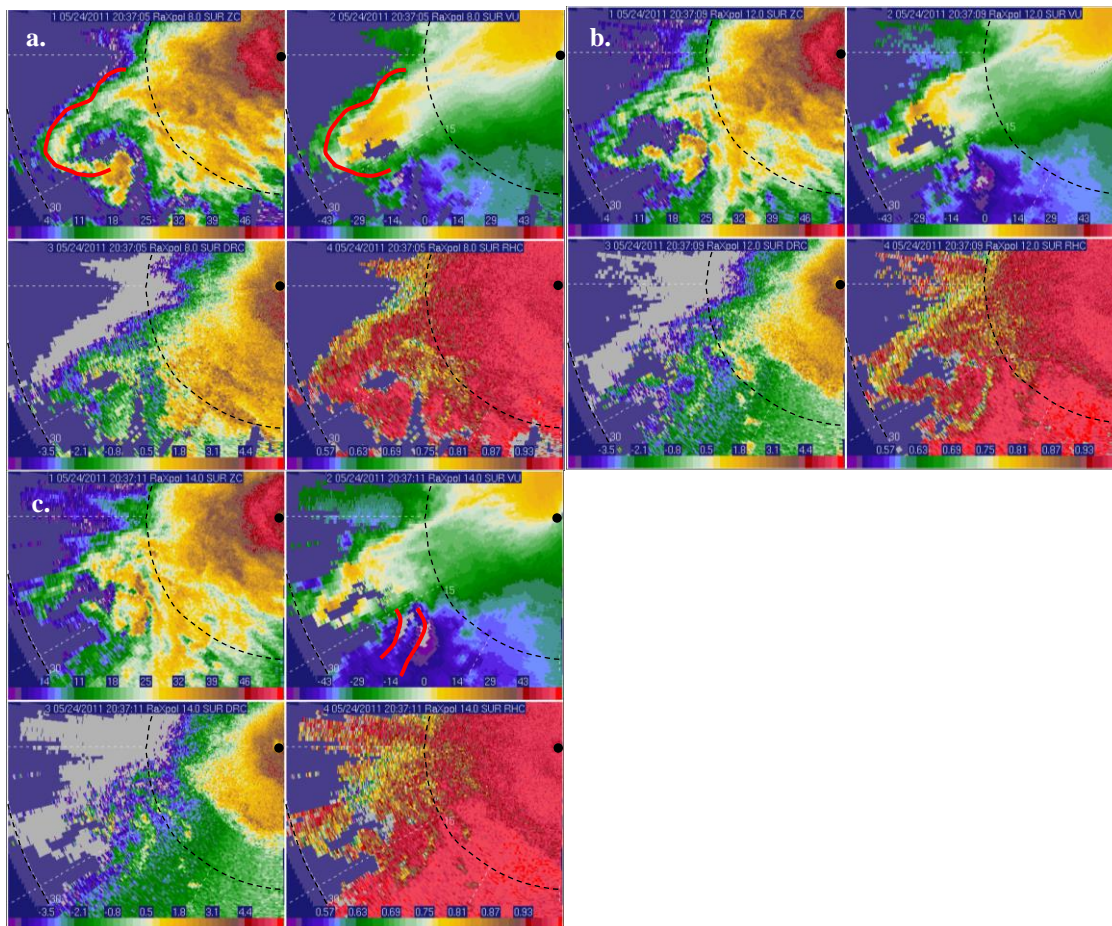


Figure 45: Four-panel images (Reflectivity, radial velocity, differential reflectivity, and cross-correlation coefficient) as in Figure 44, of the hook at (a), 8° (red lines depict the collocation of the hook echo and the narrow band of outbound radial velocities); (b) 12° and (c) 14° elevation (red lines identify two scales of circulation.) Times are 203705, 203709 and 203711 respectively. Range rings (dashed lines) are 15 and 30 km. Radar is located at the black dot.

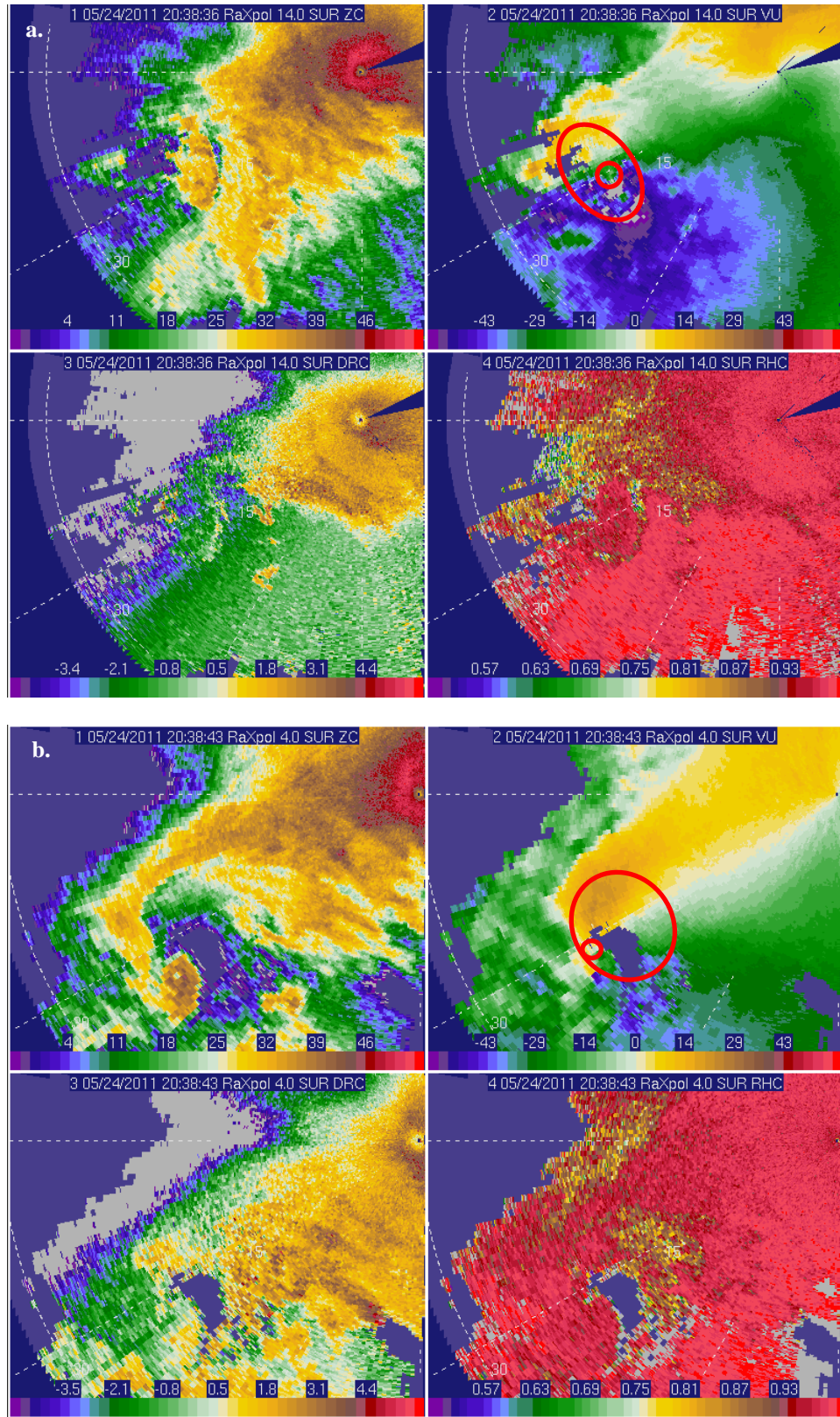


Figure 46: Same as Figure 44 except for a) 14° at 203843 and b) 4° at 203843. Red ellipses indicate the two scales of rotation.



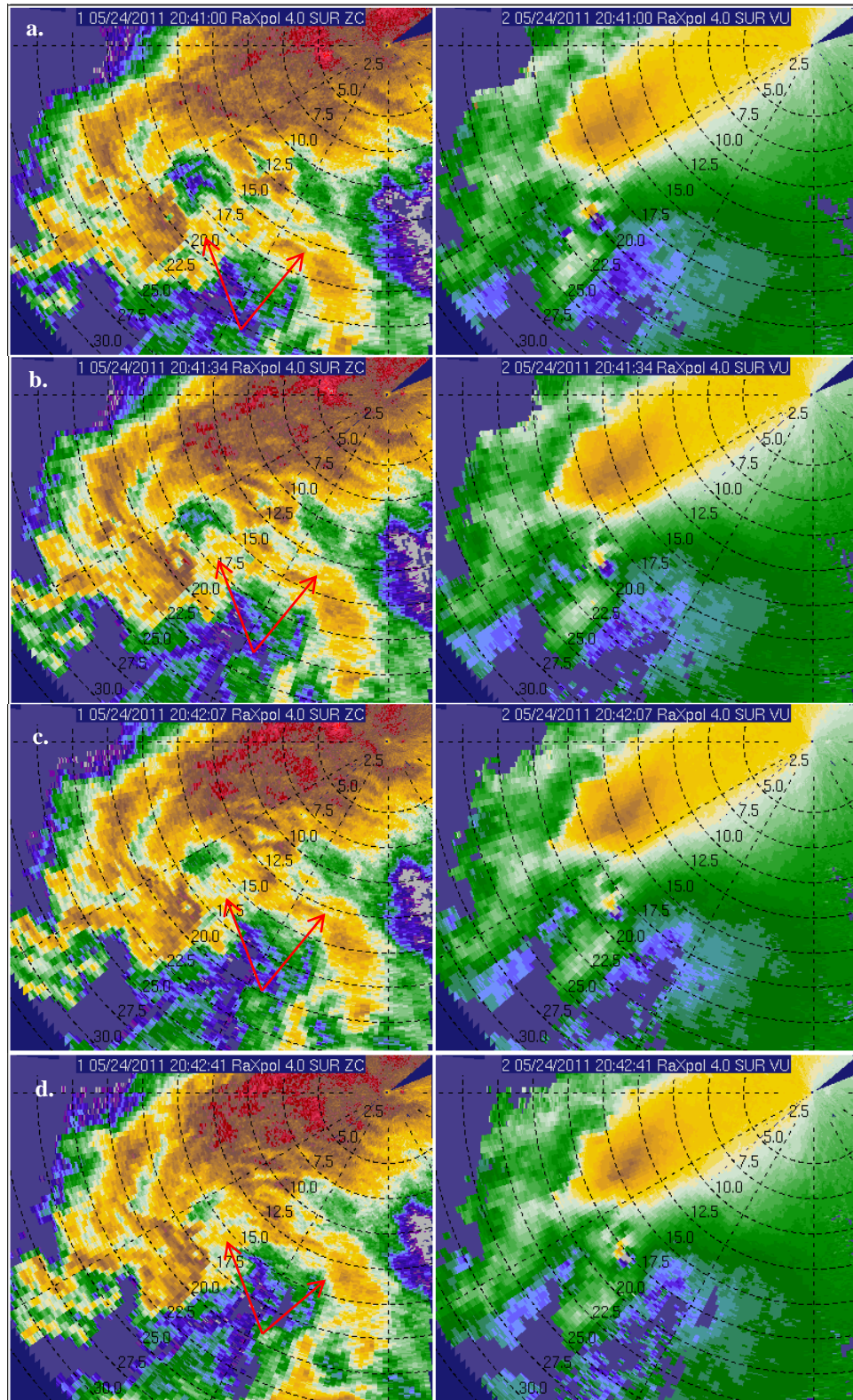
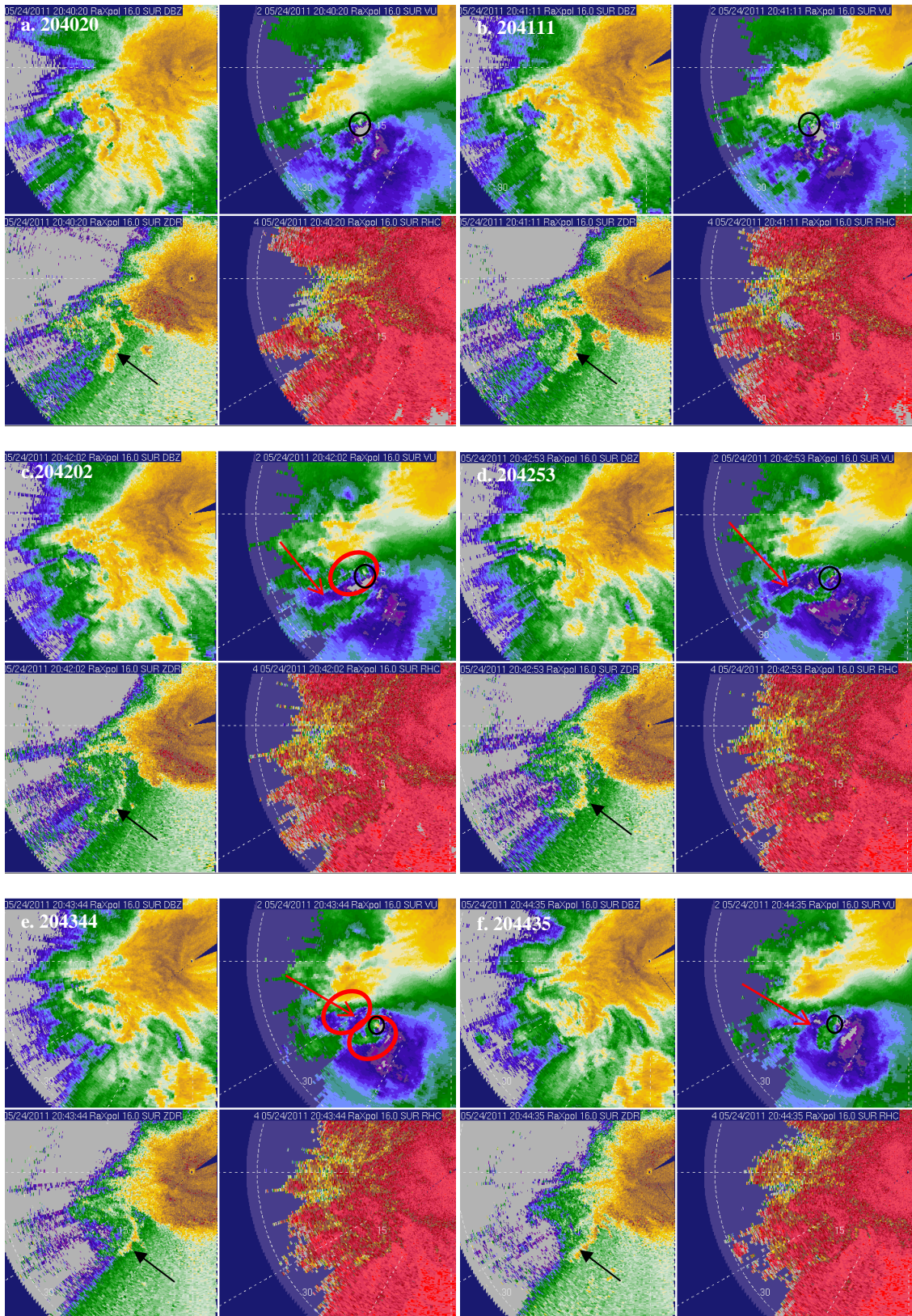


Figure 47: Reflectivity (left hand panels) and radial velocity (right hand panels), of a storm merger between the supercell and convection from its south. (a) 204100; (b) 204134; (c) 204207; (d) 204241. Red arrows point to non-supercell convection.





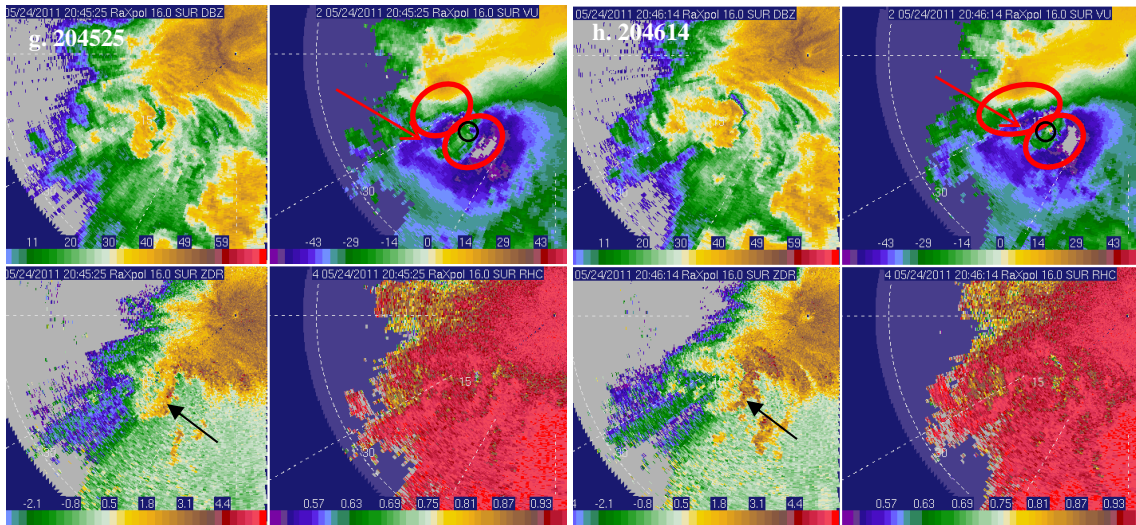


Figure 48: Series of 4-panel images depicting the evolution of midlevel ( $16^{\circ}$  elevation,  $z \sim 5$  km) rotation. Valid at (a) 204020; (b) 204011; (c) 204202; (d) 204250; (e) 204344; (f) 204335; (g) 204525; (h) 204614. Red ellipses indicate cyclonic mesocyclones, black indicate the tornado circulation. Black arrows point to Zdr protrusion, red arrows point to jet of strong inbounds.



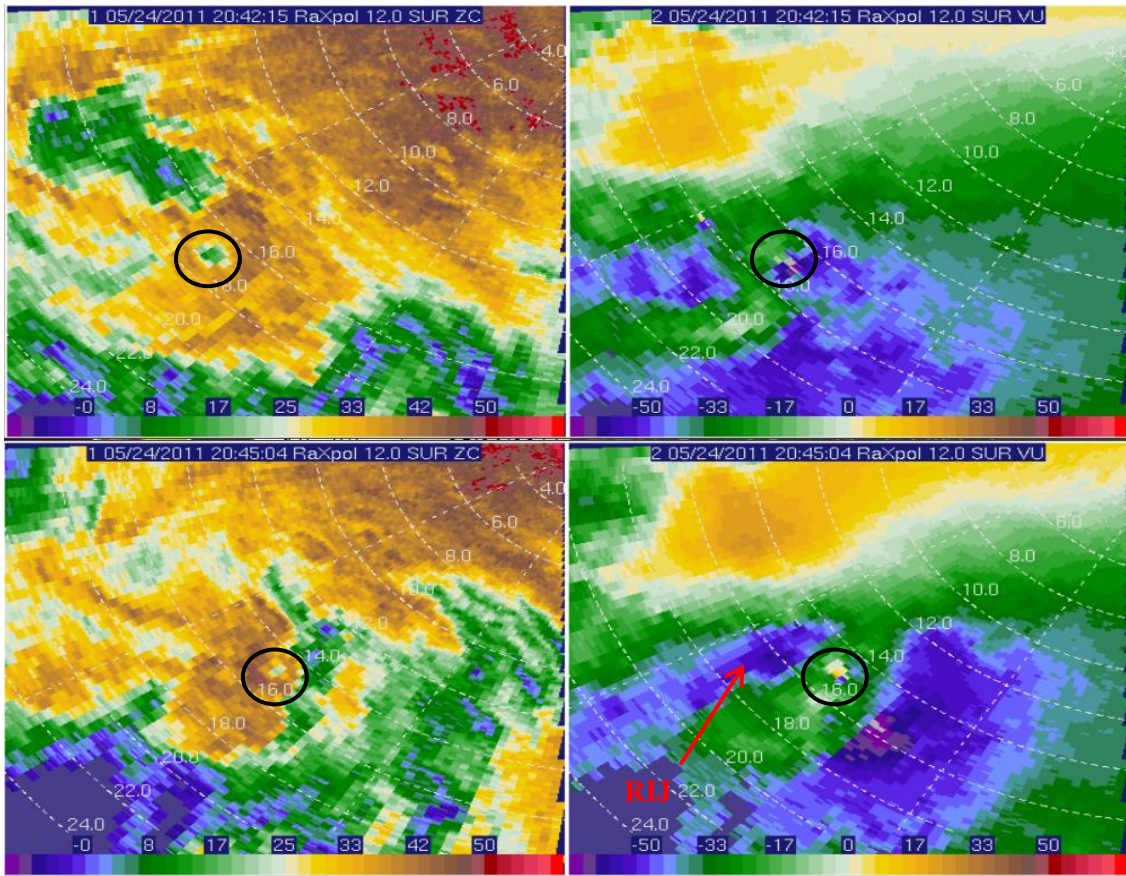


Figure 49: Reflectivity (left panel) and radial velocity (right panel) for 12° elevation (z~3 km). The tornado circulation (circled in black) becomes removed from the storm-scale mesocyclone between (a) 204215 and (b) 204504.



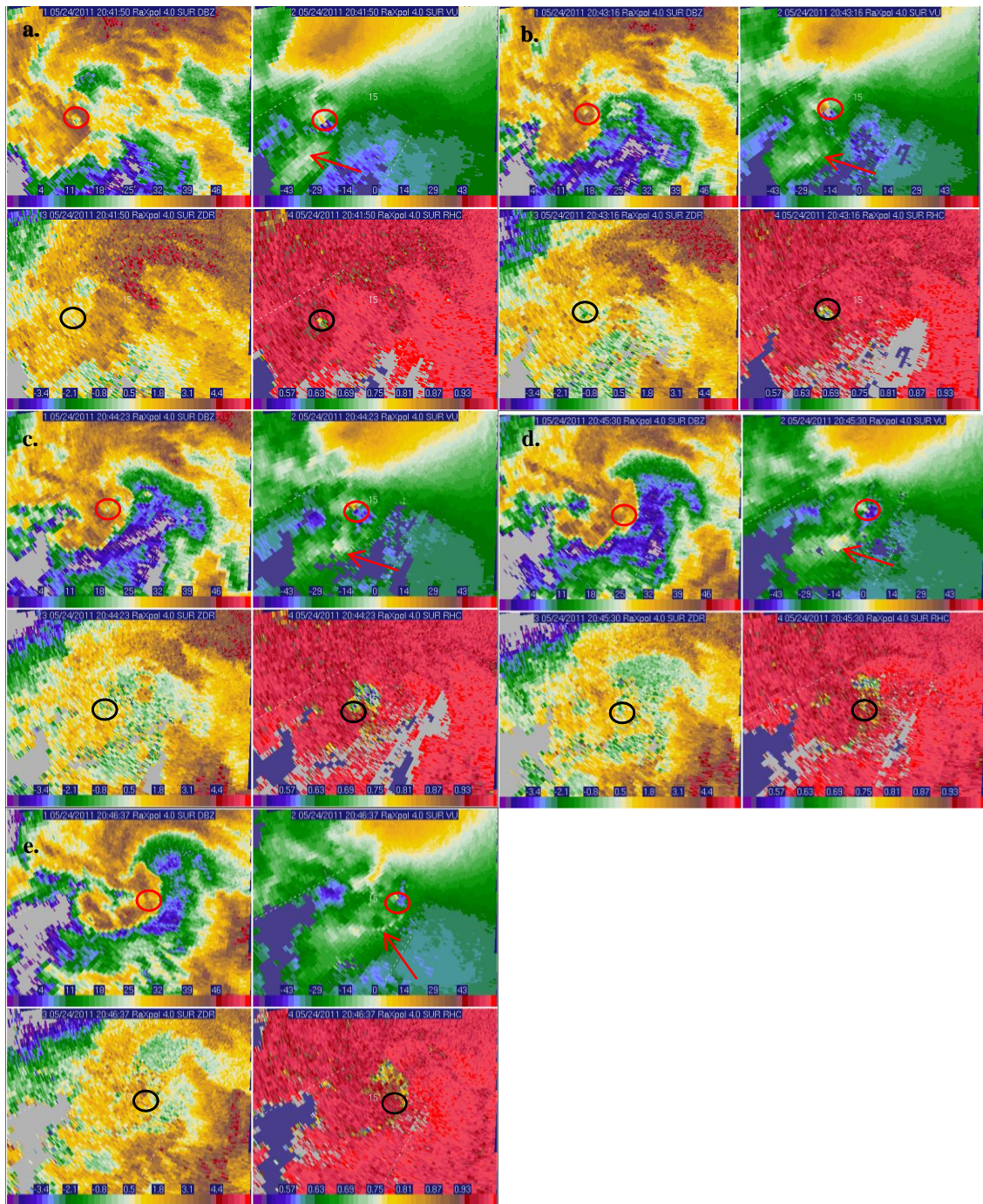


Figure 50: 4-panel images from (a) 204150, (b) 204315, (c) 204423, (d) 204530, and (e) 204637 at 4° elevation angle. Red and black circles indicate locations of tornado vortex, red arrow indicates location of wind shift associated with the primary RFGF.

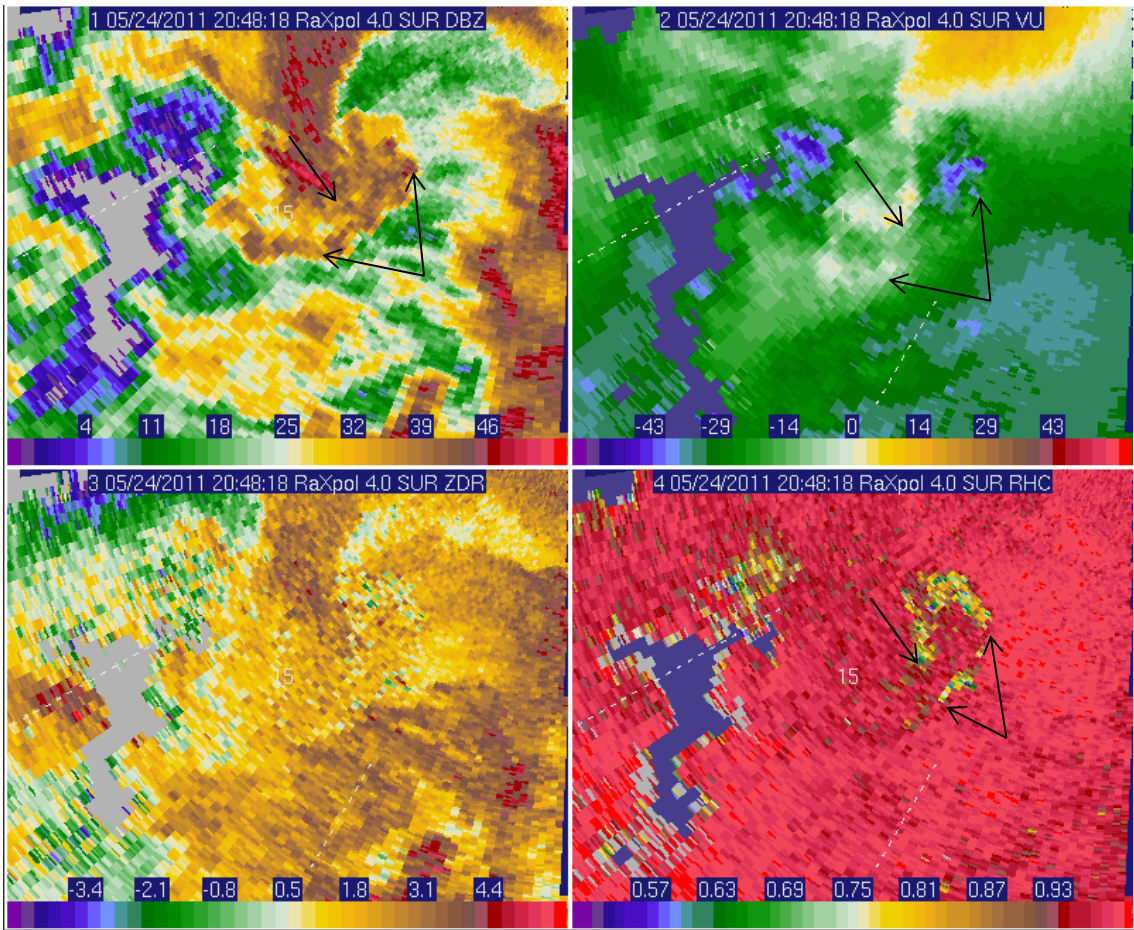


Figure 51: 4° elevation angle 4-panel of secondary RGFG surge at 204818. RGFGs are indicated by black arrows.



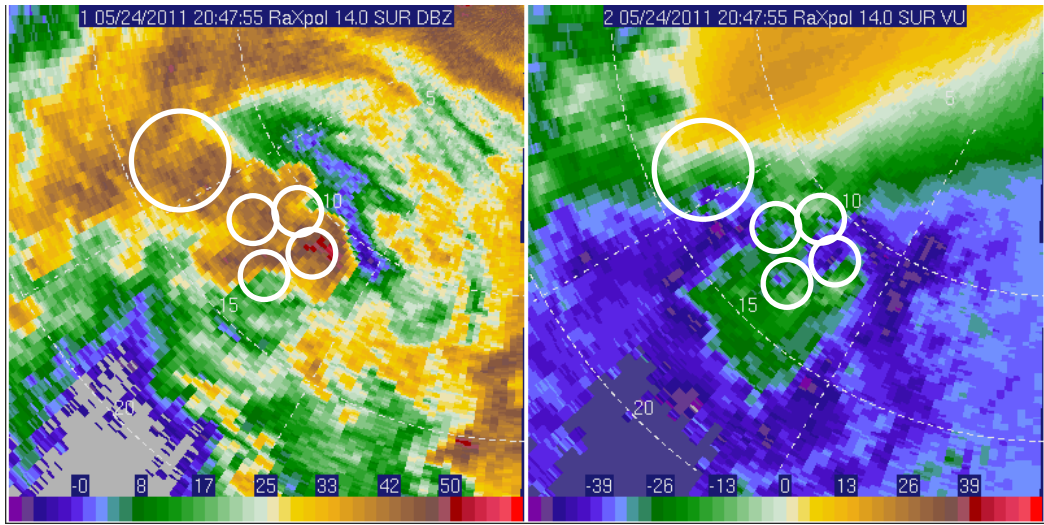


Figure 52: Reflectivity and radial velocity of midlevel ( $z \sim 3$  km) rotation between tornadoes, at 204755. Vortex signatures and larger circulation are circled.

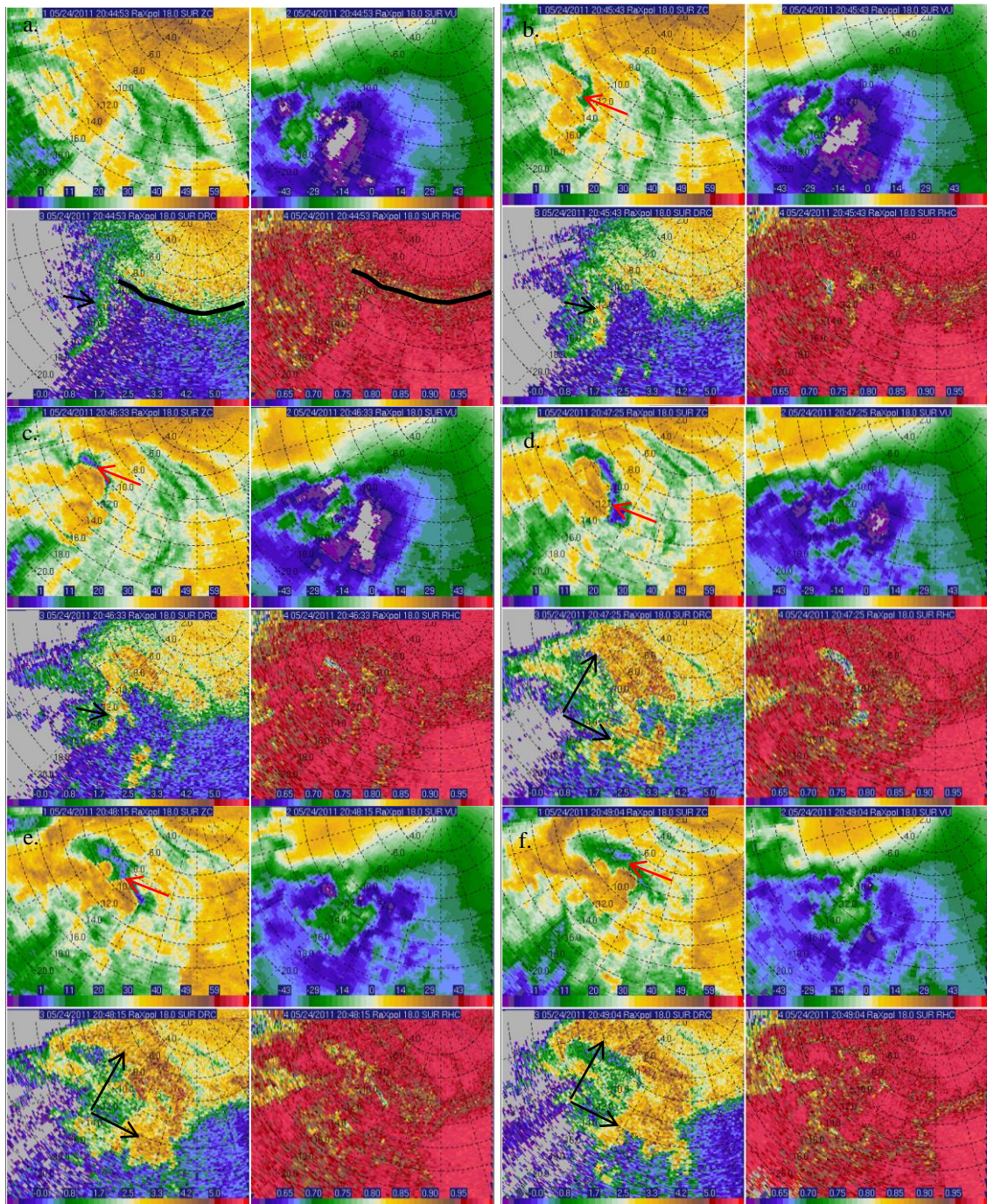


Figure 53: Four-panel images (18° elevation angle) of the development of a  $Z_{DR}$  column and BWER. (a) 204454; (b) 204543; (c) 204633; (d) 204725; (e) 204815; (f) 204904. Red arrows point to the BWER, black to the  $Z_{dr}$  column. The freezing level is indicated by the black line in the  $Z_{dr}$  and  $\rho_{hv}$  panels in (a).



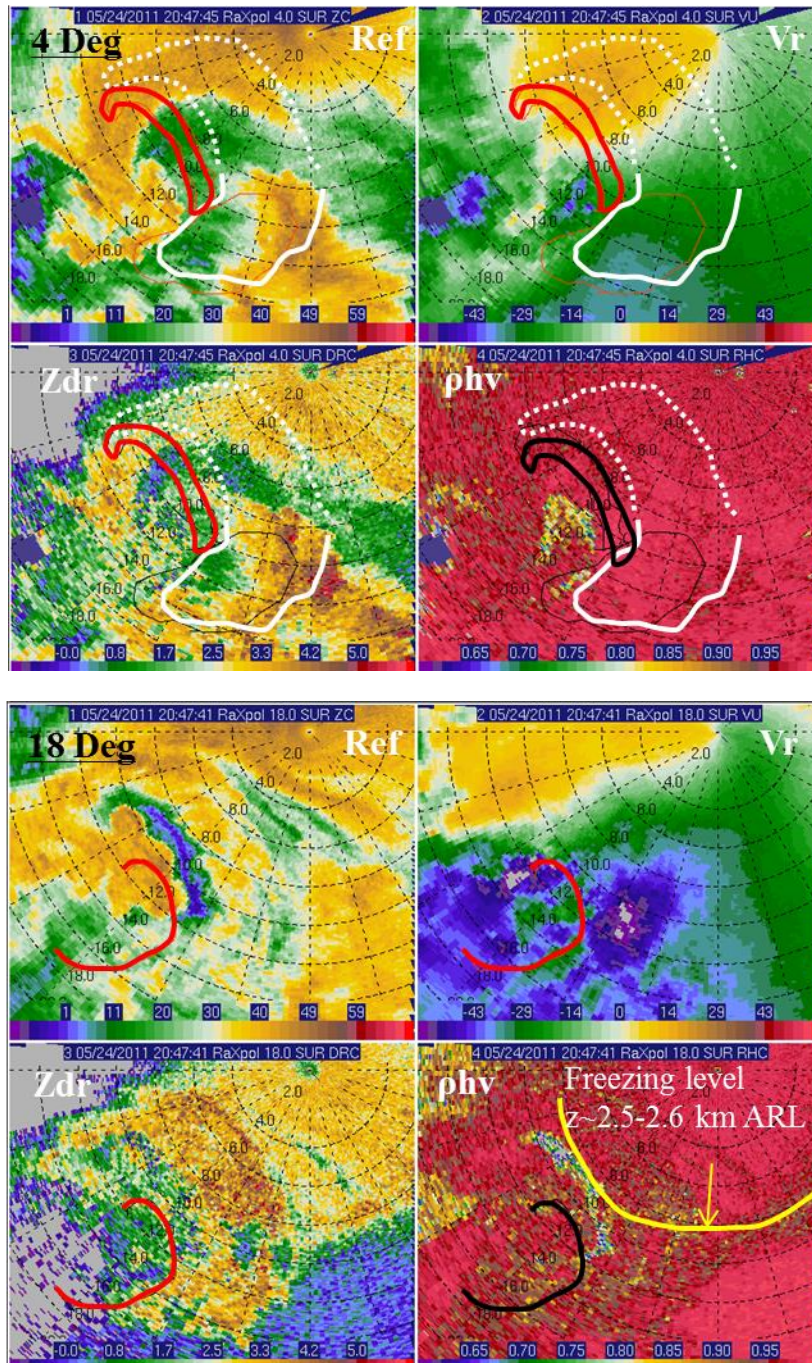


Figure 54: a) 4 panel plot from the 4° elevation angle at 204745 with overlays of the BWER (red) and Zdr (white) column from aloft. Stippled white outline indicate likely location of Z<sub>dr</sub> column even though the beam is below the freezing height at this level. B) 4 panel plot from the 18° elevation angle at 204741 with overlays of the leading edge of the reflectivity hammer head from the 4° sweep (red) and an indication of the location of the freezing level.

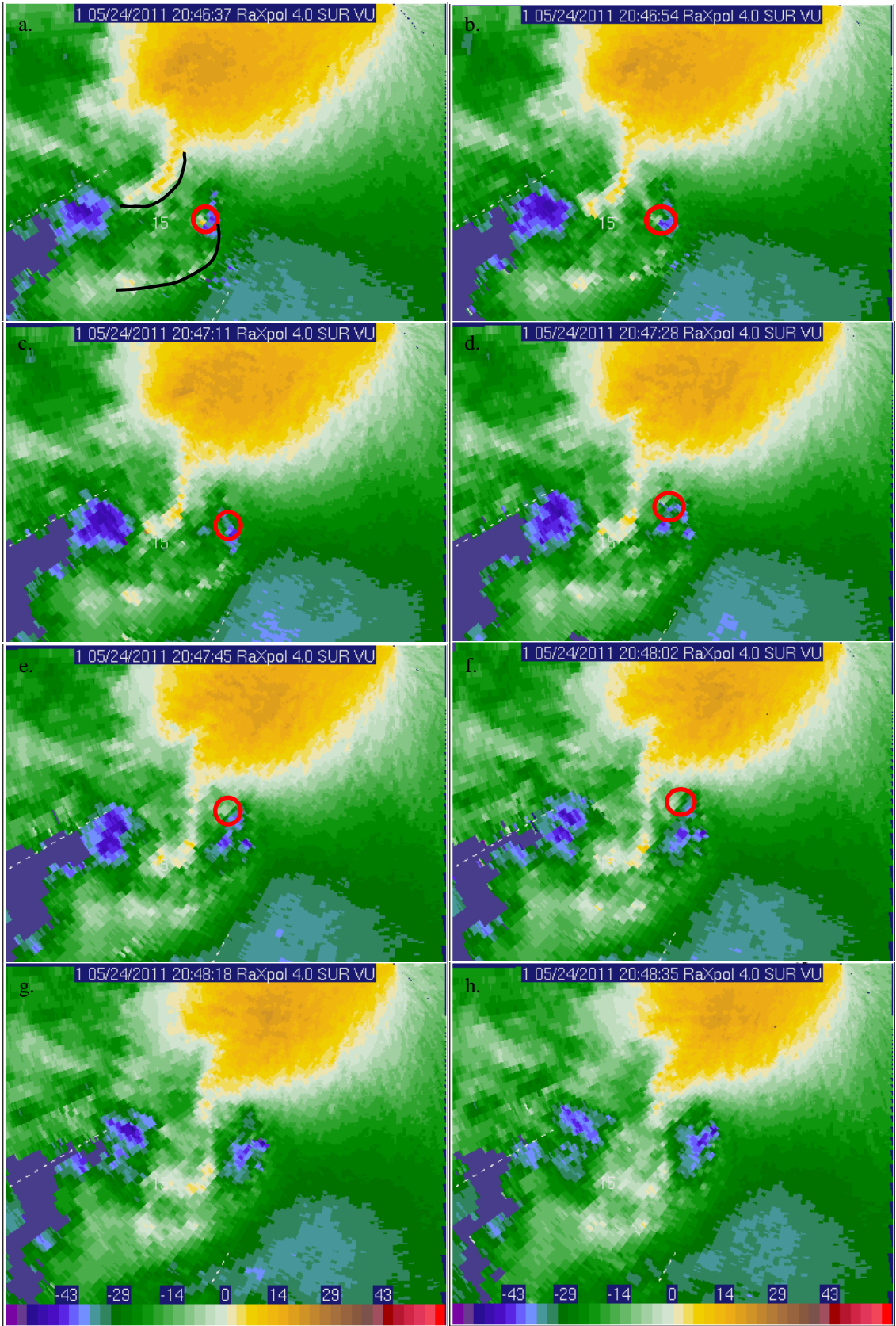


Figure 55: Evolution of low-level rotation from radial velocity at  $4^\circ$  elevation angle prior to tornadogenesis. Images are valid every 17 s from 204637 – 204835. Red circle indicates the remnant circulation from tornado 1. Black lines in (a) denote RFGF locations.



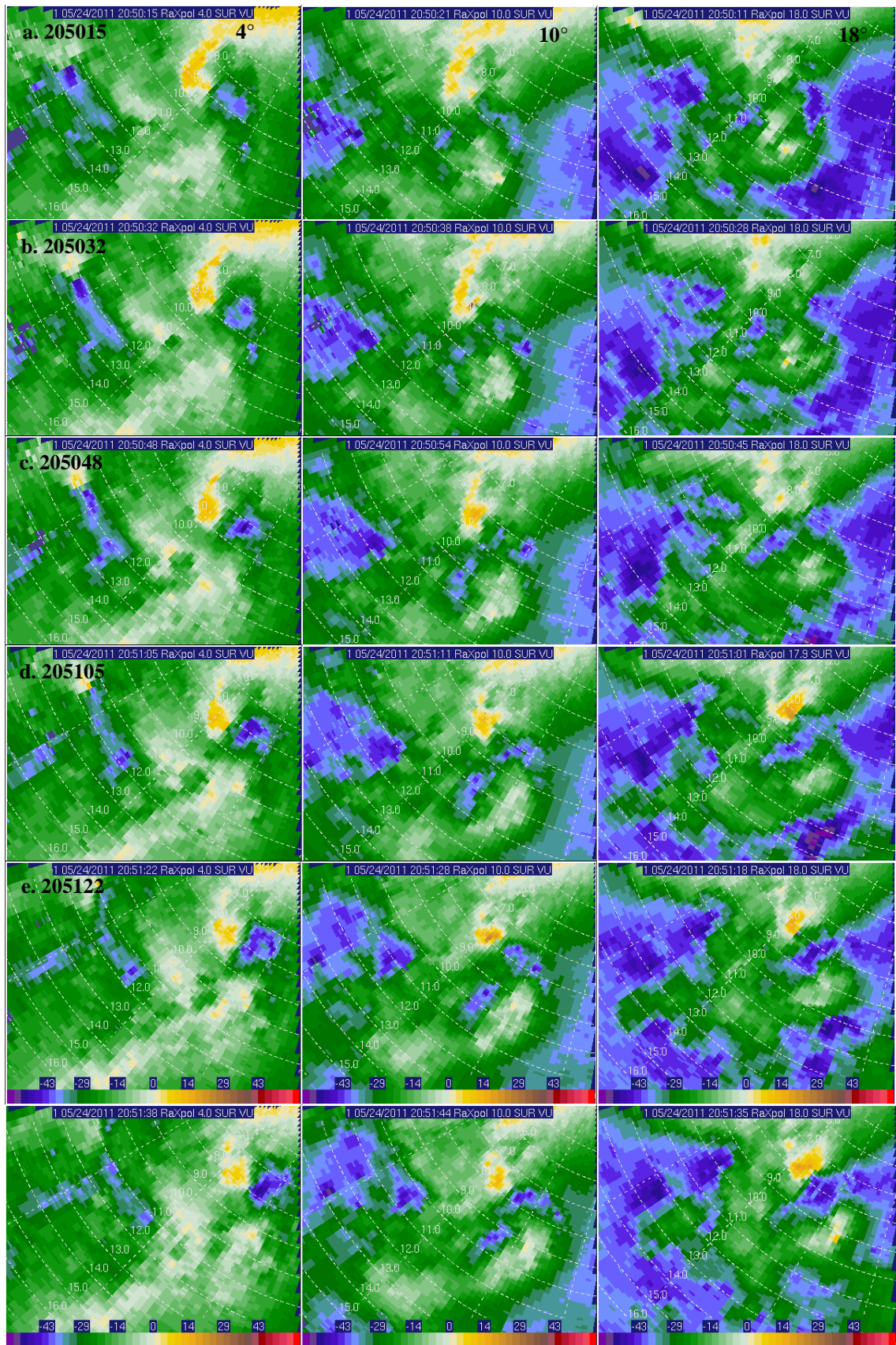


Figure 56: Evolution of rotation at increasing elevation angles every 17 s between 205015 and 205135. Left panels:  $4^\circ$  elevation angle, middle panels:  $10^\circ$  elevation angle, right panels:  $18^\circ$  elevation angle. Tornadogenesis occurred between 205122 and 205138.



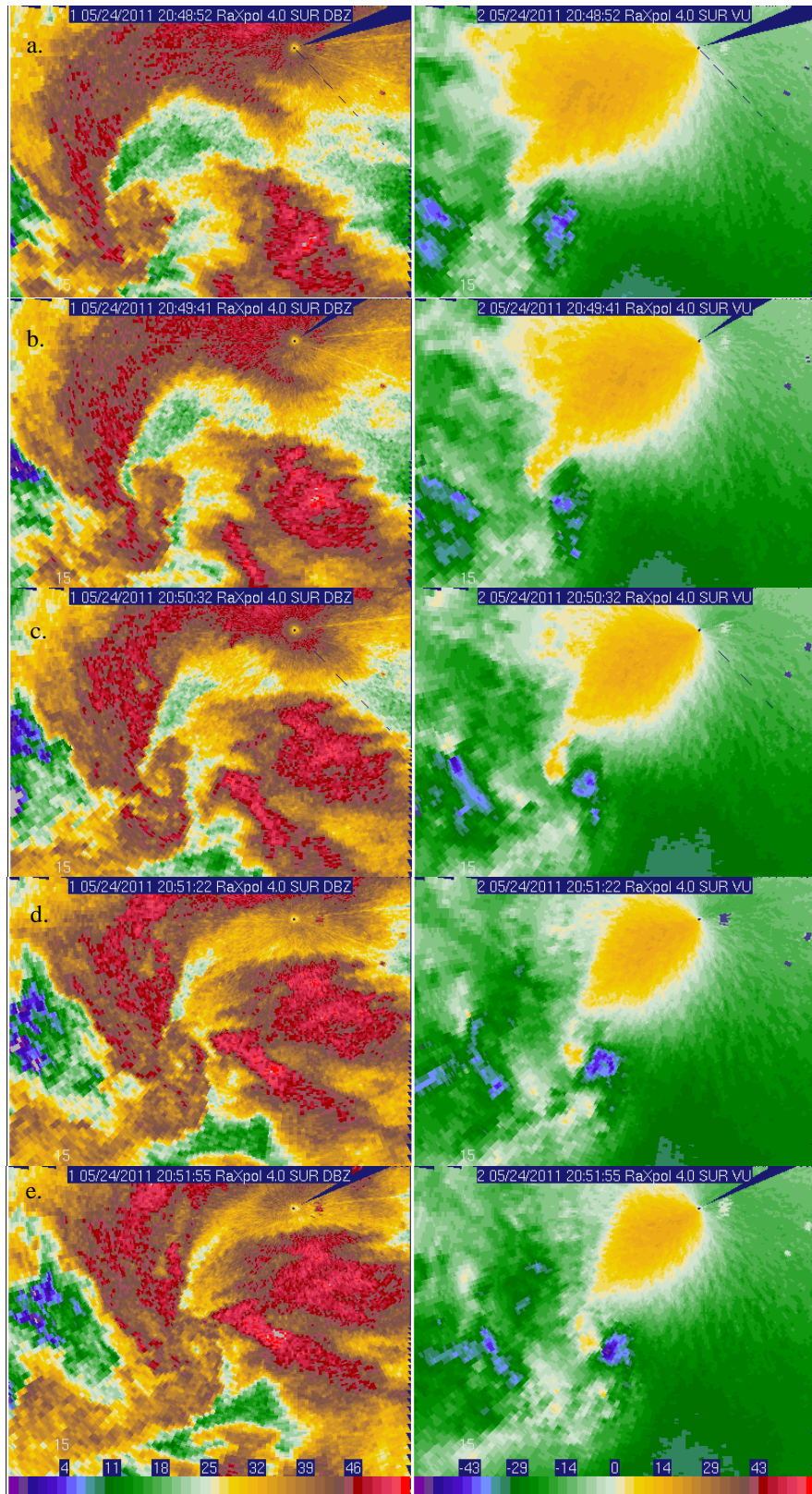


Figure 57: Storm merger process at 4° elevation angle. Left panels are reflectivity, right panels are radial velocity. (a) 204852; (b) 204941; (c) 205032; (d) 205122; (e) 205155.

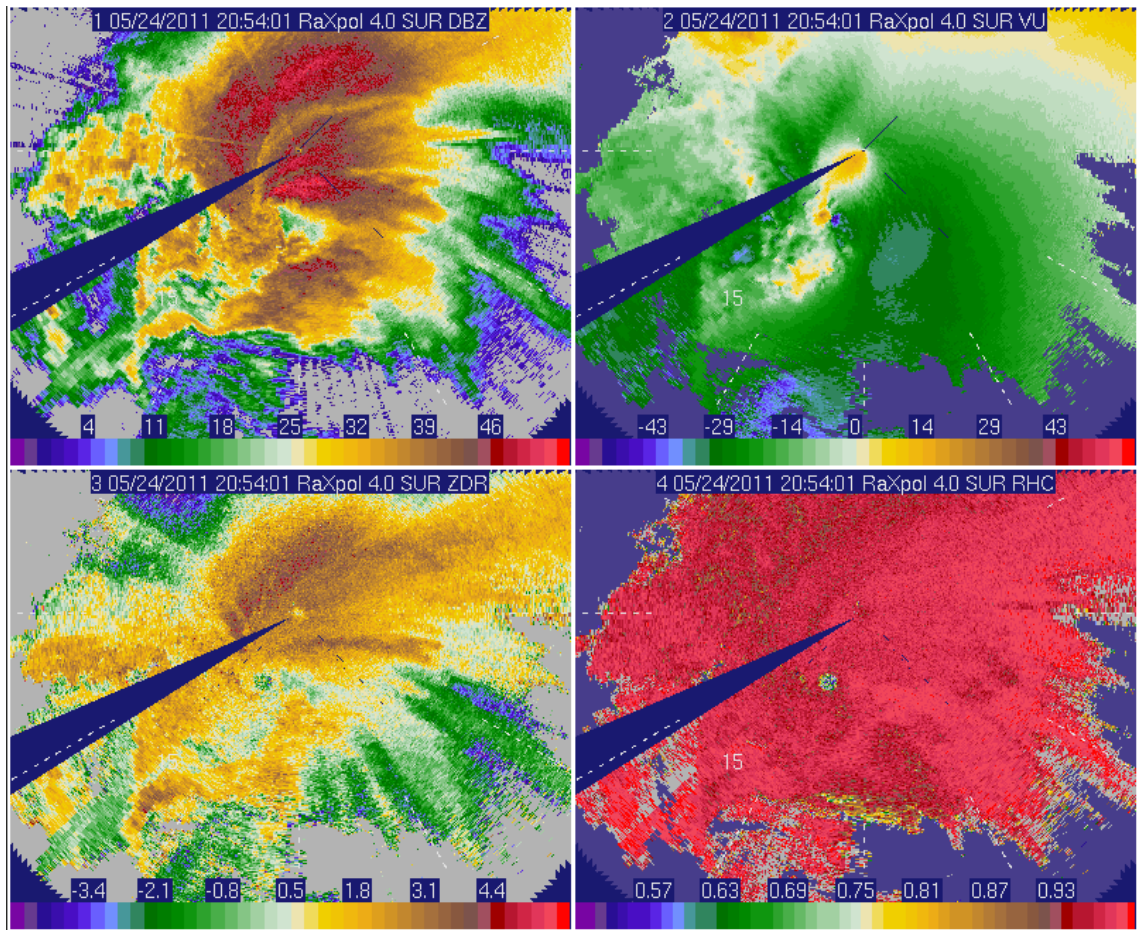


Figure 58: 4-panel image of storm-scale structure during tornado intensification. Valid at 205401, at an elevation angle of 4°

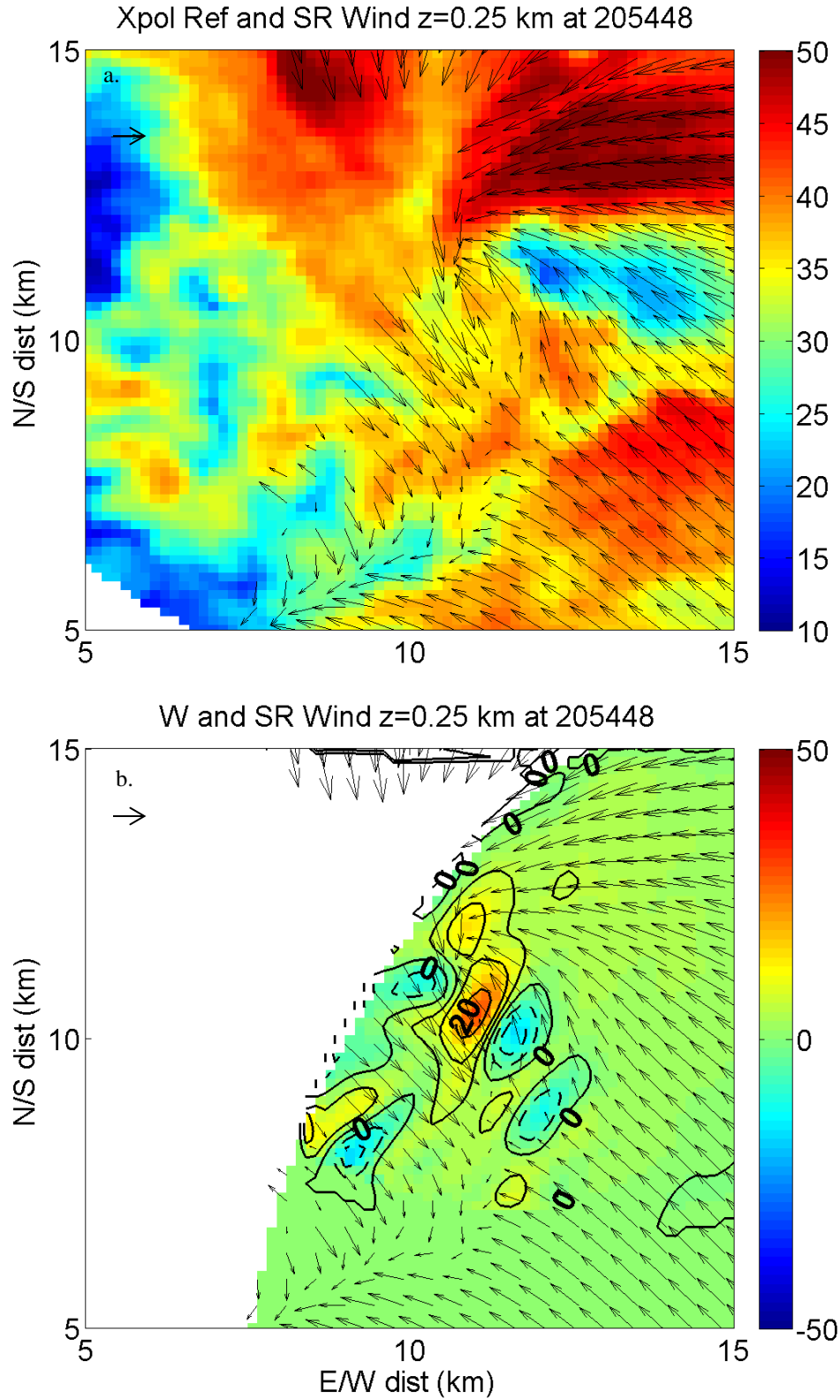


Figure 59: Storm structure from dual-Doppler analysis at a height of 250 m. (a) RaXPol reflectivity and storm-relative horizontal (u v) wind vectors. (b) Same as (a) except for vertical velocity. Analyses valid at 205448. Reference vector below letter is  $20 \text{ m s}^{-1}$ .



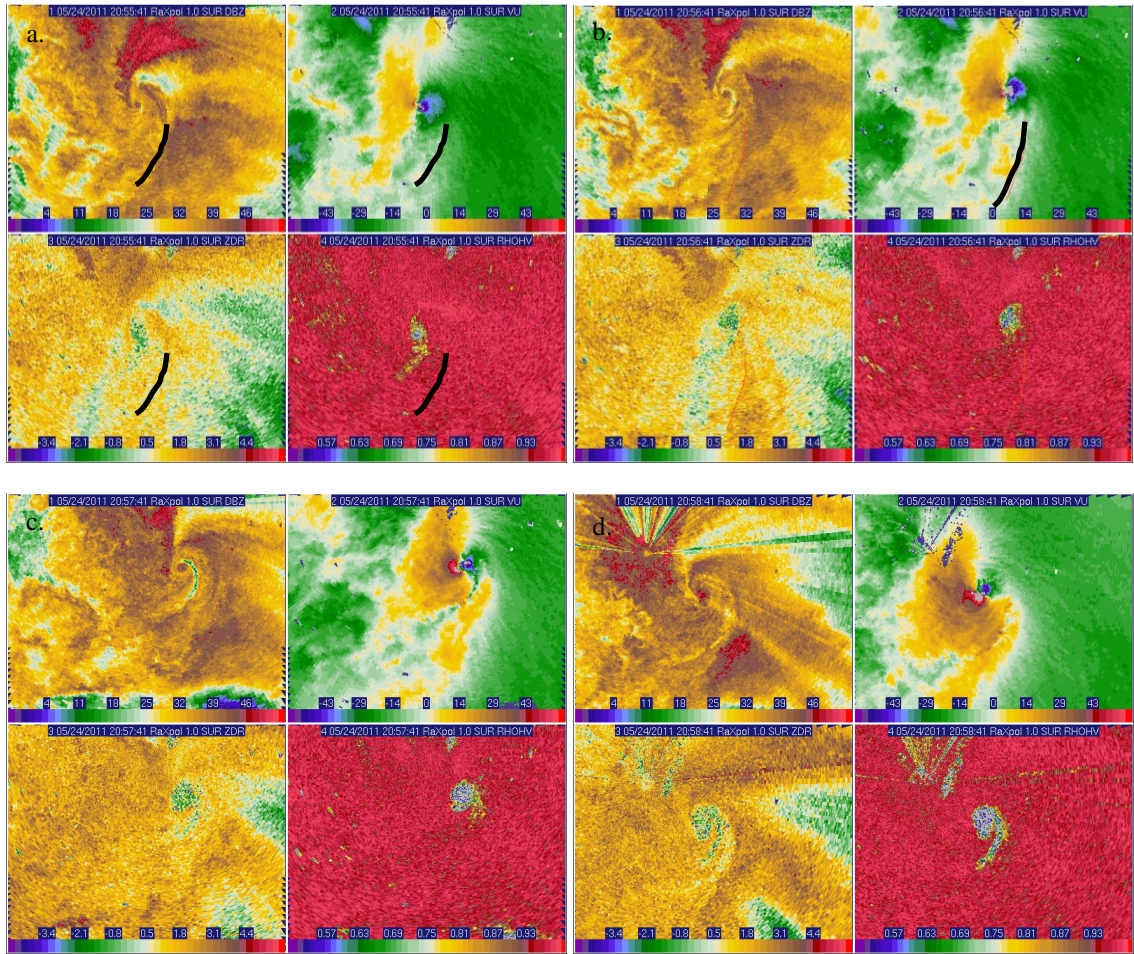


Figure 60: Series of 4-panel images of the radial velocity boundary between the hook and impinging non-supercellular convection at 205541, 205641, 205741 and 205841 from an elevation angle of  $1^\circ$  ( $z \sim 100$  m).



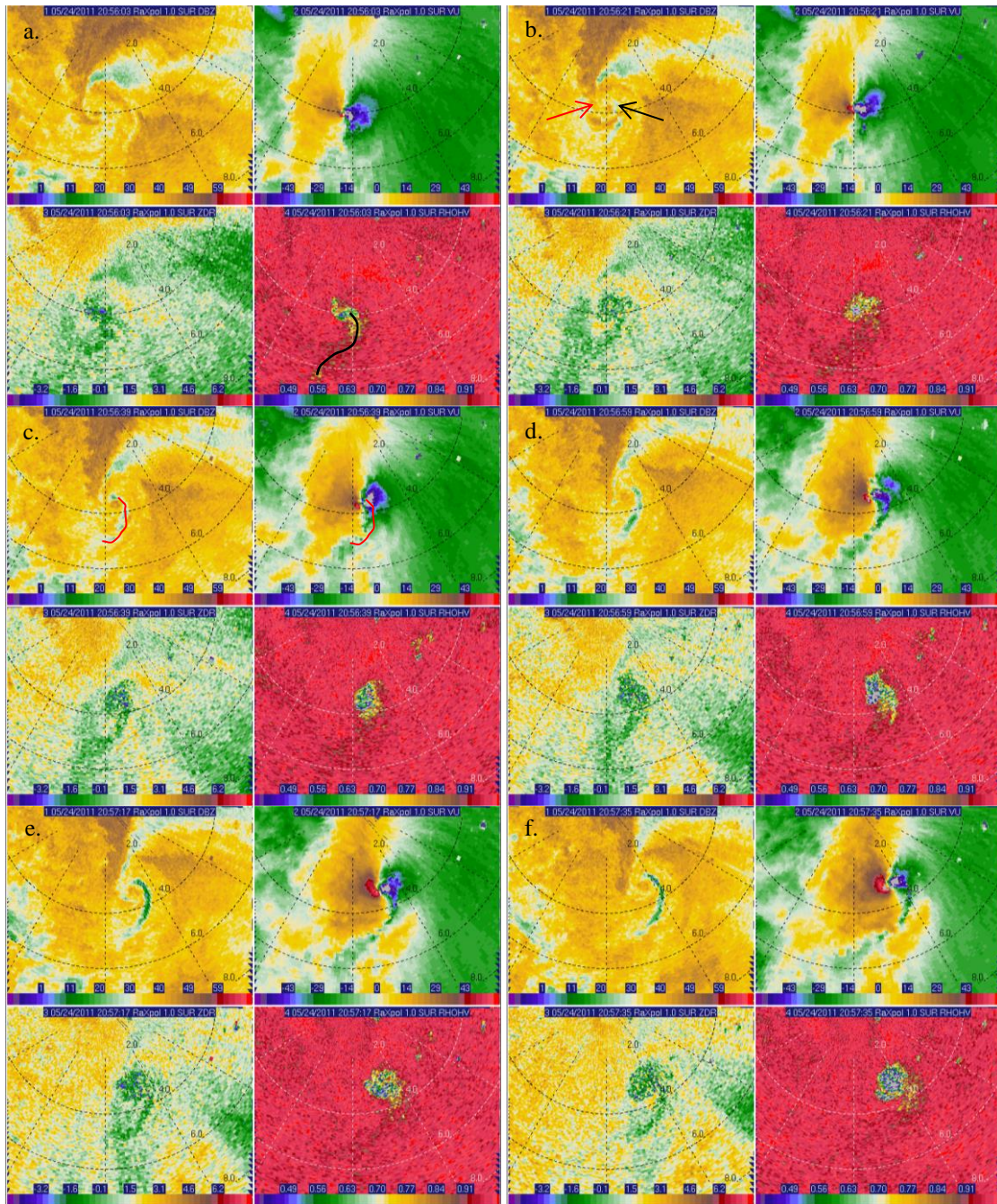


Figure 61: 4-panel plots of the development of the WRB from 1° elevation angle at (a) 205603; (b) 205621; (c) 205639; (d) 205659; (e) 205715; and (f) 205735. The black line in (a) indicates a zone of reduced  $\rho_{hv}$ . The black arrow in (b) indicates the developing WRB and the red indicates a band of slightly higher reflectivities. The red lines in (c) indicate the location of the WRB with respect to the velocity shift associated with the RFGF.

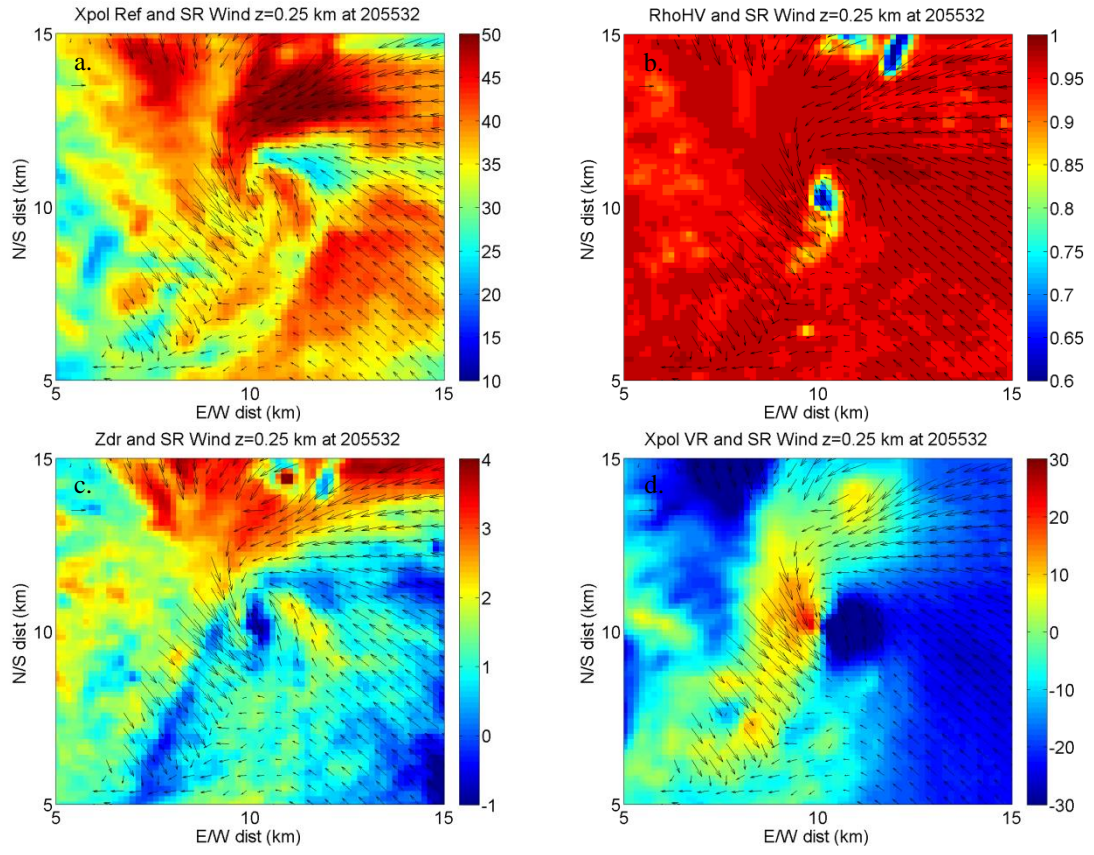


Figure 62: Dual-Doppler analyses valid at 205532 for  $z = 250$  m. (a) reflectivity; (b)  $\rho_{hv}$ ; (c) Zdr; (d) RaXPOL storm-relative radial velocity. Reference vector below the sub-letter is  $20 \text{ m s}^{-1}$ .



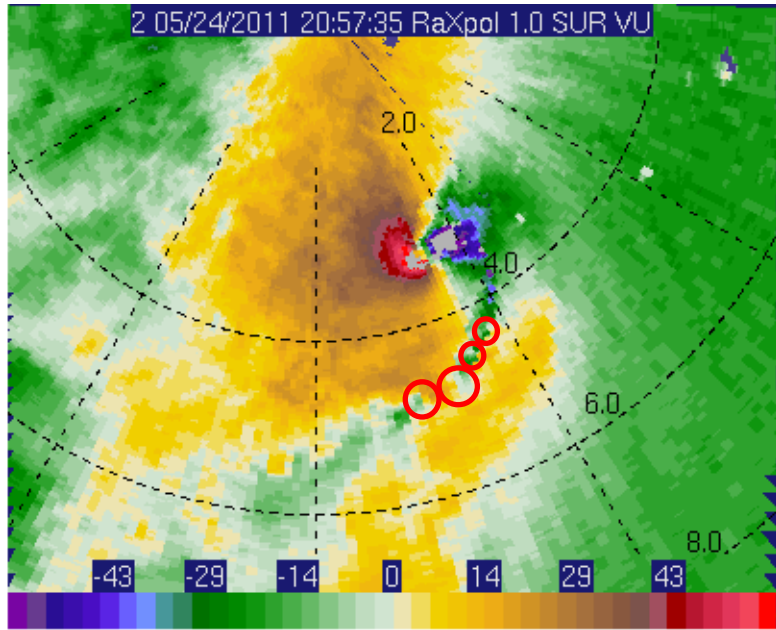


Figure 63: Zoomed-in radial velocity panel from Figure 61f. Red circles indicate locations of misovortices along the leading edge of the WRB.

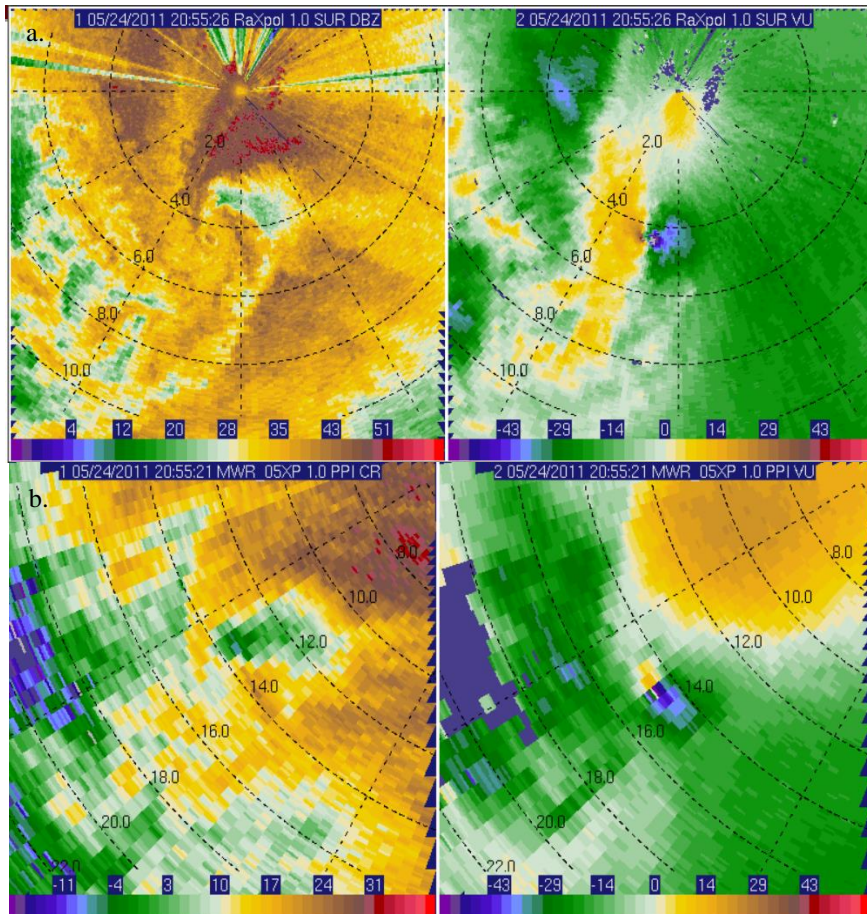


Figure 64: Reflectivity and radial velocity for 205526, just prior to the development of the WRB. (a) RaXPol; (b) MWR-05XP. (Both images for 1° elevation angle.)

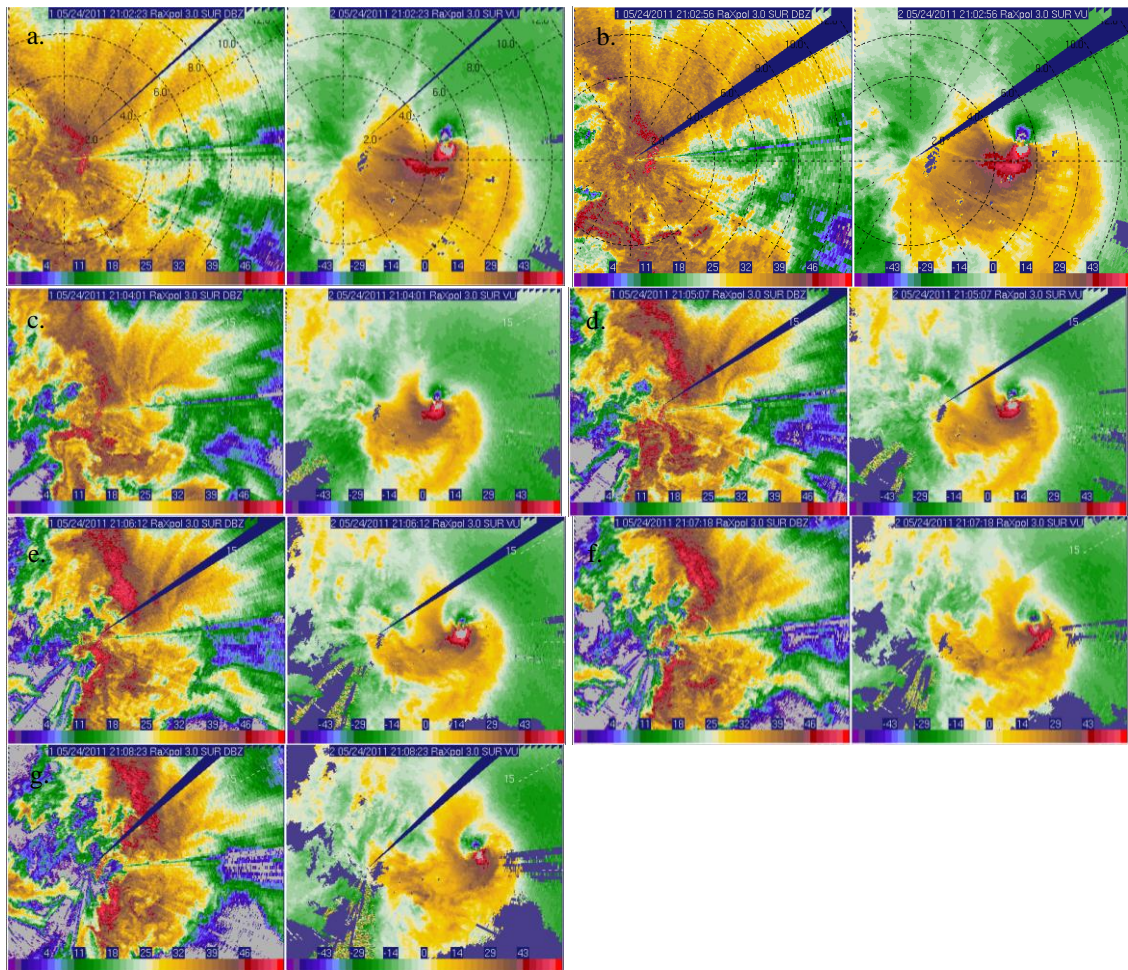


Figure 65: 4-panels illustrating the evolution of outflow surrounding tornado from 3° elevation angle for (a) 210223; (b) 210256; (c) 210401; (d) 210507; (e) 210613; (f) 210718; (g) 210823. Note that the time between figures b-g is constant (1 minutes 6 s), but there are only 33 seconds between a and b. This is done to better illustrate the evolution of the outflow winds between a and b and because 210223 is the first time data are available at 3° after the volume scans are resumed.

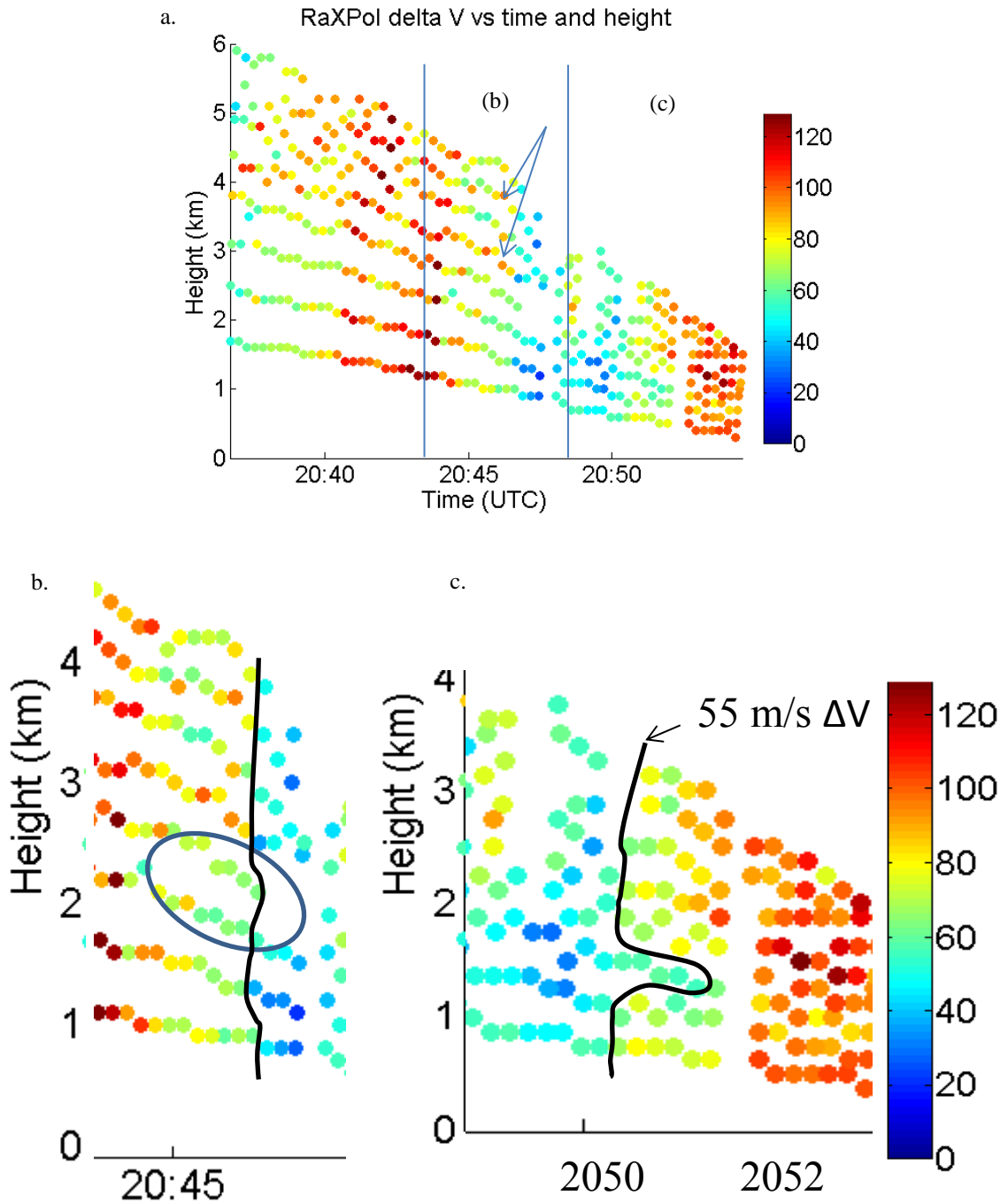


Figure 66: Plot of  $\Delta V_{\max}$  with time (abscissa, increasing to the right), and height (ordinate, increasing up) (a) for the entire first portion of volumetric data collection (2036-2054). The magnitude of  $\Delta V_{\max}$  is indicated by the color ( $\text{m s}^{-1}$ ). Vertical lines indicate portion of graphic zoomed in for (b) and (c), and arrows point to increased circulation aloft that did not become tornadic (b) As in (a) except zoomed in on tornado decay. The ellipse indicates the region of initial weakening at mid-levels. (c) As in (a) except zoomed in on tornadogenesis.



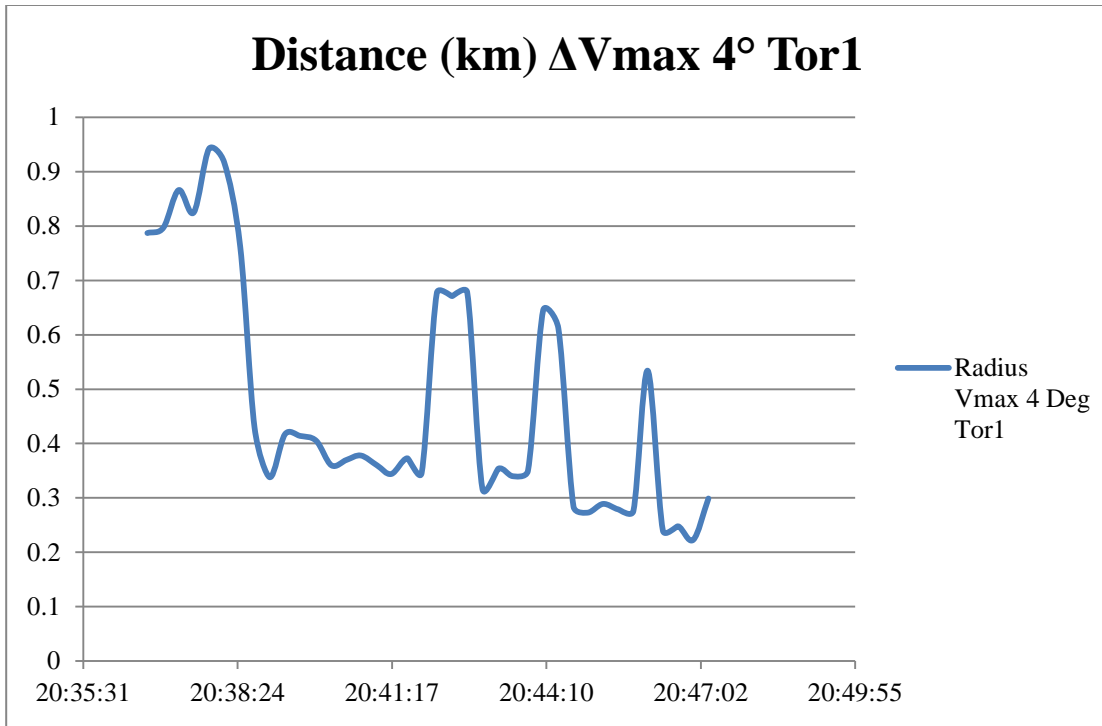


Figure 67: Distance between the maximum and minimum radial velocities of  $\Delta V_{\max}$  (y axis, km) with time (x axis)



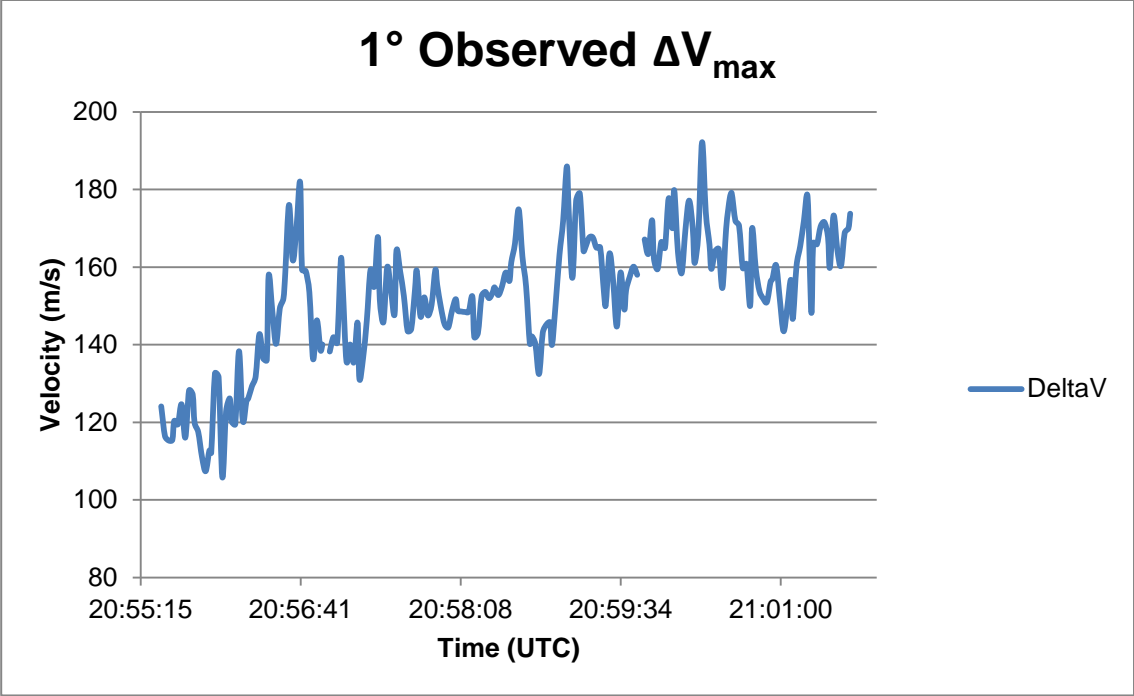


Figure 68:  $\Delta V_{\max}$  with time for the 1° elevation angle PPIs.

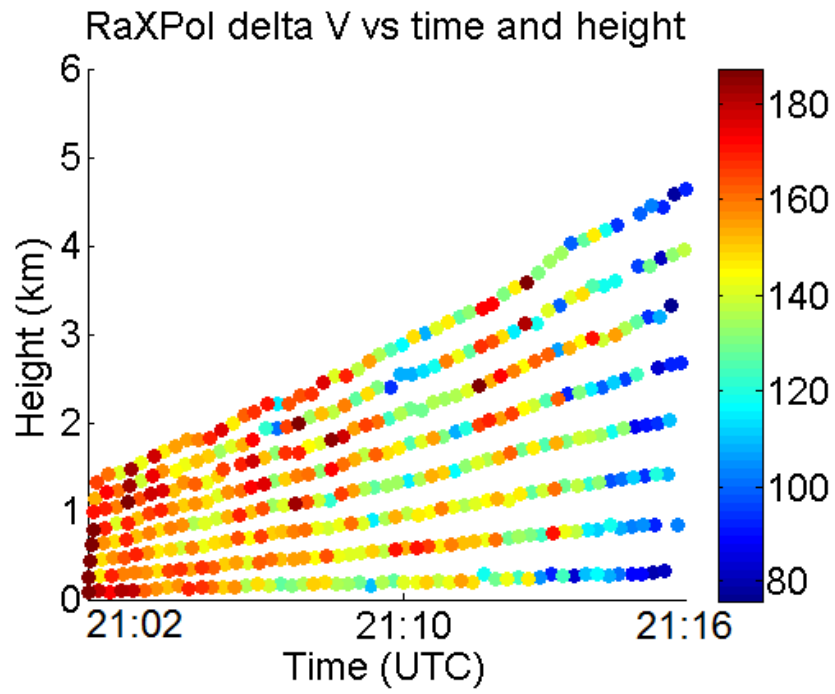


Figure 69: Same as Figure 66 except for 2102 – 2116.

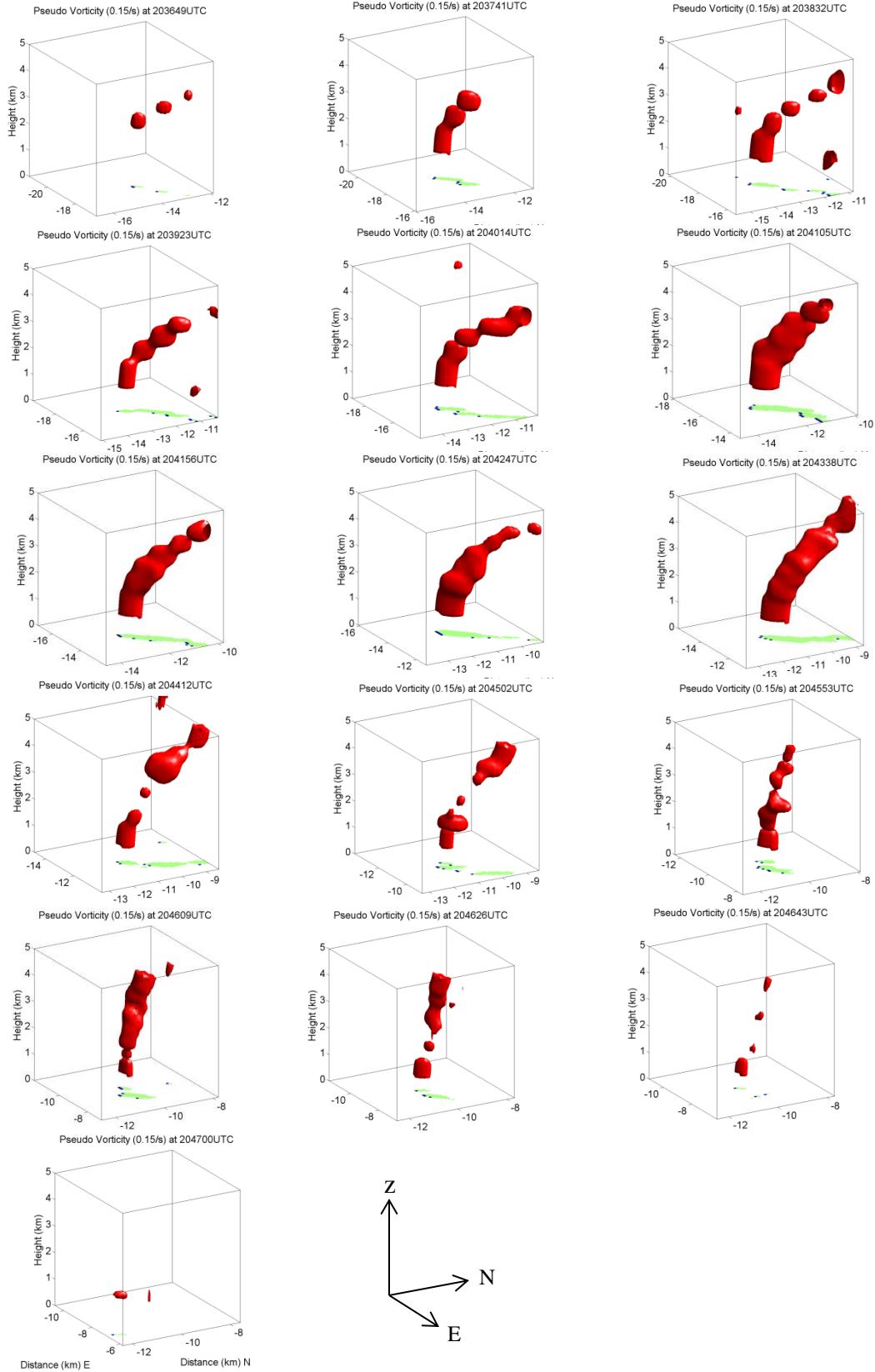


Figure 70: Pseudovorticity isosurfaces of the  $0.15 \text{ s}^{-1}$  contour and shadow projection on the x-y plane over the duration of tornado 1 for which data are available.

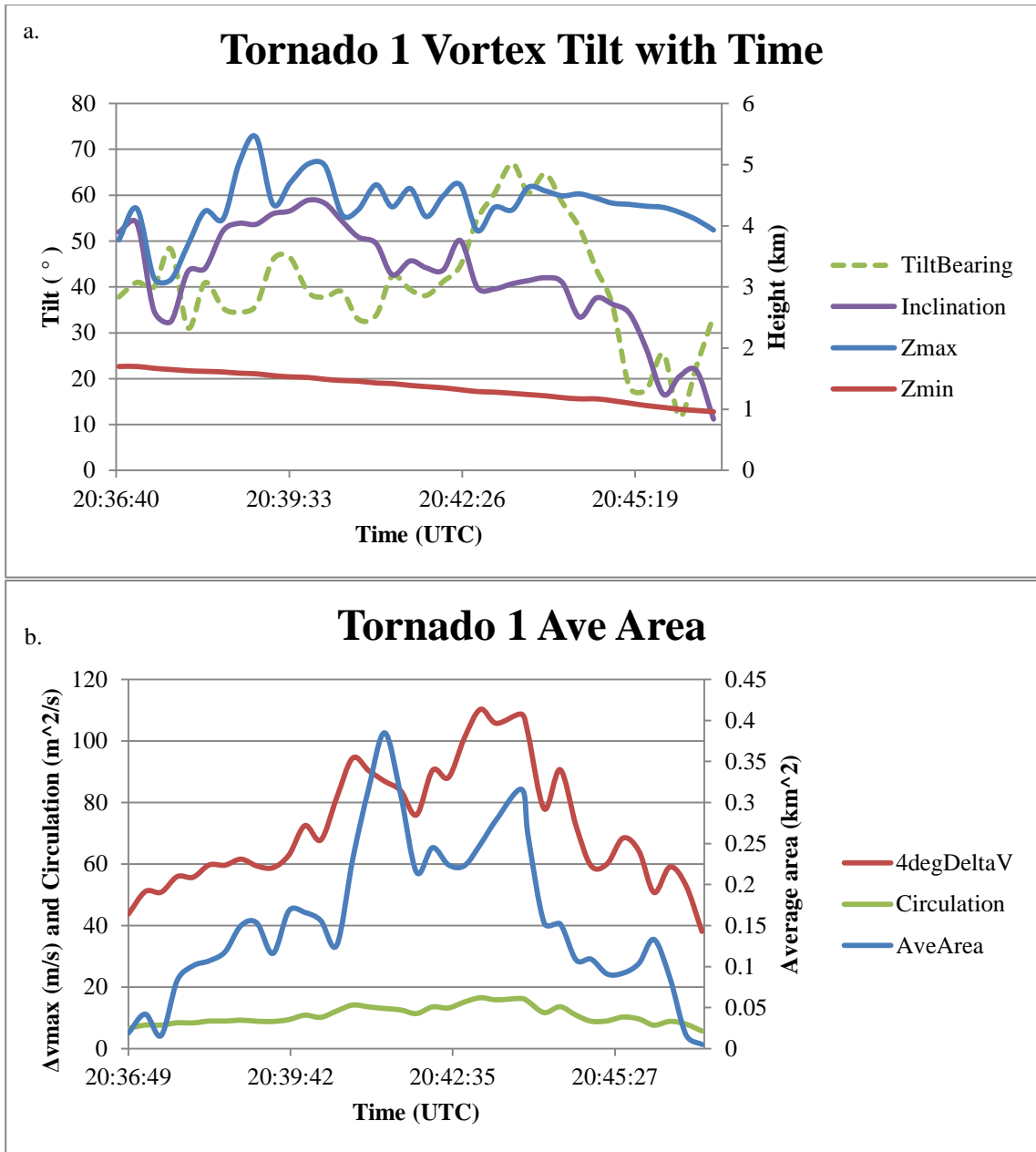


Figure 71: Structure of tornado 1 over the duration observations are available (2036-2047). (a) Inclination angle (tilt) ( $0^\circ$  is vertically erect) between the center of the TVS at lowest elevation angle to the center of the TVS at the highest elevation angle (purple line), tilt bearing (azimuthal direction of tilt) (purple line), height of the beam for the top elevation angle at the TVS ( $Z_{max}$  blue line), and height of the beam for the lowest elevation angle at the TVS ( $Z_{min}$  red line). (b) Average area ( $\text{km}^2$ ) of the region bound by the  $0.15 \text{ s}^{-1}$  vorticity isopleth.

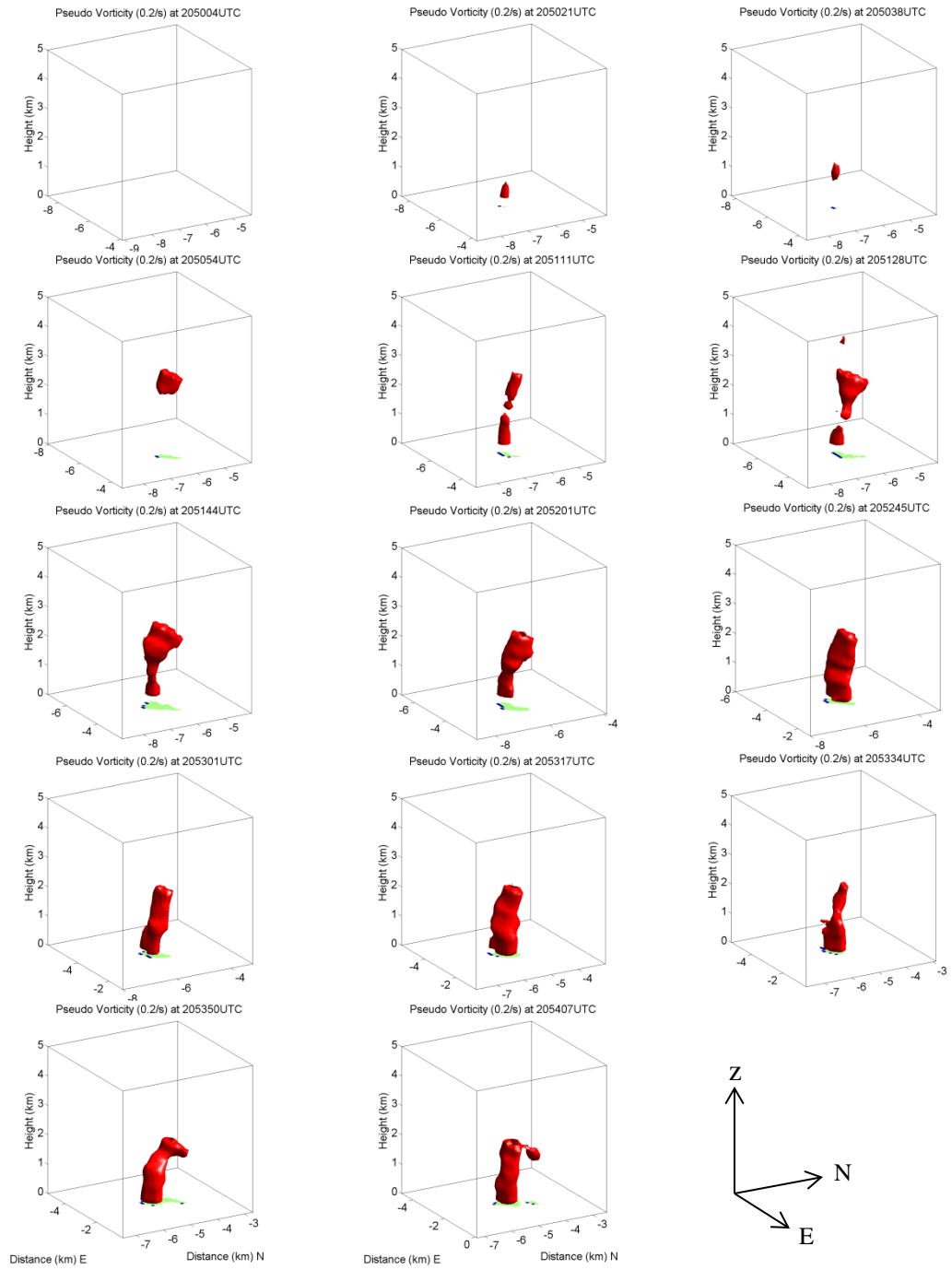


Figure 72: Same as Figure 70 except for the  $0.2 \text{ s}^{-1}$  isosurface.

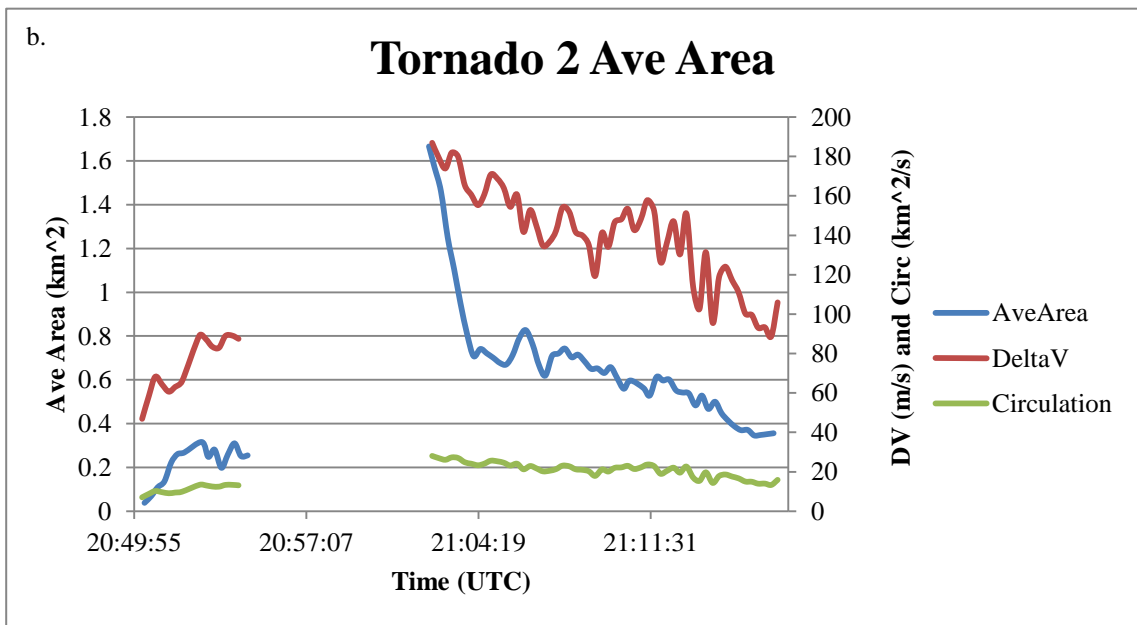
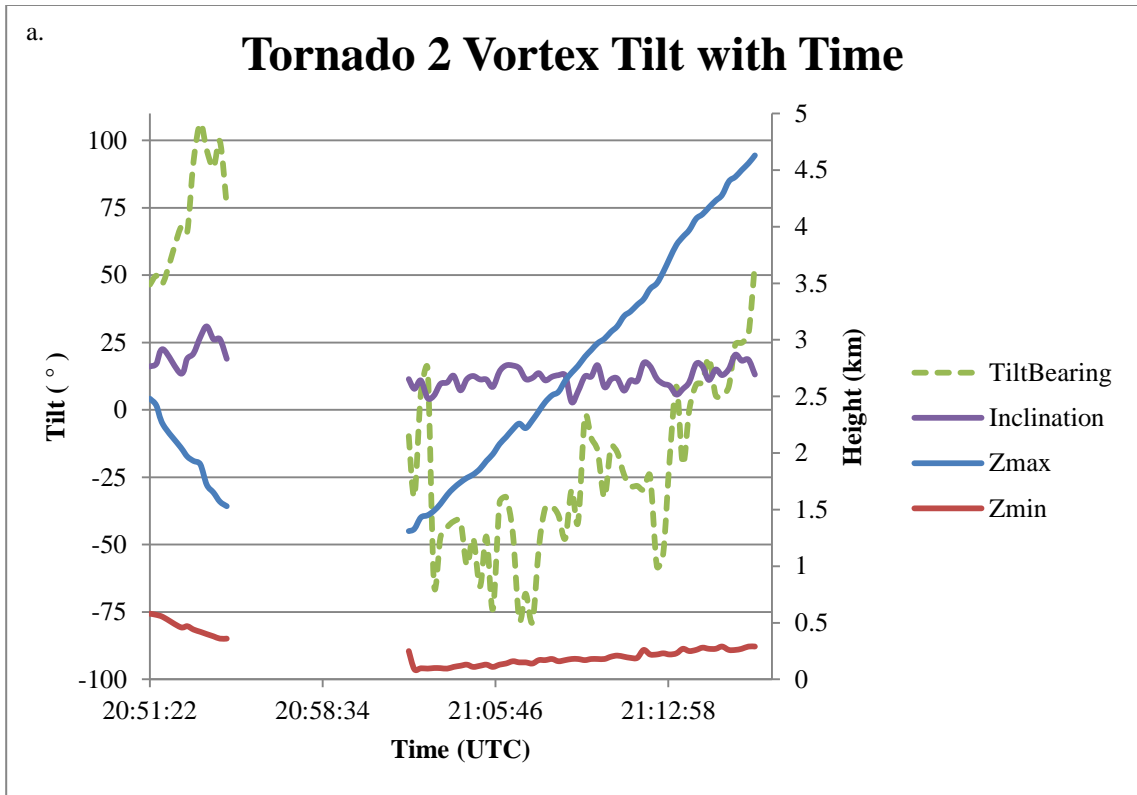


Figure 73: Same as Figure 71 except for tornado 2.

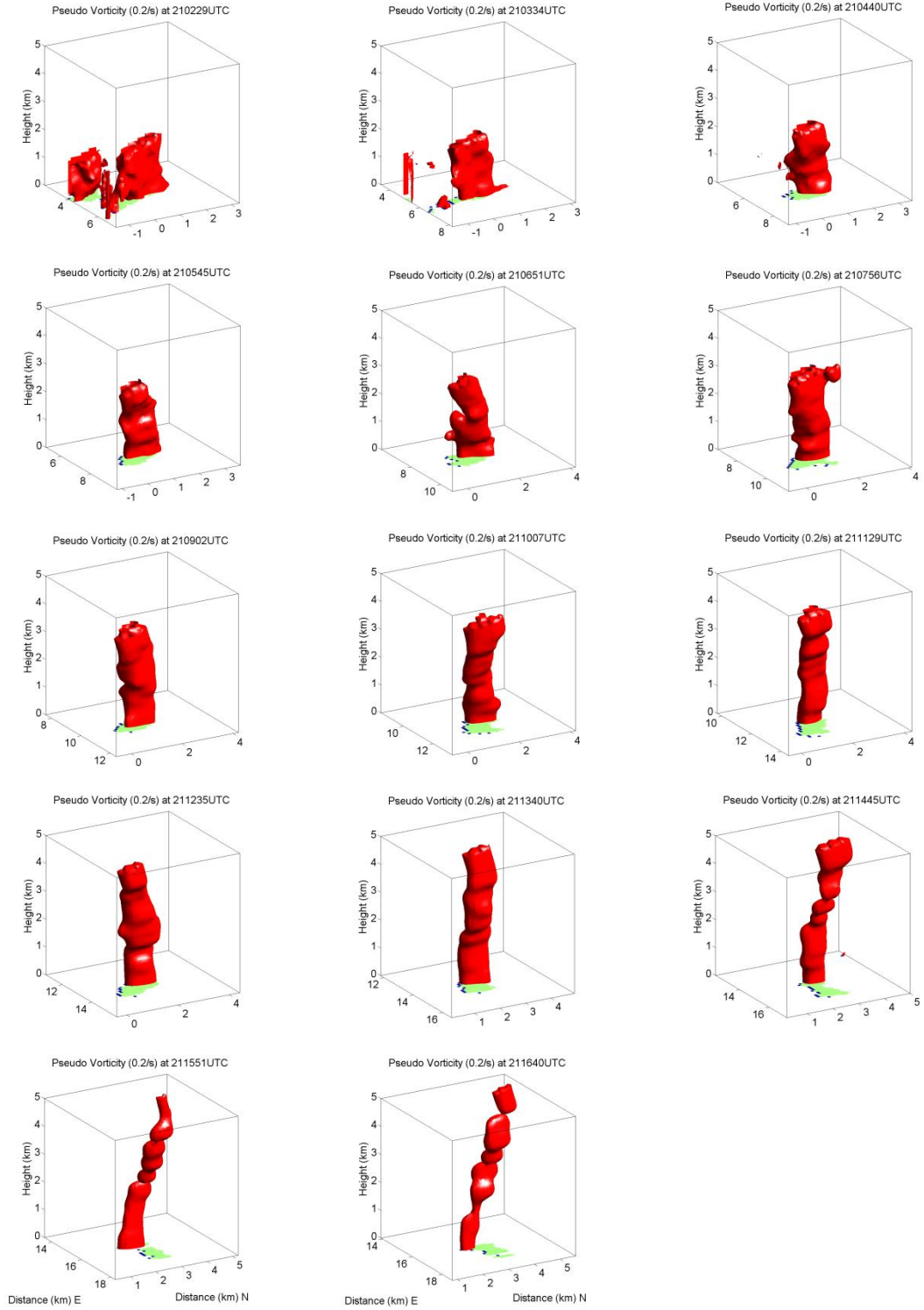


Figure 74: Same as Figure 70 except for 2102-2116.  $\Delta t=70$  s.

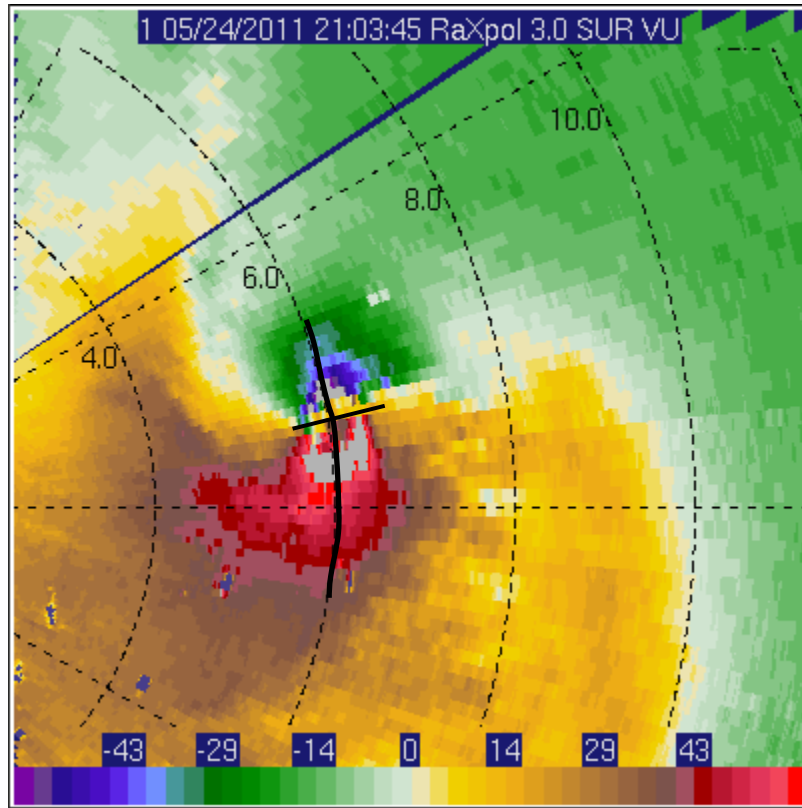
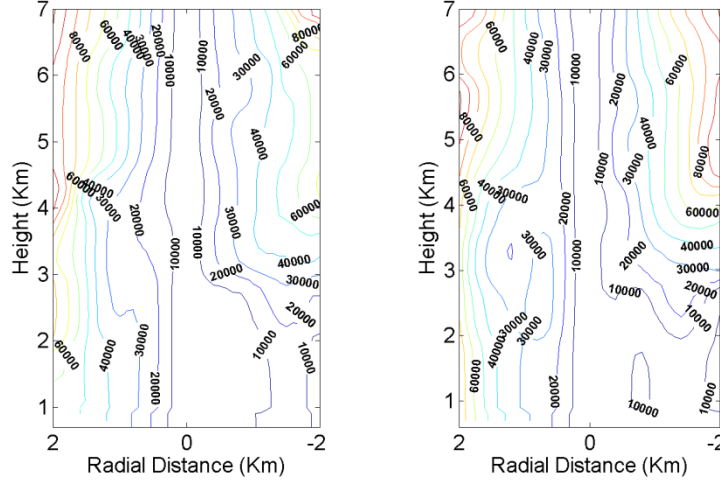


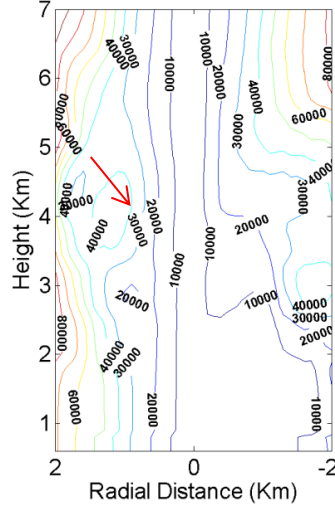
Figure 75: Radial velocity from 210345. Illustration of different lengths of axial and radial diameters of the tornado. Gray areas indicate radial velocities greater than or less than the color bar values. Specified color bar was retained for clarity of radial velocity gradients.



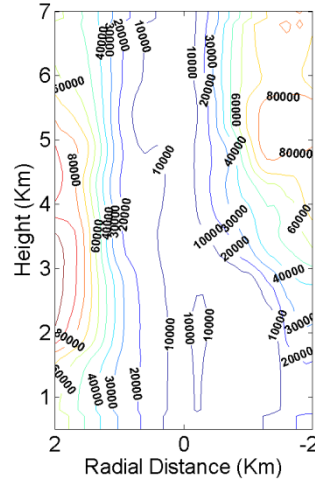
Angular Mom ( $m^2/s$ ) at R=23.7 km 203649 Angular Mom ( $m^2/s$ ) at R=22.2 km 203832



Angular Mom ( $m^2/s$ ) at R=20.7 km 204014



Angular Mom ( $m^2/s$ ) at R=19 km 204156



Angular Mom ( $m^2/s$ ) at R=17.2 km 204338 Angular Mom ( $m^2/s$ ) at R=15.2 km 204519

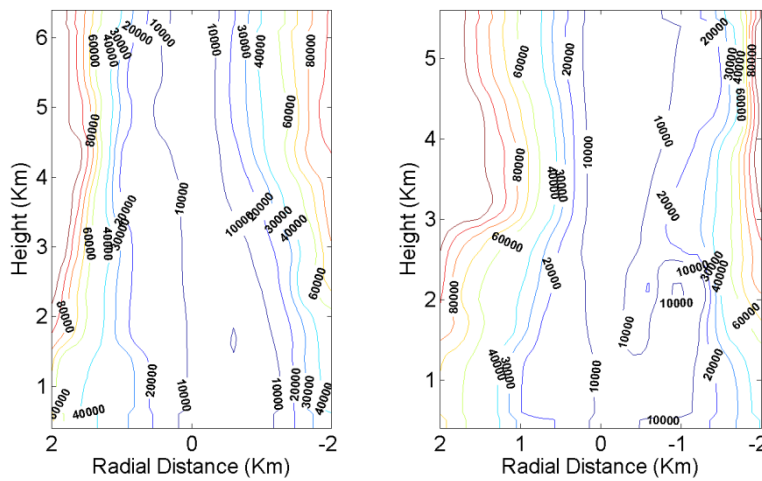


Figure 76: Constant radius cross section plots of pseudo angular momentum (contours,  $m^2 s^{-1}$ ) calculated from the storm-relative radial velocity for tornado 1. Time of the analysis is given in the title, as is the

distance from the radar. Radial distance is the distance from the center of the tornado. Red arrow points to undulation.

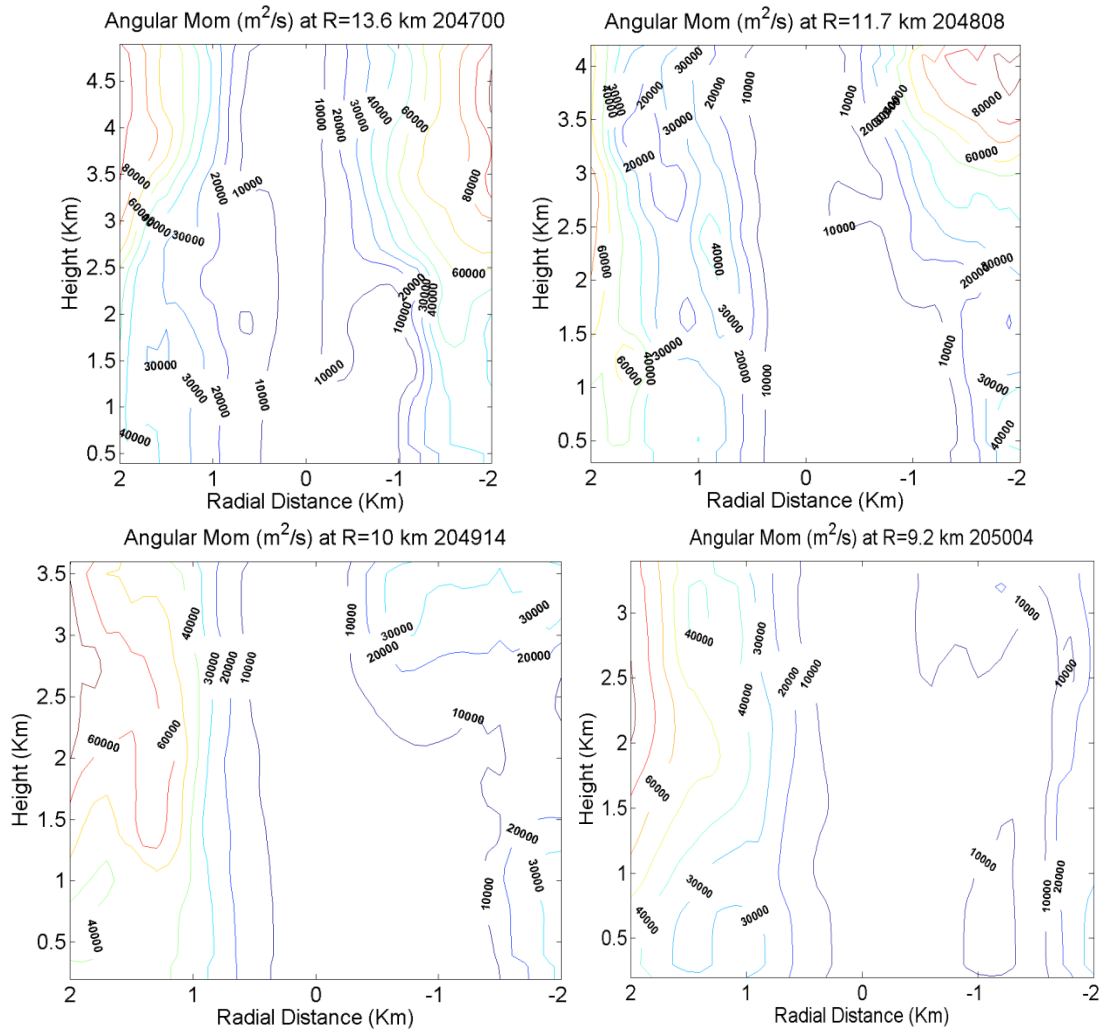


Figure 77: Same as Figure 76 except for the pretornadic tornado 2 circulation.

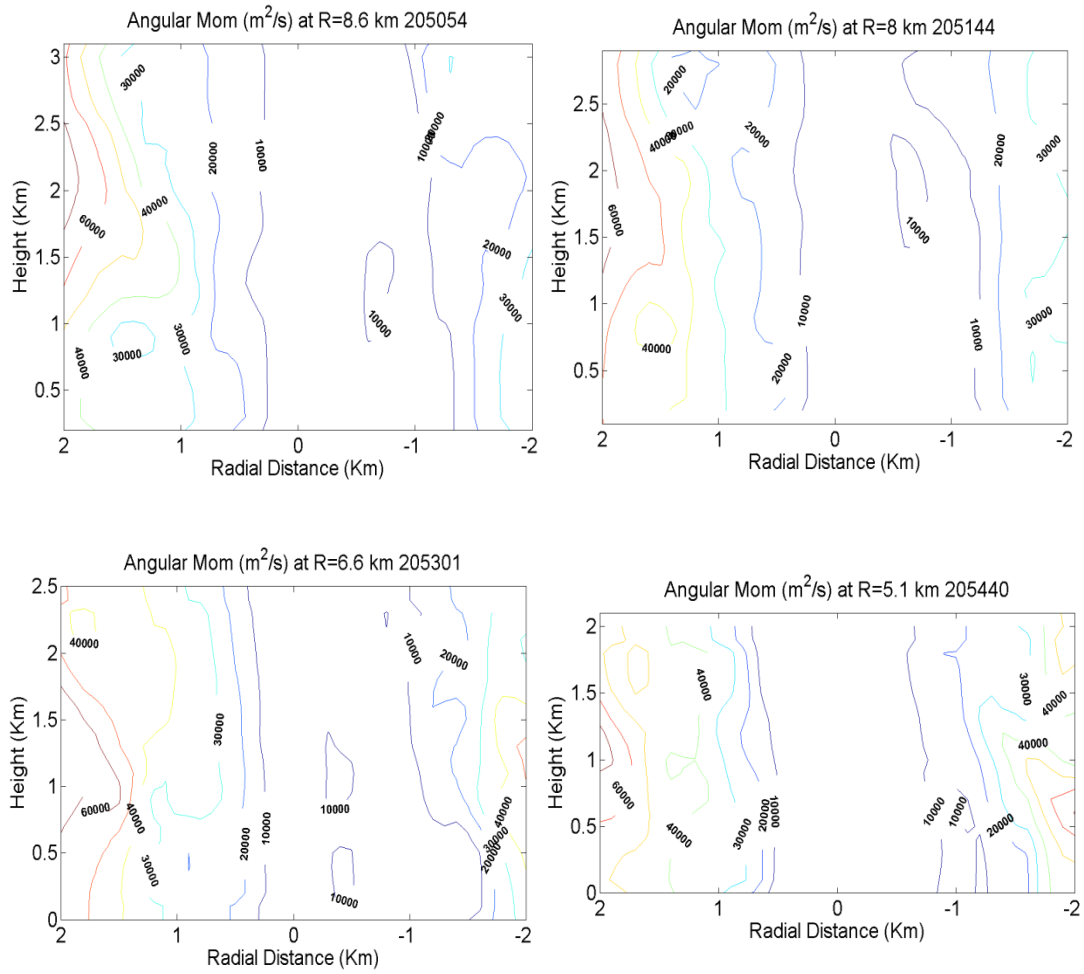


Figure 78: Same as Figure 76 except for genesis and initial intensification of tornado 2.

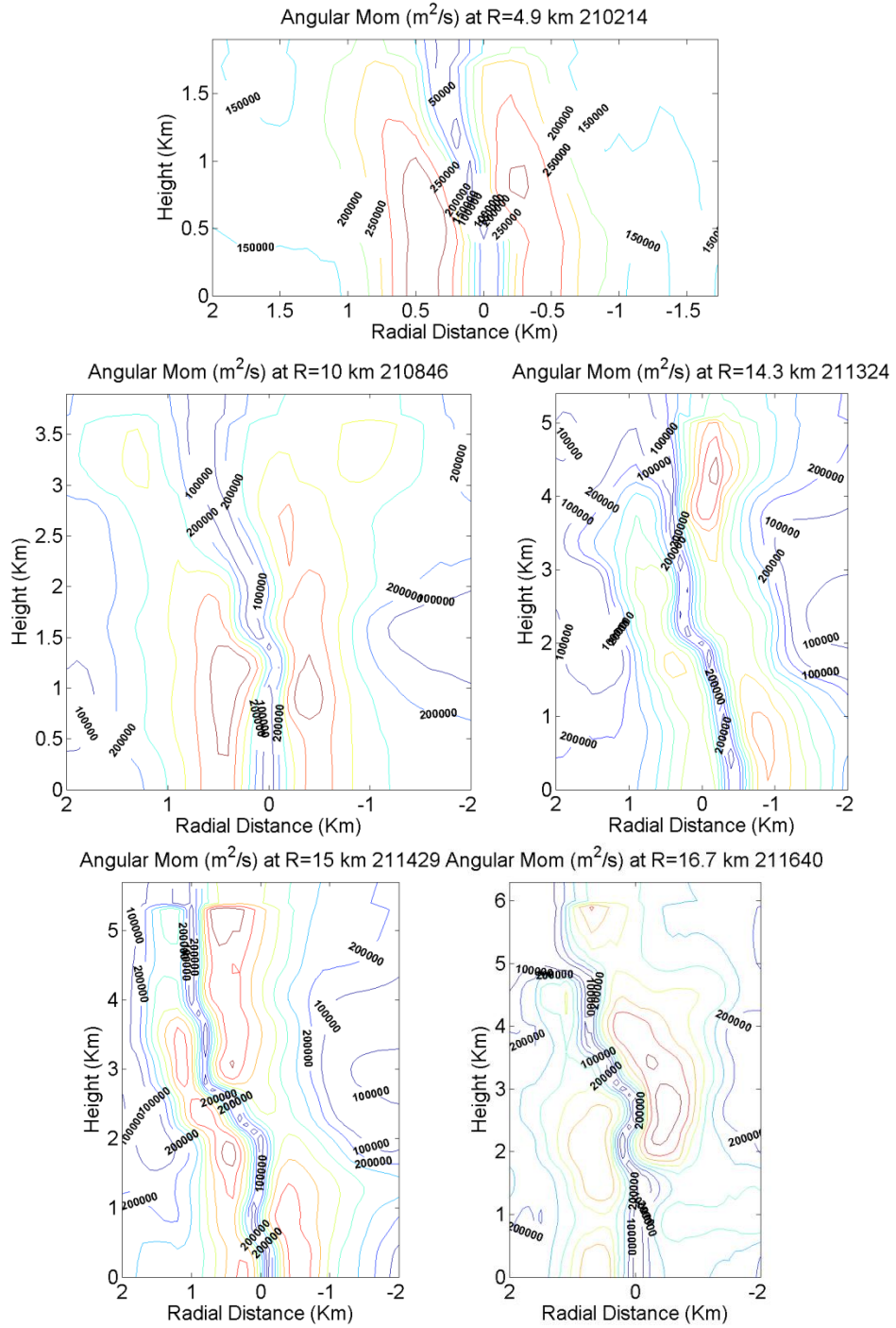


Figure 79: Same as Figure 76 except for the last portion of tornado 2 volume scans.

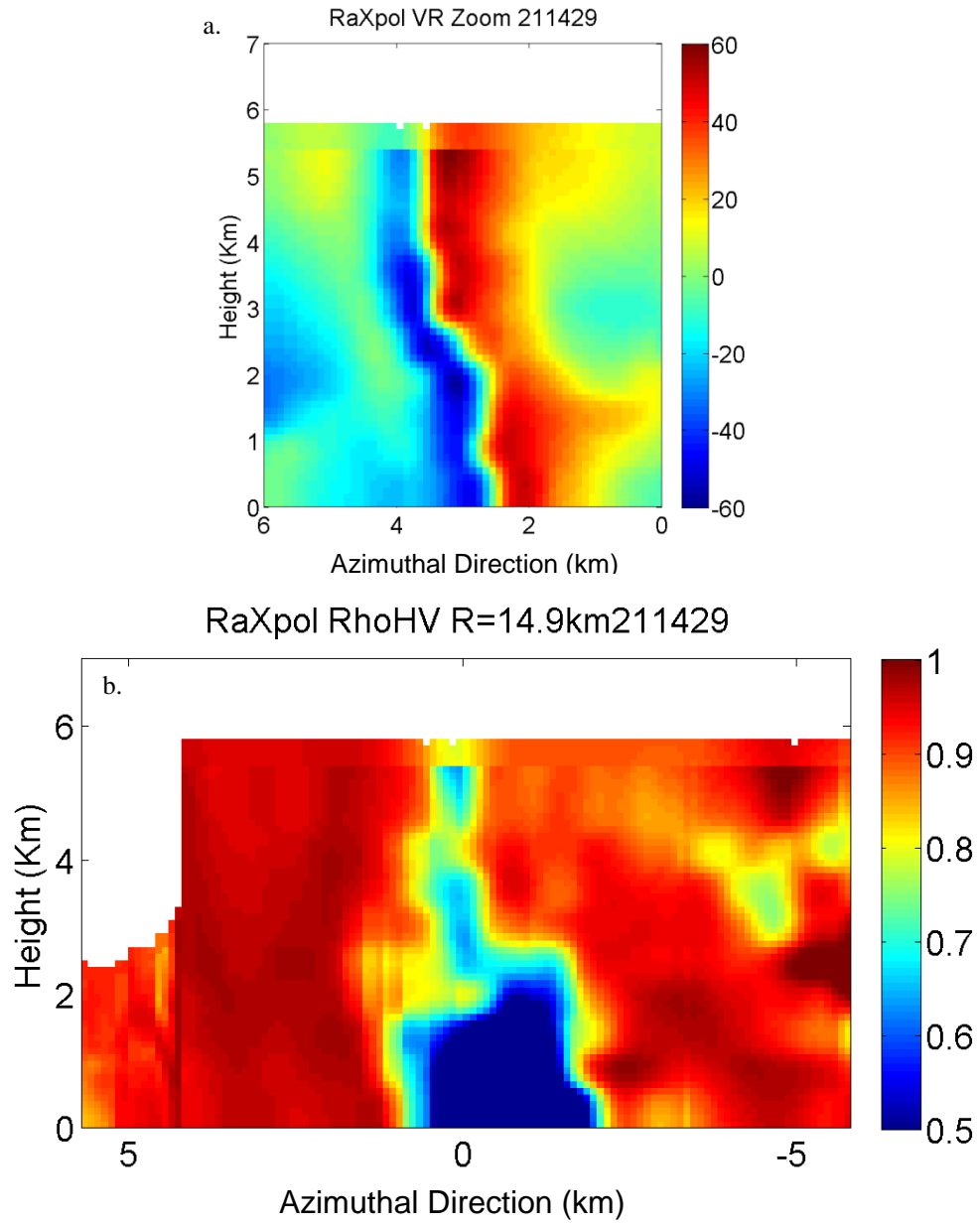


Figure 80: Constant radius vertical cross sections of (top) radial velocity, and (bottom),  $\rho_{hv}$  depicting oscillations along the inner wall of the tornado vortex at the 211429 analysis time.

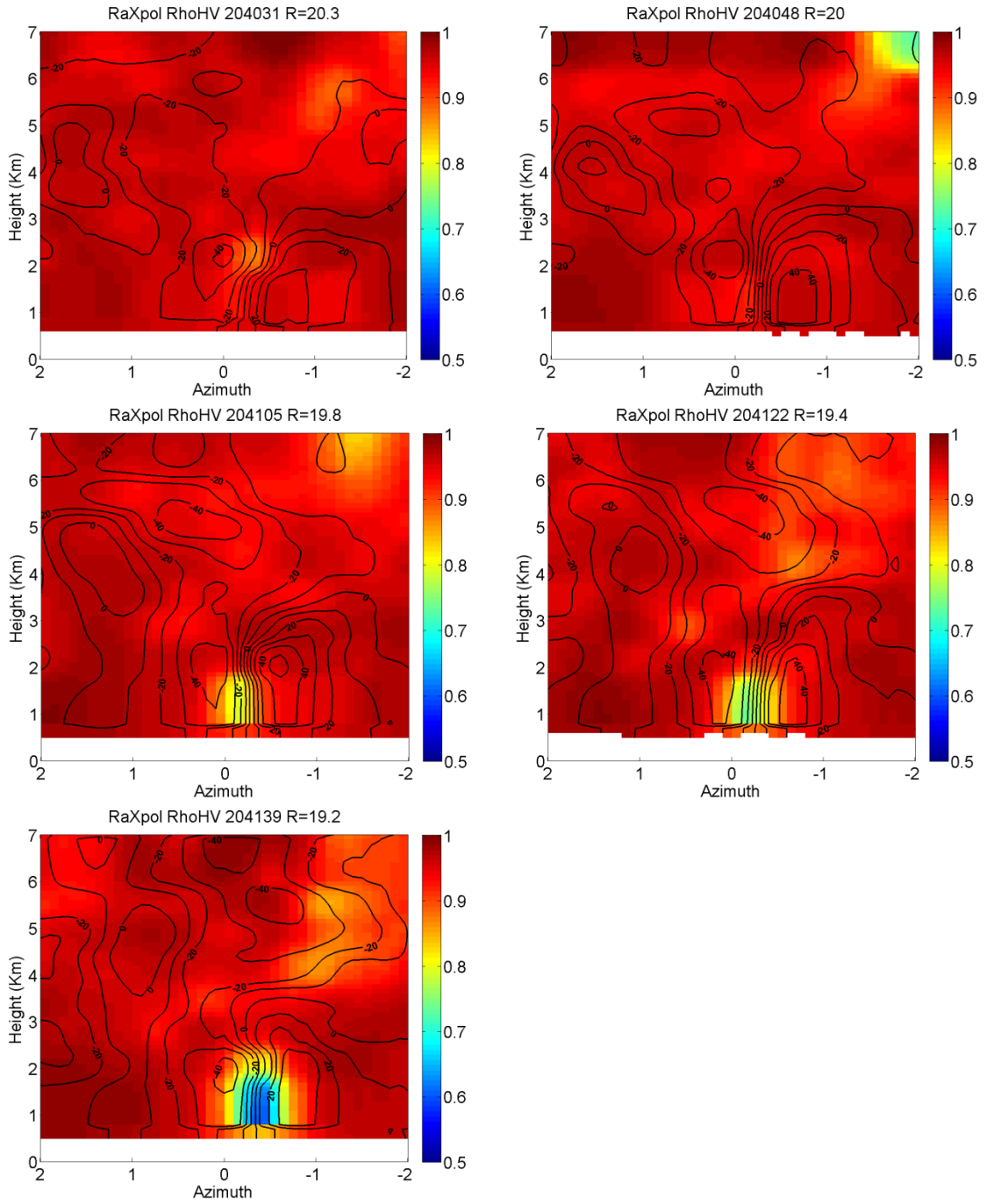


Figure 81: Series of constant radius, (i.e. azimuthal) vertical cross sections of  $\rho_{hv}$  and storm-relative radial velocity contours ( $\text{m s}^{-1}$ ). Times given in the titles of the images. The azimuth notation on the abscissa is arc length (km) from the center of the tornado.

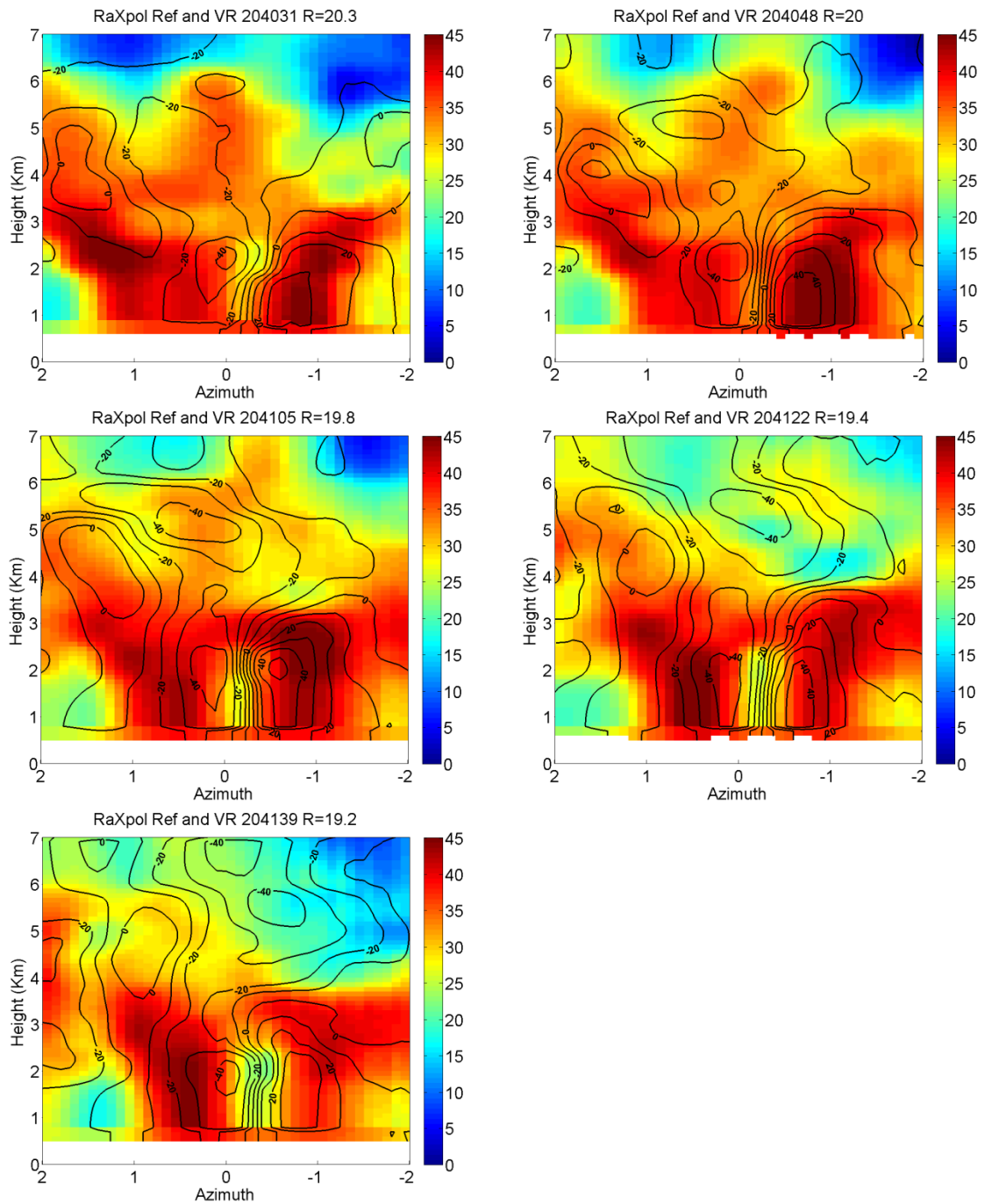


Figure 82: Same as Figure 81 except for reflectivity.

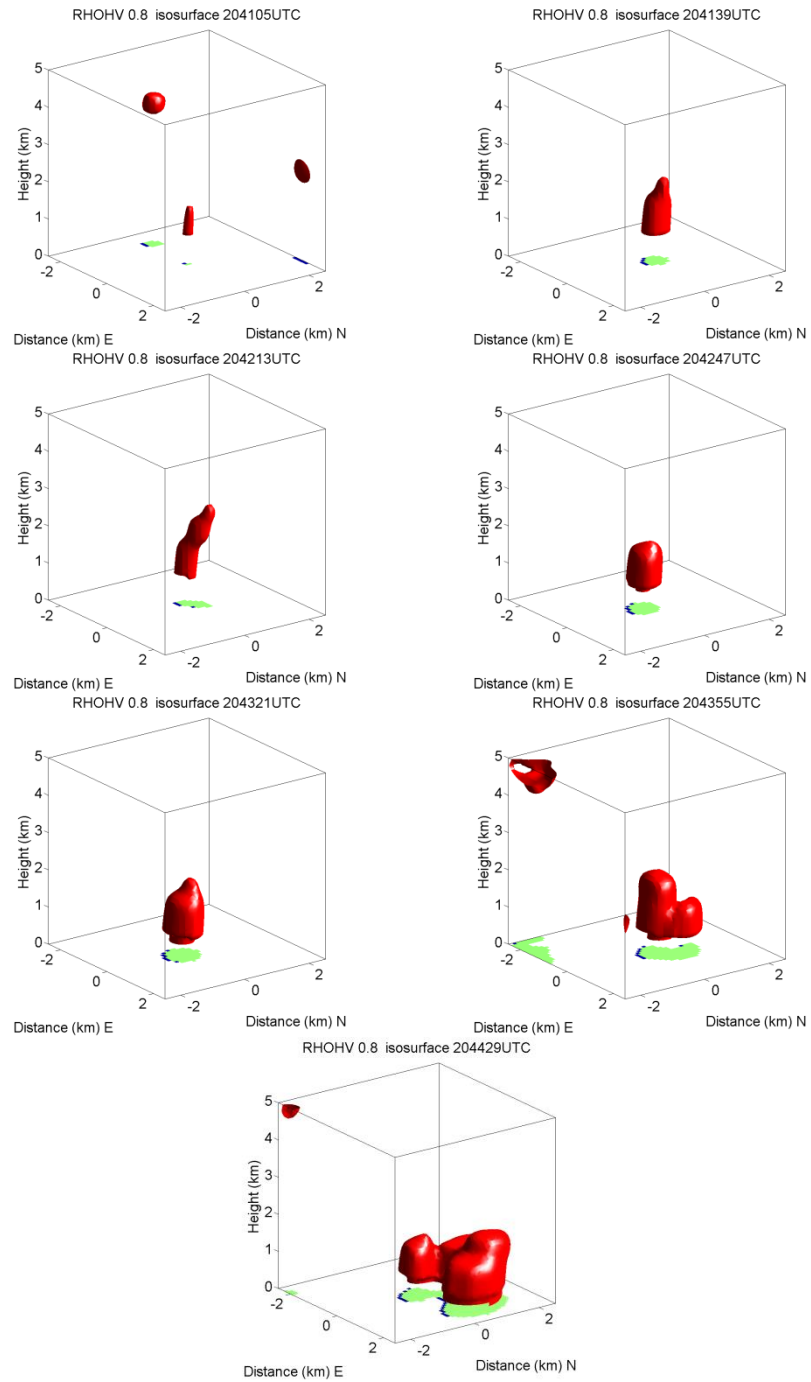


Figure 83: Three-dimensional isopleths of constant  $\rho_{hv} = 0.8$  for the evolution of the TDS of tornado 1.



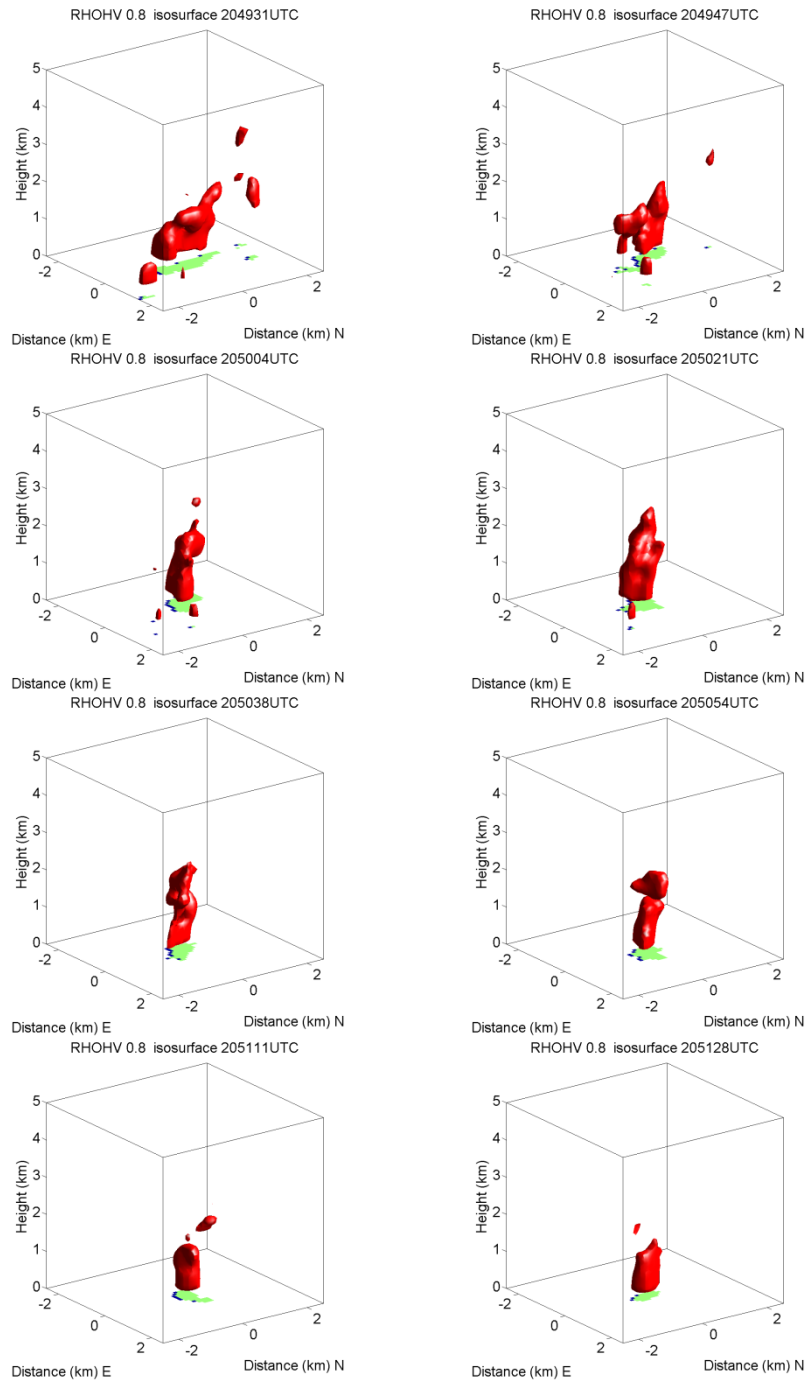


Figure 84: As in Figure 83 except for the genesis of tornado 2.

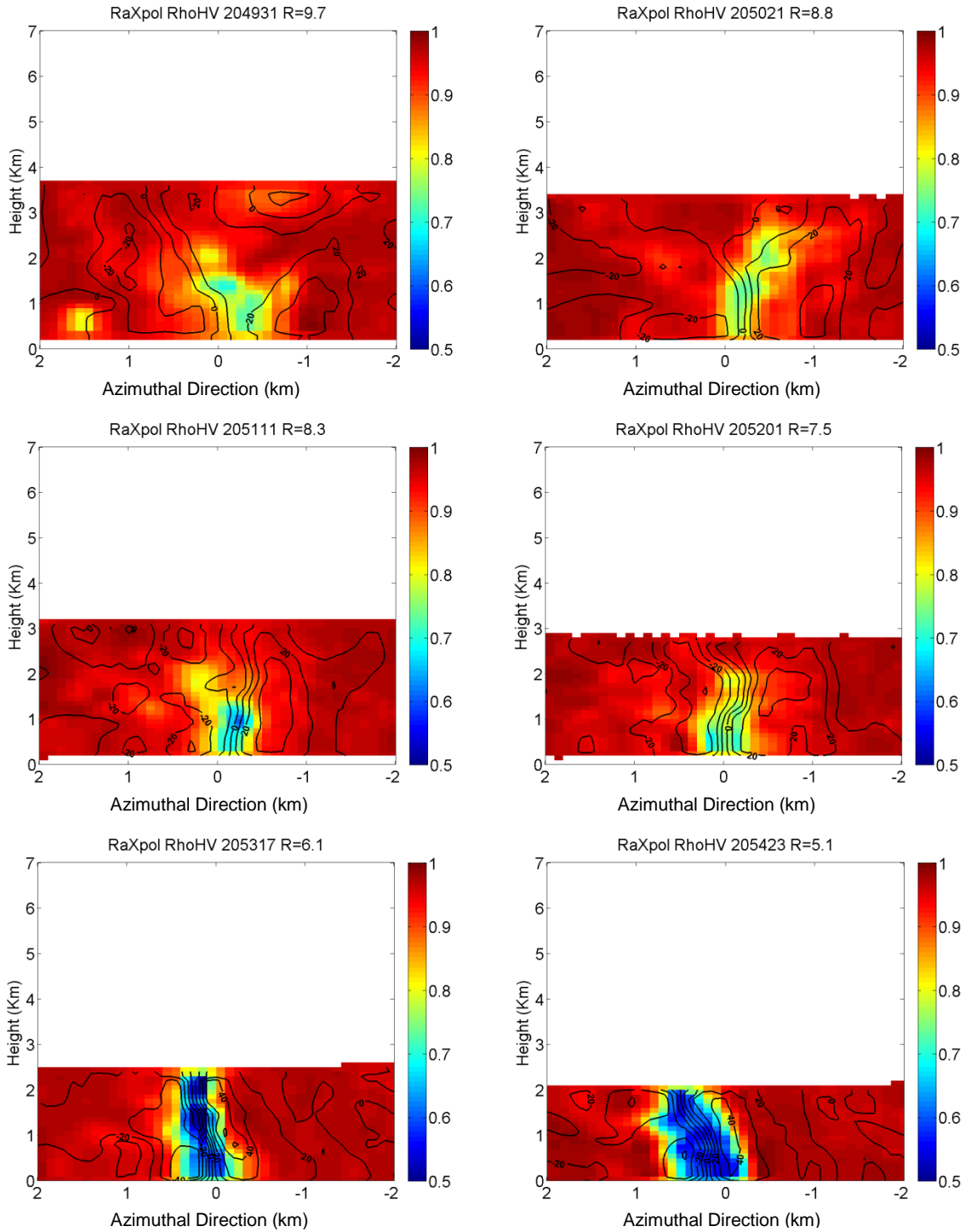


Figure 85: Same as Figure 81 except for the genesis of tornado 2.

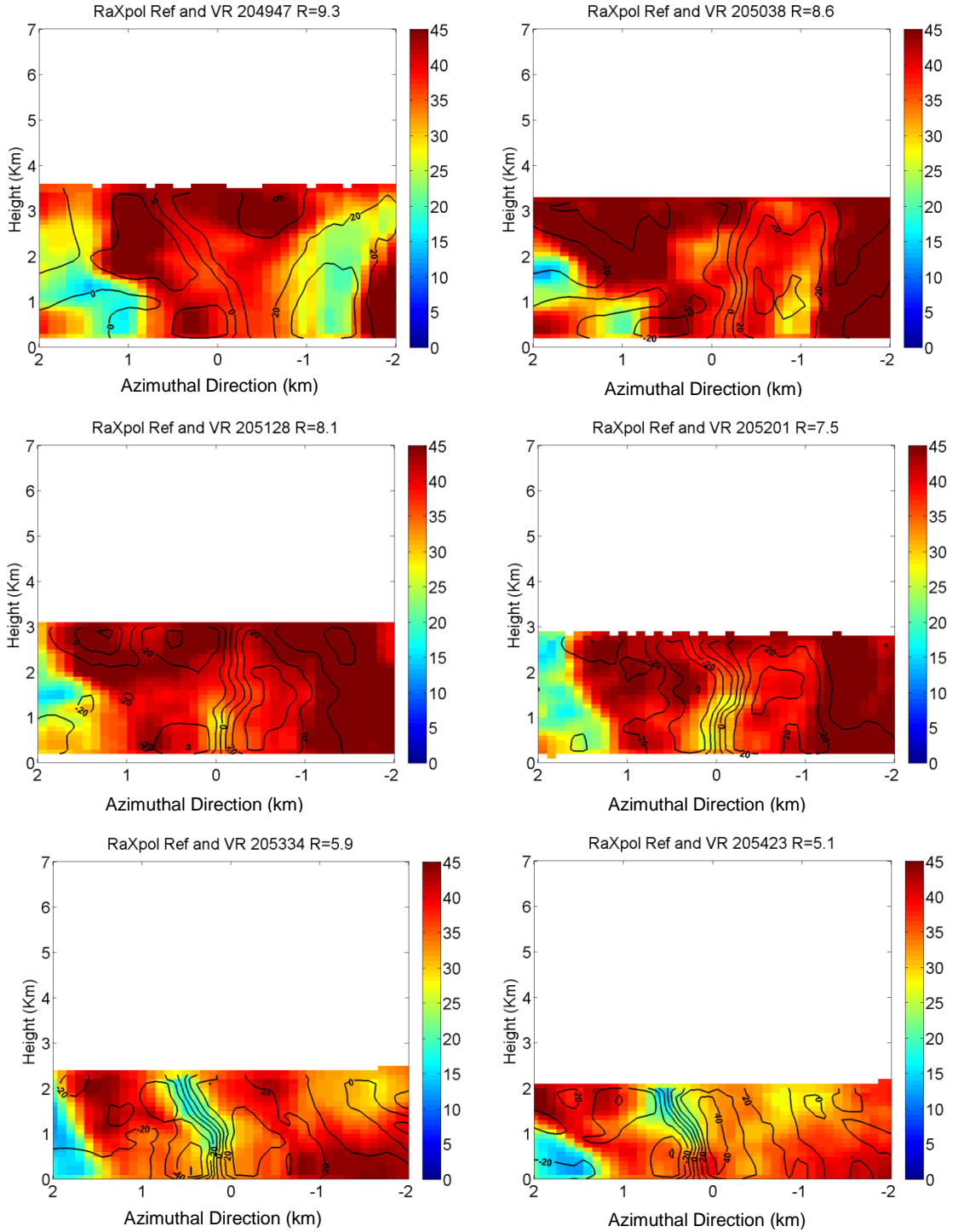


Figure 86: Same as Figure 82 except for the formation of tornado 2.

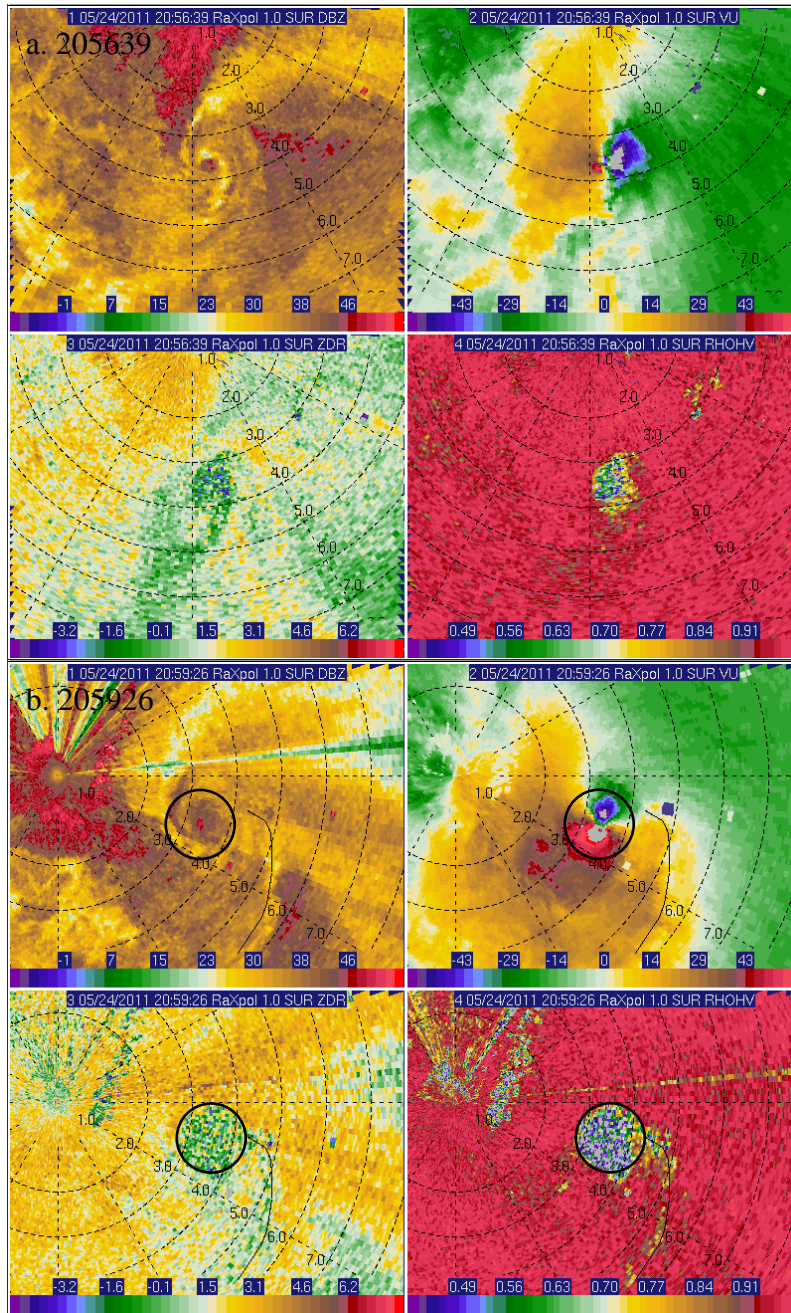


Figure 87: 4-panel images at  $1^\circ$  elevation angle of horizontal extend of TDS and debris ball near the beginning (a) and end (b) of the  $1^\circ$  PPI strategy. The circle identifies the TDS and the thin black line locates the band of low  $\rho_{hv}$  from the RFGF. Range rings are in km



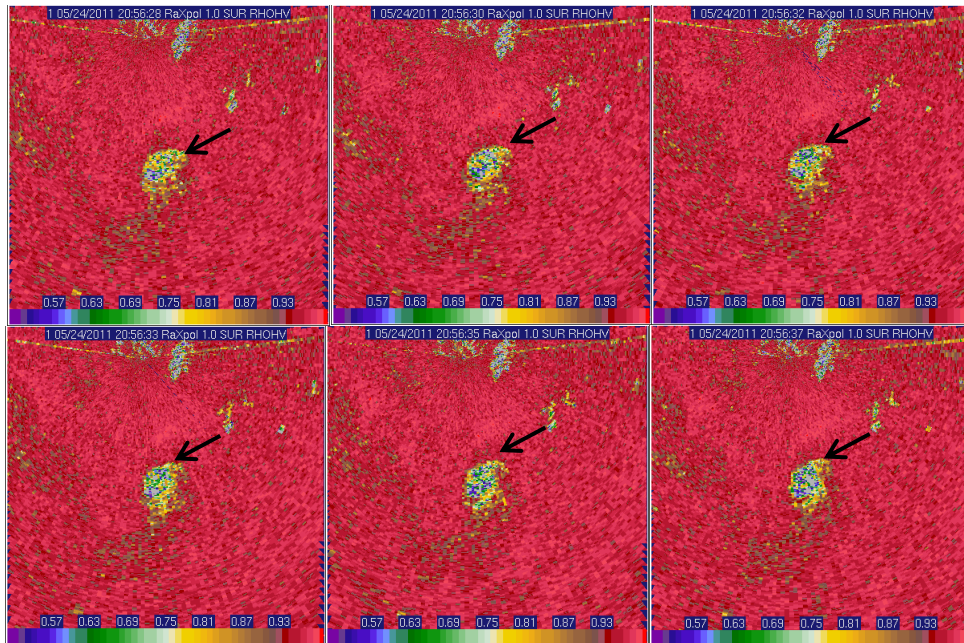


Figure 88: Debris shedding and saw-tooth structure in  $\rho_{hv}$  every 2 seconds between 205628 and 205637.

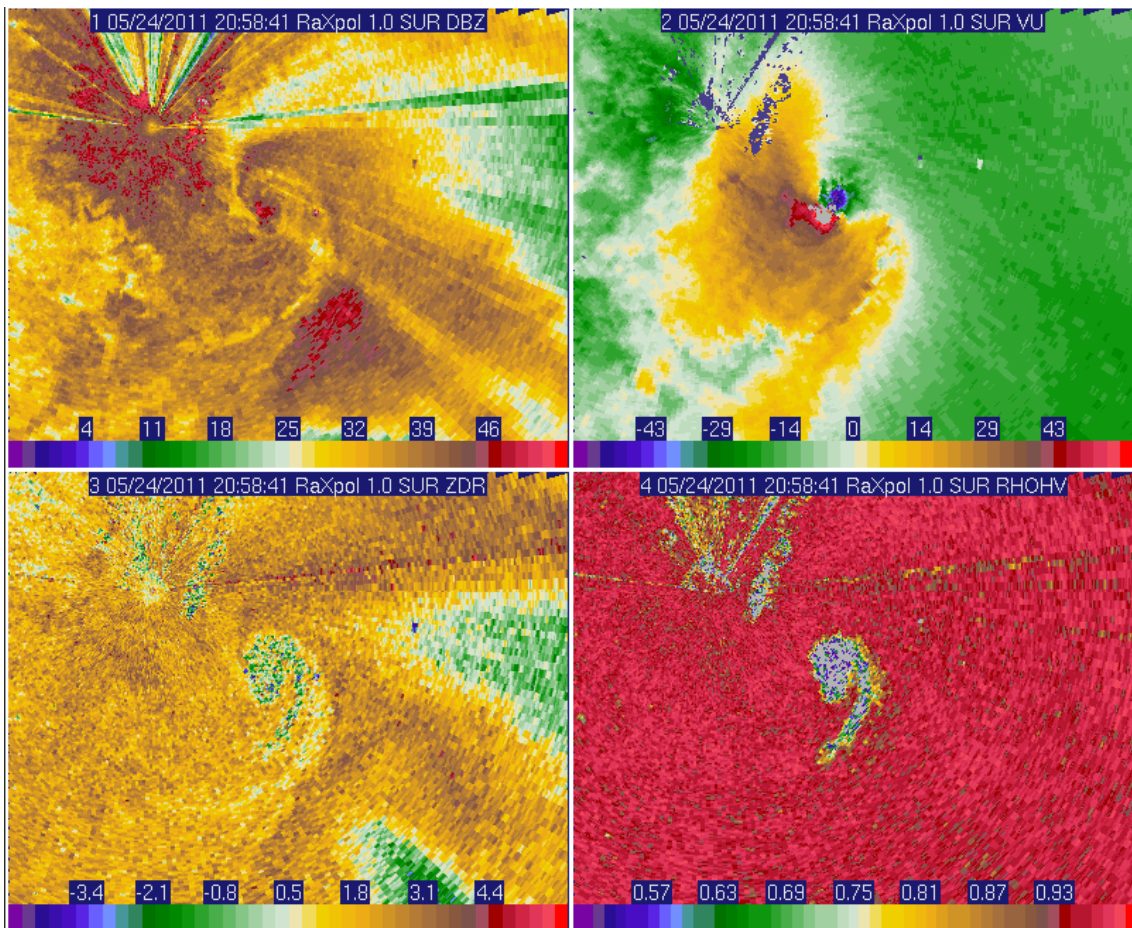


Figure 89: 4-panel illustration of a debris tail for  $1^\circ$  elevation angle at 205841. Beam height  $\sim 70$  m.

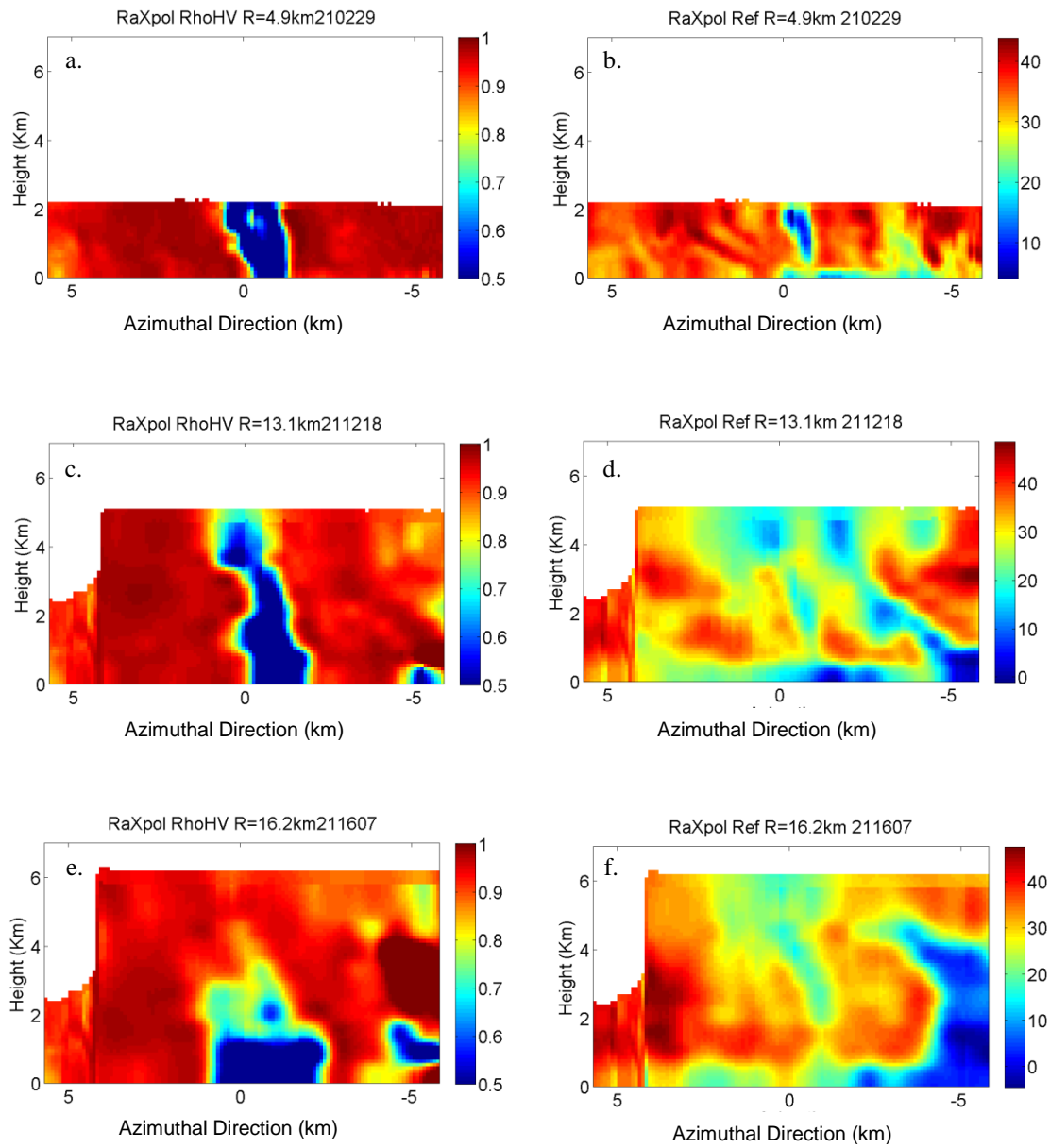


Figure 90: Constant radius vertical cross sections of  $\rho_{hv}$  (left) and reflectivity (right) for (a, b) 210229, (c, d) 211218), (e, f) 211607.

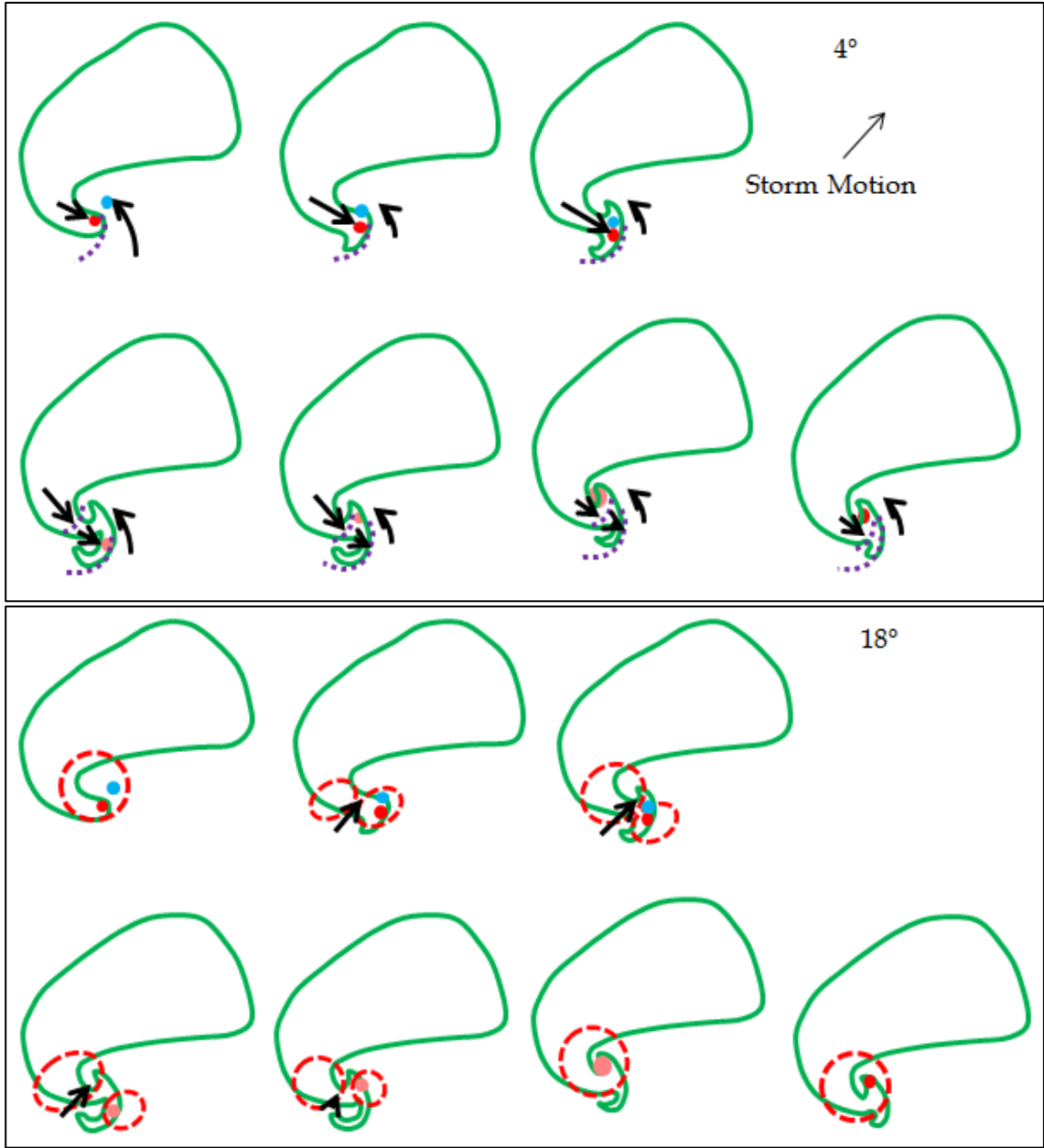


Figure 91: Conceptual model of the cycling process observed between the dissipation of tornado 1 and the genesis of tornado 2. The green outline represents the 25 dBZ reflectivity contour at low-levels. a) Features observed at 4°. Red dot indicates low-level TDS, pink dot indicates subornadic circulation, arrows indicate inflow/outflow, blue dashed curves indicate RFGF locations. b) Features observed at 18°. Blue dot = midlevel TVS, red and pink dots are the low-level circulation, as in (a), the red dashed circles indicate the locations of cyclonic mesocyclones, and the arrow indicates the location and magnitude of the rear inflow jet.

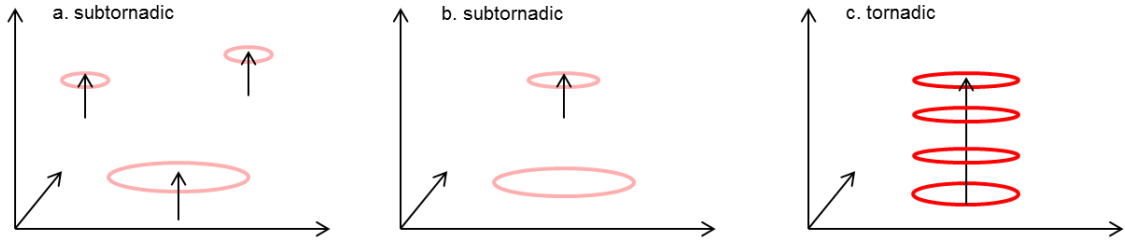


Figure 92: Conceptual model of vertical velocities and the collocation of rotation aloft and at low-levels. Arrows indicate dynamically-induced vertical motion from the low pressure perturbation associated with rotation: pink (red) circles indicate localized regions of subtornadic (tornadic) cyclonic vorticity. a) Transient vortices aloft, b) collocation of vorticity aloft with near-ground vorticity (magnitude of vorticity aloft is presumed to be larger than that below.) c) development of tornado by vertical stretching associated with mid-level rotation. Relative sizes of circulations are indicated by the size of ellipses.



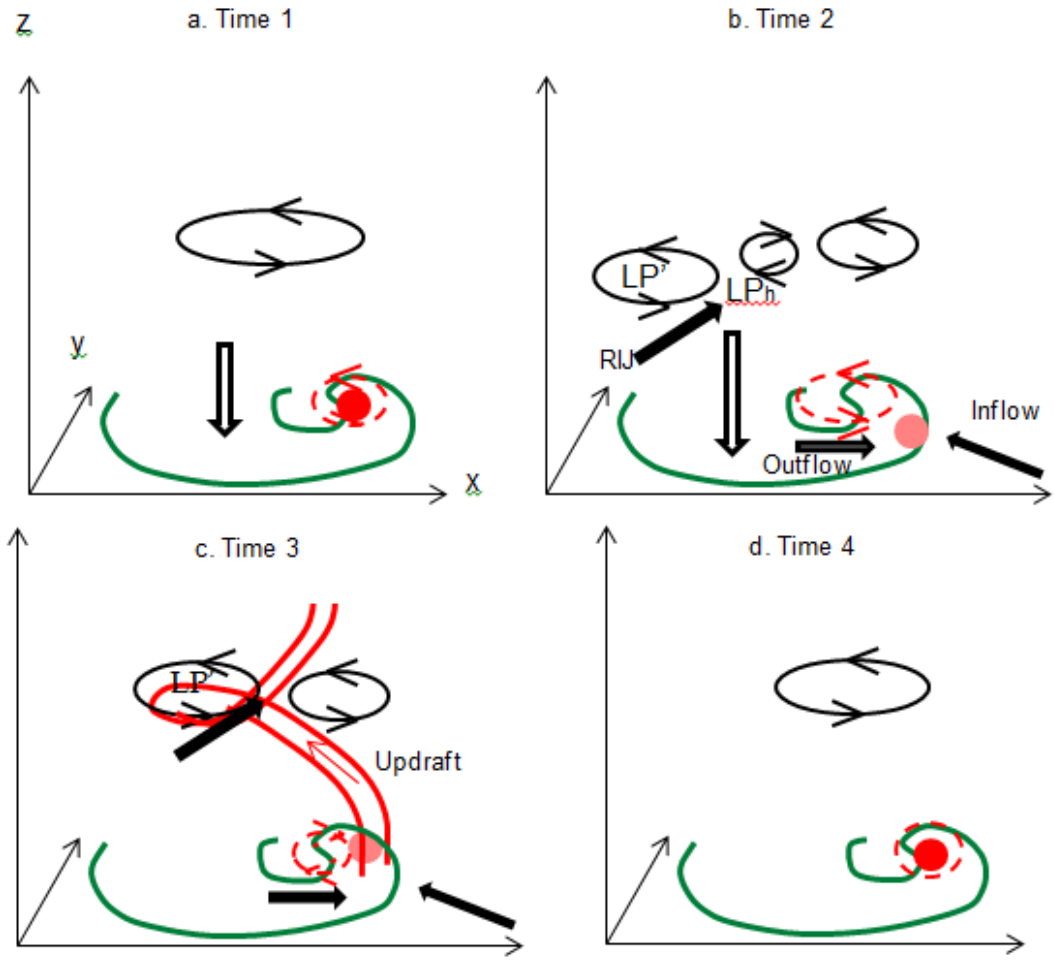


Figure 93: Conceptual model of storm-scale features driving the rear-inflow jet and subsequent intensification of updraft. Green outline indicates approximate 25 dBZ reflectivity contour at low-levels. Red (pink) dots indicate tornadic (subtornadic) vortices. Mesocyclone (low-level mesocyclone) circulations indicated by the black (dashed red) circles. Areas of low perturbation pressure indicated by LP' and hydrostatic low pressure by LP<sub>h</sub>. Solid (outlined) arrows indicate horizontal (vertical) wind motion, length indicates magnitude.

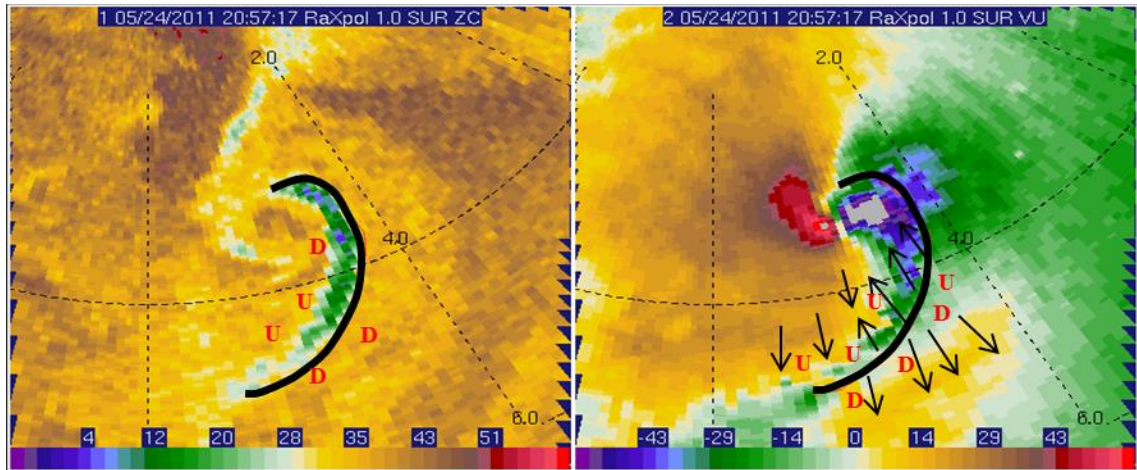


Figure 94: Diagram of convergence and divergence as well as inferred vertical motion associated with the WRB.



Figure 95: Visual images of the horizontal vortex and tornado during the time the WRB was observed in radar. Note the funnels pendant from the horizontal vortex. The red arrow points to the clear area on the western side of the vortex. (Photos © Jeff Snyder.)

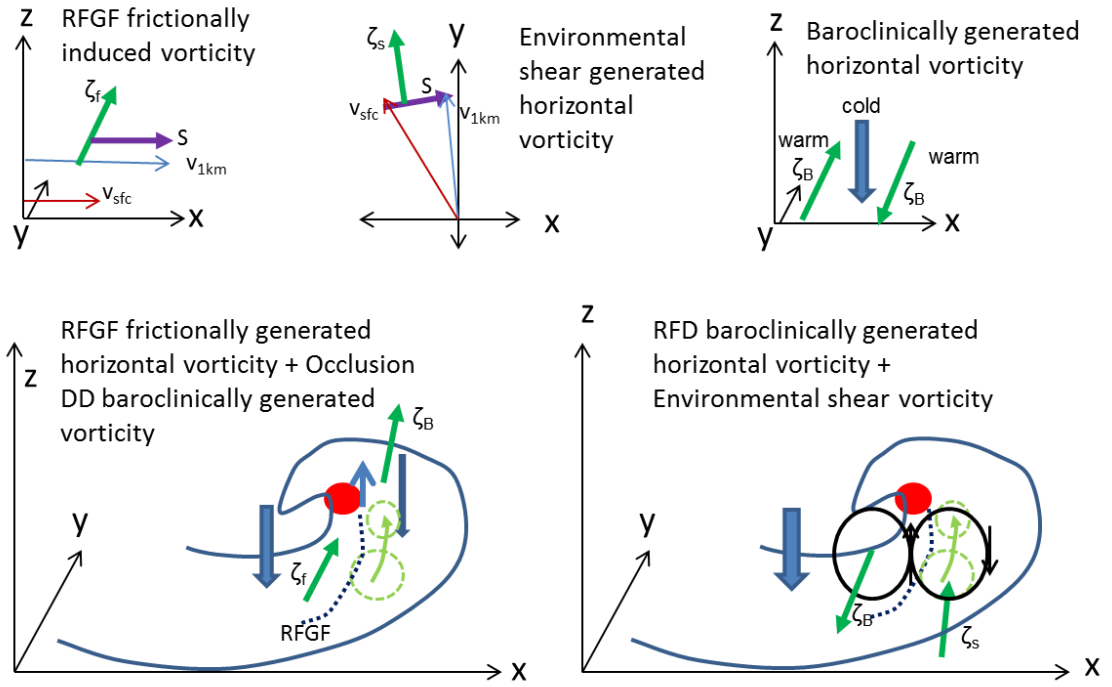


Figure 96: Conceptual figures illustrating the possible mechanisms of forming the horizontal vortex and WRB. Top row: Horizontal vorticity and the orientation of the resulting vorticity vectors induced by: (left) frictional effects on horizontal winds, (middle) vertical wind shear, and (right) a downdraft with a negative temperature perturbation. Purple arrows indicate direction of the shear vector, red (light blue) arrow indicates winds at the surface (1 km), green arrows indicate direction of horizontal vorticity. Bottom row: Generation of horizontal vorticity by (left) gradients in  $w$  and (right) frictional generation behind the RFGF and by balance of environmental wind shear and RFGF shear. Dark blue arrows indicate vertical motion; green vectors indicate the magnitude and direction of the horizontal vorticity vector. The blue outline denotes the 25 dBZ contour near the surface; the green dashed circles indicate the horizontal roll. The dotted blue curve represents the RFGF, and the red circle represents the tornado.

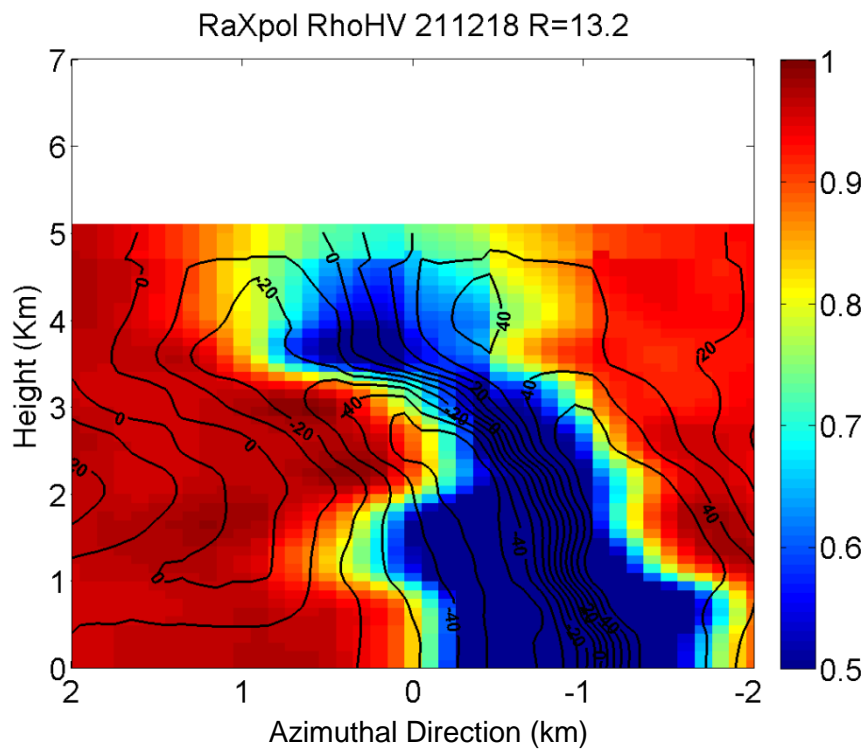
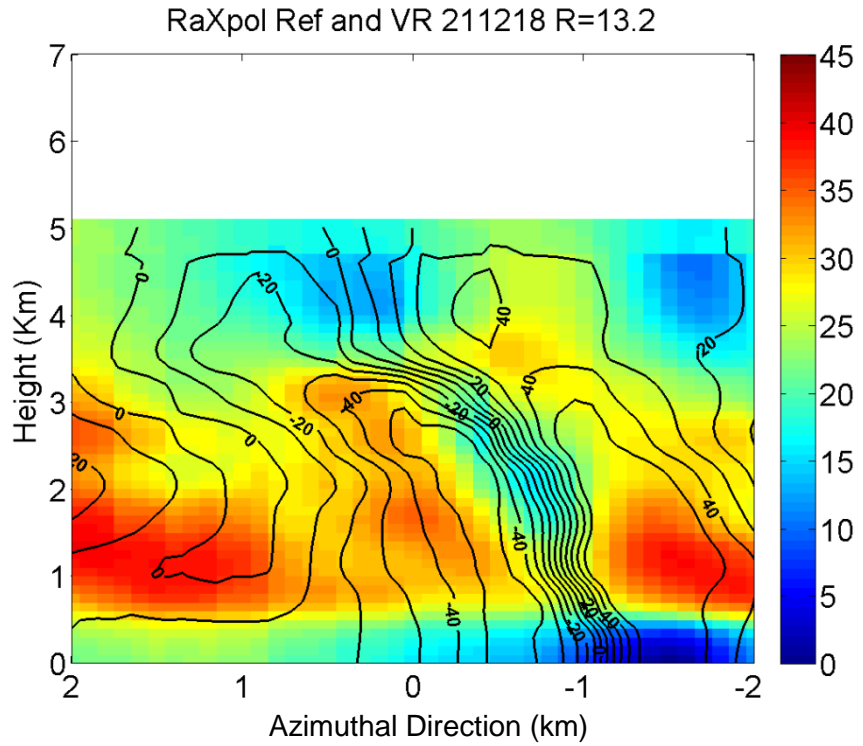


Figure 97: Weak echo hole (top) and tornadic debris signature (bottom) with storm-relative radial velocity contours for the 211218 analysis.